Localized Surface Plasmon Imaging: a non intrusive optical tool to cover nanometer to micrometer scales in biological systems.

Thibault Roland

N° d'ordre: 538
N° attribué par la bibliothèque: _ENSL538

THÈSE

en vue d'obtenir le grade de

Docteur de l'Université de Lyon - École Normale Supérieure de Lyon

spécialité: Physique

LABORATOIRE DE PHYSIQUE et LABORATOIRE JOLIOT CURIE

École Doctorale de Physique et Astrophysique de Lyon

présentée et soutenue publiquement le 30/10/2009

par Monsieur ***Thibault ROLAND***

Titre:

Localized Surface Plasmon Imaging: a non intrusive optical tool to cover nanometer to micrometer scales in biological systems.

Directeur de thèse: Mademoiselle Françoise ARGOUL

Après avis de: Monsieur Brahim LOUNIS
Madame Anne SENTENAC

Devant la commission formée de:

Mademoiselle Françoise ARGOUL, Membre
Monsieur Laurent BONNEVIOT, Membre/Président
Monsieur Samuel T. HESS, Membre
Monsieur Tapas Kumar KUNDU, Membre
Monsieur Brahim LOUNIS, Membre/Rapporteur
Madame Anne SENTENAC, Membre/Rapporteur

La théorie, c'est quand on sait tout et que rien ne fonctionne. La pratique, c'est quand tout fonctionne et que personne ne sait pourquoi. Ici, nous avons réuni théorie et pratique: rien ne fonctionne... et personne ne sait pourquoi !

Albert Einstein.

Quais de la Saône pendant la fête des Lumières 2008, Lyon.

Remerciements

Je tiens tout d'abord à remercier les membres de mon jury d'avoir accepté d'en faire partie et de juger mes travaux. Un merci tout particulier pour Anne Sentenac et Brahim Lounis qui ont rapporté ce manuscrit. *A huge thanks to Sam Hess and Tapas Kundu who, even if they could not be among us for the defense, read this manuscript in details, commented it and asked questions that bettered it.* Enfin, un grand merci à Laurent Bonneviot, qui a accepté, sans hésiter et à la dernière minute (!), d'être dans mon jury et s'est donc vu attribuer le rôle du président. Merci également pour les connaissances que tu m'as apportées et tes avis éclairés, pour tes encouragements, et bien entendu pour les conversations photographiques que nous avons eues.

Je souhaite bien évidemment remercier ma directrice de thèse, Françoise Argoul, pour son encadrement et pour m'avoir permis de réaliser cette thèse dans les meilleures conditions possibles. Merci pour les portes que tu m'as ouvertes, l'enthousiasme que tu m'as communiqué sur ce sujet et cette technique, ainsi que les discussions scientifiques que nous avons eues et qui ont permis de faire avancer les choses dans la bonne direction. J'ai ainsi pu développer mes compétences et mes intérêts grâce à des projets à l'interface entre la physique, la biologie, mais également la chimie, ce qui me tenait particulièrement à cœur.

Merci également au reste de l'équipe (agrandie), car la recherche n'est bien entendu pas faite du travail que d'une personne !! Dans le désordre:
Un merci tout spécial à Lotfi Berguiga, grâce à qui cette thèse n'aurait pas pu être ce qu'elle est : si tu ne m'avais pas formé sur l'optique, si tu n'avais pas volé à mon secours certains jours, si tu n'avais pas fait preuve de cette patience, ou encore si l'on n'avait pas pu réfléchir aux problèmes ensembles... qu'ils soient expérimentaux ou théoriques... Merci également pour les bon moments passés dans la "salle de manips", ou en dehors, et pour les blagues très "dijonnaises".
Merci à Audrey Fahys pour tout: tes explications, ta capacité à rendre simple les choses compliquées, et les discussions scientifiques - ou pas -, les très bon moments, ton amitié et bien entendu ton soutien lors de ce marathon... Bien évidemment merci aussi à ta moitié, Alexis Mosset, et bonne vie à vous deux - et bientôt trois !
Merci à Juan Elezgaray : pour ta modélisation qui nous a permis d'en apprendre beaucoup, et qui continuera d'apporter nombre de réponses. Merci aussi pour tes explications, mais aussi pour ta patience en particulier lors de mon "harcèlement" des derniers mois.
Merci à Pascale Milani pour tes explication sur la biologie, pour les moments à s'arracher les cheveux ensemble dans la salle AFM sur nos expériences respectives, pour ta bonne humeur, et ton amitié. Et bien entendu, merci aussi pour les flyers des expos, et l'affiche de la soutenance !
Un grand merci à André Khalil: pour ton étude des surfaces d'or. Merci car grâce à toi la théorie ne m'a jamais parue aussi simple ! Merci également pour ta bonne humeur et tes coups de main.

Je tiens également à remercier Karine Monier, pour tout ce qui touche à l'imagerie cellulaire. Merci également pour le partage de tes connaissances dans les différents types de microscopie, et pour nos discussions.
Enfin, merci aux "anciens" de l'équipe, qui nous ont beaucoup apporté, et ce à de nombreux niveaux. Merci Nicolas pour m'avoir encouragé le premier à me lancer dans la photo de façon un peu plus "professionnelle" (attention, tu as peut-être ouvert la boite de Pandore; ma conquète du Monde de l'Art est lancée !), pour tes idées originales, ton humour, et tout le reste. Merci San Jun pour ta bonne humeur, je te souhaite de réussir ce que tu entreprendras pour la suite. Et finalement, merci Jürgen et Wenxue pour ce que vous m'avez apporté lors de votre passage.

Je veux également remercier les membres passés et présents du bureau des "étudiants", qui ont contribué à me faire passer un peu plus de trois années à la vitesse de la lumière, grâce à leur enthousiasme et les pétages de plombs occasionnels. Ce fut un réel plaisir de vous côtoyer.
Anaïs, j'espère juste avoir à nouveau quelqu'un comme toi dans mon futur bureau... mais étrangement, j'en doute. Bon courage pour ce qui va arriver (trop vite, tu verras), mais je ne m'en fais pas trop pour toi.
Sabrina, thanks for your friendship and your happiness. If the AFM bothers you too much and you want to give it a gentle... smash, please give it another one from me !
Rémi, il y a de grandes chances que je vienne t'embêter de l'autre côté de l'atlantique (hé hé ! *rire démoniaque*).
Claudia, I'm gonna miss laughting about tBBT's episodes with you... .
Brice et Cong Rong, j'espère que tout se passera bien pour vous dans l'avenir.

Une pensée et un grand merci aussi aux membres du laboratoire Joliot-Curie.
Voici une liste non exhaustive des biologistes, des physiciens, ainsi que des chimistes qui y sont encore ou n'ont fait qu'y passer, et j'y tiens : dans le désordre le plus parfait ! Manu, Alain, Salim, Laurence, Guillaume, Kévin, Christophe, Benoît, Julien, Maggy, Delphine, Fabien, Zofia, Arnaud, Elodie, Cédric, Lamia, Rodrigo, Gilles, Martin, Hélène, Sadhan, Philippe, Fabien, Antoine, Lea, Cristina, Ali, Xavier, Marie-Thérèse, Marie-Jo, Benjamin, Amélie, et Cendrine.
Je n'oublie pas non plus Belen, ni les membres du laboratoire de Physique.

Merci également à de très bons amis, qui ont fait beaucoup pour moi et qui me manqueront durant les quelques temps que je passerai outre-atlantique.
Luc et Maëlle, prennez bien soin de Calista ainsi que de la nouvelle graine qui pousse, qui pousse... J'espère que vous viendrez vite me rendre visite !
Christophe, merci encore pour les discussions sur l'avenir du monde ou sur le nôtre, pour les coups de main, d'avoir été là quand j'en avais besoin. Surtout, si tu en as assez de notre vieille Europe, et que tu veux conquérir l'Amérique, que ce soit pour un court séjour ou y

faire grandir ton Art, n'hésite pas !!
Merci Amandine pour ces petites joutes verbales toujours très divertissantes. De même, si tu veux monter à l'assaut de l'Amérique et y devenir la nouvelle Papesse de la Mode... ;)
Merci à Aurélia, Martine, Pierrick et Fabio pour les super moments lyonnais. A quand le prochain tarot ? A quand le vrai jeu de rôle ? Peut-être en anglais ? ;)
Evidemment un merci tout spécial à ceux qui ont pu assister à la soutenance et participer au pot, dans la bonne ENS ! ;)
Merci à Arnaud, Florent, Anne et les anciens de la Fac...
Et enfin, merci à toutes celles et à tous ceux qui n'ont pas pu venir, mais qui m'ont pourtant soutenu, ont pensé à moi le jour fatidique... et m'ont envoyé des ondes positives, y compris depuis le Chili !

Pour terminer en beauté, un énorme **MERCI** à ma famille pour leur patience, leurs sacrifices, et leur soutien durant toutes ces années et l'apogée que furent ces derniers mois de rédaction. Merci aussi à Didier et Sylvie, pour ces dernières années et tous ces bon moments. Plus particulièrement, une pensée et des remerciements à mes grands-parents et mes parents, sans qui je ne serais pas là où je suis aujourd'hui, ni là où je serai demain. Et pour finir, merci à vous d'être venus assister à ces moments très particuliers qui consistent en l'aboutissement d'un certain voyage, et le début d'un nouveau. Je vous aime.

Abstract

Most of the microscopy techniques used to study biological samples or processes relies on the use of markers (and particularly on fluorescent probes), or on physical probes (AFM or SNOM tips...), that can interact more or less strongly with the observed samples. As a consequence, these techniques may artificially modify the phenomena that are measured.
In order to propose an alternative to these techniques, a high resolution Scanning Surface Plasmon Microscope (SSPM) has been developed in the Laboratoire de Physique and the Laboratoire Joliot-Curie at the Ecole Normale Supérieure de Lyon. This microscope relies on the excitation of surface plasmon waves that consist in collective oscillations of the free electrons at the surface of a metal layer. This resonance is extremely sensitive to the variation of the dielectric index at the interface (and so, to the adsorption of objects such as biological samples). This phenomenon is already used in the global measurement of molecular interactions between two populations (such as antigen-antibody), that are not necessarily marked (Biacore-like or wide field surface plasmon microscopy techniques). The SSPM technique relies on the use of a very high numerical aperture objective lens that focuses the incident light on a small area of the metal surface. The propagation of the plasmon waves towards the center of the illuminated area leads to their structuring and it is actually because of the scanning on the sample that the local variations of the dielectric index are detected.

In the first chapter of this thesis manuscript, we present the principles of high resolution surface plasmon microscopy, both from an experimental and a theoretical point of view. We also present a model of the optical response of the microscope which is based on a multipolar expansion of the Maxwell equations.
In chapter two, we characterize layers of gold that have been deposited onto glass substrates by thermal evaporation. We demonstrate that the SSPM method is able to detect with a very high sensitivity the surface or bulk inhomogeneities of these metal layers. It can also be used to compare samples with varying structures, obtained with different preparation recipes. We address in a third chapter the problem of imaging isolated nanomaterials (metallic and dielectric particles) of different sizes (from 10 to 200 nm of diameter). We show that this method is well suited to visualize such objects and also to discriminate their size or the material they are made of (depending on their dielectric index).
Finally, we apply in the last chapter the SSPM to the visualization of unlabelled biological samples, such as nucleosomes (nucleoproteic complexes) or human fibroblasts in which we resolve several cellular structures (nucleus, nucleolus, cytoskeleton structures).

Keywords: Surface Plasmon Resonance, SPR, Interferometric Surface Plasmon Microscopy, Sub-Wavelength Resolution Imaging, Plasmon Phase Imaging, Atomic Force Microscopy, AFM, Physical Vapor Deposition, Thin Gold Films, Surface Roughness, Wavelet-Based Surface Analysis, NanoParticle, DNA, Nucleosome, Label-Free Cellular Microscopy, Sub-Cellular Structure Detection.

Résumé

La plupart des techniques de microscopie utilisées dans l'étude d'échantillons ou de processus biologiques repose sur l'utilisation de marqueurs (en particuliers fluorescents), ou de sondes physiques (pointes AFM, SNOM...), pouvant interagir plus ou moins fortement avec les échantillons observés. Potentiellement, ce type de technique risque donc de modifier artificiellement les phénomènes mesurés.
Afin de proposer une alternative à ces techniques, un microscope haute résolution reposant sur l'utilisation des plasmons de surface (Scanning Surface Plasmon Microscope, ou SSPM) a été développé au sein du laboratoire de Physique et du laboratoire Joliot-Curie de l'Ecole Normale Supérieure de Lyon. Ce microscope repose sur l'excitation des plasmons, modes d'oscillations collectives des électrons libres d'une couche métallique, dont la condition de résonance est extrÍmement sensible à la variation d'indice diélectrique (et à donc la présence d'objets, en particulier biologiques) au niveau de cette surface. Ce phénomène est déjà utilisé pour la mesure globale d'interactions moléculaires entre deux populations (type antigène-anticorps), non nécessairement marquées (techniques de type Biacore, et de microscopie plasmon en champ large). L'atout essentiel du SSPM est l'utilisation d'un objectif à forte ouverture numérique qui focalise la lumière incidente dans une petite zone de l'interface métal/milieu d'observation. La propagation des ondes plasmoniques vers le centre de la zone illuminée conduit à leur structuration et c'est grâce au balayage de l'échantillon que les variations locales d'indice diélectrique des échantillons sont révélées par cet outil.

Dans le premier chapitre de cette thèse, nous nous attachons à présenter les principes de microscopie haute résolution à plasmon de surface d'un point de vue expérimental mais aussi théorique, en particulier par la modélisation de la réponse optique du microscope par l'intermédiaire d'un développement multipolaire des équations de Maxwell.
Dans un deuxième temps, nous effectuons la caractérisation de couches minces d'or déposées par évaporation thermique sur des substrats de verre. Lors de cette étude, nous montrons que la méthode SSPM permet de détecter avec une très grande sensibilité les inhomogénéités de volume ou de surface de ces couches métalliques, ainsi que leurs variations suivant la préparation des échantillons.
Nous abordons dans une troisième partie la visualisation par microscopie SSPM de nanomatériaux synthétiques (particules métalliques et diélectriques) isolés de différentes tailles (de 10 à 200 nm de diamètre). Nous montrons ainsi que cette méthode est tout à fait adaptée pour imager de tels objets et qu'elle permet aussi de les différencier suivant leur taille ou le type de matériau dont ils sont faits (via leur indice diélectrique).
Enfin, nous appliquons l'imagerie SSPM à la visualisation d'objets biologiques non marqués comme des nucléosomes (complexes nucléoprotéiques d'une taille d'environ 5nm d'épaisseur et 11nm de diamètre), ou encore des fibroblastes humains pour lesquels nous résolvons certaines sous structures (noyau, nucléoles, structures du cytosquelette).

Mots clés: Résonance de Plasmon de Surface, SPR, Microscopie de Plasmon de Surface Interférométrique, Imagerie Sub-Longueur d'Onde, Imagerie Plasmonique par dÈtection de la Phase, Microscopie à Force Atomique, AFM, Dépôt Physique par Phase Vapeur, Couche Mince d'Or, Rugosité de Surface, Analyse de Surface par Détection en Ondelettes, NanoParticule, ADN, Nucléosome, Microscopie Cellulaire Sans Marquage, Détection de Sous-Structure Cellulaire.

Abbreviations

List of the main abbreviations used in this manuscript:

- 3D-ME: 3D Multipolar Expansion
- AFM: Atomic Force Microscopy
- ATR: Attenuated Total Reflection
- DIC: Differential Interference Contrast
- DNA: DeoxyriboNucleic Acid
- ds-DNA: double stranded DeoxyriboNucleic Acid
- FDTD: Finite-Difference Time-Domain
- FWHM: Full Width at Half Maximum
- kDa: kiloDalton
- NA: Numerical Aperture
- NP(s): NanoParticle(s)
- PHI: Photothermal Heterodyne Imaging
- PRP(s): Plasmon Resonant Particle(s)
- PSF: Point Spread FunctionRMS
- RMS: Root Mean Square
- SPP(s): Surface Plasmon Polariton(s)
- SPR: Surface Plasmon Resonance
- SSPM: Scanning Surface Plasmon Microscopy
- SVWF: Spherical Vector Wave Functions
- XPS: X-ray Photoelectron Spectroscopy

Contents

General introduction

In the last half of the XXth century, many high resolution and highly sensitive imaging systems have been developed in order to study, in particular, biological samples. However, most of them rely on the use of markers that are specifically bound to objects of interest (from cellular or nuclear membranes, to subcellular structures, specific proteins such as antibodies, or even to DNA fragments...). Usually, these markers are used to tag specific molecules so that their presence can be detected *in vivo* or *in vitro* and enable the study of cellular structures or processes for instance. The most commonly used labels are dielectric or metallic nanoparticles (conventional optical microscopy, Surface-Enhanced Raman Scattering microscopy), heavy metals (for Electron Microscopy mainly), or fluorescent probes and quantum dots (Confocal Microscopy, Total Internal Reflection Fluorescence Microscopy, Fluorescence PhotoActivation Localization Microscopy, 2-photon microscopy, Second Harmonic Generation...). Therefore, another family of highly resolved techniques that can also be used to study biological samples, rely on the use of physical probes (functionalized or bare cantilevers, optical fibers...) that investigate the local properties of the considered samples; their topography, stiffness, chemistry, their optical properties... (Shear Force Microscopy, Atomic Force Microscopy, Near-field Scanning Optical Microscopy, Scanning Tunneling Microscopy...). However, markers or physical probes may induce detrimental modifications to the biological samples that are studied, and as a consequence artificially perturb the systems: from changes in the rates and overall dynamics of the processes (steric hindrance of the fluorescent markers preventing protein associations...) to toxicity for the host (phototoxicity, aggregation of the NPs or quantum dots...), the partial destruction of the samples (addition of contrast agents, DNA intercaling agents, drying of the samples...), or even their fixation (chemical treatments, deposition of a metallic layer...).
In other words, even if these techniques present many advantages and in particular a high lateral resolution, their intrusiveness must be checked on each case to prevent disrupting the processes and samples studied.
Another group of microscopy techniques have then been developed recently in order to combine both a high lateral resolution and a high sensitivity, and yet minimize the intrusiveness by avoiding the use of markers. One of the most popular methods uses light structuring in such a way that it is considered as a "virtual probe" (Structured Illumination microscopy). Another family of techniques uses the resonance the free electrons located at the interface between a metal surface and a dielectric medium to enhance locally the evanescent electromagnetic field, and probe with no need of markers, either specific chemical bonds of a sample (Surface enhanced Raman spectroscopy), or minute changes in the dielectric index of the

sample (Surface Plasmon Resonance (SPR) methods).

Combining SPR with light structuring (localization of the evanescent field) can be afforded by scanning the sample with a high numerical aperture objective lens. Such a localized plasmon imaging system was developed in Joliot-Curie laboratory: the Scanning Surface Plasmon Microscope (SSPM). Moreover, in order to improve the sensitivity and lower the noise level, a method involving an heterodyne interferometric detection was also implemented. The main purpose of this new tool is to image in a non intrusive and non destructive manner unmarked biological samples, from *in vitro* to *in vivo* environments, and from the nanoscale of macromolecular complexes (such as the nucleosomes, consisting into nucleoproteic assemblies that correspond to the first degree of DNA compaction in the nucleus of eukaryotic cells) to the micrometer scale of a single cell.

We introduce in Chapter 1 the theory of the localized and delocalized Surface Plasmon Resonance (SPR) phenomenon, and some of the SPR microscopy techniques that are devoted to the study of biological samples, from prism-based methods to high numerical aperture objective couplers. Afterwards, we present the SSPM experimental set-up developed in laboratory Joliot-Curie, and a full 3D modeling of this system: the optical response of the SSPM is computed by resolving the Maxwell equations by a multipolar expansion. We report also in Chapter 1 maps of the electric field in the observation medium, and the contrast images of simple nanosized objects such as metallic and dielectric nanoparticles. Therefore,

In Chapter 2, we consider the problem of the preparation of thin ($\sim$45 nm) metal films deposited onto glass coverslips used for surface plasmon imaging. We investigate by Atomic Force Microscopy (coupled with a 2D Wavelet Transform Modulus Maxima analysis of the images of the layers topology), X-ray Photoelectron Spectroscopy and SPR-based experiments, the influence of both the rate of gold deposition, and the chemical treatment of the glass substrates prior to this deposition, on the homogeneity and structures of the gold films. The objective of these studies is to determine if it is possible to enhance the quality (homogeneity) of the thin layers of metal by modifying two physical parameters that are of great importance in their preparation protocol. Finally, thanks to these careful studies, we propose a model taking into account the physical processes involved in the formation of the metal films by thermal evaporation.

Before addressing the problem of imaging unlabeled biological samples, we study in Chapter 3 the SSPM response of synthetic NanoParticles (NPs). Because their dielectric index being likely to vary very little from one colloid to another, and because their optical properties behave intermediately between bulk materials and proteins. We start by considering the visualization in air of metallic (gold) and dielectric (latex) NPs of diameters ranging from 10 to 200 nm, and compare our results with what is expected from the multipolar expansion model. We also discuss the problem of differentiating by SSPM their size and dielectric index. Then, the visualization metal and dielectric NPs is carried out in water, and finally we address the influence of the incident light polarization on the contrast of NPs and on the resolution of the SSPM apparatus.

Finally, we consider in Chapter 4 the question of detecting and visualizing unmarked biological samples (either isolated macromolecular complexes such as nucleosomes, or larger systems such as whole cells: IMR-90 and 293T lines), in air and with a radially polarized

light. Since the SSPM apparatus is constructed around an heterodyne interferometer, it is possible to reconstruct SSPM images of either amplitude or phase variations induced by the presence of samples at the metal surface. Therefore, we present the first phase images of unmarked nanosized or micrometer sized biological samples, and make a comparison of the SSPM amplitude and phase images for the same IMR-90 cell.

Chapter 1

Surface Plasmon fundamental aspects; from Surface Plasmon Resonance to Scanning Surface Plasmon Microscopy

Plasmon confers to metals original optical properties. This plasmon consists in free electron coherent oscillations of a metal, at their normal frequency[1]. Because of both their high density ($\sim 10^{23}$ cm^{-3}) and their charge, they are associated with an ElectroMagnetic (EM) field. Two situations are usually considered: the *volume plasmon* in bulk materials, that are not spatially confined, and *Surface Plasmon (SP)*, which can be either localized (see Section A.2.1) or propagative (in other words delocalized, see Section A.2.2). To study SP and determine their nature (resp. localized or propagative), it is necessary to consider not only the interaction between the charge oscillations and the incident EM field, but also the boundary conditions of this field, and as a consequence the geometry of the system[1] (resp. nanomaterials or flat interfaces between a metal and a dielectric medium).

In Section A, we introduce the plasmon resonance (both historically and from a physical point of view), and discuss the phenomenon of localized SP in the case of NanoParticles (NPs), or propagative SP on an ideally flat film, or a rough metallic surface. We also address the question of the plasmon excitation by light (Section A.3), and focus more precisely on the so-called Kretschmann configuration. In Section B, we present briefly surface plasmon microscopy techniques and we compare amplitude- and phase-based sensors. In Section C, we consider the Scanning Surface Plasmon Microscopy (SSPM) technique that was developed in Joliot-Curie laboratory, and used in particular to detect nanomaterials or biological samples in Chapters 3 and 4 respectively. Finally, modeling of SP and SSPM is presented in Section D.1.

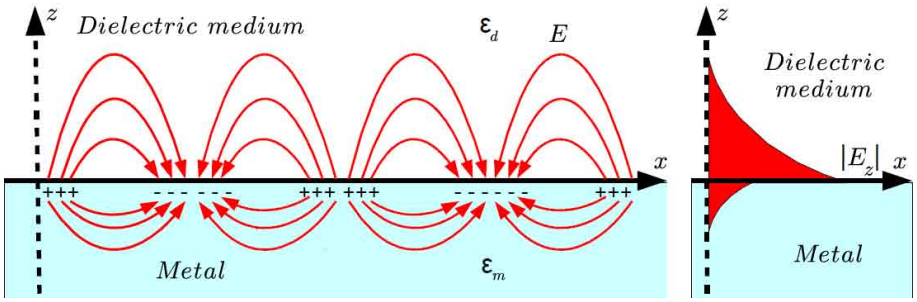

Figure 1.1 Sketch of the electric field distribution at surface plasmon resonance. (a) Transversal view of the interface between a metal and a dielectric medium (air, water...). (b) Amplitude of the plasmon electric field. ϵ_m and ϵ_d are the dielectric permittivities of the metal and dielectric medium respectively. Image extracted and modified from the manuscript of S.J. Zhang[2].

A Introduction to the plasmon resonance

A.1 The plasmon resonance

Surface Plasmon Polaritons (SPPs) are electromagnetic waves propagating at the interface between two materials with dielectric constants of opposite signs, that is a conductive (metal) and a dielectric medium. They are induced by the collective oscillations of the free electrons of the metal (considered as quasi-particles of energy $\mathrm{E}_P = \hbar\omega_P$ with ω_P the frequency of the oscillations) and their amplitude in both materials decay exponentially with the distance to the interface (see Figure 1.1). They can be excited by light and, as addressed in Section A.3, their condition of excitation is extremely sensitive to minute modifications at the interface.

This ability of SPPs to probe minute variations of the surface dielectric index has attracted much interest since the first application of SPR sensing 30 years ago[3]. This phenomenon has proven powerful in particular to characterize and quantify in real time biomolecular interactions[4,5] without the need of labels (such as fluorescent probes) and thin films formation and organization.[6,7]

The phenomenon of delocalized SPPs was first described by Wood in the early twentieth century thanks to the diffraction of light by gratings[8]. However, the excitation of delocalized surface plasmon waves by the method of Attenuated Total Reflection (ATR) was only demonstrated in the late 1960s, by Kretschmann and Raether[9] and by Otto[10].

On the other hand, SPPs can also be confined in NPs embedded in a non metallic dielectric medium of smaller index: these SPPs are considered localized. Numerous studies have been carried out with such structures, especially on biological samples[11].

A.2 Localized versus propagative plasmon resonance

In this section, we address the question of the excitation of plasmon waves from a physical point of view, for several configurations: (i) localized SPPs for a single metallic NP, (ii) delo-

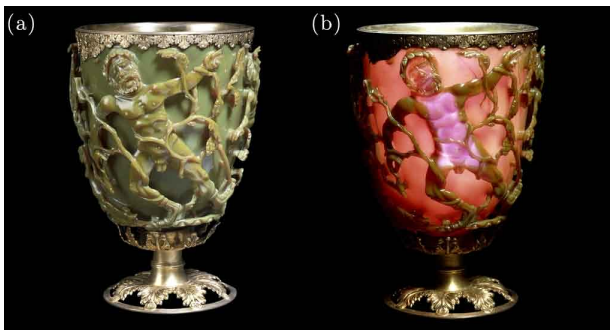

Figure 1.2 Lycurgus cup. (a) (resp. (b)) Photograph of the cup in reflection (resp. transmission). Photographs extracted from the British Museum website.

calized SPPs of a thin film, and (iii) SPPs on a rough metal surface.

A.2.1 Localized Plasmon Resonance (LPR) of NPs

Introduction

This property of nanomaterials raised considerable interests for centuries as they were used as pigments for stained glass (mainly from churches). One of the most famous examples of such a decorative application is the Lycurgus cup (Figure 1.2), dated from the IVth Century B.C., showing a green color in reflection and a red color in transmission (see the British Museum website).

However, applications of nanomaterials to biological systems started in the fifties[12,13]. Nowadays, Plasmon Resonant Particles (PRPs) have found a wide range of applications, for instance in photothermal therapy[14], or as optical tags in microscopy techniques[15]. Moreover, they can also be used to probe variations of the local dielectric index of chemical or biological analytes,[11] or even to enhance fluorescence[16,17] or the spectroscopic signal[18] of molecules in the vicinity of the nanomaterials.

Resonance criterion for a small NP

In the following, we consider spherical metallic NPs which diameter D_{NP} ranges from a few nanometers to ∼100 nm ($D_{NP} << \lambda$). The incident light setting into motion the free electron cloud of the NP, creates an oscillating dipole that emits EM waves (see figure 1.3).

Incident light (of frequency (ω)) couples to plasmon polaritons when the NP dielectric permittivity scales linearly with that of the surrounding medium ($\epsilon_d(\omega)$)[1,19]:

$$\epsilon_m = -\epsilon_d \frac{1+l}{l} \qquad l = 1, 2, 3... \tag{1.1}$$

An infinite number of excitation modes exists, and the lowest one ($l = 1$) is given by[1,11,19,20]:

$$\epsilon_m = -2\epsilon_d \tag{1.2}$$

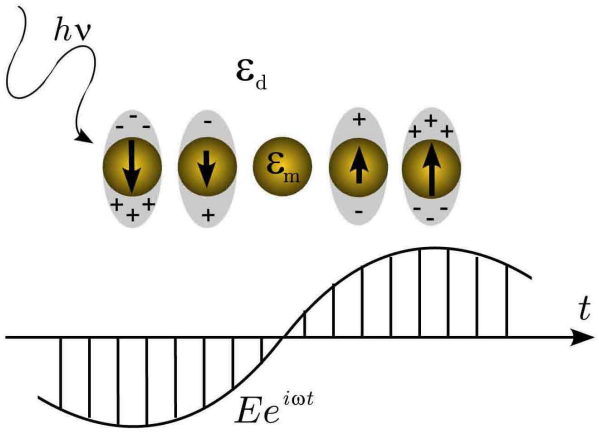

Figure 1.3 Schematic view of the excitation of the localized plasmon particle induced by the motion of the electron cloud under an external EM field (light). The dielectric permittivity of the NP (resp. surrounding medium) is ϵ_m (resp. ϵ_d).

Note that the frequencies ω of the different waves (light, plasmons...) considered in this thesis, together with the dielectric permittivity of the observation medium (air, water) are assumed as being real. However, the dielectric permittivity of noble metals can take complex values: $\epsilon_m(\omega) = \epsilon_m^{'}(\omega) + i\epsilon_m^{''}(\omega)$.
The frequency ω_F corresponding to this first mode (the *Fröhlich mode*[21]) is called the *Fröhlich frequency*[21], for which the polarization of the sphere is uniform (and the particle behaves like a dipole).

For considerations on bigger particles, we refer the reader to References[19–21].

Drude model and frequency of resonance

Thanks to the Drude model[19] that describes the optical properties of metals, we can take into account the oscillations of the free electrons. Now, the dielectric constant reads:

$$\epsilon_m = 1 - \frac{\omega_p^2}{\omega^2 + j\gamma\omega} \tag{1.3}$$

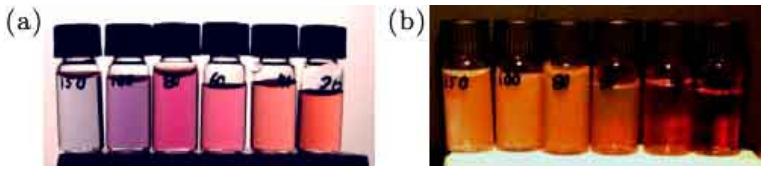

Figure 1.4 Suspensions of spherical gold NPs of various sizes (from left to right: 150, 100, 80, 60, 40, and 20 nm) in water. Photograph in transmission (a) or in reflection (b). The concentration of the NPs is less than 0.01% (weight). Figure extracted from Sönnichsen[22].

with the real and imaginary parts:

$$\epsilon_m^{'} = 1 - \frac{\omega_p^2}{\omega^2 + \gamma^2} \tag{1.4}$$
$$\epsilon_m^{''} = 1 - \frac{\gamma\omega_p^2}{\omega(\omega^2 + \gamma^2)}$$

where γ is the damping constant. $\omega_p = \sqrt{\frac{n_e e^2}{m\epsilon_0}}$ is the so-called *plasma frequency (or Langmuir waves)*, consisting in the rapid oscillations of the electron density in conducting media at low temperature (with n_e the density of the electrons, e their elemental charge, and m their mass).

For small spherical NPs near the plasmon frequency ω_{sp} (for which $\epsilon_m = -2\epsilon_d$), and by assuming $\omega_p^2 >> \gamma^2$, we get from Equation 1.5 the frequency of resonance of the NP in the embedding medium:

$$\omega_{sp} = \frac{\omega_p}{\sqrt{1 + 2\epsilon_d}} \tag{1.5}$$

Therefore, Equation 1.5 confirms that *via* ω_p, and more precisely the density of the electrons n_e, the NP resonance frequency depends on its nature.

Absorption and scattering of NPs

Let us now focus on the absorption and scattering phenomena for a small spherical NP of radius r_{NP} ($r_{NP} << \lambda$).

The model describing the response of a small metallic sphere has been developed by Lord Rayleigh and neglects the effects of self-induction by the EM fields (retardation). In this case, the absorption and diffusion of the NP can be computed using the electrostatic approximation (the EM field inside the NP is considered as constant, *i.e.* when $r_p \lesssim \lambda/10$).

Therefore, the polarizability of the sphere reads[19,20]:

$$\alpha_0 = 4\pi r_p^3 \frac{\epsilon_m - \epsilon_d}{\epsilon_m + 2\epsilon_d} \tag{1.6}$$

which gives us the scattering and absorption cross-sections:[19]

$$C_{sca} = \frac{k^4}{6\pi} |\alpha_0|^2 = \frac{8}{3}\pi \; r_p^6 \; k^4 \; \left| \frac{\epsilon_m - \epsilon_d}{\epsilon_m + 2\epsilon_d} \right|^2 \tag{1.7}$$

$$C_{abs} = k \; \Im\{\alpha_0\} = 4\pi \; r_p^3 \; k \; \Im\left\{ \frac{\epsilon_m - \epsilon_d}{\epsilon_m + 2\epsilon_d} \right\} \tag{1.8}$$

where $k = 2\pi/\lambda$.

Figure 1.4 illustrates the dependence of the NP's frequency of resonance with their size. Note that one of the main reasons why PRPs made of gold (Au), silver (Ag), or copper (Cu) have attracted such an interest in the last few decades is that their condition of resonance is fulfilled for visible light[24,25]. Furthermore, such materials are easy and inexpensive to synthesize in a wide range of shapes and sizes[26], and they also present the advantage to

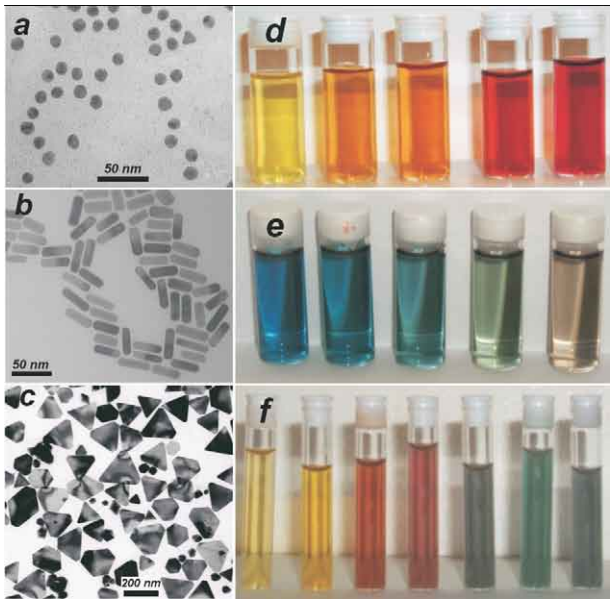

Figure 1.5 Dependence of the NP's frequency of resonance with their shape. Left panel: transmission electron micrographs of gold nanospheres (a); nanorods; (b) silver nanoprisms (c). Right panel: (d) colloidal dispersions of Au/Ag alloy NPs with increasing gold concentration; (e) gold nanorods of increasing aspect ratio; (f) silver nanoprisms with increasing lateral size. Figure extracted from Liz-Marzàn[23].

be conveniently functionalized by chemical and biomolecular ligands[27], so as to make them biocompatible.

Moreover, it has also been demonstrated that the frequency of excitation of the plasmon waves does not only depend on the surrounding medium[28] or on the NP's material or size[19,20,22]. Indeed, it also depends on its shape[14,29,30] (see Figure 1.5 for an illustration).

NPs assembly

Finally, it has been shown[31–35] that coupling interactions between NPs (see Figure 1.6) can influence the LPR.

Figures 1.7[33] and 1.8(a) and (b)[35] illustrate the influence of the interparticle distance for two spherical NPs or nanorods respectively. It can also be noted from these figures that the direction of the polarization (orientation of the electric field) is an important parameter of the extinction phenomenon.

The same way, it has been demonstrated that the size of the NP aggregates (see Figure 1.8(c) and (d)) affects the conditions of excitation of the plasmons[31,35], that "delocalize" since the electronic coupling between the NPs increases[34]. Eventually, for large enough aggregates (see Figure 1.9), the situation converges to the thin gold film configuration presented in the following section, and the plasmon waves propagate along the assembly.

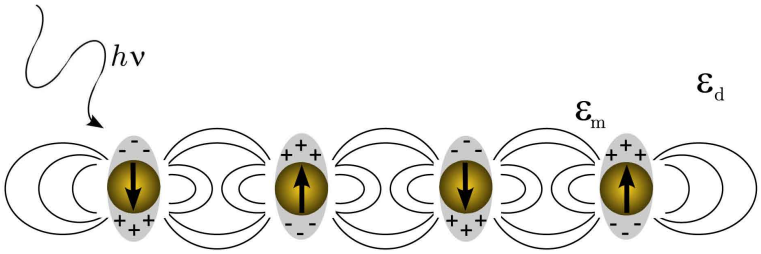

Figure 1.6 Schematic view of the excitation of the localized plasmon waves induced by an external EM field (light) for an assembly of metallic NPs. The dielectric permittivity of the NP (resp. the surrounding medium) is ϵ_m (resp. ϵ_d).

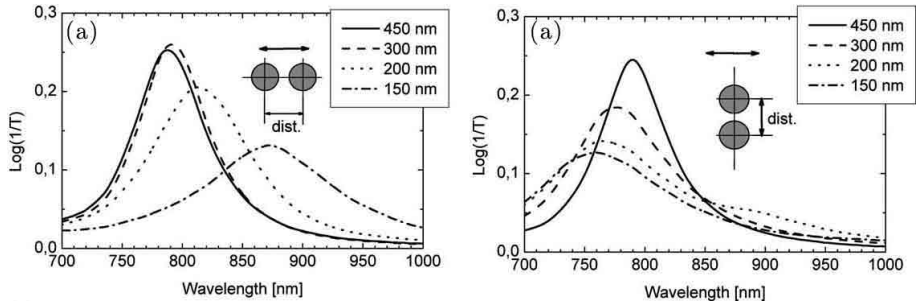

Figure 1.7 Extinction ($log(1/Transmission)$) spectra of a 2D array of gold NP pairs for varying interparticle center-to-center distances (150, 200, 300, and 450 nm). The polarization direction of the exciting light (represented by the double arrow) is (a) parallel to the interparticle axis and (b) orthogonal to it. Figure extracted from Rechberger *et al.*[33].

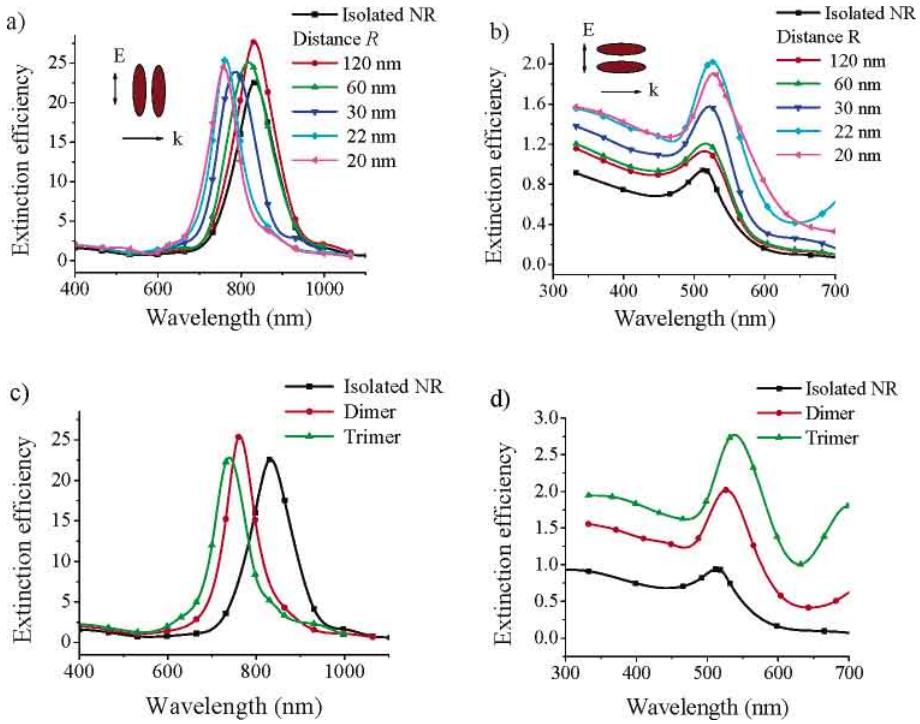

Figure 1.8 Simulated extinction efficiency spectra of gold nanorods (long and short axis are $\sim$ 80 nm and $\sim$ 20 nm respectively) for varying interparticle center-to-center distance (120, 60, 30, 22, and 20 nm, where the nanorods touch each other): the polarization direction of the exciting light is (a) parallel (longitudinal) or (b) orthogonal (transverse) to the long axis of the nanorods. (c) Longitudinal and (d) transverse plasmon excitation of a NP cluster made of isolated dimer or trimer of nanorods. The internanorod distance is fixed to 22 nm. Figure extracted from Rechberger *et al.*[33].

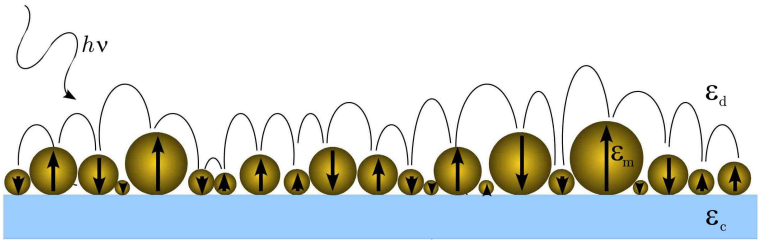

Figure 1.9 Schematic view of the excitation and electronic coupling of the localized plasmon waves for an assembly of metallic NPs lying on a substrate.

A.2.2 Propagative (delocalized) Surface Plasmon Polaritons (SPPs) of an ideal thin metallic film

These surface waves were studied first in the early 20^{th} century by Zenneck[36] and Sommerfeld[37] in the field of wireless telegraphy (for radio frequencies, and not visible light). In this section, we address the question of the excitation by visible light of delocalized plasmon waves at the interface between a thin and perfectly flat metal film and a dielectric medium (see Figure 1.10).

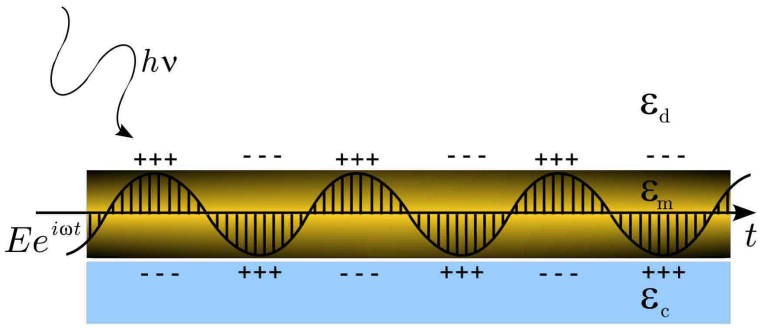

Figure 1.10 Schematic view of the excitation of the delocalized surface plasmon on a perfectly flat metal film by an external EM field (light). The dielectric permittivities of the coupling medium, metal and the (dielectric) observation medium are ϵ_c, ϵ_m and ϵ_d.

Resonance criterion for an ideal thin metallic surface

Propagative SPPs can be excited by visible light, and the coupling conditions for a smooth interface are given by the dispersion relation:[1,38–40]

$$k_{sp} = \frac{\omega}{c}\left(\frac{\epsilon_m \epsilon_d}{\epsilon_m + \epsilon_d}\right)^{1/2} > k_{light} = \frac{\omega}{c}\sqrt{\epsilon_d} \tag{1.9}$$

Assuming that $\epsilon_m^{''} << |\epsilon_m^{'}|$, the real and imaginary parts of the wave vector ($k_{sp} = k_{sp}^{'} + ik_{sp}^{''}$) read:

$$k_{sp}^{'} = \frac{\omega}{c}\left(\frac{\epsilon_m^{'} \epsilon_d}{\epsilon_m^{'} + \epsilon_d}\right)^{1/2} \tag{1.10}$$

$$k_{sp}^{''} = \frac{\omega}{c}\left(\frac{\epsilon_m^{'}\epsilon_d}{\epsilon_m^{'}+\epsilon_d}\right)^{3/2}\frac{\epsilon_m^{''}}{2{\epsilon_m^{'}}^2} \tag{1.11}$$

Equations 1.10 and 1.11 imply that $\epsilon_d < |\epsilon_m^{'}|$, which is generally fulfilled for metals in visible light.

The polarization of the light used to illuminate the metal interface is of great importance, since only p-polarized light, for which the electric field is in the plane of incidence can set the free electrons of the metal into motion, and then induce the excitation of SPPs (see Sections A.3.2 and C.4).

Properties of the evanescent field

When SPPs are excited by light (see Section A.3), one has $k_{light} = k_{sp}$, and an evanescent EM field is created both in the metal and in the dielectric media. The *penetration depth* $\delta_{z,i}$ of this field in the metal or in the dielectric medium ($i = m, d$ respectively), defined as the distance (normal) to the surface for which the field amplitude decreases by a factor e, reads[1,39]:

$$\delta_{z,i} = \frac{1}{|k_{z,i}^{''}|} \tag{1.12}$$

that is:

$$\delta_{z,i} = \left|\Im\left\{\epsilon_i\left(\frac{\omega}{c}\right)^2 - {k_{sp}}^2\right\}\right|^{-1} = \frac{\lambda}{2\pi}\left(\frac{|\epsilon_m^{'}+\epsilon_d|}{{\epsilon_i^{'}}^2}\right)^{1/2} \tag{1.13}$$

with $i = m, d$ for the metal or the dielectric medium.

From Equation 1.13, we can estimate $\delta_{z,i}$ in the two materials considered: for $\lambda = 633$ nm, the penetration depth in air ($\epsilon_d = 1$) and in gold ($\epsilon_m = -12.8 + j1.36$, see Thèye[41]) are $\delta_{z,d} \sim 350$ nm and $\delta_{z,m} \sim 27$ nm respectively.
The same way, the penetration depth in water ($\epsilon_d = 1.77$) and in gold are $\delta_{z,d} \sim 190$ nm, $\delta_{z,m} \sim 26$ nm respectively.

The same way, we can define the *propagation length* (L_x) of the surface wave along the interface by the distance for which the amplitude of the EM field is decreased by a factor e:

$$L_x = \frac{1}{2k_{sp}^{''}} \tag{1.14}$$

Thanks to Equation 1.11, we get:

$$L_x = \frac{\lambda}{2\pi}\left(\frac{\epsilon_m^{'}+\epsilon_d}{\epsilon_m^{'}\epsilon_d}\right)^{3/2}\frac{{\epsilon_m^{'}}^2}{\epsilon_m^{''}} \tag{1.15}$$

We can now estimate L_x for $\lambda = 633$ nm from Equation 1.15 for gold/air (resp. water interface): $L_{x,air} = 10.7$ μm (resp. $L_{x,water} = 4.1$ μm).

In conclusion, we have seen in this section that the excitation of SPPs by light induces the creation of an EM field that is confined within few hundreds of nanometers at the metal-

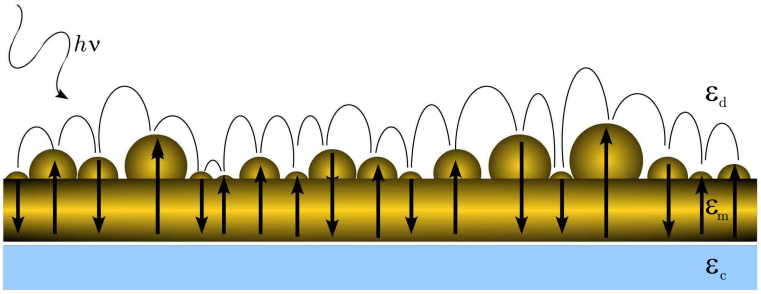

Figure 1.11 Schematic view of the excitation of the delocalized surface plasmon on a rough metal film by an external EM field (light). The dielectric permittivities of the coupling medium, metal and the (dielectric) observation medium are ϵ_c, ϵ_m and ϵ_d.

-dielectric interface. However, the propagation length of these surface waves is much longer, typically $\sim$ 5 to 10 μm (in water or in air respectively).

A.2.3 Influence of the film roughness on the Surface Plasmon Resonance (SPR)

Rather few theoretical or experimental works carried out on SPR have taken into account the inhomogeneities of the metallic films on which the SPPs are launched. Indeed, the preparation of thin ($d \sim 45$ nm) metal films usually leads to surface and bulk inhomogeneities (see Chapter 2 for a detailed presentation and study of this aspect), no matter how the substrates are prepared. However, it was early recognized[1,42–45] that the inhomogeneities of the metallic films, and in particular the roughness (see Figure 1.11), may lead to modifications in the SPR phenomenon. We discuss first the influence of this roughness on the excitation of the surface waves, and second on the EM field at the interface.

Influence of the roughness on the conditions of excitation of the SPPs

In 1988, Raether[1] showed that the metal film inhomogeneities (both in volume and and surface) can be considered as perturbations of its dielectric permittivity:

$$\epsilon_m(x,y,z) = \epsilon_m + \Delta\epsilon_m(x,y,z) \tag{1.16}$$

As a consequence, he suggested to add an extra term in Equation 1.9 so as to take into account the perturbations Δk_{sp} in the dispersion relation:

$$k_{sp}^{'} = \frac{\omega}{c}\left(\frac{\epsilon_m^{'}\epsilon_d}{\epsilon_m^{'}+\epsilon_d}\right)^{1/2} + \Delta k_{sp}^{'} \tag{1.17}$$

Note that a more detailed study of the influence of the roughness on the dispersion relation (in the case of a prism-coupling configuration) can be found in Reference[1].

Influence of the surface roughness on the SPPs propagation length

We saw in the previous section that the EM field of the plasmon waves propagating along a perfectly flat metallic surface decays in the lateral direction, and that this distance is given by L_x (see Equations 1.14 and 1.15).

However, for rough films, it has been seen earlier that surface inhomogeneities induce the localization of plasmon waves[43,44].
As a consequence, it was demonstrated theoretically that the propagation length of the plasmon waves can be influenced by two processes: first, the surface roughness can reradiate photons in the dielectric medium[1], and second, the SPPs are scattered[1,45] in different directions (with no change in the absolute value of the wave vector).
The relations of the mean free path lengths[1] for radiation loss (L_{rad}) or scattering (L_{sca}) in presence of roughness, not bulk are given by Equations 1.18 and 1.19 respectively, when assuming that $|\epsilon_m^{'}| >> 1$ and $k_x\sigma << 1$:

$$L_{rad} = \frac{3}{4}\left(\frac{\lambda}{2\pi}\right)^5 \frac{|\epsilon_m^{'}|^{1/2}}{\sigma^2\delta^2} \tag{1.18}$$

$$L_{sca} = \frac{2}{3}\left(\frac{\lambda}{2\pi}\right)^5 \frac{|\epsilon_m^{'}|}{\sigma^2\delta^2} \tag{1.19}$$

with the parameters δ and σ characterizing the roughness of the surface, respectively its Root Mean Square (RMS) and the correlation length of the corrugations.
If the surface has a roughness comparable to those we prepare by thermal evaporation ($\delta \sim$ 1.5 nm and $\sigma \sim 50$ nm for instance), we can estimate from Equations 1.18 and 1.19 the mean free path lengths for the scattering and radiation losses: L_{sca} ∼15.74 mm and L_{rad} ∼4.95 mm respectively. Therefore, we see that these distances are several orders of magnitude higher than the propagation length of the SPPs ($L_{x,air} = 10.7$ μm, see Section A.2.2, and more precisely Equation 1.15), which indicates that in this case the surface roughness alone does not appear to have much influence on the surface waves. However, let us note that if we also take into account the bulk roughness of the layers ($\delta \sim 30$ nm) with the same approach, we have L_{sca} ∼39 μm and L_{rad} ∼12.3 μm, which gets closer to the propagation length, and shows that in this case light is reradiated by the metal films.
As a consequence, we make the first-order approximation that the surface roughness can be neglected when considering typical SPR spectroscopy or microscopy techniques (contrary to high resolution SPR microscopy, see Chapter 2).

A.3 Coupling between photons and surface plasmons

SPPs can be excited through several configurations (see Figure 1.12 for the most commonly used ones): nanostructures as seen in the previous section, waveguide coupling[46] (Figure 1.12(B)), fiber optics[47–49] (Figure 1.12(C)), side-polished fiber coupling[47] (Figure 1.12(D)), gratings[1,20,46] (Figure 1.12(E)), or even with prisms (Figure 1.12(A)) of appropriate dielectric constant. In this section we focus prism coupling.

A.3.1 Exciting surface plasmon polaritons in the Attenuated Total Reflectance (ATR) configuration

If light is reflected by a metallic film (ϵ_m, complex) placed between two dielectric media, one of them being the coupling medium (ϵ_c), such as a glass prism, and the other the observation

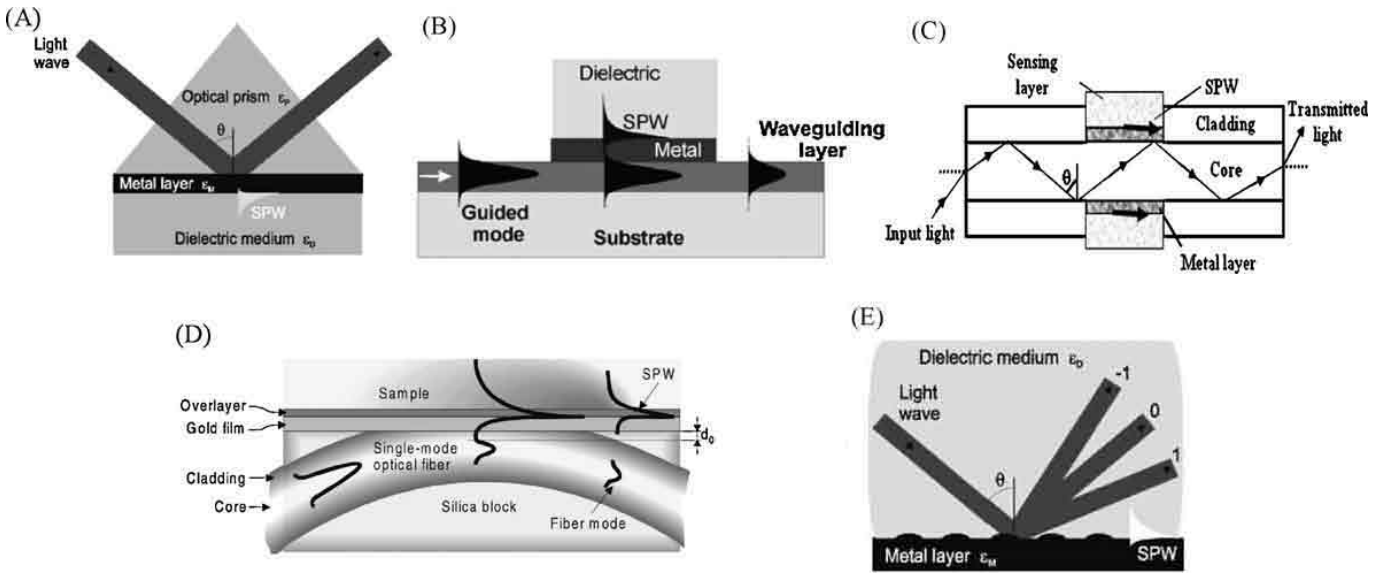

Figure 1.12 Various SPR sensor configurations. (a) Prism coupling, (b) waveguide coupling, (c) optical fiber coupling, (d) side-polished fiber coupling, (e) grating coupling. Figure extracted from Fan *et al.*[50].

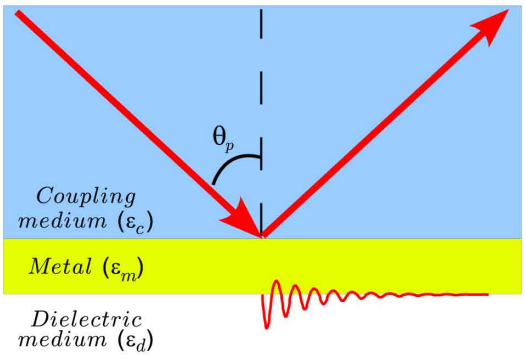

Figure 1.13 Coupling between light and the SPPs: the EM field propagates inside the coupling medium and launches the SPPs at the metal/observation medium interface, for the angle of incidence θ_P (see Equation 1.21).

medium(ϵ_d), such that $\epsilon_c > \epsilon_d$, the projection of the wave vector along the surface reads:

$$k_x = \frac{\omega}{c}\, n_c\, \sin\theta \tag{1.20}$$

with θ_P the angle of incidence depicted in Figure 1.13.

Figure 1.14 illustrates the coupling relation between light and SPPs at the angle of incidence θ_P:

$$k'_{sp,x} = \frac{\omega}{c}\left(\frac{\epsilon'_m \epsilon_d}{\epsilon'_m + \epsilon_d}\right)^{1/2} = \frac{\omega}{c}\, n_c\, \sin\theta_P \tag{1.21}$$

Such an excitation can be achieved by either of the two configurations presented in Figure 1.15. For the first one (Fig. 1.15(a)), named the Otto configuration, the glass prism and the metal film are separated by a dielectric layer (air) whose thickness is of the order of the wavelength, leading to a coupling of the evanescent wave at the glass/air interface with the SPPs at the metallic surface. Figure 1.15(b) shows the so-called Kretschmann configuration, where a thin (∼50 nm) metal film is directly in contact with the coupling medium. In this

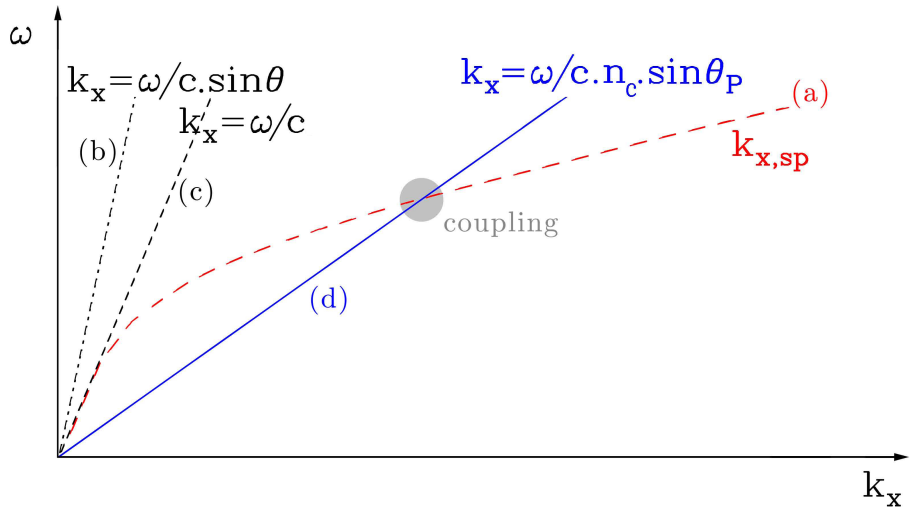

Figure 1.14 Dispersion curves for the multilayered system presented in Figure 1.13. (a) dispersion curve for surface plasmon waves at the metal/observation medium interface (see Equation 1.10). (b) limit of the light cone for an EM field propagating in air. (c) propagation of light reflected at the incidence θ. (d) propagation of light reflected by the metal layer for the angle of incidence θ_P. The intersection between (a) and (d) shows that the conditions of coupling between light and the SPPs are achieved for θ_P.

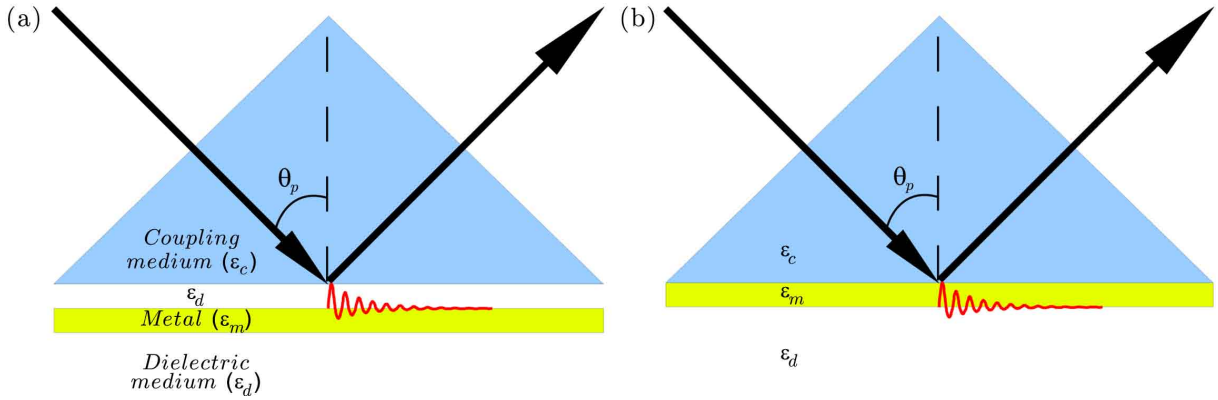

Figure 1.15 Two ATR configurations to excite the SPPs. (a) Otto[10] and (b) Kretschmann[9] configurations.

case, light couples with the surface waves, and the properties of the evanescent EM field are given in Section A.2.2.

Table 1.1 presents the SPR angle θ_P for the configurations considered in this thesis, as computed from Equation 1.21, and shows that increasing the dielectric index of the coupling medium leads to a smaller value of the angle of SPPs excitation.

observation medium (ϵ_d)	coupling medium	angle of resonance
air; $\epsilon_d = 1$	$n_c = 1.515$	$\theta_P = \sim 43°$
water; $\epsilon_d = 1.33^2$	$n_c = 1.515$	$\theta_P = \sim 71°$
water; $\epsilon_d = 1.33^2$	$n_c = 1.785$	$\theta_P \sim 53°$

Table 1.1 Determination of the SPR angle θ_P for the configurations considered in this thesis, as computed from Equation 1.21, for a gold layer of 45 nm thick ($\epsilon_m = -12.8 + j1.36$ at 633 nm).

A.3.2 Evidencing the surface plasmon

Most of the studies dedicated to the detection of molecular species or interactions, or even SPR microscopy assays rely on the use of Kretschmann-based set-ups. Figure 1.16 presents a schematic view of a typical SPR sensor, which is based on the variations of the dielectric index at the metal/observation medium interface. Probe molecules (such as antibodies) are immobilized at the metal surface, and injected target species (not necessarily labeled; for instance antigens, flowed by a microfluidic system) specifically bind to the probes, and change the local dielectric index of the interface. As a consequence, the conditions of light coupling with SPPs is changed, and the angle of resonance θ_P changes too. By monitoring the variation of θ_P, it is then possible to probe interactions taking place at the surface.

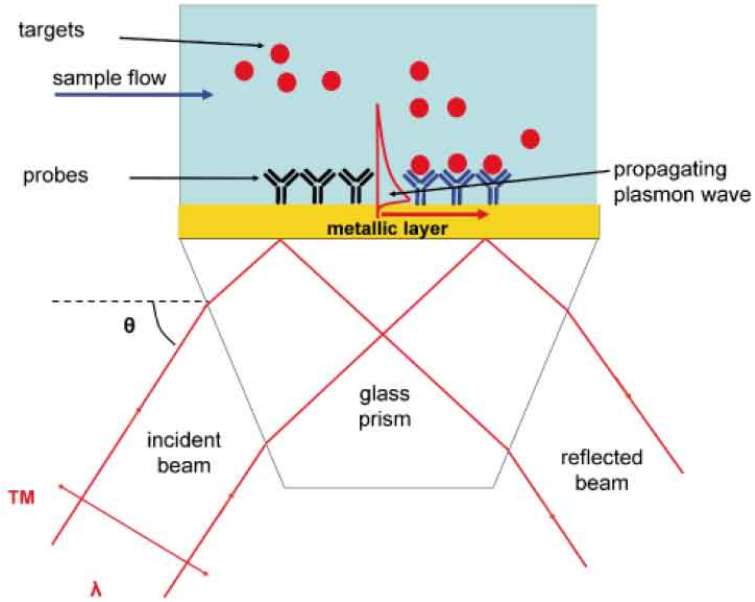

Figure 1.16 Schematic of an SPR sensor in Kretschmann configuration: probe molecules are immobilized at the metal surface. Target species are flowed by a microfluidic system and specifically bind to the probes. Figure extracted from Velasco-Garcia[51].

In SPR spectroscopy, variations of θ_P can be monitored by measuring either the intensity or the phase of the reflected light with respect to time. We present in Figure 1.17 the theoretical SPR intensity and phase curves for dielectric layers ($\epsilon_d = 2.56$) of different thicknesses (d_S) adsorbed on a flat gold surface.
The first remark we can make from Figures 1.17(a) and (b) is that varying the angle of incidence of the purely s-polarized light[52] (dashed curves) does not change much the reflected beam intensity I_S (or phase φ_S). However, when light is purely p-polarized,[52] a very large drop in the reflected intensity I_P (or phase φ_P) occurs. This variation is characteristic of the surface plasmon excitation, and the angle θ_P corresponding to the minimum of the intensity curve (or to the maximum of the slope of the phase curve) corresponds to the angle of resonance. Adding a dielectric layer ($\epsilon_d = 2.56$) of 5 nm on top of the gold film shifts the angle of resonance by $\sim 0.7°$.

Figure 1.17(a) and (b) show the $I_P/I_S(\theta)$ and $[\varphi_P - \varphi_S](\theta)$ curves around the angle of resonance, for thicknesses d_S of the extra dielectric layer ranging from 0 to 5 nm. We observe from these curves that the adsorption of a complete dielectric layer of 1 nm shifts the angle of resonance by $\Delta\theta_P = 0.115°$. The typical resolution in angle of such sensors being in the order of 0.001 degrees (and may be pushed down to $\sim 10^{-6\circ}$ for phase detection[53]), we see how these biosensors can be sensitive to the interaction of even a smaller number of molecules at the metal surface than a complete monolayer.

To conclude this section, we have shown that surface plasmon can be either localized (for curved metallic structures like NPs) or propagative (on rather smooth surfaces).
We saw that when the size of the NPs is small compared to the wavelength of the incident

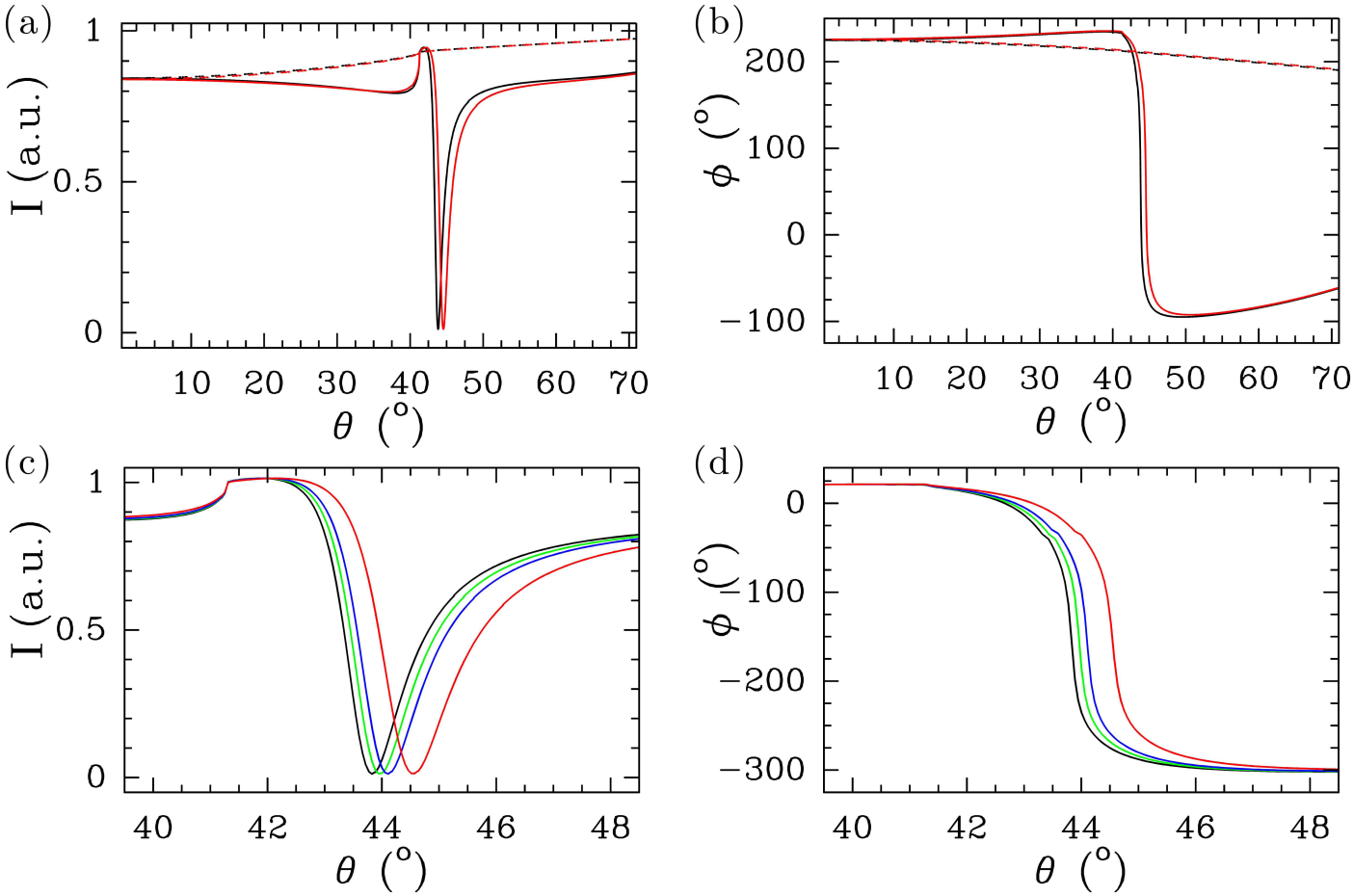

Figure 1.17 Theroretical SPR intensity I and phase φ curves of dielectric layers ($\epsilon_d = 2.56$) of thickness d_S adsorbed on a flat gold surface: d_S =0, 1, 2, or 5 nm (black, green, blue or red curves). The thickness of the gold film is 45 nm and the wavelength $\lambda = 633$ nm. Left panel: (a) $I_P(\theta)$ (plain line) and $I_S(\theta)$ (dashed line) curves for a purely p- or s-polarized light[52] respectively; (c) $I_P/I_S(\theta)$ curve around the angle of resonance θ_P. Right panel: (b) $\varphi_P(\theta)$ (plain line) and $\varphi_S(\theta)$ (dashed line) curves for a purely p- or s-polarized light respectively; (d) $[\varphi_P - \varphi_S](\theta)$ curve around the angle of resonance θ_P.

light, its interaction with the NP EM field sets the free electrons into a coherent motion (the NP behave like a dipole), and leads to the creation of a plasmon resonance. The wavelength of this plasmon wave depends on the nature, the size, and the morphology of the nanomaterial. We have also seen that SPPs can be excited at a metal/dielectric interface, and lead to the creation of an evanescent field that decays exponentially with the distance to the surface, and propagates along this interface for long distances (~ 10 μm).
Finally, we saw that delocalized SPPs can be excited with several configurations, and in particular with prism-based set-ups. We also noted that such sensors are ideal to monitor molecular interactions (with no need of labels, especially fluorescent), and present a high sensitivity to minute modifications of the interface dielectric index.

B Surface plasmon microscopy techniques

We propose in this section to make a brief overview of the different microscopy techniques that use SPR as a biosensor to probe minute modifications at a metal/dielectric medium interface. As more and more set-ups are developed for specific sensing (see Figure 1.12), we do not claim to be exhaustive, but rather to present the evolution of SPR-based microscopy techniques towards high resolution imaging of biological samples. We present first the simplest and most widespread techniques, that rely on the coupling of light with SPPs using a prism, and afterwards we address the question of plasmon waves excited by high Numerical Aperture (NA) objective lenses. For both coupling methods, we detail the set-ups using amplitude, or phase detection.

B.1 Prism-based microscopy techniques

B.1.1 Amplitude imaging

We focus in this section on the most commonly used SPR microscopy technique since its development by Rothenhausler and Knoll[56] in 1988. We present in Figure 1.18 two typical set-ups based on the detection of the reflected light intensity to probe the small variations of the dielectric index of biological samples.

Such microscopy set-ups rely on the use of the prism to excite the SPR waves, and a system of a lens and CCD camera to conjugate and acquire the image of the surface. Usually, the angle of incidence of the p-polarized light is chosen close to the angle of resonance θ_P for the bare metal (often gold). Therefore, the local modifications of the dielectric index along the interface lead to changes in the condition of the SPPs coupling, that shift θ_P to higher values (see the green, blue and red curves in figure 1.17(a) and (b)). As a consequence, for a fixed angle of incidence θ, the contrast of the SPR image is ruled by the difference in the reflectivity along the surface (due to local modifications of the dielectric index).
We present in Figure 1.19 examples of SPR images, of dielectric spots in (a) (the feature

size is ∼100 μm and ∼50 μm for A and B respectively) or a goldfish glial cell in (b). From these images, we see that SPR microscopy is very sensitive to minute modifications of the neighborhood of the interface. However, they also illustrate very clearly the main drawback of such a technique, that is the relatively low lateral resolution (few micrometers) which is

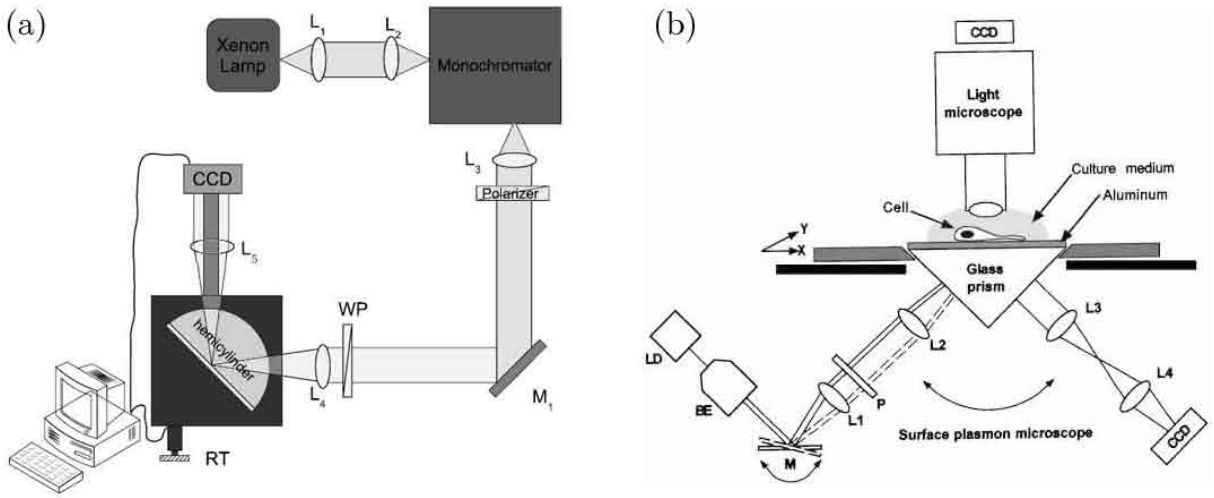

Figure 1.18 (a) Schematic view of a typical SPR microscopy set-up. L_1, L_2, L_3, L_4, L_5: lenses; M_1: mirror; WP: $\lambda/2$ (half wave) plate; RT: rotation table; CCD: camera. Figure extracted and modified from Zhang *et al.*[54] (b) Schematic drawing of the surface plasmon microscope used by Giebel *et al.*[55] Cells are deposited on the metal-coated glass prism and observed from above with a conventional light microscope and from below with surface plasmon microscopy. LD: laser diode; BE: beam expander; M: rotating mirror; L_1-L_4: lenses; P: polarizer; CCD: camera.

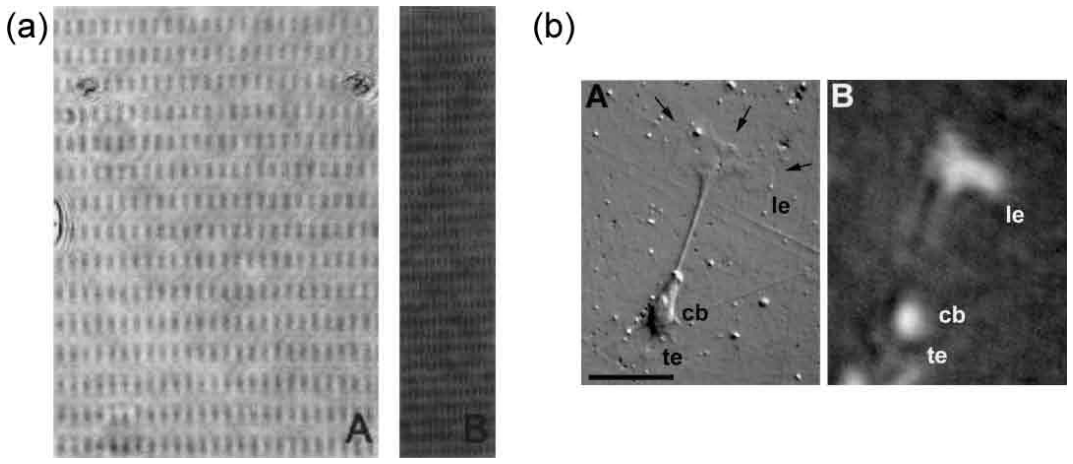

Figure 1.19 (a) SPR images of patterned surfaces (consisting of two regions with different refractive indices). Images are the difference between p- and s-polarized light ($I_P - I_S$) and for λ =880 nm. The minimum feature size is ∼100 μm and ∼50 μm for A and B respectively. Figure extracted from Fu *et al.*[57] (b) Images of a goldfish glial cell in liquid medium and deposited onto an aluminum substrate. The cells are imaged in epi-illumination (A) and SPR microscopy (B). Scale bar is 100 μm. Figure extracted from Giebel *et al.*[55]

limited by the propagation length of the plasmon waves (see Equation 1.15). Actually, it has been shown that resolution and sensibility (in other words the contrast) evolve in opposite directions[56,58].

Note that even if this kind of SPR microscope is mainly used for SPR microarray assays,[59] SPPs launched by prism configurations are also used to excite fluorescent probes, and even two-photon luminescence[60,61].

B.1.2 Phase imaging

As explained in section A.3.2, the excitation of SPPs can be detected by measuring either the intensity of the reflected light (see Figures 1.17(a) and (c), and Section B.1.1), or its phase (see Figures 1.17(b) and (d)). We present in Figure 1.20 the two main techniques used to measure the phase shifts caused by the presence of samples in one of the two arms of a MachñZehnder interferometer. Thanks to the detection of the phase, the sensitivity of SPR microscopy set-ups based on prisms can be improved to $\sim 10^{-6}$ RIU (refractive index units)[62]. As an illustration of surface plasmon phase microscopy, we present in Figure 1.21 an image of an array of salt solutions ranging from 0% to 16%, extracted from Wong *et al.*[63]

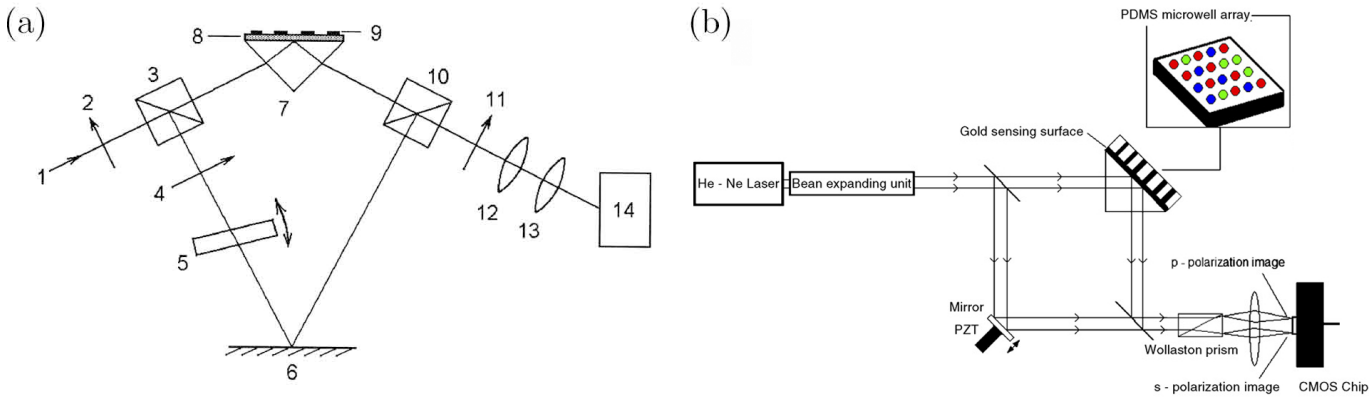

Figure 1.20 (a) Scheme of a SPR microscope based on a Mach-Zehnder interferometer. 1: laser beam; 2, 4: polarizers; 3, 10: beam-splitting cubes; 5: phase-retarding glass plate; 6: mirror; 7: glass prism; 8: gold film; 9: samples; 11: analyzer; 12, 13: imaging lenses; 14: CCD camera. Figure extracted from Nikitin *et al.*[64] (b) SPR microscope developed by Wang and Hsieh[63].

B.2 High numerical aperture objective-based microscopy techniques

We saw in the previous sections that prism-based SPR microscopies, and in particular those detecting the phase of the reflected light, are very sensitive to local modifications of the dielectric index. However, the lateral resolution of such techniques is limited by the propagation

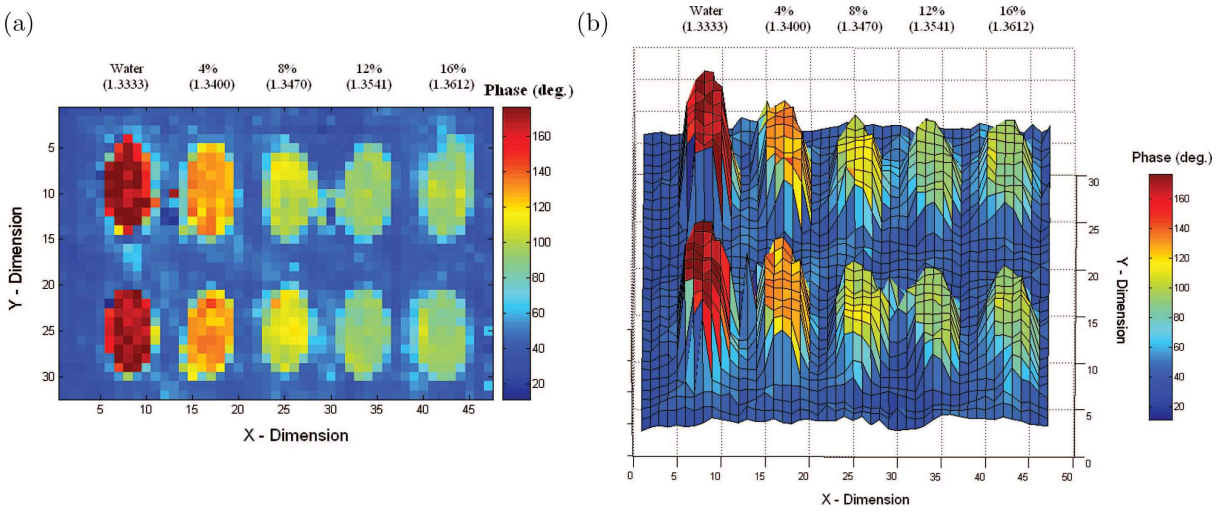

Figure 1.21 (a) Two-dimensional SPR phase map obtained from an array of salt solutions of concentrations ranging from 0% to 16%. (b) 3D view of (a). Figure extracted and modified from Wong *et al.*[63]

length of the SPPs, and prevent imaging of objects smaller than ∼10 μm in air, or ∼6 μm in water. To overcome this problem, and image biological samples with higher resolution, Kano *et al.*[65–67] developed in 1998 a microscope that uses an objective lens of high Numerical Aperture (NA) to focus the light and excite surface waves (see Figure 1.22). We refer the reader to the detailed study carried out by Novotny *et al.*[68] on the consequences of focusing light through a high NA objective lens. In this section, we give a brief overview of the techniques which have been implemented to excite SPPs through a high NA objective lens.
Note that even if we do not develop this aspect in this thesis, this configuration can also be used to excite fluorescence[60].

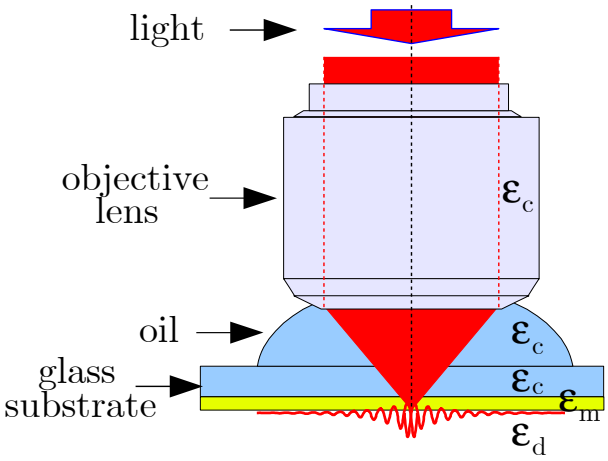

Figure 1.22 Light/SPPs coupling configuration using an objective lens of high numerical aperture (Kretschmann configuration).

B.2.1 Amplitude imaging

We present in Figure 1.23 several SPR imaging techniques that detect the intensity of the reflected light, after focusing it through a high NA objective lens and exciting the SPPs at the metal/observation medium interface. Thanks to this focusing by the objective, SPPs are

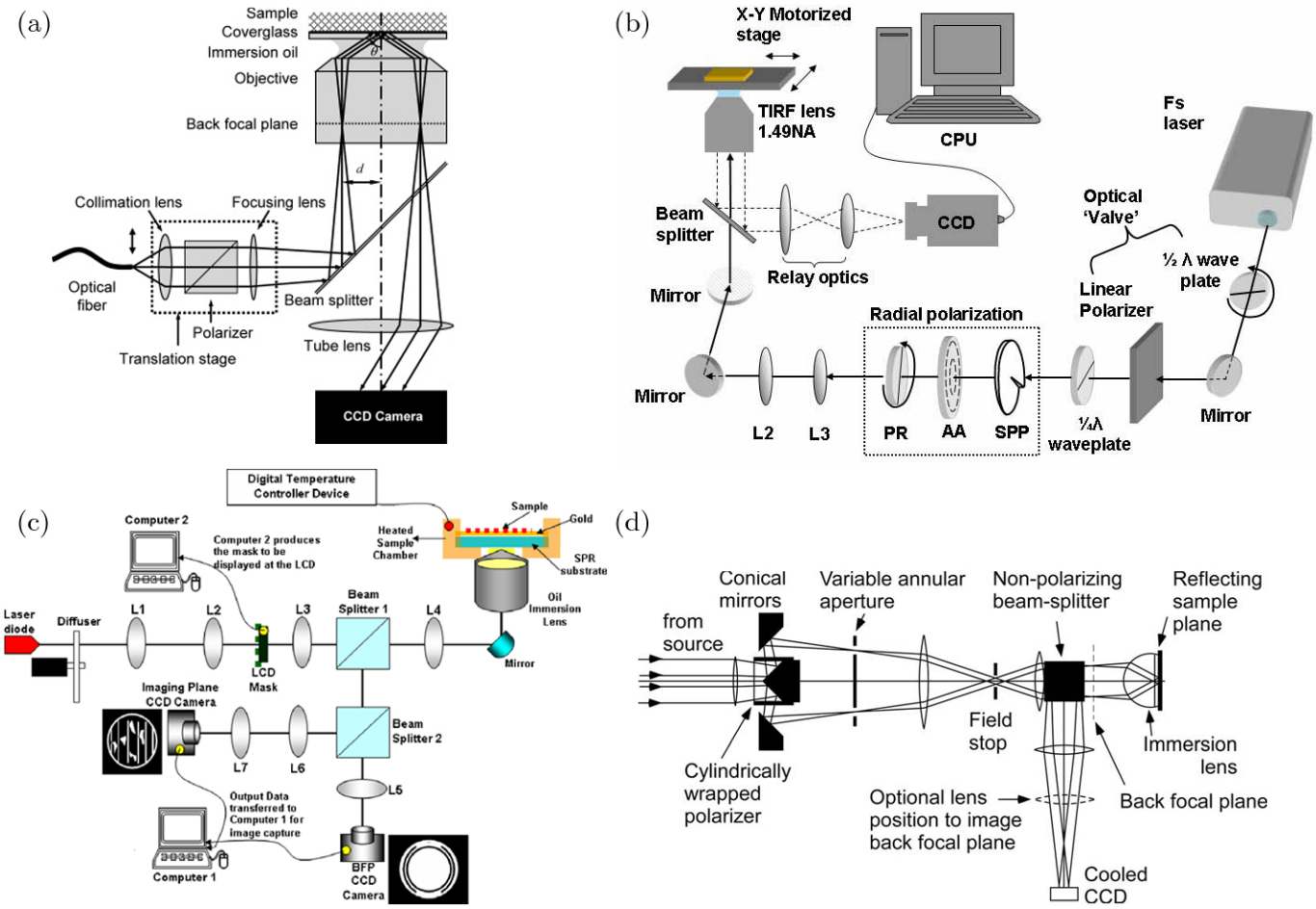

Figure 1.23 SPR imaging set-ups based on the use of objective lenses. Figures extracted from (a) Huang *et al.*[72], (b) Moh *et al.*[71], (c) Jamil *et al.*[69,73], (d) Vander and Lipson[74].

excited from all directions for the angle of incidence θ_P (see Section C), and the surface waves are localized on a small area of the surface. Therefore, the lateral resolution gets close to 1 μm[69] for widefield microscopy, and has been shown to be diffraction-limited[70] when the sample is scanned[70,71]. It has also to be noted that both the resolution and sensitivity of the SPR microscope can be improved by using a radially polarized light[71] (that is purely p-polarized, see Section C.1).

Figure 1.24 shows images obtained in air or in aqueous medium by the set-ups presented in Figure 1.23. We observe from this figure that biological samples can be imaged with a relatively high resolution ($\sim$1 μm) both in air (Fig. 1.24(c)) and in aqueous medium (Fig. 1.24(b)). However, such techniques are not resolutive and sensitive enough to identify the inner structure of such samples.

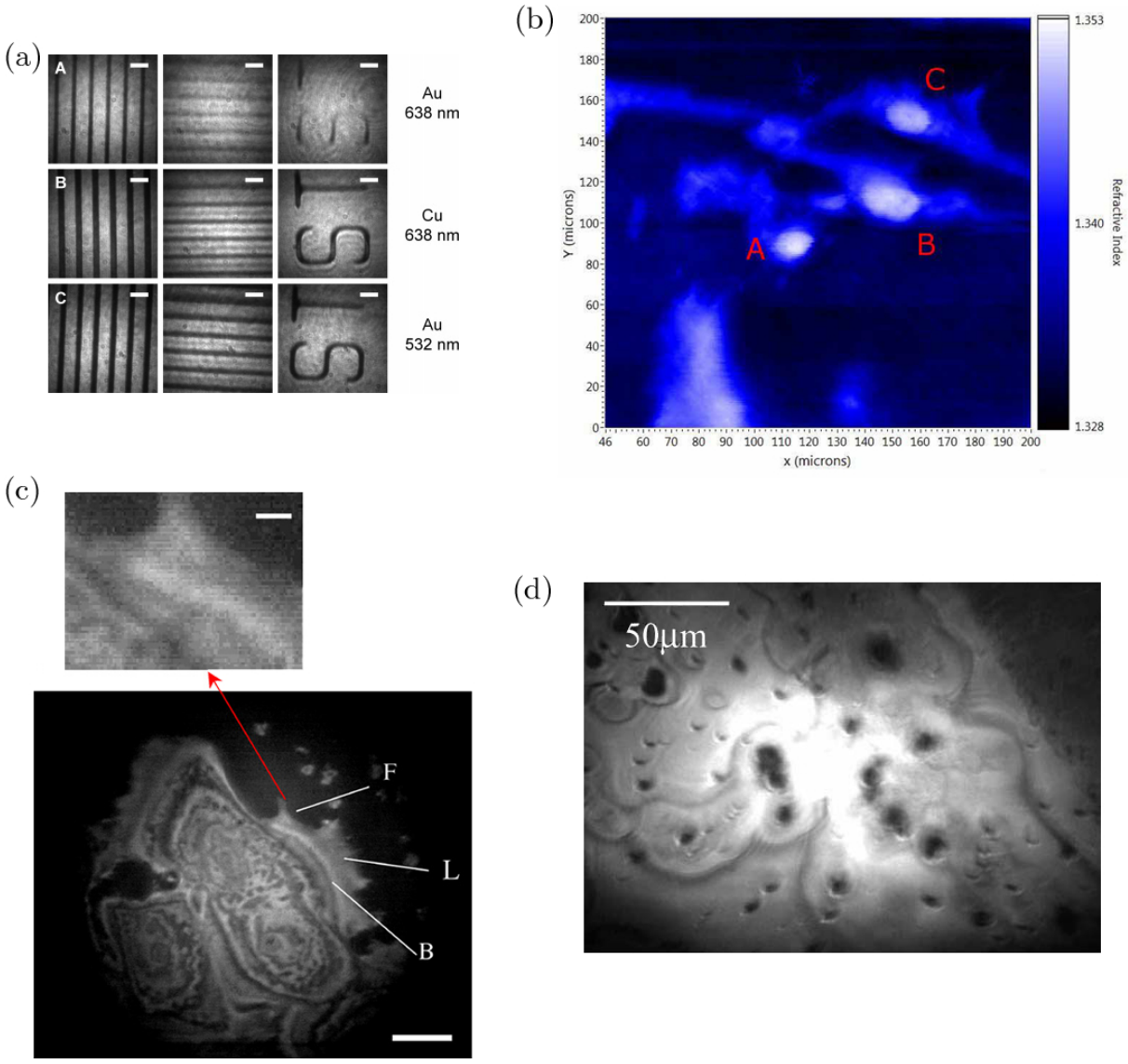

Figure 1.24 SPR images acquired with the objective-based set-ups presented in Figure 1.24. (a) Images of a PDMS stamp in air[72] on a (A) gold film with 638 nm laser, (B) gold film with 532 nm laser, and (C) copper film with 638 nm laser. The incident angle is set at the SPR resonance angle of the metal/air interface. Scale bars are 6 μm. (b) Refractive index image of fixed 3T3 fibroblast cells in aqueous medium[71]. (c) HaCaT cells imaged in air[69,73]. Scale bar is 12 μm (scale bar of the exert is 2 μm). (d) Image of a blood smear[74].

B.2.2 Phase imaging

To increase even more the resolution and the sensitivity, a Scanning Surface-Plasmon Microscope (SSPM), inspired by scanning acoustic microscopy techniques[75], was developed by Somekh *et al.*[76,77]. This microscope relies both on the scanning of the samples, and on the detection of the phase shifts induced by the dielectric index variations at the metal/observation medium. To monitor these phase variations, an interferometer is set (see Figure 1.25(a)), and the optical frequencies of the two arms are slightly shifted by ω_1 and ω_2 respectively. The optical signal is then detected at $\omega_1 - \omega_2$ in order to decrease the noise level (hetero-

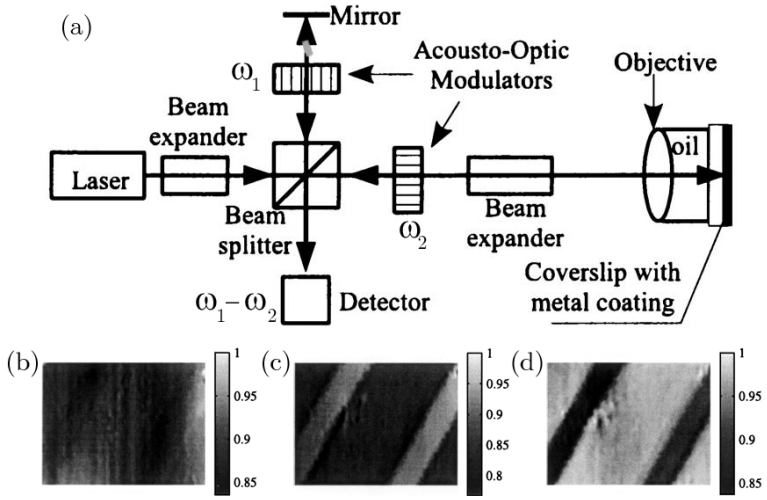

Figure 1.25 (a) Schematic of the SSPM set-up developed by Somekh *et al.*[76,77]. (b), (c) and (d) SSPM Images in air of a structured dielectric sample (2 μm width gold strips followed by SiO_2 strips, 6 μm width and 1 nm thick) for different defocalizations (see Section C.4) of the objective with respect to the metal surface[76,77]: $z = 0$ μm, $z = 1.5$ μm, $z = 1.85$ μm. Image dimensions: 9 μm x 12 μm.

dyning). Note that for this configuration, the objective can be defocused with respect to the gold/observation medium interface. A detailed discussion about this important parameter can be found in Section C.4.

We also present in Figure 1.25 the first images in air[76,77] of a structured dielectric sample, acquired for different values of the defocus Z. We observe from these images that depending on the value of the defocus Z, 1 nm thick SiO_2 stripes can easily be detected.

We discuss in the next section the principle of Scanning Surface Plasmon Microscopy (SSPM) and we provide a quantitative argumentation to explain why this microscope can combine both a high sensitivity and a high spatial resolution.

C The Scanning Surface Plasmon Microscope

In this section, we present the set-up that was inspired from Somekh *et al.* and developed at Ecole Normale Supérieure de Lyon. We discuss first the effects of focusing polarized light on a metallic surface. In a second time, we present the SSPM experimental set-up used in this thesis, and finally we present the theoretical response of the SSPM apparatus with respect to the defocalization (I(Z) and $\varphi(Z)$ curves).

C.1 Introduction: focusing light through a high NA objective lens and influence of the polarization

Figure 1.26 presents the focusing of light through an objective lens, from a geometrical optics point: the objective is seen from above (resp. from the side)in the upper (resp. lower) panel. The arrows represent the electric field $\overrightarrow{E_0}$, that is rotated after passing through the objective

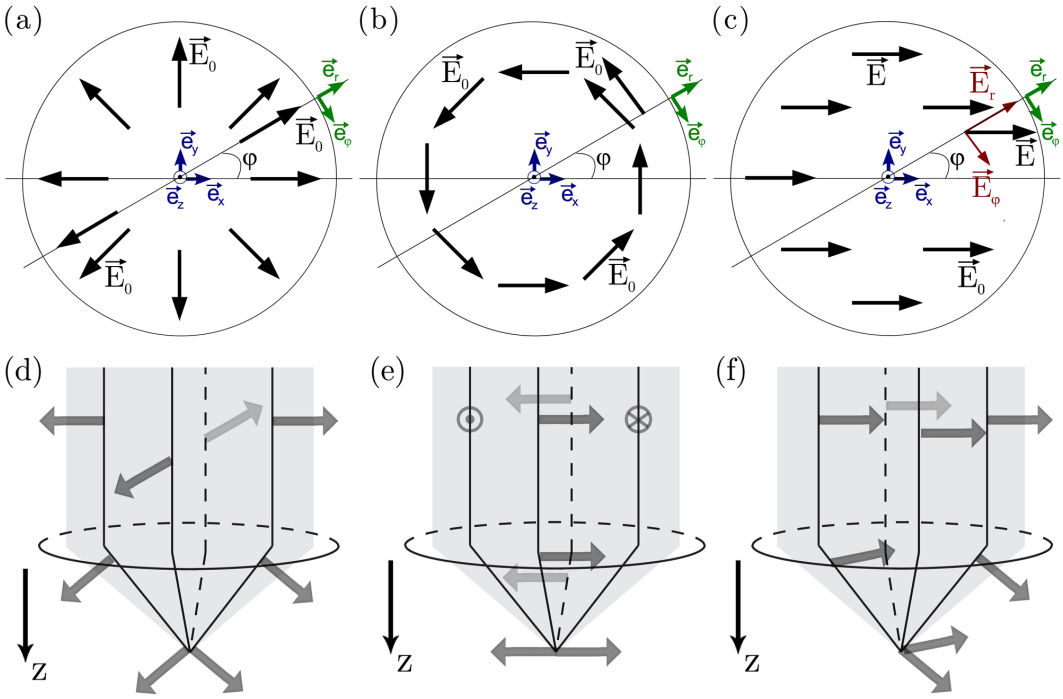

Figure 1.26 Electric field orientation before the high NA objective lens and at the focus. View from above the objective in (a), (b) and (c); from the side in (d), (e) and (f). (a) and (d), radial polarization ($\vec{E}$ is in the plane of incidence); (b) and (e) azimuthal polarization ($\vec{E}$ is normal to the plane of incidence); (c) and (f) linear polarization (the initial direction of $\vec{E}$ is parallel to X). For radial polarization, E_z is maximum, whereas it is null for azimuthally polarized light, and in-between for linear polarization.

lens. (a) and (d) (resp. (b) and (d)) correspond to the radial (resp. azimuthal) polarization, for which $\overrightarrow{E_0}$ is in (resp. normal to) the plane of incidence for all incoming rays; (c) and (d) represent the linear polarization configuration, where $\overrightarrow{E_0}$ is in the plane of incidence for $\varphi = 0$ and π, normal to it for $\varphi = \pi/2$ and $3\pi/2$, and only a component of it is in the plane of incidence in-between.

We observe from Figure 1.26(d) to (f) that because of the orientation of the polarization, the E_z component of the electric field is maximum at the focus in the case of radially polarized light. Moreover, E_z being the main contribution to the SPPs excitation[1,65,78], we expect this configuration to be ideal to launch plasmon surface waves. Indeed, for this configuration, the radial symmetry of the objective lens leads also to the enhancement of the EM field at the interface (the rays coming from all directions will couple with SPPs), which is likely to increase the sensitivity of the the SSPM apparatus to local variations of the dielectric index at the surface.

C.2 The SSPM set-up

We present in Figure 1.27 the optical SSPM set-up inspired from Somekh *et al.*[76,77] and used in this thesis. Linearly polarized light is emitted by a 2 mW 633 nm laser (LHRP--0201 from Research Electro-Optics Inc., USA) stabilized in intensity, and goes through a polarization-maintaining optical fiber (OF). The beam is then expanded 3-fold (BE), and a system composed of a half wave ($\lambda/2$) plate and a radial polarization converter (RPC) purchased from Arcoptix (Switzerland) is used to set the appropriate polarization (linear, azimuthal or radial). The first difference with standard SPR imaging is the presence of a beam splitter (BS) to set an interferometer and detect eventually the phase shift between a reference arm (presence of a mirror, M), and the sample arm. On the sample arm, the laser beam is expanded 5 times (so that its diameter is finally ∼10 mm), and collimated with a lens (L) before entering the high NA objective lens (Ob). SPPs are excited on the metal surface, and light is back reflected through the objective. Acousto-optic modulators (AOM) placed in both arms after the beam splitter (BS) modulate the frequency of the light (heterodyne interferometer) in such a way that the phase difference induced by the SPR retardation at the interface (see next section for a more detailed explanation of this step) can be detected by a H5783P photomultiplier (PM; Hamamatsu Photonics) and converted by a 7280 DSP lock-in (Perkin Elmer). Raw data is finally saved on a computer and data is analyzed with Matlab. The SSPM image of the local phase variations is formed by scanning the sample with a P527 3CL (X,Y) piezoelectric stage from Physik Instrumente (Germany) at a fixed defocus Z, driven by a P721.LLQ Pifoc from Physik Instrumente. A 500x500 pixel image is recorded in about 50 s. Both XY and Z piezoelectric stages are controlled by a PCI 6259M acquisition card from National Instruments that is driven thanks to a homemade LabWindows /CVI (National Instruments) program.
Light is focused with a 60x NA = 1.45 objective lens from Olympus (resp. 100x NA = 1.65

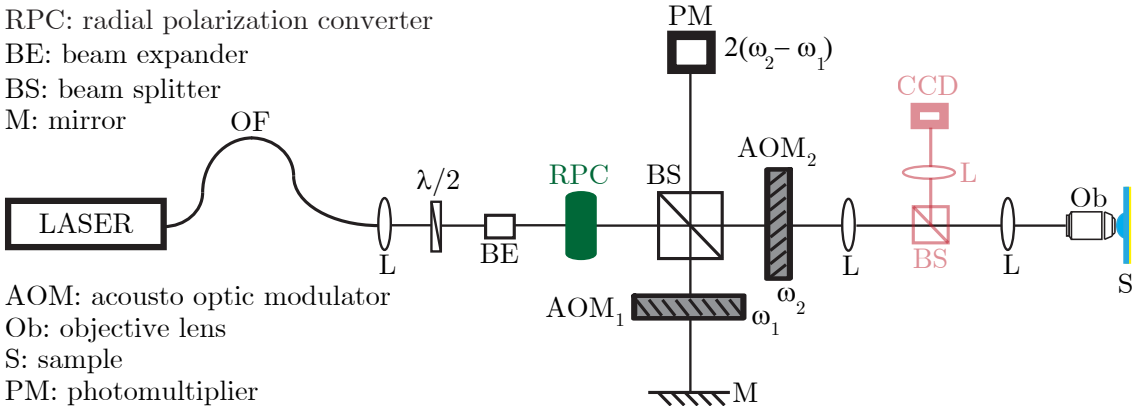

Figure 1.27 Schematic of the SSPM set-up used in this thesis. OF: optical fiber; L: lens; $\lambda/2$: half wave plate; BE: beam expander; RPC: radial polarization converter; BS: beam splitter; AOM: acousto-optic modulator; M: mirror; Ob: high NA objective lens; S: sample; CCD: CCD camera; PM: photomultiplier. Note that RPC, and BS_2 can be removed from the light trajectory when they are not needed. The presence of the AOMs shifts the frequency of each arm by ω_1 or ω_2, and the detection is done at $\omega_2 - \omega_1$.

Olympus) for experiments in air (resp. in aqueous medium). To ensure the continuity of the optical index between the objective and the glass substrate, an immersion oil purchased from Cargille (Cedar Grove, New Jersey USA) is used : n_C =1.5139 (resp. n_C =1.7845) for air (resp. aqueous) assays at $\lambda = 632.8$ nm.

The three important points of this apparatus are (i) the focusing of light by a **high NA objective lens**; (ii) the **scanning of the sample** in the lateral direction by the piezoelectric stage (for a fixed defocalization value); the phase detection by an **heterodyne interferometer**.

C.3 Influence of the defocalization parameter Z

In this section we consider the optical response of the SSPM apparatus while varying the defocalization Z of the objective,[76,77,79] whereas the lateral position (X,Y) is kept constant. As depicted in Figure 1.28, this value Z is defined as the distance of the focus with respect to the metal/observation medium interface, and is negative when the focus is situated in the coupling medium (glass).

Figure 1.28 presents a simplified view (in geometrical optics) of the three configurations corresponding to different positions of the focus: (a) $Z = 0$ (the objective is at focus), (b) $Z < 0$ (focus in the coupling medium) and (c) $Z > 0$ (focus in the observation medium).
A, B and C represent the incoming rays (corresponding either to the angle of incidence θ_P, or to $\theta = 0$ for the central ray), whereas B', A' and D are the back reflected rays.
When the objective is at focus (Figure 1.28(a)), all rays are back reflected no matter their angle of incidence θ. However, SPPs are excited only by the rays A and B that arrive at the metal surface with an incidence θ_P, and depending on the polarization of the light, only a part or all of the rays of incidence θ_P will participate to the surface waves excitation.

Figure 1.29 shows two dimensional images of the experimental back reflected light for radial (a), azimuthal (b) and linear (c) polarizations. The black area corresponding to the SPPs excitation is either a ring (a) or two crescents in the direction of the polarization (c). As expected, when the polarization is azimuthal (b), SPPs are not coupled to light.

Therefore, the only area of the back reflected light providing information on the SPPs excitation corresponds to the narrow black ring (radial polarization) or crescents (linear polarization).

When the objective focuses light in the coupling medium as depicted in Figure 1.28(b), SPPs can still be excited for rays arriving at the incidence θ_P. However, for this configuration, the surface waves propagate away from the center of the illuminated area. Even if SPPs can reradiate light[1] (see Section A.2.3), none of these rays is originated from the focus point, and as a consequence is conjugated through the objective. We see then that SSPM imaging at negative values of the defocalization will give very little, if not any, insights on the studied biological samples.

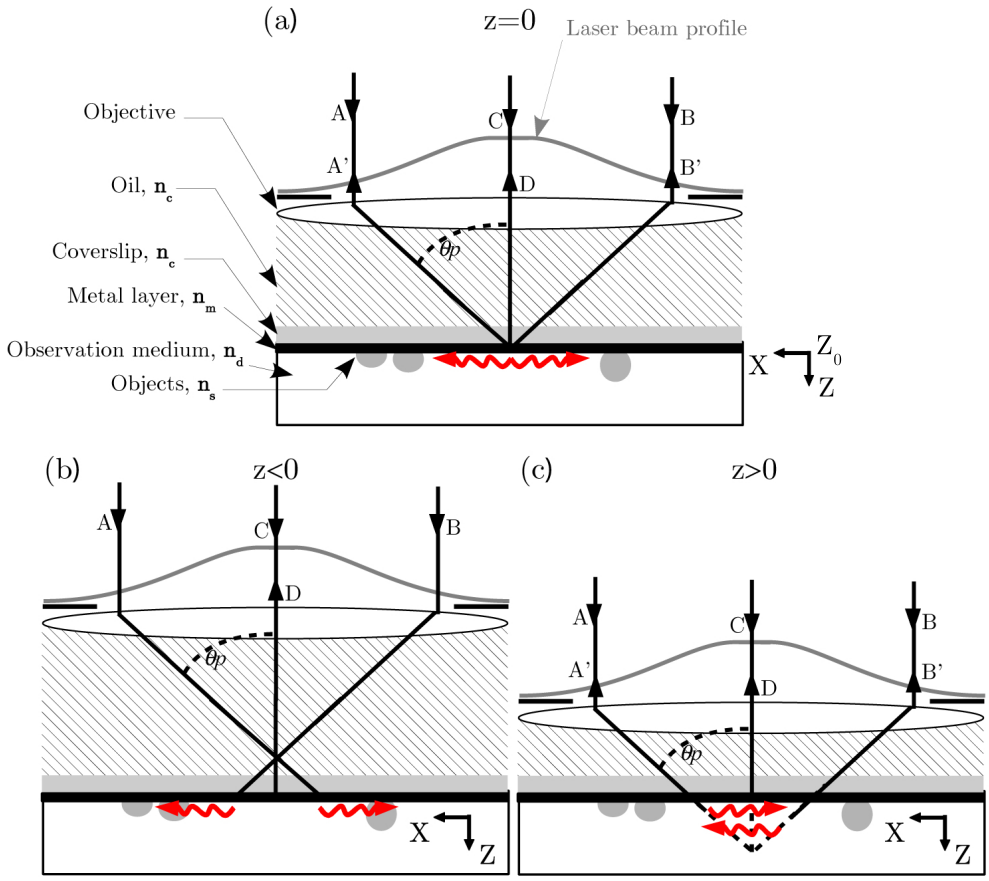

Figure 1.28 Excitation of SPPs by a high NA objective lens. A Gaussian shape laser passes through a high NA lens and launches the SPPs (depicted as red ripples) for the incident ray angle corresponding to θ_P. A', B' and D represent the back reflected rays containing the SPPs information, and A, B and C the corresponding incoming rays. The objective is (a) at focus $Z = Z_0 = 0$ (with Z_0 the origin of defocuses), (b) defocalized in the coupling medium $Z < 0$, or (c) in the observation medium $Z > 0$.

On the other hand, when the objective is focused in the observation medium, the incident ray A (resp. B) still excites SPPs, that propagate towards the center of the illuminated area, and reradiate light on the way. When the surface waves reach the symmetrical ray B (resp. A), the reradiated light is conjugated back by the objective lens, and can be detected at infinity. Note that the presence of converging SPPs leads to interferences of the surface waves, and to the specific distribution of the electric field that gets laterally confined below the interface (this distribution depending on the polarization of the incident light, see Figure 1.32). Hence, the conditions of excitation of the plasmon, and the propagation of the SPPs along the interface both affect the SP phase retardation of these rays.
On the contrary, the ray C that is not coupled to SP is simply reflected back (D) with no variation of phase. As a consequence, the phase difference between the back reflected rays D and those reradiated because of the SPPs is detected by making them interfere with the beam from the reference arm. Hence, the phase retardation between rays A' (or B') and D changes with the defocalization of the lens and/or the variations in the SPP coupling conditions. It has to be noted that the other rays that are not coupled with the SPPs do not contribute to the optical response, because they are not conjugated back by the objective after being reflected. Defocusing the objective into the observation medium helps then reducing the noise

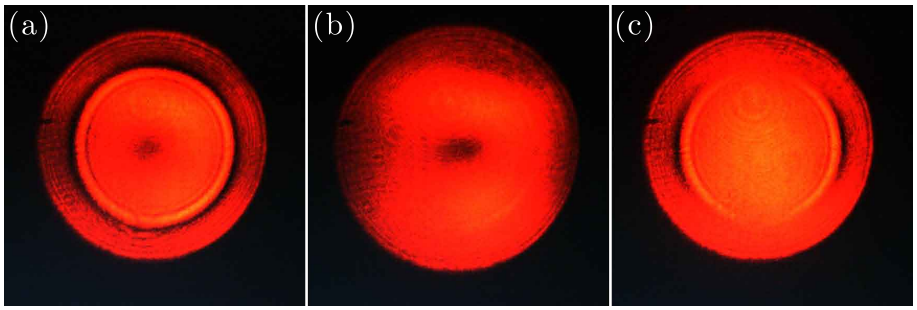

Figure 1.29 Experimental images of the distribution of the reflected light at the metal/air interface for (a) a radial (purely p-), (b) an azimuthal (purely s-), or (c) a linear polarization. Images are recorded in air, for Z =0, and with a 45 nm thick film of gold deposited on top of a $\sim$ 2 nm adhesive layer of chromium.

due mainly to the metal inhomogeneities.

As a conclusion, we have seen that the SSPM signal is mainly ruled by the conditions of excitation of the SPPs when the objective is focused in the observation medium. However, when the objective is focused at the interface, both the plasmon resonance conditions and the reflection of the other rays contribute to the overall optical signal. Therefore, depending on the **defocalization value** Z, the SSPM apparatus will provide information either mainly on the variations of the surface dielectric index ($Z > 0$), or both of the surface waves, and the metal layer inhomogeneities ($Z = 0$).

C.4 The I(Z) curve

C.4.1 Theoretical background of the I(Z) curve

In this section, we consider the optical interference response of the SSPM apparatus as a function of the defocalization Z, for a fixed lateral direction (X,Y). Somekh *et al.*[76,77] have derived the theoretical $V(Z)$ signal from the electric field of the reference arm and the field reflected back from the objective lens $E_{reflected}$:

$$E_{reflected} \sim P^2(\sin\theta)\left[r_P(\sin\theta)\cos^2\varphi + r_S(\sin\theta)\sin^2\varphi\right]\exp(i\ 2n_C k\cos\theta\ Z) \tag{1.22}$$

where $P(\sin\theta)$ is the pupil function (squared because light goes through the objective twice), and r_P (resp. r_S) the Fresnel reflection coefficient of light coming from the coupling medium, for a multilayer system and a purely p- (resp. s-)polarization[2,52]. Note that the term $\exp(i\ 2n_C k\cos\theta\ Z)$ corresponds to the phase shifts induced by the focalization by the objective.

Because of the heterodyne interferometer, the optical signal interfering at the detector is of the form:

$$I(t) = {E_0}^2 + {E_{reflected}}^2 + {E_0}^* E_{reflected}\ \cos(2\pi\Omega t + \Delta\Phi) \tag{1.23}$$

with E_0 the electric field of the reference beam, and $\Omega = 2(\omega_2 - \omega_1)$ the shift in frequency between the two arms (see Figure 1.27).

Therefore, the optical signal is detected at the difference of frequency Ω of the acousto-optic modulators, *i.e.*:

$$E_{reflected} {E_0}^* \tag{1.24}$$

By assuming a uniform reference beam E_0 and omitting constant terms, we have[76,77]:

$$V(Z) = \iint_{lens\ aperture} P^2(\sin\theta) \left[r_P(\sin\theta)\cos^2\varphi + r_S(\sin\theta)\sin^2\varphi \right] \exp(i\ 2n_C k\cos\theta\ Z)\ \sin\theta d\theta d\varphi \tag{1.25}$$

where φ is the angle defined in Figure 1.26, and θ the angle of incidence. Note that $V(Z)$ is complex.

Thanks to the heterodyne interferometer, it is possible to reconstruct from the optical signal both the module I(Z) and the phase $\varphi(Z)$ of $V(Z)$. In this thesis, we have focused on the interpretation of the module of $V(Z)$, but note that phase $\varphi(Z)$ signals can also be reconstructed from the detected optical signal (thanks to the heterodyne interferometer and the lock-in amplifier system) and that phase images are presented in Chapter 4.

C.4.2 Computation of the $V(Z)$ signal

A model adapted from the work of Somekh *et al.*[76,77] (see Equation 1.25) is used in the next section to compute the theoretical optical response of the SSPM apparatus $V(Z)$. To compute this response, the assumption that the metal layer is perfectly flat and exempt from any defects in bulk is made. Therefore, the reflection coefficients r_P and r_S corresponding to a multilayer system are calculated with the Fresnel equations[2,52].

C.4.3 The theoretical I(Z) curve

Figure 1.30 shows the evolution of the module of $V(Z)$ with the defocalization Z and for a fixed lateral location (X,Y), namely the I(Z) curve:

$$I(Z) = |V(Z)| \tag{1.26}$$

The black (resp. red) curves in (a) and (c) correspond to radial (resp. azimuthal) polarization, whereas the curves in (b) and (d) give the optical response of the SSPM apparatus for linearly polarized light. Note that for all computations presented in Figure 1.30, the objective lens is illuminated by a plane wave. The upper (resp. lower) panel corresponds to the ideal (resp. real) case for which the numerical aperture of the objective lens is $NA = n_C$ (resp. 1.45).

We observe that no matter the polarization of light, the I(Z) curve is maximum (I_0) when the objective lens is focused in a close vicinity of the metal/observation medium interface, and

decreases rapidly as Z is varied (for both negative and positive values). This can be easily understood by the fact that light is reflected with a higher efficiency when the objective is at focus.

When looking more closely to the evolution of I(Z) in Figures 1.30(a) and (b), we notice that I(Z) decays smoothly for purely s-polarized light, whereas it oscillates as Z increases ($Z > 0$) when the polarization of light is radial. Actually, these oscillations are characteristic of the excitation of SPPs, and both their shape and period ΔZ are ruled by the local conditions of resonance of the surface waves (*via* the angle θ_P). Their period ΔZ can be determined by estimating the optical path difference between the rays A/B and C/D presented in Figure 1.28. By doing so, the period reads:

$$\Delta Z = \frac{\lambda}{2n_C(1 - \cos\theta_p)} \tag{1.27}$$

We can estimate from Equation 1.27 the period of the oscillations in the case of bare gold in air ($\theta_P = 43.8°$), for λ =633 nm and $n_C = 1.515$: $\Delta Z = 755$ nm.

We also notice from Figure 1.30(a) that the maximum value of the I(Z) curve, namely I_0, is

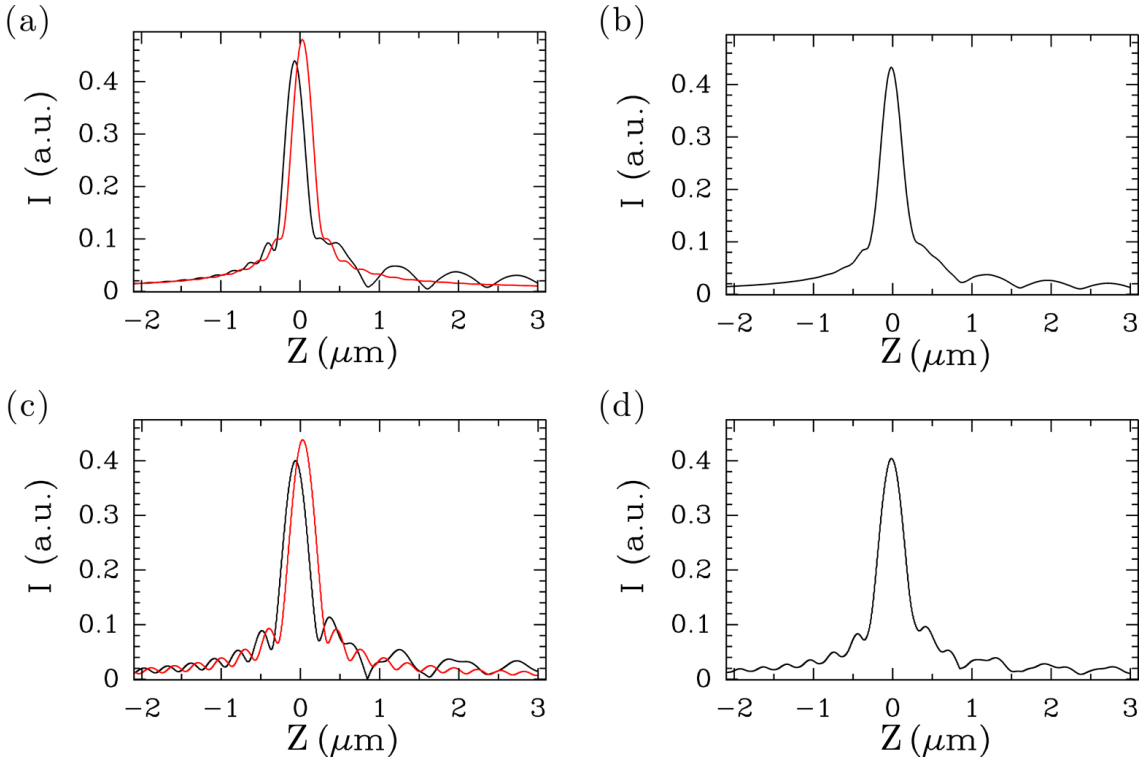

Figure 1.30 Theoretical I(Z) curves of a bare gold surface in air, for a fixed position (X,Y). The objective lens is illuminated by a plane wave, computation done from Equations 1.25 and 1.26, and by using the Fresnel equations (see Chapter 1, Section C.4.2). The upper (resp. lower) panel corresponds to the ideal (resp. real) case for which the numerical aperture of the objective lens is $NA = n_C$ (resp. 1.45). (a) and (c): black (resp. red) curves correspond to radially (resp. azimuthally) polarized light; (b) and (d): optical response for linearly polarized light. The thickness of the gold film is 45 nm and the wavelength $\lambda = 633$ nm.

shifted by δz ∼150 nm when the polarization is changed from radial to azimuthal. In 2001, Novotny *et al.*[68] have hypothesized this phenomenon to be due to an extra phase shift of radially polarized light. More precisely, we see in Figure 1.30(a) that the phase shift between s- and p-polarized light displaces the apparent reflection point beyond the interface between two dielectric media. Comparing purely p-polarized light, black curve in Figure 1.30(a), with linear polarized light in (b), we observe that the oscillations of the I(Z) curve are decreased. This was expected since the amount of light exciting SPPs for a linear polarization is less important. As the shape and period of these oscillations are ruled by the local conditions of resonance, we conclude that the SSPM apparatus should be more sensitive to variations of the dielectric index for radially polarized light.

On the other hand, no oscillation are observed for $Z < 0$. We think this is due to the fact that even if SPPs can be excited by the light beam in this situation (their angle of incidence is still θ_P), the surface waves do not converge to the center of the illuminated area, and as a consequence, there is no constructive structuring of the field below the interface. Therefore, when $Z < 0$, the variation of the dielectric index due to the presence of a sample at the metal surface should not be detected.
However, the observations done in Section C.3 and in this section have been carried out by considering geometrical optics. Actually, the focusing by the objective is not punctual (it is of the order of $\lambda/3$ to $\lambda/3$). As a consequence, we suspect that experimentally, a variation of the dielectric index at the interface could still induce a very slight modification of the optical signal, even for negative values of Z close to $Z_0 = 0$ (focus at the metal/observation medium interface).

The lower panel of Figure 1.30 presents the I(Z) curves in the realistic case, that is for the 1.45 objective lens used in air. Now, another set of oscillations is present no matter the polarization. The main impact of these oscillations is to modulate of the plasmon oscillations, whose global period is unchanged. There is then no reason for the sensitivity of the SSPM to be affected by this phenomenon.

C.5 Towards SSPM imaging: construction of the contrast via the I(Z) curve

We saw in Section C.4 that for bare gold surfaces, the interference optical signal of the SSPM apparatus varies with the defocalization according to the so-called I(Z) curve. We present in Figure 1.31 the theoretical I(Z) curves for lipid layers ($\epsilon_d = 2.56$) of various thicknesses d_S adsorbed on a flat gold surface, for radially (a) or linearly (b) polarized light. The first remark we can make is that the global shape of the I(Z) curve does not change much with the thickness of the adsorbed lipid layer. More precisely, the central peak is almost unchanged when the local dielectric index is varied, whereas we notice that the oscillations corresponding to the SPPs are modified (see the insets).

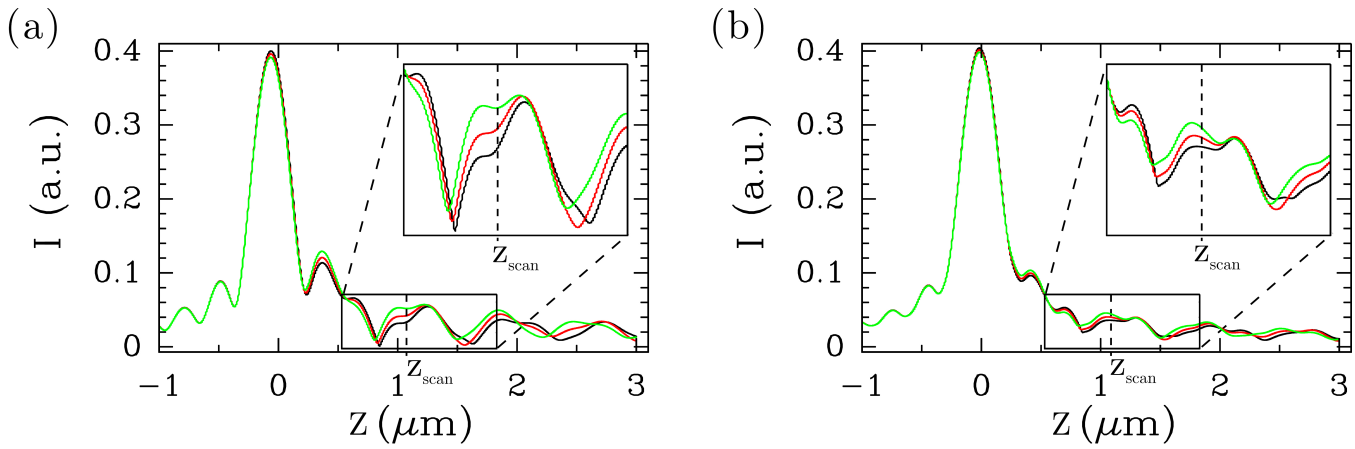

Figure 1.31 Theoretical I(Z) curves, for a fixed position (X,Y), of lipid layers ($\epsilon_d = 2.56$) of thickness d_S adsorbed on a flat gold surface: d_S =0, 5, or 10 nm (black, red, or green curves). (a) radially polarized light; (b) linearly polarized light. The thickness of the gold film is 45 nm and the wavelength $\lambda = 633$ nm. A zoomed view of the I(Z) curves can be found in the insets. Computation done from Equations 1.25 and 1.26, and by using the Fresnel equations (see Chapter 1, Section C.4.2).

These I(Z) curves are obtained for a fixed lateral position (X,Y), when varying the defocalization parameter Z. When the sample is scanned in the lateral direction at a fixed defocalization value Z_{scan} (with $Z_{scan} \geq 0$), the intensity detected by the SSPM apparatus varies with the local dielectric index (presence of objects at the surface). For instance, at the fixed defocalization value $z_{scan} = 1.08$ μm and for a radially (resp. linearly) polarized light, the detected intensity varies by ∼50% (resp. ∼10%) from a sample made of bare gold to a gold layer of the same thickness with an additional 20 nm thick layer of lipid (see Figure 1.31). Therefore, by mapping the variations of the intensity detected while scanning the sample, one get an image contrast reproducing the local modifications of the dielectric index.
On the other hand, these variations of the intensity depend drastically on the chosen defocalization value Z_{scan} and the contrast of the SSPM images changes dramatically with the defocalization parameter. As a consequence, the sample will be scanned at the same height Z_{scan} to compare the optical signal for all points in the SSPM image.
Note that in the same way as for Figure 1.30, SPPs oscillations are less marked for linearly polarized light; local variations of the dielectric index at the interface have a smaller impact on the SSPM image contrast.
The maximum value I_0 of the I(Z) curve, and the corresponding defocalization value Z_0 are important experimental parameters, since Z_0 serves as origin for the experimental I(Z) curves. Before acquiring a SSPM image, an I(Z) curve is measured, and the chosen defocalization value Z_{scan} is defined using I_0 and Z_0. I_0 is used as a normalization parameter for the I(Z) curves (now considered as I(Z)/I_0 curves) and the SSPM images (the pixel values are divided by I_0) so that the experiments can be compared (because I_0 changes by ∼5% with the optical alignment).

In conclusion, we have seen in this section that by scanning laterally the surface for a fixed

defocalization, the SSPM apparatus can be used to image the objects adsorbed at the interface, and that the contrast is ruled by the local variations of the dielectric index. Therefore, the defocalization value Z has to be chosen appropriately to optimize the contrast of the SSPM image.

D Modeling SSPM with a full solution of Maxwell equations

The r_P and r_S reflection coefficients that we have used in Figures 1.30 and 1.31 are computed assuming that the gold/dielectric medium interface is perfectly flat, homogeneous, and that no object or nanoparticle is adsorbed on the metal surface. In that case, r_P and r_S are straightforwardly computed using the Fresnel equations.
However, when the dielectric medium is not invariant in space, or when nanoobjects are in the vicinity of the gold surface, the Fresnel equations loose their validity and Maxwell equations must be solved in three dimensions. In collaboration with J. Elezgaray (Université de Bordeaux 1, ENITAB, IECB, Bordeaux, France), a 3D-Multipolar Expansion (3D-ME) of the Maxwell equations has been developed to recover the 3D map of the electric field above and below the gold/dielectric medium interface.
The interaction between SPPs and a spherical nanosphere (of diameter $D \leq 200$ nm) can then be computed, and the SSPM optical response is then derived for the simplest configuration, *i.e.* a perfectly flat gold film (45 nm thick) deposited on a coupling medium (the glass coverslip). The NP is separated from the metal layer by 1 nm and embedded in a dielectric medium (air). The influence of the roughness of the metal film and the non spherical shape of the NanoParticle (NP) are disregarded. Although restrictive, the existence of exact solutions for this model is very useful for the understanding of experimental measurements with the SSPM apparatus. In the following, all numerical examples assume that the incident wavelength in vacuum is $\lambda = 633$ nm.
In this section, we first present the key equations enabling the computation of the electric field at the interface and the SSPM response of the apparatus. A more detailed presentation of this model can be found in Elezgaray *et al.*[80]. Afterwards, we show the distributions of the transmitted electric field in the plane of the interface ($Z = 0$), and in the plane of incidence ($Y = 0$). Finally, we present the reflected field distribution and the expected image of a single NP through the SSPM.

Solutions of the Maxwell equations can also be achieved with a Finite-Difference Time-Domain (FDTD) model. However, the grid used to compute the EM fields has to be dense enough to resolve the smallest geometrical features of the system, that is the thin gold film (~ 45 nm), or the NPs (as small as 10 nm of diameter). Therefore, because of this high discretization, such FDTD algorithms are very time-consuming. Moreover, artificial boundaries of the system must be set so as to first, prevent an excessive amount of computation, and second, to absorb the EM field going through it (in such a way that no edge reflection can perturb the overall computation).

D.1 Description of the 3D-ME model

The model presented in this section relies on the configuration sketched in Figure 1.28. This calculation considers the ideal case of a sphere of diameter D and optical index n_m, lying on a perfectly flat gold surface of optical index n_m separating the coupling medium (coverslip and oil) of index n_c and the observation medium (air or water) of index n_d. The wave vector in vacuum is $k_0 = 2\pi/\lambda$.

D.1.1 Description of the incident electric field

The description of the electric field in the vicinity of the focus is given by the Richards-Wolf theory[81]. The total field in the coupling medium (n_c) is obtained when taking into account the reflection of the waves at the gold interface:

$$\mathbf{E}_{ref}(\mathbf{X}) = E_0 \int \sin(\theta) d\theta d\varphi \ \cos(\theta)[-P_\rho(\varphi)\hat{e}_\theta r_P(\theta) + P_\varphi \hat{e}_\varphi r_S(\theta)] \\ e^{i\mathbf{K_{c\parallel}}\cdot\mathbf{X}_\parallel} e^{ik_z(z+2Z)} \tag{1.28}$$

where r_S and r_P denote the reflection coefficients for the s- and p-polarizations, $\mathbf{X} = (\mathbf{X}_\parallel, z)$, Z the defocalization value presented in Section C.4 (*i.e.* the distance of the focus from the gold/air interface, along the axis z, normal to this interface), and (θ, φ) are the spherical angles of the points located on the objective as viewed from a frame centered on the focus, $\mathbf{K_c} = (\mathbf{K_{c\parallel}}, k_z) = k_0 n_c(\sin\theta\cos\varphi, \sin\theta\sin\varphi, \cos\theta)$. Note also that the angular integration in θ is limited by the angular aperture of the objective and that the expression 1.28 is only valid for points located in the n_C medium. The phase factor is divided into two contributions corresponding to the projections along the Z axis and the (X, Y) plane: $\mathbf{K_c}\cdot\mathbf{X} = \mathbf{K}_{c\parallel}\cdot\mathbf{X}_\parallel + k_z Z$. $(\hat{e}_r, \hat{e}_\theta, \hat{e}_\varphi)$ are the unit vectors in spherical coordinates (centered at the focus). $P_\rho(\varphi)$ and $P_\varphi(\varphi)$ characterize the polarization of the incident light: $P_\rho(\varphi) = \cos(\varphi)$ and $P_\varphi(\varphi) = -\sin(\varphi)$ for a linear polarization along the X axis, or $P_\rho(\varphi) = 1$ and $P_\varphi(\varphi) = 0$ for a radial polarization.

Taking into account the fact that only p-polarized waves generate plasmon resonances, the main difference between the linear and radial polarizations is therefore the loss of part of the incident energy to generate s-polarized waves.

The same way, the transmitted electric field in the region below the gold deposit can be written in p-polarization as:

$$\mathbf{E}^t_{ref}(\mathbf{X}) = \int \sin(\theta) d\theta d\varphi \ \sqrt{\cos(\theta)}\hat{e}_\theta(\theta', \varphi) t_P(\theta) \frac{n_c}{n_d} e^{i\mathbf{K}\cdot\mathbf{X}} e^{ik_z Z} \tag{1.29}$$

where θ' is defined by $n_d \sin(\theta') = n_c \sin(\theta)$ and $\mathbf{K} = k_0 n_d(\sin(\theta')\cos(\varphi), \sin(\theta')\sin(\varphi), \cos(\theta'))$ The Z component of the electric field is dominant in the vicinity of the focus and the field decreases exponentially as Z goes to $+\infty$.

D.1.2 Multipolar expansions of the incident field

We now consider the influence of the presence of a NP located below the gold layer. In order to get an exact solution of the Maxwell equations, the electric fields will be decomposed into a set of spherical multipolar waves, which is more appropriate to deal with spheres. Therefore, these spherical multipolar waves will be denoted in the following by $M^3_{n,m}(\mathbf{x}), N^3_{n,m}(\mathbf{x})$ (radiating multipoles, singular at the origin) and $M^1_{n,m}(\mathbf{x}), N^1_{n,m}(\mathbf{x})$ (non radiating multipoles, regular at the origin)[80,82–84].

When expanding the incident field as a superposition of nonradiating multipoles $\mathcal{M}^1_{nm}$ and $\mathcal{N}^1_{nm}$, we get:

$$\mathbf{E}_{ref}(\mathbf{X}) \propto \sum_{n,m} \left[a_{n,m} M^1_{m,n}(k_0 n_d \mathbf{X}) + b_{n,m} N^1_{m,n}(k_0 n_d \mathbf{X}) \right] \tag{1.30}$$

The expressions of $a_{n,m}$ and $b_{n,m}$ can be found in Elezgaray *et al.*[80].

The scattered field due to the NP can be expressed as a multipolar expansion of the radiating Spherical Vector Wave Functions (SVWF) $\mathcal{M}^3_{nm}$ and $\mathcal{N}^3_{nm}$ [80,82,83]:

$$\mathbf{E}_{sca}(\mathbf{X}) = \sum_{n,m} e_{n,m} M^3_{n,m}(n_d k_0 \mathbf{X}) + f_{n,m} N^3_{n,m}(n_d k_0 \mathbf{X}) \tag{1.31}$$

with $n = 0, 1, \ldots, \infty$, and $m = -n, -n+1, \ldots, n-1, n$.

According to the T-matrix formalism used by Doicu *et al.*[83], the coefficients $e_{n,m}$ and $f_{n,m}$ can be expressed as a function of a series of the $a_{n,m}$ and $b_{n,m}$ terms, in such a way that the appropriate boundary conditions are ensured (continuity of the tangential components of the electric and magnetic field) at the NP surface[80,84]:

$$(e_{n,m}, f_{n,m}) = T((a_{n,m}, b_{n,m}) + \mathcal{R}(e_{n,m}, f_{n,m})) \tag{1.32}$$

where $\mathcal{R}(e_{n,m}, f_{n,m})$ is a correction term that accounts for the reflection of the multipolar fields on the surface of the metal[80,84].
Equation 1.32 can be numerically solved by truncating the series at the n^{th} term. It turns out that the convergence is rather fast[80], particularly when the particle radius R is such that $R/\lambda << 1$.

D.1.3 Asymptotic behaviour of the detected field

The interference between the incident and the reflected electric field is measured by the SSPM apparatus. Therefore, let us consider the reflected electric field E_∞. For radially polarized light, the "direct" contribution, independent of the NP reads:

$$E_{\infty,0}(\theta, \varphi, r) = \sqrt{\cos\theta}\ r_P(\theta)\ \frac{2\pi i}{r k_0} e^{i k_0 r} e^{2 i k_0 Z} \hat{e}_\theta \tag{1.33}$$

On the other hand, the "perturbed" contribution, that depends on the NP is given by:

$$\delta E_\infty(r,\theta,\varphi)e^{i\mathbf{K}\cdot\mathbf{X}} \sim_{r\to\infty} \sum_{n,m}\left[A_n^m e_{n,m} + B_n^m f_{n,m}\right]\hat{e}_\theta + \sum_{n,m}\left[C_n^m e_{n,m} + D_n^m f_{n,m}\right]\hat{e}_\varphi \quad (1.34)$$

where X is the relative position of the focus with respect to the NP center. $A_P^{n,m}$, $B_P^{n,m}$, $C_S^{n,m}$ and $D_S^{n,m}$ are coefficients depending on n, m, and the transmission coefficients t_P and t_S for p- and s-polarizations[2,52].

The optical response $V(\mathbf{X}, Z)$ acquired by the interferometric set-up depends on both the lateral position of the NP ($\mathbf{X}$) and also on the defocalization value (Z) of the objective with respect to the gold layer. It is derived (up to constant terms) from the integration over the surface of the pupil of the product $\hat{\mathbf{e}}_\rho \cdot (\mathbf{E}_{\infty,\mathbf{0}} + \delta\mathbf{E}_\infty)$, *i.e.* for linearly polarized light[80]:

$$V(\mathbf{X},Z) = \int d\theta d\varphi R_{obj}\sin(\theta)\cos(\theta)\{P_\rho(\varphi)[\mathbf{E}_{\infty,\mathbf{0}}+\delta\mathbf{E}_\infty]\cdot\hat{\mathbf{e}}_\theta - P_\varphi(\varphi)[\mathbf{E}_{\infty,\mathbf{0}}+\delta\mathbf{E}_\infty]\cdot\hat{\mathbf{e}}_\varphi\} \quad (1.35)$$

with R_{obj} the radius of the objective. Notice that, without the perturbation of the bead and for a linear polarization, the expression 1.35 reduces to that given by Equation 1.25[76,77], except for the pupil function that is squared in Equation 1.25. For a radial polarization, we get:

$$V(\mathbf{X},Z) = \int d\theta d\varphi R_{obj}\sin(\theta)\cos(\theta)[\mathbf{E}_{\infty,\mathbf{0}} + \delta\mathbf{E}_\infty]\cdot\hat{\mathbf{e}}_\theta \quad (1.36)$$

We saw in Section C.5 that the maximum value of the I(Z) curve is used to normalize the SSPM images. We can also compute the maximum of $V(\mathbf{X_b}, \mathbf{F})$ for a radial polarization:

$$I_0 = \max_{\mathbf{F}}\left|\int d\theta d\varphi R_{obj}\sin(\theta)\cos(\theta)[\mathbf{E}_{\infty,\mathbf{0}} + \delta\mathbf{E}_\infty]\cdot\hat{\mathbf{e}}_\theta\right| \quad (1.37)$$

D.2 Distribution of the electric field below the interface

D.2.1 In the plane of the interface (for Z=0)

Several groups[68,78,85–88] have addressed in the past few years, both theoretically and experimentally, the question of focusing light through a high NA objective lens at the interface between two media, and especially at a metal film and a dielectric medium such as air.
As sketched in Figure 1.28(a), at focus ($Z = 0$), for a fixed lateral location and a p-polarized incident light, all back reflected rays contribute to the electric field below the metal layer[78,86]. Figure 1.32 shows the distribution of the electric field $|E|$ (and its components $|E_Z|$ and $|E_X + E_Y|$) below the gold/air interface, after focalization of a radially (a), (b) and (c), or linearly (d), (d) and (f), polarized light. The defocalization value is $Z = 0$ (objective at focus). This field has been computed with the 3D-ME model described in the previous sections, for a 45 nm thick metal layer and for the configuration in air. (a) and (d) represent the $|E|$ distribution; (b) and (e) the $|E_Z|$ distribution; and (c) and (f) represent the $|E_X + E_Y|$ distribution. The polarization of the incident light has a strong influence on the intensity distributions of the electric field below the metal surface. We see from Figure 1.32(h) that first, the two lobe pattern of the $|\mathrm{E}_z|$ component for linearly polarized light is transformed into a single peak

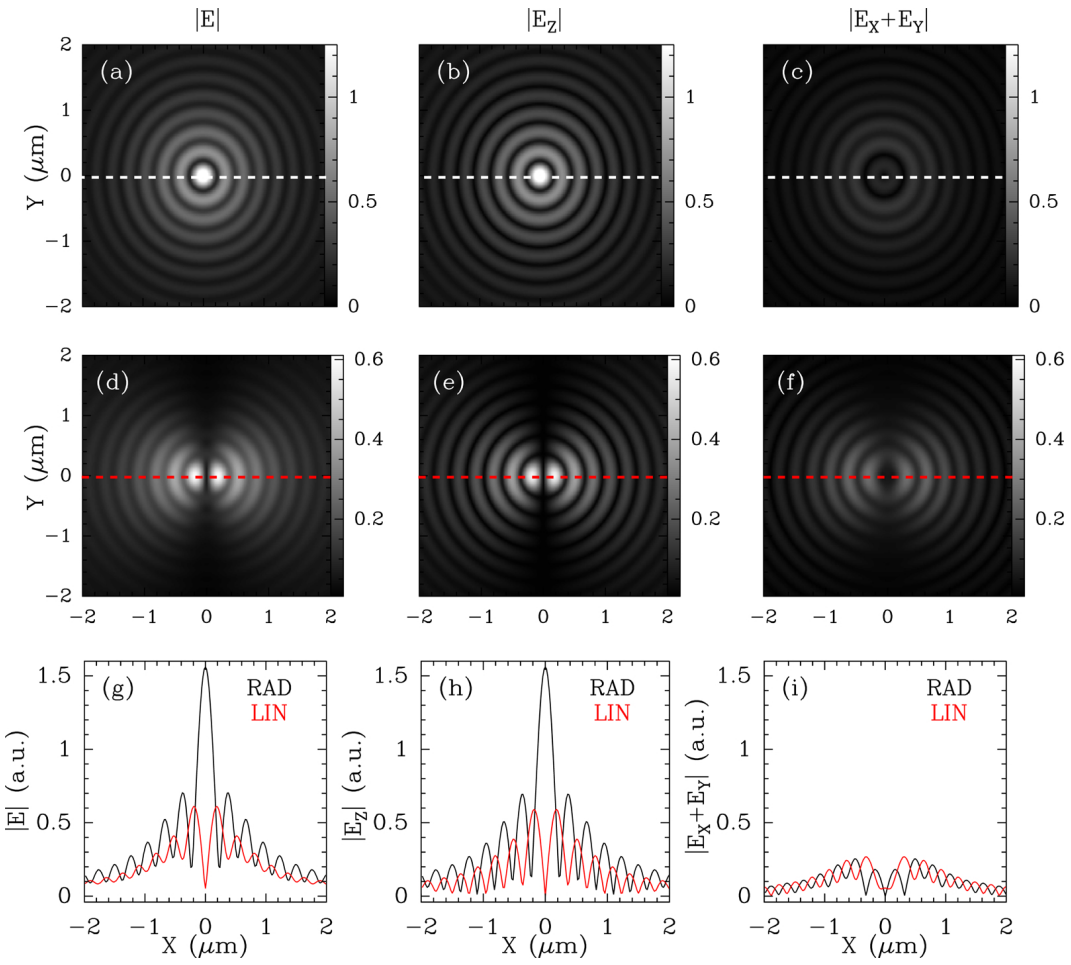

Figure 1.32 Intensity distributions of the electric field below the gold-air interface (at $Z = 0$), and after focusing of the incident light by the objective. Computation done with the multipolar model presented in Section D, for a 45 nm thick gold film that is perfectly flat. (a), (b) and (c) (resp. (d), (e) and (f)) represent the intensity distributions for a radial (resp. linear) polarization. (a) and (d) correspond to the $|E|$ distribution, (b) and (e) to $|E_Z|$, and (c) and (f) to $|E_X + E_Y|$. The cross-section corresponding to each distribution are shown in (g), (h) and (i). Black (resp. red) curves represent the radial (resp. azimuthal) polarizations. Note that the contrast scales of the images are fixed for each polarization.

when light is purely p-polarized. This implies that the localization of the electric field below the metal layer is enhanced when the polarization is switched to radial. Moreover, we also notice from these cross-sections that the maximum value of the $|E_z|$ distribution is clearly higher (by a factor 2.6) for radially polarized light.

As a conclusion, since the E_z component expresses approximately the distribution of the localized surface plasmon[1,65,78], purely p-polarized light seems to be the best candidate to excite SSPs and use them as a virtual probe to measure the local variations of the dielectric index. Indeed, this increase of the lateral confinement of the electric field is very likely to enhance first, the Point Spread Function (PSF; *i.e.* the image of a point source) of the SSPM

set-up to ∼230 nm (as compared with ∼600 nm for the FWHM of the two lobe pattern with a linear polarization), and also its sensitivity, *via* the increase of the E_Z amplitude: from ∼0.59 for a linear polarization to ∼1.56 for p-polarization. The other reason explaining the higher sensitivity of the microscope with radially polarized light is the fact that all rays participate into the excitation of the plasmon waves, and eventually lead to the creation of an EM field that is more sensitive to the presence of unlabelled nanoobjects such as biological samples.

D.2.2 In the plane normal to the interface

We present in this section the distribution of the transmitted electric field |E| in the plane (X,Z), normal to the interface. The computation is done with the 3D-ME model and a radial polarization. The metal surface (45 nm thick) is situated at $Z = 0$, and as previously, $Z > 0$ corresponds to focusing the objective lens in the observation medium (air). The left, middle and right panels correspond to focusing in air ($z = 0.8$ μ m), at the interface ($z = 0$), and in the coupling medium ($z = -0.8$ μm). The upper (resp. middle) panel presents a large (resp. zoomed) view of the distribution of |E|, whereas the lower panel of Figure 1.33 shows the sections for $X = 0$ of the field distribution corresponding to the black lines in (d), (e) and (f).

We observe from (c), and (f) that when the focus is in the coupling medium ($Z = -0.8$ μm), most of the electric field is indeed located in a relatively small area around the position $Z \sim -0.8$ μm. However, when looking at the cross-section (i), we notice that as expected, no coupling is present below the interface for $X = 0$.

Now, when the objective focuses the light at the interface (b) and (e), the energy is localized mostly in the area where 50 nm$< Z < 0$, *i.e.* in the metal layer and decreases exponentially from the interface for $Z > 0$: the penetration depth at $1/e$ is ∼100 nm, which is ∼0.3 fold smaller than the estimation made from Equation 1.13. We attribute this difference to be caused by the integration of all incidence angles in the objective configuration described by in Equation 1.36, whereas Equation 1.13 takes into account the sole angle θ_P.

On the other hand, once the objective has been defocalized in the air medium ($Z = 0.8$ μm), the distribution of the electric field can be described by two main characteristics. First, we note that the field remains very strong in the zone of the coupling medium for which $Z \sim -1$ μm. This "spot" actually corresponds to the strong reflection of all the rays for which the angle of incidence is different from the condition of excitation of the SPPs (θ_P). The second, and more interesting feature is the presence for $X = 0$ (see the cross-section in (g)) of an evanescent (exponential decay) field below the interface, in the air medium. We also note that the evanescent field is as strong as when the objective is focused at the interface, but decays more smoothly than for a defocalization value $Z = 0$: ∼0.2 μm at $1/e$, which gets closer to the estimation made from Equation 1.13 (∼350 nm). It appears then that the penetration depth computed with the 3D-model increases with the defocalization Z. We believe that a careful study of this aspect is of great interest to understand the impact of the presence of samples on the SSPM optical response. However, we expect the sensitivity of the apparatus to dielectric modifications to be enhanced when the objective focused in the observation medium.

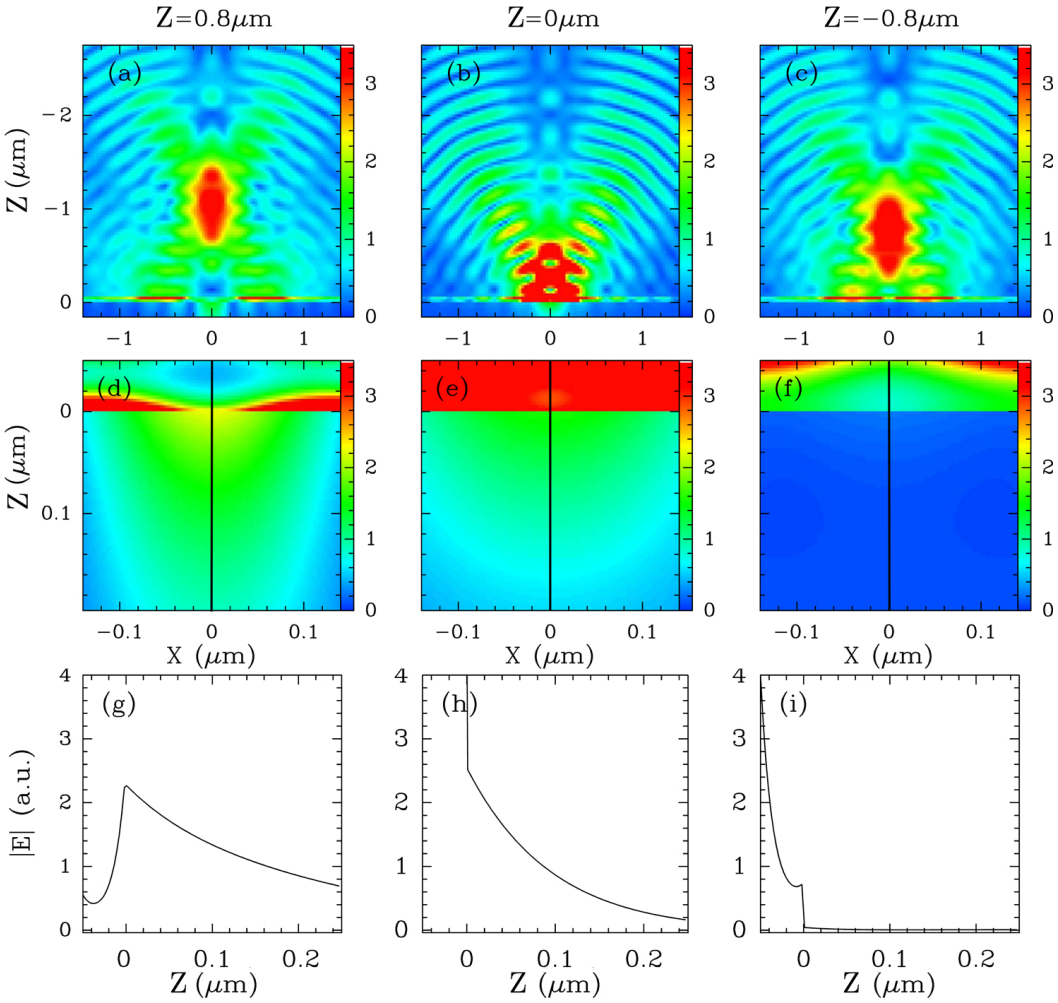

Figure 1.33 Plot of the modulus of the incident electric field $|E|$ below the gold surface, in the plane normal to the interface. Modeling done with the 3D-ME model (Section D.1) for a radial polarization and a 45 nm thick gold film in air. The defocalization of the objective is (a) and (d) $z = 0.8$ μm, (b) and (e) $z = 0$ μm, (c) and (f) $z = -0.8$ μm. (d),(e) and (f) are zoomed views of (a), (b) and (c) respectively. (g), (h) and (i) are the cross-sections of (d),(e) and (f) for $X = 0$ (see black lines).

D.3 SSPM imaging: theoretical point spread function

In this section, we address the question of the theoretical PSF of the SSPM apparatus. As said previously, the PSF represents the response of a point object through the microscope, such as a very small isolated NP. We use the 3D-ME model described previously to compute the expected PSF, that is the optical response of for example a 30 nm gold or latex NP. Figure 1.34 presents the theoretical SSPM images of such NPs, at a defocalization value $Z = 0$, for a 45 nm thick gold film, and a linearly or radially polarized light. This figure confirms that

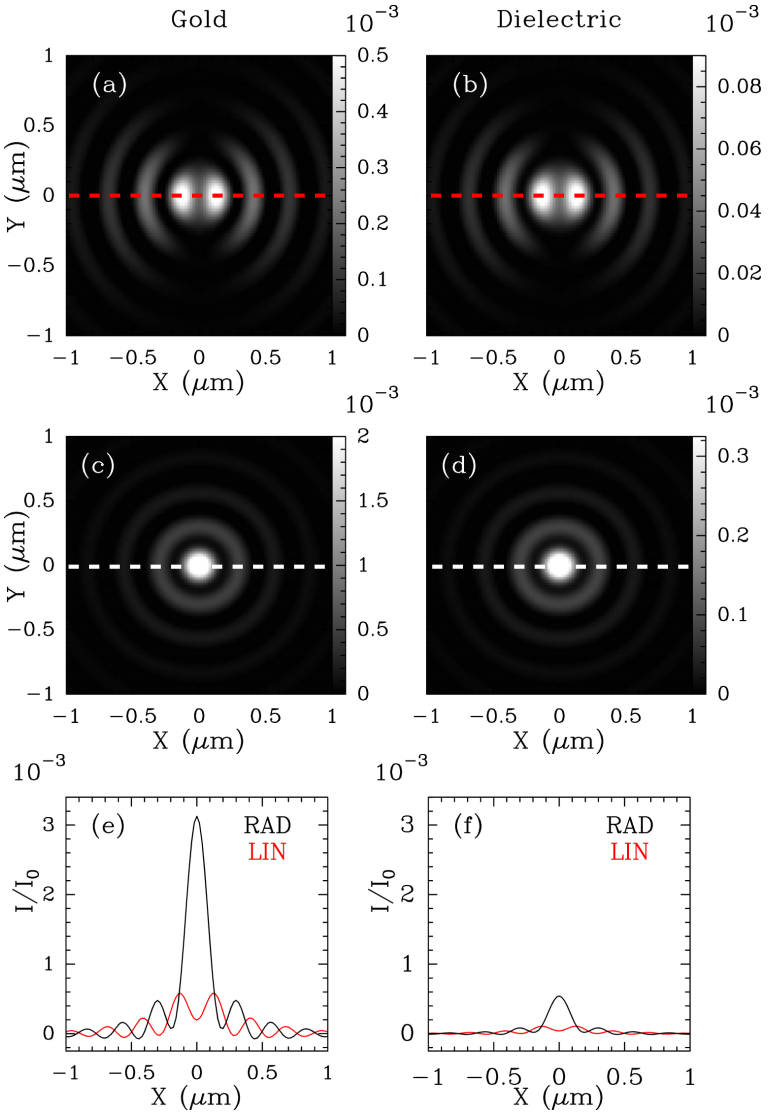

Figure 1.34 SSPM images of 30 nm gold (a) and (c) or latex (c) and (d) NP, for a linearly (upper panel) or radially (lower panel) polarized light. Computation was performed with the 3D-ME model (Section D.1) for a 45 nm thick gold film in air. The number of multipoles used for the computation is $n = 2$ and the dielectric constants are $\epsilon_{NP} = \epsilon_m = -12.8 + j1.36$ or 2.56 for gold or latex NP respectively. The defocalization of the objective is $Z = 0$. The dynamics of the images has been changed for clarity reasons. The cross-sections of the images corresponding to the dashed white lines ($Y = 0$) in the images are presented in (e) and (f).

the shape of the PSF is ruled by the distribution of the $|E_Z|$ field shown in Figure 1.32: two lobes in case of linearly polarized light, or a single lobe when it is radially polarized. The FWHM of the PSF is: 190 nm for radially polarized light, and 410 nm when it is linearly polarized (for the two lobes, which are separated by 270 nm). Hence, we confirm that the FWHM of the SSPM images for a radial polarization, is comparable with that of the $|E_Z|$ distribution presented in the previous sections (Figure 1.32). On the other hand, we notice

that the ratio between the maxima of the cross-sections is higher for the images (5.4) than for the $|E_Z|$ distributions (2.6). Finally, we observe that no matter the type of polarization, the contrast of a 30 nm gold NP is about 5.5 time larger than that of a dielectric NP.

E Conclusions

We have seen in this chapter that SPR-based techniques are numerous, and very sensitive to modifications of the dielectric index in the surroundings of either a metal NP (see Section A.2.1), or a metal surface (Section A.2.2). Many microscopy techniques have been derived from this phenomenon (Section B), and some of them were developed especially to overcome the inherent problem of the important propagation length of the SPPs at the metal surface that limits the lateral resolution of classic SPR microscopy (Section B.1.1).

A high resolution Scanning Surface Plasmon Microscope, based on the use of a high NA objective lens and the detection of the optical signal by the mean of an heterodyne interferometer, has then been developed in the laboratory, as inspired from Somekh *et al.*[76,77]
As explained previously, the purpose of this apparatus is to image unlabelled biological samples, and in regards to this issue the polarization of the incident light is of great importance (Section C.1). When the light is linearly polarized, the distribution of the electric field at the metal/observation medium consists in a two lobe pattern, and the expected PSF of the set-up is limited by this distribution. Moreover, a purely p-polarized light leads to an enhancement of this electric field below the surface (Section D.2.1), and also to a shrinking of the PSF (Section D.3).
Finally, we have also considered the influence of the defocalization parameter Z of the objective with respect to the interface, and noted that the optical response of the SSPM apparatus is highly dependent on it (Section C.4), and that for a fixed Z value, the map of the dielectric index variations at the surface can be imaged when the sample is scanned in the (X,Y) directions (Section C.5).

Chapter 2

Preparation of thin gold layers

The preparation of thin ($\sim$ 45 nm) metal layers is a very important stage in the elaboration of many surface plasmon resonance (SPR)-based biosensors, such as DNA[89,90] or protein[90,91] microarrays. It has indeed attracted much interest since the 1960s, because they provide an easy way to sensitively probe surface modifications with SP polaritons (SPP)[92,93].
Most of these biosensors use the so-called Kretschman's configuration[9]. But one of the major problems with this technique is the discontinuous structure of the metal films prepared by evaporation, as it was recognized very early[94]. Indeed, small islands are formed first on the solid glass substrate and as deposition continues, the islands grow, agglomerate and eventually form a continuous rough film. In particular, several theoretical studies have recently been carried out on the influence of the surface roughness on the scattering of light[95–97].
Usually, thermal evaporation and cluster beam evaporation are indifferently used to prepare thin gold films, and it has been shown that these two methods give similar deposition behaviors[98]. More recently, a model was proposed, assuming the formation of charged clusters by gas phase initiation[99] and their subsequent deposition on the substrate surface on which the metal film is formed. Barnes and coworkers[99] claimed that the presence of nanoclusters in the metal films prepared by these methods was not suspected before for two reasons. First, because their nanometer size was a limitation for their characterization, and second because the films which were formed were at that moment undistinguishable from a film deposited by epitaxy. As these films cannot be distinguished by standard optical methods, most models of evaporated thin gold films only take into account the roughness of gold surface, and do not include bulk heterogeneity.
We show in this chapter that atomic force microscopy (AFM) and near field optics, in particular surface plasmon resonance, can be used to characterize the surface and bulk heterogeneity of thermally evaporated gold films. The question of the quality of the metal layers is addressed first by changing the rates of deposition during the evaporation process, and then by chemically treating the glass substrates with molecules compatible with both glass and gold.

A Influence of the evaporation rate

Thermal evaporation of gold is generally done by ohmic heating of a piece of gold up to fusion. The rate of this heating defines the velocity at which gold is vaporized. S.J. Zhang focused on the influence of this rate on the properties of the gold films[2,54]. The characterization of these films was done by AFM, SPR and SSPM.

A.1 Surface roughness of the layers

A.1.1 Presentation of SPR curves for two sets of gold films

Variations in the gold structure influence the local refractive index of the gold layer itself, hence modifying the conditions of excitation of the SPPs, and in consequence decreasing the sensitivity of this technique. It is then of great interest to monitor precisely such structure modifications, in order to gain in reproducibility in the SPR measurements.

The SPR reflectivity curves, presented in Figure 2.1 have been recorded on distinct coverslips or several locations on a same coversplip, prepared for a given deposition rate. Two rates of depositions are shown here (a) 0.02 nm/s (slow deposition mode) and (b) 0.4 nm/s (fast deposition mode). The errorbars, corresponding to the root mean square over the different recorded curves, give the dispersion of the measurements and demonstrate the good reproducibility of both the sample preparation and their optical characterization. Six different wavelengths (600, 633, 647, 676, 700 and 750 nm) are used in the following to test SPR curve parametrization.

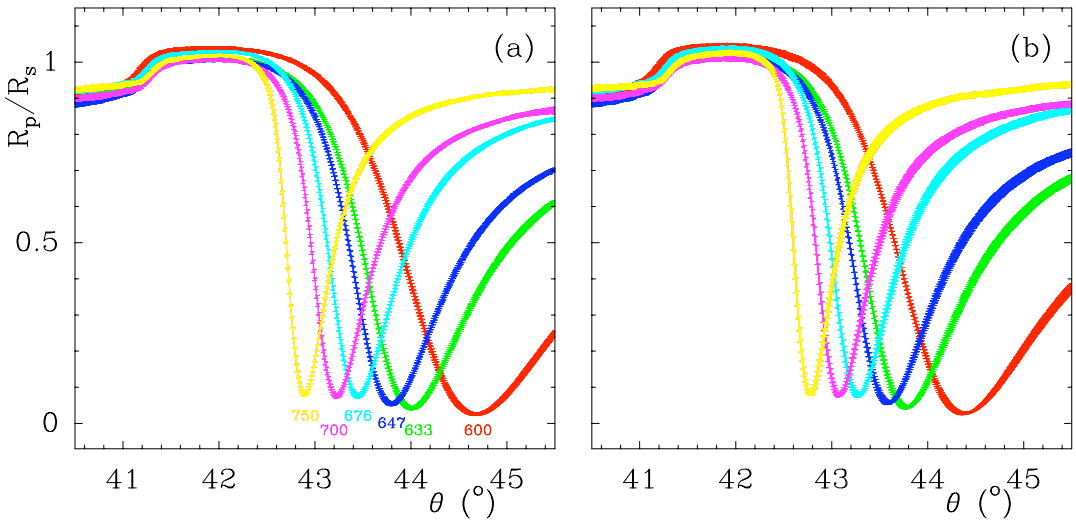

Figure 2.1 Sets of experimental SPR curves (R_p/R_s versus the angle θ) averaged on distinct coverslips or several locations on a same coverslip. (a) Slow gold deposition mode. (b) Fast gold deposition mode. Six wavelengths are shown: 600, 633, 647, 676, 700 and 750 nm.

Figure 2.1 presents the ratio R_P/R_S of the light intensities after reflection by the sample

(either the slow (a) or fast (b) deposited gold layer), as a function of the angle of incidence of the rays. The increase of the reflected light around 41.2° is characteristic of the attenuated total reflection (ATR) angle, and the dramatic drop of R_P/R_S corresponds to the condition of excitation of the surface plasmon at a given wavelength. The angle for which the SPR curve is minimum is called the resonance angle, θ_P.

The resonance curves corresponding to the same wavelength in Figure 2.1 (between (a) and (b)) show differences that can only be explained by a change in the structure of the gold layer when the evaporation rate is changed. To determine if this behaviour is due to surface and/or bulk variations, AFM is first used to image the topography of the gold films. The SPR curves are afterwards fitted using different models, and finally SSPM experiments are carried out and presented in the following sections.

A.1.2 Analysis of gold surfaces by Atomic Force Microscopy

The topography of gold films was characterized by tapping mode AFM[100], and two images for each deposition mode are reported in Figure 2.2 at two different scales (2 μm and 400 nm). The AFM images are flattened line by line, by subtracting to each pixel the mean of the line they belong to (0^{th}order flattening).
Several observations can be made from a visual inspection of these images. The first one is that the gold surface is not atomically flat, which is probably due to the fact that gold is deposited in small clusters or droplets. The second one is that the structures which are revealed by AFM are rather smooth and round in shape. Finally, the size of these blobs is limited to a narrow range of scale, and this range does not change over the surface of the coverslip (∼2 cm wide). Comparing figures 2.2(a-b) and 2.2(c-d) we note also that the faster the deposition, the smaller the gold objects.

All these observations are confirmed by the computation of 1D power spectra and histograms of heights, reported in Figure 2.3. The power spectra in Figure 2.3(a) have been computed from 1D sections of the AFM images and averaged twice: first on the 512 lines of each image, and second over a large set of 1 μm wide images (24 for the slow mode deposition and 26 for the fast mode deposition). These power spectra show one domain at small frequencies below $f = 0.01$ nm^{-1} (larger scales) and another one at large frequencies above $f = 0.2$ nm^{-1} (small scales) where $P(f)$ does not change much. The intermediate range of scales between these two domains can be fitted by a linear function in log-log plot, corresponding to a power law behavior for the power spectrum: $P(f) \sim f^{\beta}$. For the slow deposition mode, fitting a linear curve in the scale interval from 9 nm ($f = 10^{-0.9}$ nm^{-1}) to 40 nm ($f = 10^{-1.6}$ nm^{-1}) gives $\beta = -3.66 \pm 0.02$. For the fast deposition mode, the same linear fitting in the scale interval from 6 nm ($f = 10^{-0.8}$ nm^{-1}) to 25 nm ($f = 10^{-1.4}$ nm^{-1}) gives $\beta = -4.57 \pm 0.02$. These exponents β can be partly explained by a growth model in which the deposited particles (for instance gold clusters) may diffuse on the surface to minimize the local curvature. If we assume that the chemical potential which controls the diffusion probability is proportional to the local curvature (the laplacian of the height of the interface), we obtain a laplacian squared term in the temporal evolution of the height of the interface: $\partial h/\partial t = -K\nabla^4 h$. Such a behavior is reflected in the power spectrum by a f^{-4} behavior. These power spectra show intermediate regimes with scaling exponents β respectively larger (slow mode deposition) and

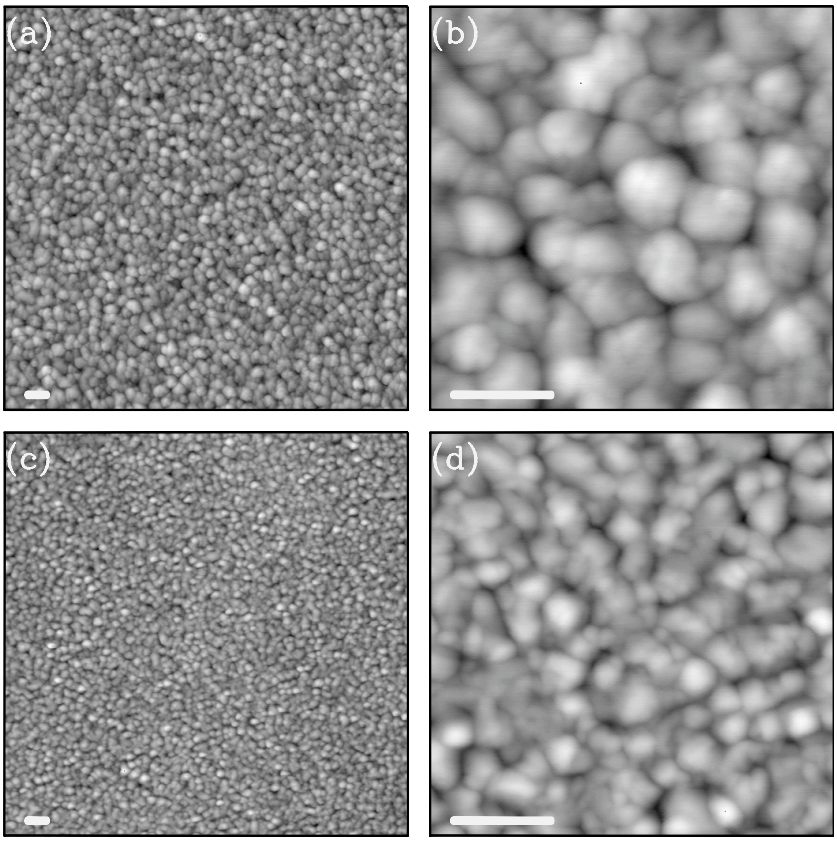

Figure 2.2 Topography of the evaporated gold surfaces imaged by tapping mode AFM. (a) and (b) slow deposition mode (the grey level coding has been done on 11.89 nm height, corresponding to the total variation of height measured from a sample of 24 AFM images). (c) and (d) fast deposition mode (the grey level coding has been done on 9.63 nm height, corresponding to the total variation of height measured from a sample of 26 AFM images). Scale of (a) and (c): 2 μm$\times$2 μm. Scale of (b) and (d): 400 nm$\times$400 nm. Scale bar is 100 nm.

smaller (fast mode deposition) than -4. The narrow range of size scales may be one of the reasons why these exponents are not exactly -4. We also think that during gold deposition, some coalescence of gold clusters may occur, leading to a different power law in the evolution equation for h. We can however conclude from this spectral analysis that in this intermediate regime the gold features adopt a continuum of sizes in a finite range of scales and that their distribution is self-similar[101].

Figure 2.3(b) shows the histograms of heights computed from the same sets of AFM images as those used for the 1D power spectra. The origin for z is set at the maximum of these histograms. If the histograms were symmetric, this maximum should correspond to the mean height of the gold layer. The histogram corresponding to slow deposited gold is wider (4.43 nm at $1/e$ of the maximum) than the fast deposited gold surfaces (3.2 nm at $1/e$ of the maximum). We conclude from this analysis that the fast deposited gold films are more homogeneous, with shallower and narrower grooves.

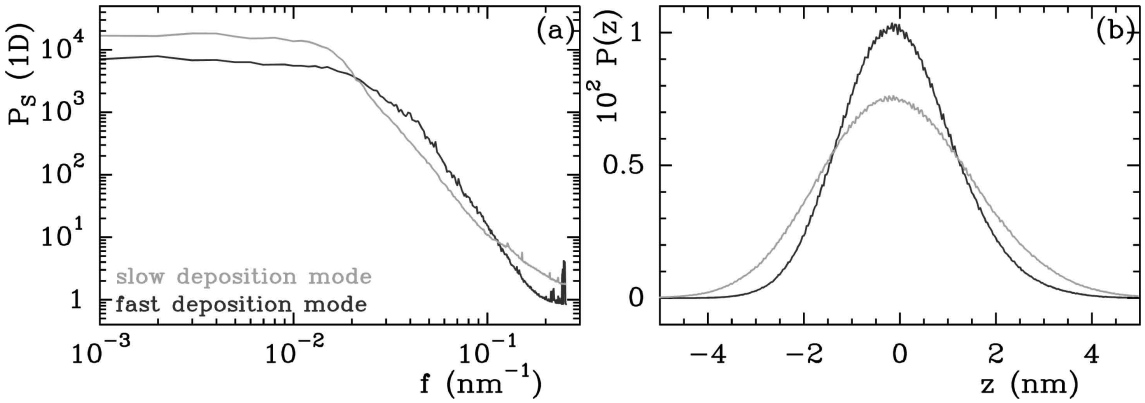

Figure 2.3 Characterization of the gold surface roughness for both slow and fast deposition modes. (a) 1D power spectra computed from 1 μm^2 AFM images. (b) Histograms of heights computed from 1 μm^2 AFM images.

In conclusion, increasing the rate of deposition during thermal evaporation has a great influence on the structure of the gold layer. The metal clusters tend to be smaller and the global roughness is decreased.

A.1.3 Parametrization of SPR curves using a three layer model

The parametrization of the SPR curves presented in Figure 2.1 is performed using Fresnel refraction and reflection equations[102]. To begin, we simply use a three layer system, such as depicted in Figure 2.4(a), with three media: glass, plain gold and dielectric (air).

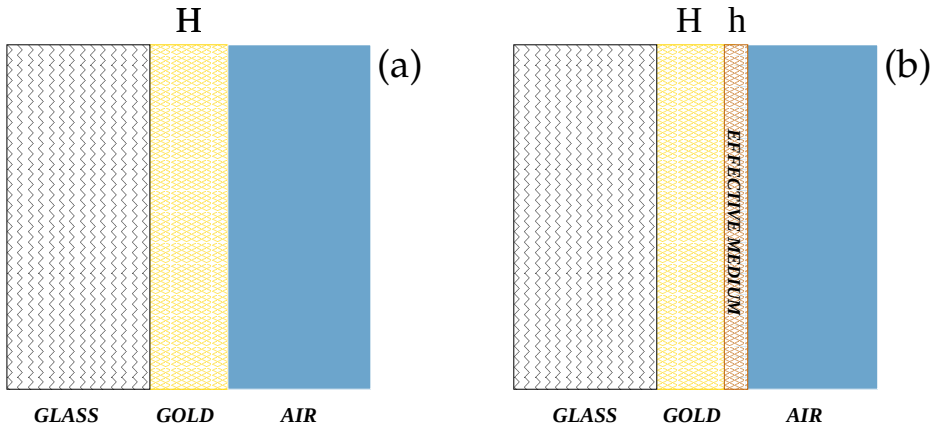

Figure 2.4 (a) Three layer model: glass, plain gold (thickness H) and air. (b) Four layer model: glass, plain gold (thickness H), an effective medium corresponding to a mix of air and gold (thickness h) and air.

The reflection coefficient for a model with three media labelled 0, 1 and 2 reads:

$$R_p/R_s = \frac{(r_{01}^{(p)} + r_{12}^{(p)} e^{-i\delta})(1 + r_{01}^{(s)} r_{12}^{(s)} e^{-i\delta})}{(1 + r_{01}^{(p)} r_{12}^{(p)} e^{-i\delta})(r_{01}^{(s)} + r_{12}^{(s)} e^{-i\delta})} \tag{2.1}$$

where r_{ij} is the refraction coefficient at the $i-j$ interface, $\delta = [4\pi(\varepsilon_1)^{1/2}\cos(\alpha_1)]H/\lambda$ and H is the thickness of the gold layer, α_1 the complex angle of the beam with the average normal of the surface inside the gold. The variables of r_{ij} depend on the polarization (p or s) of the incoming beam:

$$r_{ij}^{s} = \frac{(\varepsilon_i^{1/2})\cos\alpha_i - (\varepsilon_j^{1/2})\cos\alpha_j}{(\varepsilon_i^{1/2})\cos\alpha_i + (\varepsilon_j^{1/2})\cos\alpha_j} \quad , \quad r_{ij}^{p} = \frac{(\varepsilon_i^{1/2})\cos\alpha_j - (\varepsilon_j^{1/2})\cos\alpha_i}{(\varepsilon_j^{1/2})\cos\alpha_j + (\varepsilon_j^{1/2})\cos\alpha_i} \tag{2.2}$$

with α_i the angle of incidence in medium i, ε_i the dielectric permittivity of medium i. α_i and α_j are related by $\varepsilon_i^{1/2}\sin\alpha_i = \varepsilon_j^{1/2}\sin\alpha_j$.

These equations are used to fit SPR reflectivity curves, as shown in Figure 2.5, for the slow (a) and fast (b) deposition mode respectively. The gold indices used for this parametrization are those of M.L. Thèye[41] and can also be found in the handbook of Palik[103]. The parametrization is performed in two steps. First, a least square minimization is performed independently on each SPR profile, for 6 different wavelengths, giving a different gold layer thickness for each wavelength.

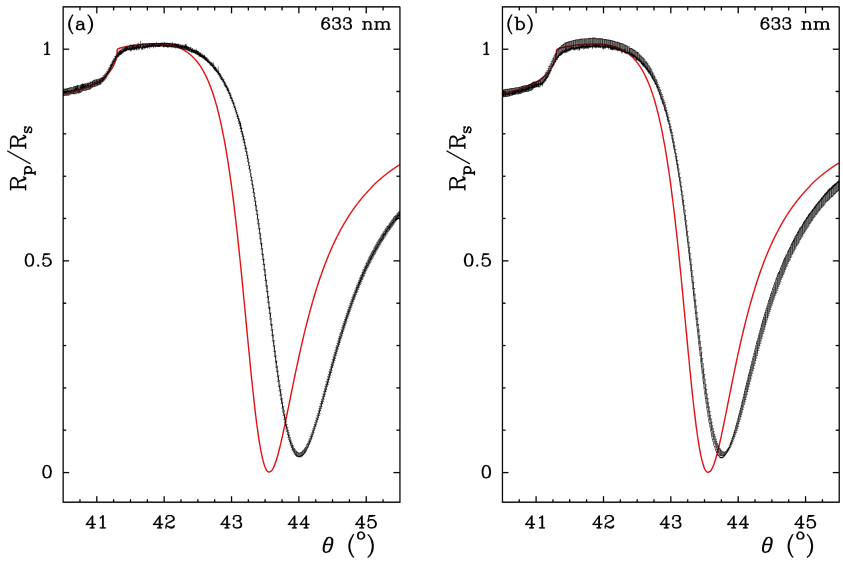

Figure 2.5 Experimental (black) and fitted (red) SPR curves (R_p/R_s) obtained for slow (a) and fast (b) deposition modes with a three layer model (as depicted in Figure 2.4(a)). The curves presented here correspond to $\lambda = 633$ nm.

Then the average of these thicknesses is computed and the SPR curves are recalculated. For the slow deposition mode, an average thickness of 44.7 ±1.7 nm is obtained, for the fast deposition mode, it is estimated to 44.5 ±1.5 nm. These two thicknesses are very close to each other, with only a 0.5% variation which is inside the error bars.

Figure 2.5 shows the experimental (black) and fitted (red) SPR curves for slow (a) and fast (b) deposition rates for $\lambda = 633$ nm (the other wavelengths are not presented here). Compared to fast deposition (b), the SPR curve of the slow one (a) is not only shifted to greater angles, but its shape is also changed, leading to wider a resonance.

Hence, we see that a simple flat model, using the indices of gold given by Thèye[41], cannot explain such a shift of the SP resonance angle θ_P, since these two gold films have a very similar thickness. The limitation of such a model is also very well illustrated considering the difference between experimental (black) and fitted (red) curves in Figure 2.5 : this difference is much greater than the experimental fluctuations. However, the good reproducibility of these SPR curves with different coverslips, and the study of the surface topography with AFM discarded the hypothesis of an optical misfit. We must therefore consider that the gold films are heterogeneous.

A.1.4 Effective medium model of gold inhomogeneity

We revisit now our model of these gold films for SPR, so as to take the gold inhomogeneities into account. The first theoretical model to propose an interpretation of the anomalous absorption of light by a thin layer of gold metal (different colors in the visible spectrum) was given by Maxwell-Garnett[104]. The effective dielectric constant of the film ε is related to dielectric constants of gold ε_1 and to the dielectric medium ε_2 by the relation:

$$\frac{\varepsilon - \varepsilon_2}{\varepsilon + 2\varepsilon_2} = \eta_1 \frac{\varepsilon_1 - \varepsilon_2}{\varepsilon_1 + 2\varepsilon_2}, \tag{2.3}$$

where η_1 is the volume fraction of gold in the film.
Note that the model of Maxwell-Garnett is disymmetric and discontinuous. However, this limitation was solved thirty years later by the effective medium model of Bruggeman (1935):[105–107]

$$\eta_1 \left(\frac{\varepsilon_1 - \varepsilon}{\varepsilon_1 + 2\varepsilon} \right) + \eta_2 \left(\frac{\varepsilon_2 - \varepsilon}{\varepsilon_2 + 2\varepsilon} \right) = 0, \tag{2.4}$$

where η_1 and η_2 are the volume fractions of media 1 and 2. The solution of this equation is the dielectric constant ε of the hybrid medium. The solution of equation (2.4) reads:

$$\begin{aligned} \varepsilon &= \frac{\varepsilon_1(2-f) + \varepsilon_2(2f-1)}{4(f+1)} \\ &\pm \frac{\sqrt{f^2(\varepsilon_1^2 + 4\varepsilon_1\varepsilon_2 + 4\varepsilon_2^2) + f(-4\varepsilon_1^2 + 26\varepsilon_1\varepsilon_2 - 4\varepsilon_2^2) + (4\varepsilon_1^2 + 4\varepsilon_1\varepsilon_2 + \varepsilon_2^2)}}{4(f+1)} \end{aligned} \tag{2.5}$$

where $f = \eta_2/\eta_1$. The shape of the solution of equation (2.5) which preserves positive values of the imaginary part of ε is plotted in Figure 2.6. Both the real part (ε') and the imaginary part (ε'') are non monotonous functions of the volume ratio of gold η_1. Note also that for η_1 larger than 0.75 the behaviors of ε' and ε'' are quasi-linear versus η_1: ε' is decreasing with η_1, and ε'' is increasing with η_1.

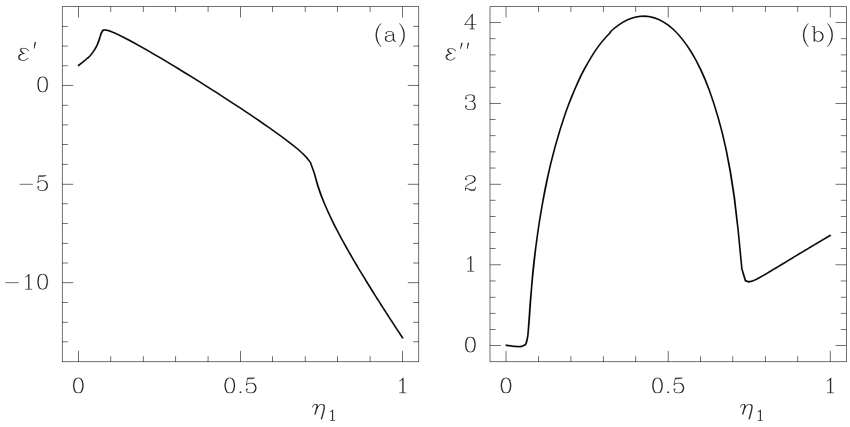

Figure 2.6 Evolution of the real (a) and imaginary (b) parts of the dielectric constants of gold versus the volume fraction of gold, as predicted by equation (2.5). The index of gold chosen for this computation can be found in reference[41] for $\lambda = 633$ nm.

A.1.5 Parametrization of SPR data with a four layer model

To improve the modeling of our gold films, we introduce a four layer model (see Figure 2.7), where we can separate the gold film into two zone, of different density: a plain gold film and an extra layer with an effective dielectric constant computed with the model of Bruggeman. The parametrization of the SPR curves for the slow and fast deposition modes with a four layer model is reported in Figure 2.7, respectively (a) and (b). Similarly to Figure 2.5, only the experimental (black) and fitted (red) curves corresponding to $\lambda = 633$ nm are shown.

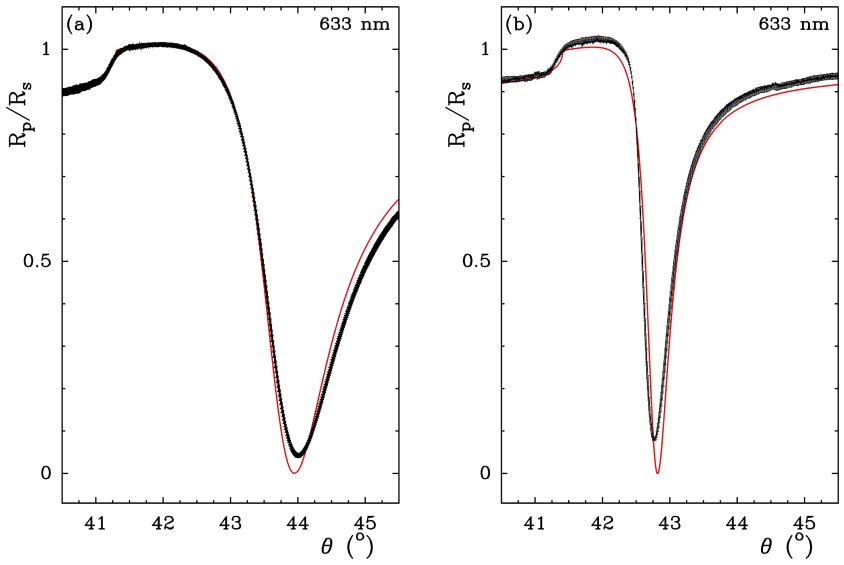

Figure 2.7 Experimental (black) and fitted (red) SPR curves (R_p/R_s) obtained for slow (a) and fast (b) deposition modes with a four layer model (as depicted in Figure 2.4(b)). The curves presented here correspond to $\lambda = 633$ nm.

The estimated thicknesses of plain gold (H) and effective medium layer (h), with the volume fraction of gold are ($H = 39.48$ nm, $h = 6.4$ nm, $\eta_1 = 0.784$) and ($H = 42.18$ nm, $h = 3.61$ nm, $\eta_1 = 0.825$) for slow and fast deposition mode respectively. The estimation of H and h is afforded by a Levenberg-Marquardt minimization on R_p/R_s without putting a different weight on these two parameters. The fact that the minimization leads to a similar value of $H + h$ in both cases (~ 45.8 nm) is in agreement with the prediction of the three layer model. It also predicts a greater amount of gold inside the film for the fast deposition mode. We also note that if the predicted value of $h = 3.61$ nm for the fast deposited gold film is rather close to the width of the histogram of heights computed from the corresponding images (3.20 nm), it is much larger in the slow deposition mode ($h = 6.4$ nm to be compared with the histogram width of 4.43 nm).

The four layer model provides also a better parametrization of the left part of the R_p/R_s curve, for angles smaller than 43.5°, but the estimation of the minimum of the SPR curves is still unprecise. The mean square deviation between the experimental SPR curves and their parametrization with a four layer model is 7.6 10^{-4} for the slow deposition mode and 7.3 10^{-4} for the fast deposition mode, to be compared with the mean square deviation obtained from the single gold layer model, using Thèye gold indices (Figure 2.5): 2 10^{-2} for the slow deposition mode and 4.1 10^{-3} for the fast deposition mode. Therefore, this four layer model brings a better approximation of the experimental curves, and this approximation reaches the same accuracy in slow and fast deposition. However, the estimation of the angle $\theta_m(\lambda)$ corresponding to the SPR minimum could still be improved since the quality of the fit depends on the wavelength (see Table 2.1),with $\theta_{exp} - \theta_{fit}$ in the range $-0.05°$ to $0.09°$. A few hundredths of a degree is not negligible since our optical set-up has an angular resolution of $0.001°$.

SLOW DEPOSITION				**FAST DEPOSITION**			
$\lambda(nm)$	$\theta_{exp}(°)$	$\theta_{fit}(°)$	$\theta_{exp} - \theta_{fit}(°)$	$\lambda(nm)$	$\theta_{exp}(°)$	$\theta_{fit}(°)$	$\theta_{exp} - \theta_{fit}(°)$
750	42.896	42.9413	-0.0453	750	42.753	42.8191	-0.0661
700	43.217	43.2635	-0.0465	700	43.062	43.1103	-0.0483
676	43.440	43.4594	-0.0194	676	43.261	43.2863	-0.0253
647	43.789	43.7616	0.0274	647	43.569	43.5586	0.0104
633	44.001	43.9509	0.0501	633	43.765	43.7280	0.0370
600	44.695	44.5963	0.0987	600	44.349	44.3080	0.0410

Table 2.1 Comparison of experimental and predicted values (with a four layer model) for the angles corresponding to minimum of R_p/R_s curves, and their differences.

In consequence, although the SPR curve fitting is improved, considering the roughness of these thin gold films, this parametrization still gives an inaccurate prediction of $\theta_m(\lambda)$ in regard with the resolution of the optical set-up.

To conclude this section, we have seen that the inability of the four layer model to fit the experimental $\theta_m(\lambda)$ is probably due to the separation of the film in two distinctive parts, a plain layer and a heterogeneous one. Moreover, the difference between the two effective medium thicknesses h predicted by the model is larger than the width at half maximum of

the histograms of heights shown in Figure 2.3. Despite the addition of an extra effective layer which brings a quantitative improvement to the SPR curve parametrization, it still lacks precision. We suspect that the gold layers may not only be rough in surface but also internally, and that the gold index values taken from the tables may be incorrect here. These dielectric indices will therefore be taken as parameters for the parametrization in the next section.

A.2 Bulk inhomogeneities of the layers

In this section, we refine our model by taking the gold dielectric index as a parameter, and we show some SSPM images that can give information about the quality of the layers.

A.2.1 Parametrization of SPR data with variable gold indices

The whole gold film is treated as an effective medium and the experimental SPR curves are fitted with two variables for each wavelength: the thickness H_e of this effective medium and its index ε_e. These parameters are again determined by a least square minimization process. Once the six thicknesses and index values corresponding to the six wavelengths are evaluated, we average the thicknesses and start again a parametrization of all the curves with the mean thickness of gold, keeping the gold indices versus wavelength as unknown parameters. The results of this parametrization for slow and fast deposition mode are presented in Figure 2.8 (a) and (b) respectively.

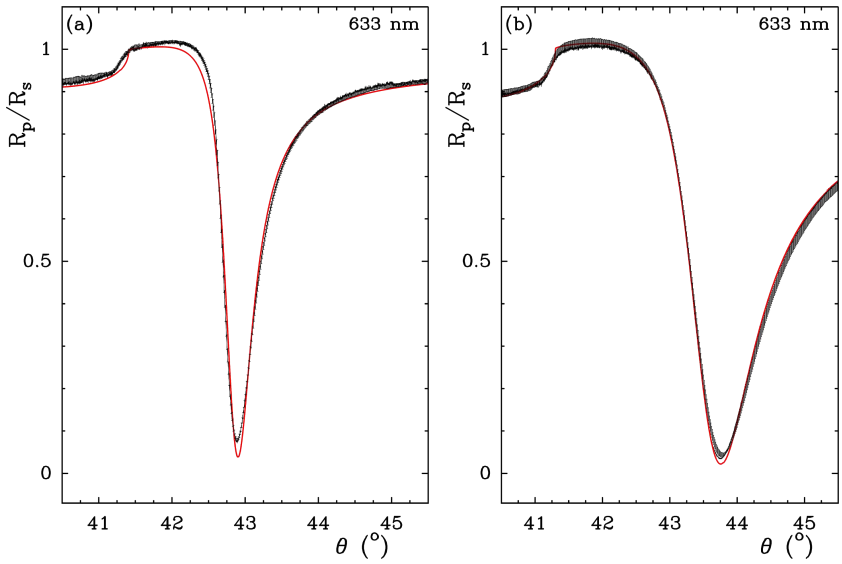

Figure 2.8 Experimental (black) and fitted (red) SPR curves (R_p/R_s) obtained for slow (a) and fast (b) deposition modes with a three layer model with adjustable gold indices. The curves presented here correspond to $\lambda = 633$ nm.

We clearly see in figure 2.8 that using an adjustable thickness and index of gold improves significantly the fit to the experimental data, regardless of the evaporation rate. The mean square deviation between the experimental SPR and the fitted curves is $(1.77 \pm 0.3)10^{-4}$ for the slow deposition mode and $(1.8 \pm 1)10^{-4}$ for the fast deposition mode. The shift in angle between theoretical and experimental SPR curves for the six wavelengths is given in Table 2.2. With this parametrization of the gold films, we get closer to the precision of the SPR apparatus which is $\sim 0.001°$, the estimation of the SPR minima is more accurate for the fast deposited gold samples. The values of gold indices are given in Table 2.3. The predicted global thicknesses of gold are 45.85 nm and 44.11 nm for the slow and fast deposition mode respectively.

SLOW DEPOSITION				**FAST DEPOSITION**			
$\lambda(nm)$	$\theta_{exp}(°)$	$\theta_{fit}(°)$	$\theta_{exp} - \theta_{fit}(°)$	$\lambda(nm)$	$\theta_{exp}(°)$	$\theta_{fit}(°)$	$\theta_{exp} - \theta_{fit}(°)$
750	42.896	42.9026	-0.0066	750	42.753	42.7737	-0.0207
700	43.217	43.2347	-0.0177	700	43.062	43.0693	-0.0073
676	43.440	43.4550	-0.0150	676	43.261	43.2630	-0.0020
647	43.789	43.8070	-0.0180	647	43.569	43.5763	-0.0073
633	44.001	44.0151	-0.0141	633	43.765	43.7601	0.0049
600	44.695	44.6926	0.0024	600	44.349	44.3567	-0.0077

Table 2.2 Comparison of experimental and predicted values (with a three layer model, and effective gold layer) for the angles corresponding to minimum of R_p/R_s curves, and their differences.

SLOW DEPOSITION				**FAST DEPOSITION**			
λ (nm)	ε'	ε''	mean square deviation	λ (nm)	ε'	ε''	mean square deviation
600	-8.89	1.13	$2.1\ 10^{-4}$	600	-9.83	1.23	$1.45\ 10^{-4}$
633	-11.07	1.074	$4.\ 10^{-5}$	633	-12.18	1.17	$3.8\ 10^{-5}$
647	-11.99	1.029	$1.4\ 10^{-4}$	647	-13.18	1.11	$1.4\ 10^{-4}$
676	-14.01	0.91	$2.4\ 10^{-4}$	676	-15.36	0.99	$2.6\ 10^{-4}$
700	-15.72	1.01	$1.5\ 10^{-4}$	700	-17.21	1.09	$1.6\ 10^{-4}$
750	-19.42	1.089	$2.7\ 10^{-4}$	750	-21.20	1.19	$3.4\ 10^{-4}$

Table 2.3 Table of gold indices estimated from the parametrization of experimental SPR curves with a three layer model. The global gold thickness is estimated by $H_e = 45.85$ nm and $H_e = 44.11$ nm for the slow and fast deposition modes respectively. The mean square deviation between the experimental and the fitted SPR curves is also reported for each case.

The differences of the gold indices, obtained with this parametrization, bring an additional evidence that the gold films prepared by either slow or fast evaporation are not identical. Moreover, the improved accuracy of the parametrization confirms our intuition that the heterogeneity of these films may not solely be interfacial, but also global. We also suspect that the shape and size of the "holes" inside the gold layer may vary with the depth.

A.2.2 Comparison of our gold index estimations with previously reported data

Comparing our predicted values for gold index with previously reported data (Figure 2.9) is very interesting since it not only allows the estimation of global fractions of gold, but also gives a criterion to judge the quality of thin gold film preparation, and their fraction of vacuum inclusions. In Figure 2.9, we report three sets of data taken from the literature, respectively the work of Thèye[41], Johnson and Christy[108], and from Handbook of Physics[109].

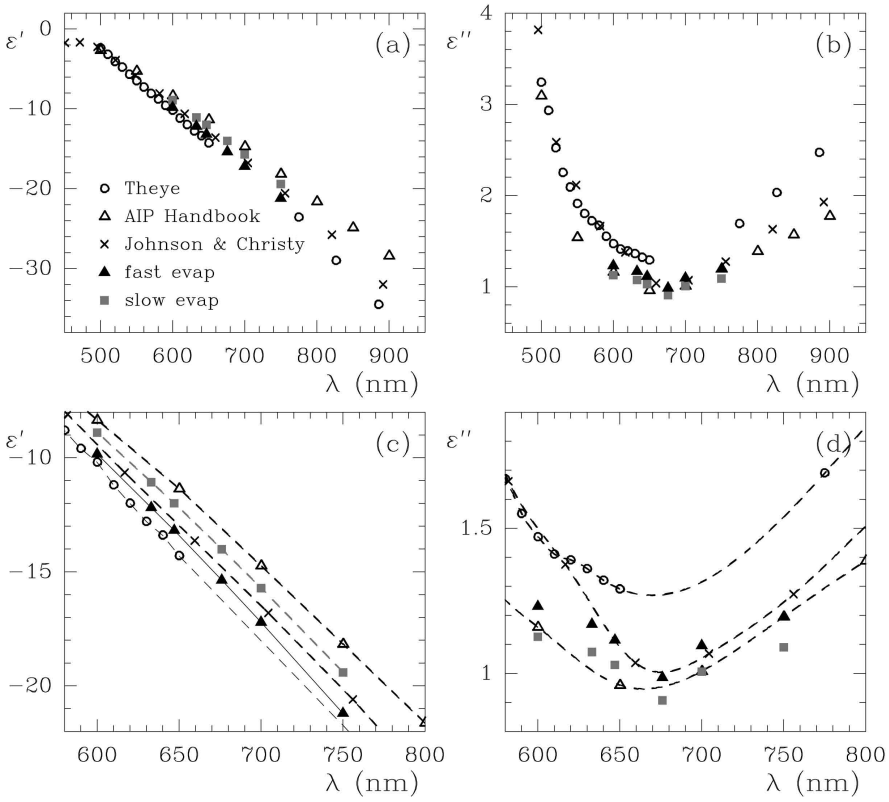

Figure 2.9 Comparison of the dielectric constants of gold predicted by our experimental data fits, with literature data of Thèye[41], Johnson and Christy[108], and Handbook of Physics[109]. (a) and (b) give the real and imaginary part of the dielectric constant. In (c) and (d) we have zoomed in on the wavelength range used for our SPR measures.

The dielectric constants (real and imaginary parts) computed from our least square fitting of two sets of evaporated gold films fall in the same interval as these literature data. We note also that our ε' values are systematically above Thèye values, whereas our ε'' values are systematically below Thèye values. In Figure 2.6, the plot of ε' and ε'' versus the volume fraction of gold η_1, close to $\eta_1 = 1$, shows that ε' is decreasing and ε'' is increasing versus η_1. We can therefore interpret the position of our two sets of data points with respect to Thèye data in Figure 2.9 as a diminution of the fraction of gold, the slow deposition mode corresponding to the smallest fraction of gold. These fractions of gold can be computed with the Bruggeman model, assuming that Thèye ε values correspond to plain gold. From the real

part of ε, we get $\eta_1 = 0.9292 \pm 0.0093$ for slow deposition mode, and $\eta_1 = 0.9714 \pm 0.0086$ for fast deposition mode.
Finally, the averaged volume fraction of gold in the fast deposition mode is higher: the metal films contain less inclusions of vacuum. To try and understand this behavior, let us first remind (see Section A.1.2, and more precisely Figure 2.3) that the size of the gold clusters depends on the speed of their extraction from the metal source. By assuming that the diffusion and coalescence rates are likely to vary little with the size of the clusters, it is likely then that the problem is simplified to a question of piling up quasi-spherical clusters, and that the proportion of vacuum inclusions goes higher with the cluster size.

A.2.3 SSPM images of the gold films

In this section, we use the high resolution SSPM to provide a spatial information that SPR measurements cannot provide. The SSPM images presented here have also been flattened with a 0^{th}order flattening. Moreover, to avoid laser intensity fluctuations, SSPM images are normalized (by using the maximum of the $I(Z)/I_0$ curve[76, 77, 79, 84, 110]). Finally, they are averaged with a sliding box of 3x3 pixels to get rid of the high frequency electrical noise of the set-up[84].

The images shown in Figure 2.10 correspond to the slow (a) and (b), and fast (c) and (d), rates of deposition. Cross-sections of those images are presented in Figure 2.10 (e) and (f), respectively for a defocalization value of the objective of $z = 0$ μm and $z = 1$ μm.
As explained in Chapter 1, the image is formed by recording the $I(z)/I_0$ optical signal for a fixed z whereas the lateral (x,y) position of the sample is varied. As a reminder, images acquired at focus (*ie.* for $z = 0$; Figure 2.10 (a) and (c)) give principally informations on inhomogeneities in bulk, whereas imaging at $z > 0$ (the objective is focused in air beyond the gold/air interface; See Figure 1.28) enhances the sensitivity of detection and also allows to recognize nanoscale variations at the gold/air interface highlighted by the surface plasmon resonance (Figure 2.10 (b) and (d)).

Images (a) and (c) ($z = 0$) are coded in the range of [-0.04, 0.03] and images (b) and (d) ($z = -1$ μm) are coded in the range of [-0.005, 0.005]. Figure 2.10 (e) reports horizontal cross-sections of images (a) and (c) and Figure 2.10 (f) reports horizontal cross-sections of images (b) and (d). Figures 2.10 (a) to (f) show that for both values of z, the images of the gold layer corresponding to the slow evaporation rate are more contrasted than those for the fast deposition mode. The greater dynamics of the images for slow deposition mode means that the gold layer is less regular spatially than in the fast deposition mode. If we analyze in detail the image contrasts for $z = 0$, we observe that for slow deposition mode, black grains with 200 nm to 500 nm lateral size are present all over the surface (see Figure 2.10(a) and the deep valleys of Figure 2.10(e)), whereas no such structure is observed for fast deposited mode (Figure 2.10(c) and (f)). We can interpret these black grains as domains where light is less reflected, in other words as domains for which the amount of gold is changed. For $z = 1$ μm, the variations of $I(z)/I_0$ are again larger for slow deposition mode, due to surface heterogeneity of gold. In Figure 2.10(b) we can still notice black grains, but they are smaller and

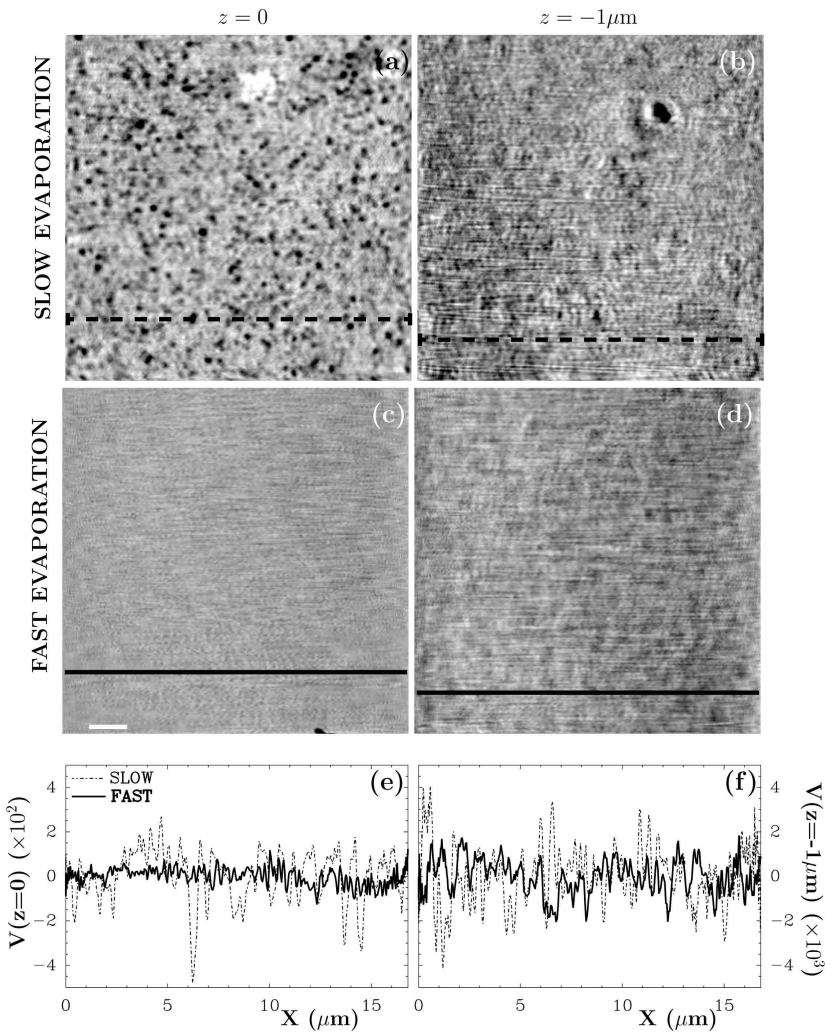

Figure 2.10 SPPM images of the two gold films. (a) and (b) correspond to slow deposition mode, $z = 0$ and $z = -1$ μm respectively. (c) and (d) correspond to fast deposition mode, $z = 0$ and $z = -1$ μm respectively. (e) horizontal cross-sections of (a) (dashed line) and (c) (black line). (f) horizontal cross-sections of (b) (dashed line) and (d) (black line). The position of the cross-sections are marked by dashed lines in (a) and (b), and by a plain line in (c) and (d). Range of $V(z)$ grey coding: [-0.04, 0.03] for (a) and (c), [-0.005, 0.005] for (b) and (d). White scale bar is 2 μm for all images.

less pronounced compared to the background fluctuations of the image. These fluctuations at $z = 1$ μm (Figure 2.10 (b), (d) and (f)) are due to surface plasmon resonance modification, introduced by the gold surface heterogeneity. The two images at $z = 1$ μm confirm therefore that the gold surface roughness is enhanced by a slow deposition rate.
In consequence, these images show not only that SSPM is a well suited tool to discriminate between surface and bulk features of thin gold films, but also that the variations in the layer structure caused by a modification in the deposition parameters can be probed with this technique.

A.3 Gold films are inhomogeneous both in surface and in bulk

We have shown by AFM and SPR techniques that the gold content of thermally evaporated gold films is highly dependent on the preparation mode, and in particular on the deposition rate.
We used three different models to interpret the surface plasmon resonance of such gold films. We showed that it is not sufficient to use the widely accepted model of a plain gold layer with surface roughness in order to fit correctly the surface plasmon resonance.
The best model to fit experimental SPR curves should assume that the thin gold films are made of a mixture of gold and vacuum inclusions. In the two sets of gold layers presented in this work the global volume fraction of gold is found to be greater than 90%. Moreover, high resolution scanning surface plasmon imaging confirms the internal heterogeneity of these thin gold layers. Additionally, the surface roughness observed both by SSPM and AFM should also be taken into account. Finally, to model both the volume and surface heterogeneity, one should consider the thin gold film as a layer with a non-uniform dielectric permittivity from glass/gold interface up to the gold/air interface.

In the next section, we study the influence of the thermal conductivity of the substrate (glass) and its wettability for gold on the surface and bulk properties of the thermally evaporated gold films.

B Modification of the gold layer structure by treatment with 11-mercapto-undecyl-methoxysilane (11MUD(MeO)$_3$Si) molecules

The preparation of thin gold films on glass by thermal evaporation requires systematically a treatment of the substrate in order to improve the wettability of gold. Usually another metal (Cr), or a mixture of metals that wet better the glass is used. However, this first layer is also inhomogeneous and it modifies the plasmon resonance curves.
We discuss in this section the possibility of replacing this intermediate metal layer with an organic self-assembled monolayer.
In order to understand more closely how the wetting of gold on the glass surface influences the topography of the metal films, we treat chemically the glass substrates with 11-mercapto-undecyl-methoxysilane (11MUD(MeO)$_3$Si) molecules that have been specifically synthesized by Prochimia (Poland) for this purpose. The idea is to play on the chemical compatibility of glass and gold to improve the structure of the films: a self-assembled monolayer (SAM) of those molecules ($\sim$ 1.5 nm thick) is formed at the surface of the glass coverslip thanks to the silane heads and the wettability of gold is enhanced because of the thiol functional groups.
In this section, AFM, SPR, X-ray Photoelectron Spectroscopy (XPS) and SSPM experiments are carried out on chemically treated glass substrates. Quantitative characterization of the surface structures are done by computing both the 1D power spectra and histograms of height from the AFM topography and phase images, and the shapes of the gold islands at the surface are determined by 2D Wavelet Transform Modulus Maxima (WTMM) segmentation method.
This study was done in collaboration with Alain Arneodo and Lotfi Berguiga (Laboratoire Joliot-Curie USR3010 and Laboratoire de Physique UMR5672 at the Ecole Normale Supérieure de Lyon, France), Laurent Bonneviot (Laboratoire de Chimie UMR5182 at the ENS Lyon, France), Juan Elezgaray (1-ENITAB IECB UMR5248, Université de Bordeaux 1, France), and André Khalil and Aaron Tanenbaum (University of Maine, USA)[111].

B.1 Surface structure analysis of the chemically treated samples after deposition of gold

B.1.1 AFM images of the gold surfaces

The topography of the gold films prepared after glass treatment with 11MUD(MeO)$_3$Si is presented in Figure 2.11. It shows AFM images in tapping mode for different scales: (a) to (e) 1x1 μm^2, (a') to (e') 2x2 μm^2, (a") to (e") and 5x5 μm^2. (a), (a') and (a") images of untreated glass substrates; (b), (b') and (b") samples treated with 10^{-3}mg.ml^{-1} of 11MUD(MeO)$_3$Si in cyclohexane; (c), (c') and (c") samples treated with 10^{-2}mg.ml^{-1} of 11MUD(MeO)$_3$Si in cyclohexane; (d), (d') and (d") samples treated with 10^{-1}mg.ml^{-1} of 11MUD(MeO)$_3$Si in cyclohexane; (e), (e') and (e") samples treated with 1 mg.ml^{-1} of 11MUD(MeO)$_3$Si in cyclohexane.

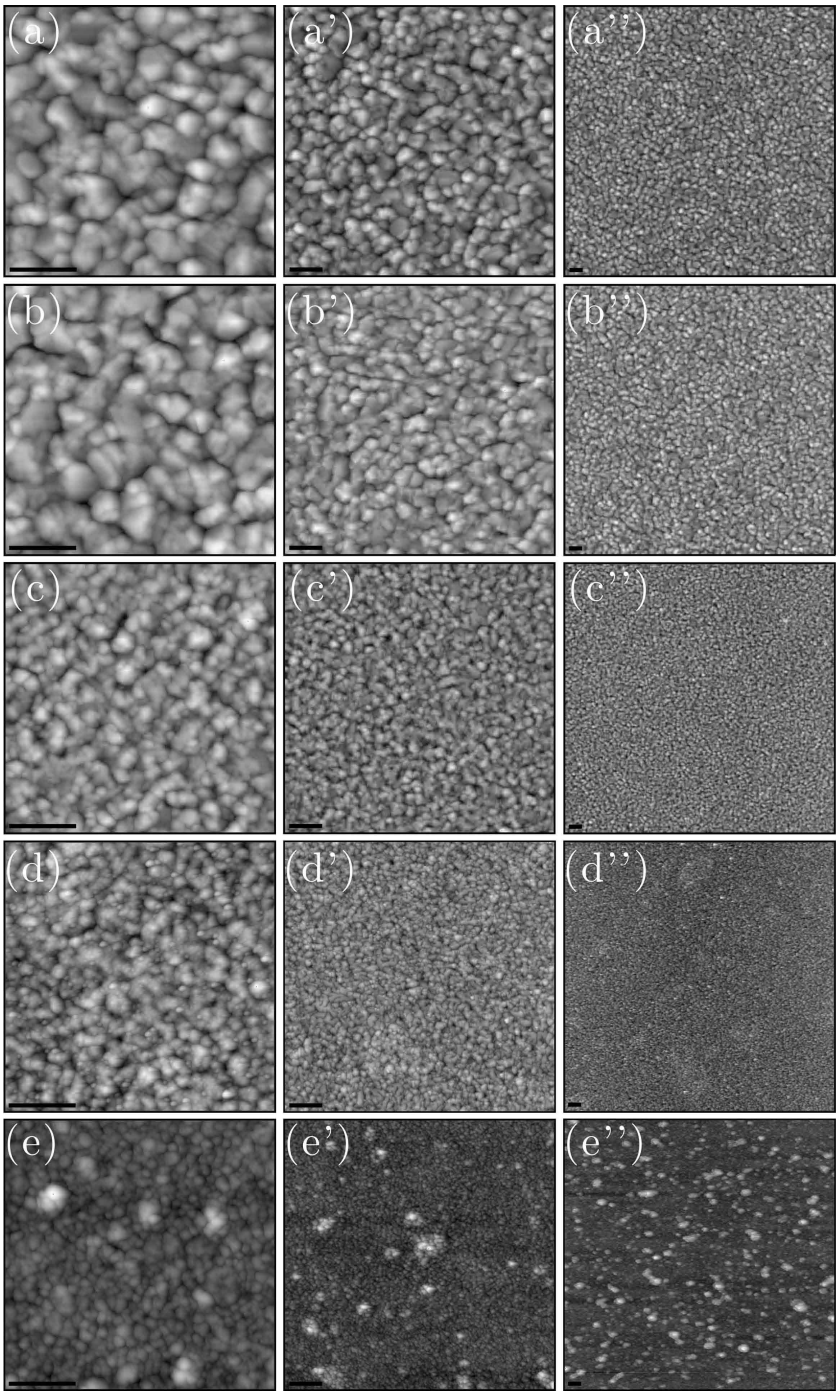

Figure 2.11 Topography of gold film surfaces prepared by thermal evaporation on glass substrates, obtained by AFM tapping imaging. (a), (a') and (a"): no treatment of glass prior to the evaporation. (b), (b') and (b"): treatment of glass by 11-mercaptoundecyltrimethoxysilane [10^{-3} mg.ml^{-1}] in cyclohexane. (c), (c') and (c"): treatment of glass by 11-mercaptoundecyltrimethoxysilane (11MUD(MeO)$_3$Si) [10^{-2} mg.ml^{-1}] in cyclohexane. (d), (d') and (d"): treatment of glass by 11-mercaptoundecyltrimethoxysilane (11MUD(MeO)$_3$Si) [10^{-1} mg.ml^{-1}] in cyclohexane. (e), (e') and (e"): treatment of glass by 11-mercaptoundecyltrimethoxysilane (11MUD(MeO)$_3$Si) [1 mg.ml^{-1}] in cyclohexane. Brighter regions indicate topmost part of the gold surface. The scale bar corresponds to 250 nm. The minimum (black) and maximum (white) height of the images respectively correspond to: (a) -20.8 nm and 20.2 nm; (a') -20.3 nm and 24.4nm; (a") -25.6 nm and 25.3 nm; (b) -23.4 nm and 20.6 nm; (b') -27.4 nm and 24.7 nm; (b") -25.6 nm and 25.3 nm; (c) -12.5 nm and 11.9 nm; (c') -11.7 nm and 14.3 nm; (c") -11.5 nm and 14.4 nm (d) -8.8 nm and 10.2nm; (d') -10.0 nm and 15.6 nm; (d") -8.8 nm and 15.7 nm (e) -7.1 nm and 18.4 nm; (e') -11.2 nm and 66.7 nm; (e") -10.63 nm and 26.9 nm.

This figure shows several interesting features. First of all, even though the image dynamic range of relief (grey level coding) of the untreated samples (a), (a') and (a") is about the same as those for gold layers prepared with 10^{-3} mg.ml^{-1} of 11MUD(MeO)$_3$Si (b), (b') and (b"), it is almost twice as large as the image dynamics of the films prepared with 10^{-2} mg.ml^{-1} of molecules (c), (c') and (c"): respectively $\sim$ 46 nm, $\sim$ 49 nm and $\sim$ 25 nm.
Furthermore, we also see a larger number of gold nuclei after treatment with 10^{-2} mg.ml^{-1} of molecules (c), (c') and (c"). It also seems that their size is about two to three times smaller than the ones corresponding to untreated (a), (a') and (a") samples or to the ones treated with 10^{-3} mg.ml^{-1} of 11MUD(MeO)$_3$Si (b), (b') and (b").
On the other hand, samples treated with 10^{-1} mg.ml^{-1} (d), (d') and (d") or 1 mg.ml^{-1} (e), (e') and (e") of 11MUD(MeO)$_3$Si show a degradation of the surface morphology: larger gold droplets form aggregates which overlay on the gold film, increasing drastically the overall roughness. These surfaces accumulate a large number of defects which are detrimental to their use as optical sensors. We will therefore limit our study to lower concentration treatment of glass surfaces for which the gold film recovers a global homogeneity (untreated samples, or coverslips treated with 10^{-3} mg.ml^{-1} or 10^{-2} mg.ml^{-1} of molecules).

As a conclusion, AFM imaging demonstrated that treating the glass substrates with 11MUD(MeO)$_3$Si has a strong impact on the surface structure of the gold films after deposition. A more detailed and quantitative analysis follows.

B.1.2 Power spectral analysis and histogram of heights of the AFM images

Figures 2.12(a) and (b) show respectively the averaged 1D power spectra (along the x direction) and histograms of heights computed from about 50 AFM images (1x1 μm^2) of the bare or treated glass coverslips after deposition of gold. These AFM images were captured for several areas of each sample, where no drastic modification in the range of sizes or in the shapes of the objects could be noted (see errorbars in the figures of the next sections). The averaging for both the power spectra and the histograms of height has been carried out over the 512 lines in the image, and for the whole set of images.

As in Figure 2.12, the power spectra for each concentration show several domains: one at small frequencies, below $f \sim 18\ \mu m^{-1}$ (70 nm; larger scales) and another one where $P(f)$ saturates at large frequencies, above $f \sim 65\ \mu m^{-1}$ (17 nm; small scales). Those two values have been chosen so that each concentration of treatment show a common range of scales where the curves can be fitted by a linear function in log-log plot.
For the untreated samples (black curve) this power law behavior leads to an estimation of the exponent $\beta = -3.4 \pm 0.1$. Coverslips treated with [10^{-3}mg.ml^{-1}] of 11MUD(MeO)$_3$Si (green line), present in the same range of scales an exponent $\beta = -3.5 \pm 0.1$, and those treated with [10^{-2}mg.ml^{-1}] of molecules (red dashed curve) give $\beta = -3.7 \pm 0.1$. Again, these exponents β are close to -4 and can be explained by the model combining growth and diffusion of the gold blobs at the glass surface (see section 2 A.1.2).

Note that the upper bound of this power law behavior is smaller for glass treated with

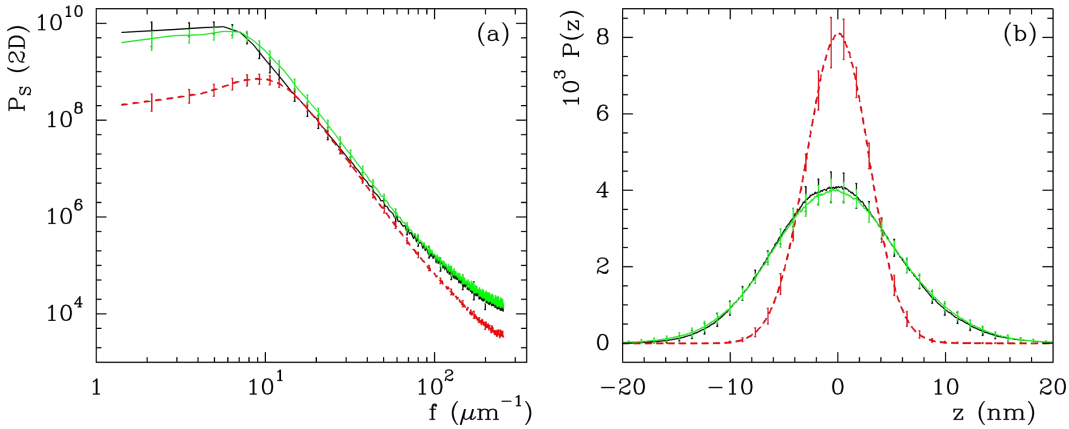

Figure 2.12 (a) averaged 1D power spectra (along the x direction) computed from 1x1 μm^2 AFM topography images of gold film surfaces. Black line: 1D spectrum averaged over 58 images of untreated glass samples. Green line: 1D spectrum averaged over 46 images of glass treated by (11MUD(MeO)$_3$Si) [10^{-3}mg.ml^{-1}] in cyclohexane. Dashed red line: 1D spectrum averaged over 85 images of glass treated by (11MUD(MeO)$_3$Si) [10^{-2}mg.ml^{-1}] in cyclohexane. (b) averaged histograms of height of the gold surface topography computed from the same set as (a), same color coding as in (a).

[10^{-2}mg.ml^{-1}] of 11MUD(MeO)$_3$Si ($\sim$ 75 nm) than for a treatment with [10^{-2}mg.ml^{-1}] of molecules ($\sim$ 100 nm). This is an indication that the higher the concentration of treatment molecules on glass, the smaller the gold features at the surface of the evaporated film.

Figure 2.12(b) presents the histograms of heights calculated from the same sets of AFM images as those used for the 2D power spectra (a). Here, the origin of heights is also set at the maximum of the (non-symmetric) histograms. The untreated (black) and the ones treated with [10^{-3}mg.ml^{-1}] of molecules (green) show a full width at half maximum (FWHM) that is almost twice as large as the one for coverslips treated with a high concentration of 11MUD(MeO)$_3$Si (red dashed line): respectively 13.3 $\pm$ 0.1 nm, 13.6 $\pm$ 0.1 nm, and 6.8 $\pm$ 0.1 nm. This actually means that the roughness of the surfaces for which the glass has been treated with a high concentration of molecules is decreased.

However, when we compare the power spectral analysis and histograms of heights of the metal layers deposited at 0.4 nm/s in section 2 (see Figure 2.3) with those of the samples prepared in this section (see Figure 2.12), we clearly see that the surface structures are not equivalent: the global roughness is higher and the gold clusters bigger in the latter case. We believe that this variation is due to a change in the type of evaporation source used during the deposition of the gold layers. Indeed, the source used in this section is coated with alumina, which decreases its wetting for the metal. The surface of gold in contact with the heat source is then lowered, as well as the energy (the heat) transferred to it. Therefore, the overall extraction of nuclei from the source behaves as if we used the evaporation source of section 2, but for a lower temperature of heating. We expect then the conditions of deposition to be the same as the ones from section 2 at 0.4 nm/s after increasing the temperature of the evaporation source.

To conclude, we have shown here that the samples treated with $[10^{-2}\text{mg.ml}^{-1}]$ of $11\text{MUD(MeO)}_3\text{Si}$ present a topography where the gold objects are smaller. We also saw that these surfaces are more homogeneous, which leads to a roughness that is finally decreased by a factor about two compared to untreated coverslips.

B.1.3 2D Wavelet Transform Modulus Maxima (WTMM) analysis of the AFM images

So as to determine more precisely the sizes and shapes of the gold objects at the surface, a 2D Wavelet Transform Modulus Maxima (WTMM)[112–114] characterization has been done in collaboration with Alain Arneodo and André Khalil.
First of all, as explained in appendix B, the AFM images are analyzed by computing their derivatives at different scales with the 2D Gaussian wavelet presented in Figure B.1 and by looking for the closed contours where these derivatives are maximum. Once the objects have been identified, several parameters are then determined for each metal particle: the area A of the gold particle, its diameter D, perimeter P, filament index F, volume V, and height H.

Figure 2.13 illustrates the segmentation results for an AFM image of a non-treated sample. The objects detected by the WTMM analysis are represented by the white contours in (a), and a 3D view of those objects is given in (b). Only a few objects (typically 15 to 20) are

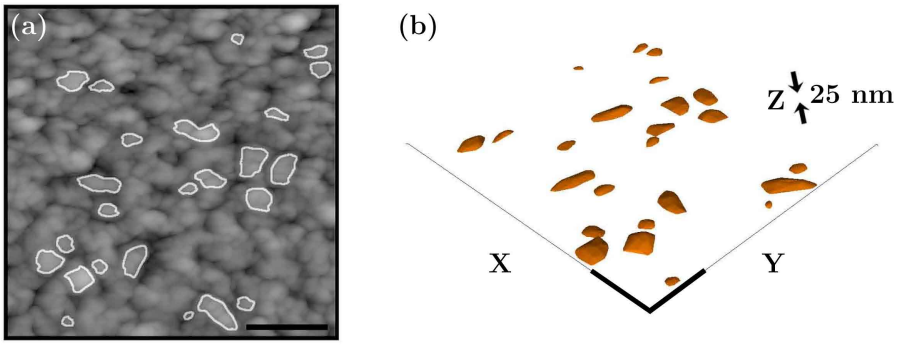

Figure 2.13 (a) Illustration of the 2D WTMM segmentation method from an AFM topography image of gold without chemical treatment. The minimum (black) and maximum (white) height of the image respectively correspond to: -16.74 nm and 20.71 nm. Note that the color of the contours has been arbitrarily chosen and does not participate to the grey scale. (b) 3D representation of the gold objects selected in (a). Scale bars in (a) and (b) correspond to 250 nm in the latteral direction and 25 nm in the axial direction in (b).

detected in each image, no matter the concentration of the chemical treatment. This might be surprising since we could anticipate distinguishing more particles. With this wavelet-based numerical method, the segmentation involves the computation of the gradient of the image at different scales and whenever the object contour is not closed, it is discarded. Therefore, this analysis requires therefore a higher number of sample images.

We can also note that the 2D shapes of the objects are not all alike: some can be small (few tens of nanometers in diameter) others big (more than one hundred nanometers in diameter), and they can present circular or more stretched shapes. In any case, they all show a rather smooth topography, that is with no drastic change in their height.

Figure 2.14 presents the distribution of the gold objects parameters after segmentation by the 2D WTMM segmentation algorithm: (a) the area A, (b) the diameter D, (c) the perimeter P, (d) the filament index F, (e) the volume V, and (f) the relative maximum height H of the gold domains. Like the previous figures, the black line corresponds to no chemical treatment, the green line to a treatment with $[10^{-3}\text{mg.ml}^{-1}]$ of 11MUD$(\text{MeO})_3$Si, and the red dashed line to glass substrates treated with $[10^{-2}\text{mg.ml}^{-1}]$.

The most striking observation from Figure 2.14 is that the geometrical parameters, and thus

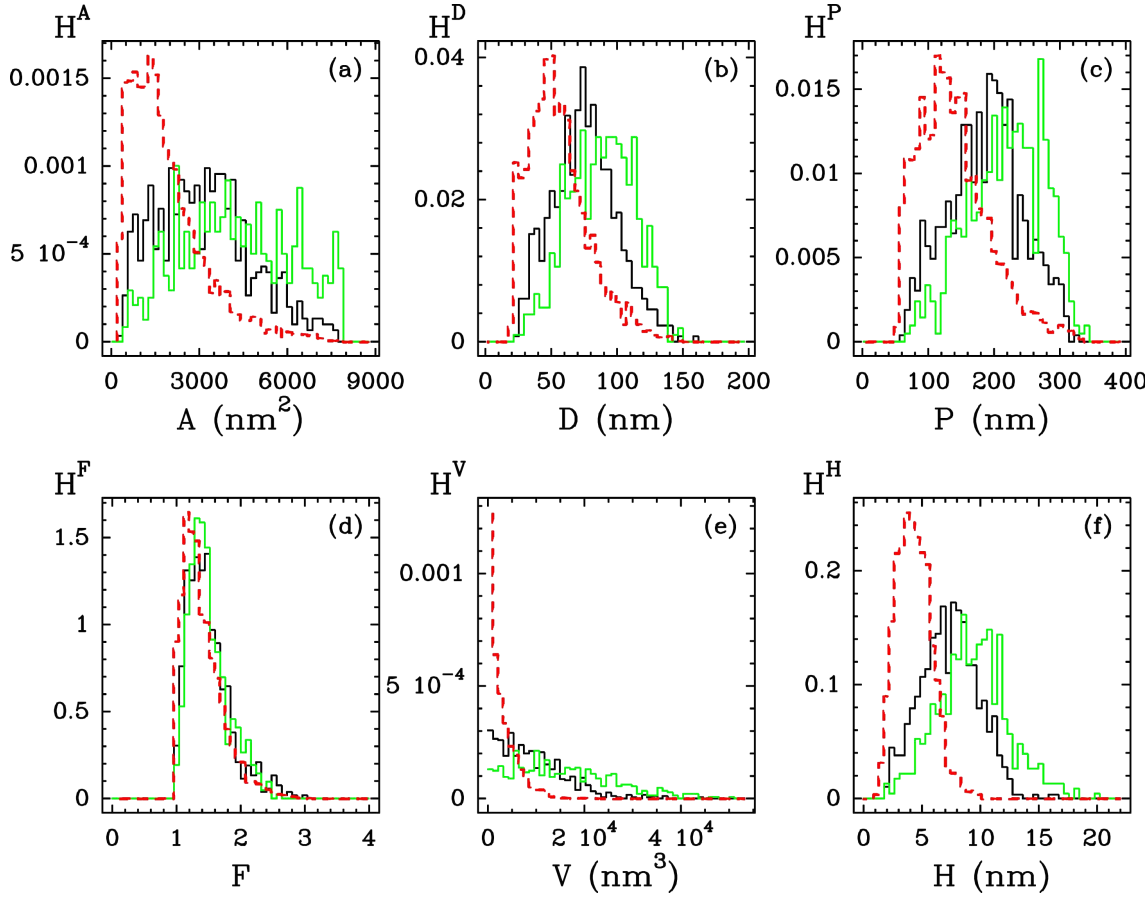

Figure 2.14 Histograms of the 2D and 3D geometrical parameters computed with the 2D WTMM segmentation method (see text), from gold surface topography images reconstructed by AFM tapping mode. (a) Area A of the domains circumscribing the gold blobs. (b) Diameter D of the domains. (c) Perimeter P of the domain contour. (d) Filament index F of the gold blobs. (e) Volume V of the gold blobs. (f) Relative maximum height H of the gold objects. Same set of surfaces as in Figure 2.12. Green line: 1D spectrum averaged over 46 images of glass treated by (11MUD$(\text{MeO})_3$Si) $[10^{-3}\text{mg.ml}^{-1}]$ in cyclohexane. Dashed red line: 1D spectrum averaged over 85 images of glass treated by (11MUD$(\text{MeO})_3$Si) $[10^{-2}\text{mg.ml}^{-1}]$ in cyclohexane.

the 3D shapes, of the gold objects after deposition on the [10^{-2}mg.ml^{-1}] treated substrates is totally different from those of untreated coverslips or samples treated with [10^{-3}mg.ml^{-1}] of 11MUD(MeO)$_3$Si. Also, the objects forming the samples corresponding to bare glass or glass treated with [10^{-3}mg.ml^{-1}] of molecules are not exactly similar.
The mean value of the histograms corresponding to each parameter is reported in Table 2.4 for each concentration of chemicals. All geometrical parameters show a minimum value for samples treated with [10^{-2}mg.ml^{-1}] of molecules, which suggests that the metal blobs are smaller after treating the glass with such a concentration of chemicals. However, the mean value of the object parameters for untreated samples are lower than those of substrates treated with a concentration of [10^{-3}mg.ml^{-1}], which is surprising since we would assess them to be intermediate between the two extreme situations.
Another remark is that the distributions of the parameters are clearly narrower in the case of a [10^{-2}mg.ml^{-1}] concentration. As we saw in the previous section, the sizes of the objects composing the surface topography are less dispersed for the highest concentration of treatment.
However, the filament index F, which measures the departure from circularity, is almost the same when increasing the concentration of treatment. It seems then that the overall shape of the contour is rather circular, and does not change much with the treatment. Still, it has to be noted that the estimation of the filament index for very small objects (about 10-15 pixels of diameter) might be less accurate since it is going to be highly dependent on the number of pixels in the object. Another aspect is that even if Khalil *et al.*[115] also argued that the estimation of this parameter can be biased for large objects of discontinuous shapes, the absence of such structures in the samples will not influence the calculations presented in Figure 2.14(d).

	Area A (nm^2)	Diameter D (nm)	Perimeter P (nm)	Filamentary index F	Volume V (nm^3)	Height H (nm)
No treatment	3500	70	190	1.45	10^4	8
[10^{-3}mg.ml^{-1}]	4500	90	220	1.45	1.75 10^4	10
[10^{-2}mg.ml^{-1}]	1750	45	125	1.25	1000	4

Table 2.4 Mean value of each distribution of the gold objects parameters presented in Figure 2.14.

In the last part of this section, we discuss the possible 3D shapes of the metal objects present at the surface by using the parameters shown in Figure 2.14.
Let us first give the relation V/H =f(A) for 3D geometrical objects that could be present at the metal surface:

- for a cube or a cylinder: $V/H = A$
- for a half sphere: $V/H = 2/3\ A$
- for a spherical cap: $V/H = \frac{1+3\tan^2\alpha}{\tan^2\alpha}\ A$ (where α is the half angle at the summit of the cone included in the spherical cap, which means that the diameter D and height H of the two shapes are the identical)

- for a cone or a pyramid: $V/H = 1/3\ A$
- for a truncated cone or pyramid (with A' the top area): $V/H = 1/3\pi(A + A' + \sqrt{AA'})$

To determine the type of structure composing the metal layer for each type of treatment, the relation V/H =f(A) is plotted in Figure 2.15(a) from the parameters computed with the 2D WTMM segmentation approach.
Each point presented in Figure 2.15 (a) and (b) corresponds to the averaged value over a set of objects of the same area or height, respectively, and the errorbars represent the mean square deviation of these sets. The dispersion of data points is greater for larger objects, due to smaller sampling, therefore we limit the linear regression fit to areas smaller than $A \simeq 2200$ nm^2. The coefficients computed from the fitted V/H =f(A) curves are reported in Table 2.5 for untreated or chemically treated surfaces.

	V/H versus A	$\sqrt{A}$ versus H	half summit angle
No treatment	$a = 0.349 \pm 0.006$	$a' = 4.16 \pm 0.25$	$\alpha = 66.9°$
[10^{-3}mg.ml^{-1}]	$a = 0.388 \pm 0.006$	$a' = 3.91 \pm 0.28$	$\alpha = 65.6°$
[10^{-2}mg.ml^{-1}]	$a = 0.332 \pm 0.007$	$a' = 4.02 \pm 0.60$	$\alpha = 66.2°$

Table 2.5 Slopes computed from the linear fits V/H versus A and $\sqrt{A}$ versus H of Figures 2.15(a) and (b) respectively. Assuming a conic or pyramid shape from those coefficients, the corresponding half summit angle α is also presented here.

We observe from this table that no matter the concentration of chemicals used to treat the coverslips, the slope is found close to 1/3.
We can therefore exclude non conical 3D shapes such as cubes or cylinders ($V/H = 1\ A$), half spheres ($V/H = 2/3\ A$) spherical caps (since $\frac{1+3\tan^2 66}{\tan^2 66} \simeq 3.2$), and truncated cones or pyramids (non-linear behavior for large A, and $V/H \simeq A$ at small scales), and assume that the structure of the gold objects is rather conical or pyramidal.

We make the assumption that the structure of the gold objects is rather conical or pyramidal (a =1/3).
We have plotted $\sqrt{A} = f(H)$ in Figure 2.15(b) in order to estimate the half summit angle α of the objects. As in Figure 2.15(a), a linear fit is done, and the slope (given by $\sqrt{\pi}\ \tan\alpha$) is computed and presented in Table 2.5. This angle is found the same for all three samples ($2\alpha = 132 \pm 4°$). This rather large value attests for flat conical objects, independently of the chemical treatment.

In conclusion, the 2D WTMM segmentation approach is a powerful tool to characterize surface structures of metal layers: the objects detected on samples without chemical treatment or treated with [10^{-3}mg.ml^{-1}] of 11MUD(MeO)$_3$Si are not only bigger, but also higher than the ones treated with [10^{-2}mg.ml^{-1}] of molecules. On the other hand, we also demonstrated that the global 3D shape of those objects does not vary much with both the scale and the concentration of the chemical treatment. Finally, the average 3D shape of these blobs was

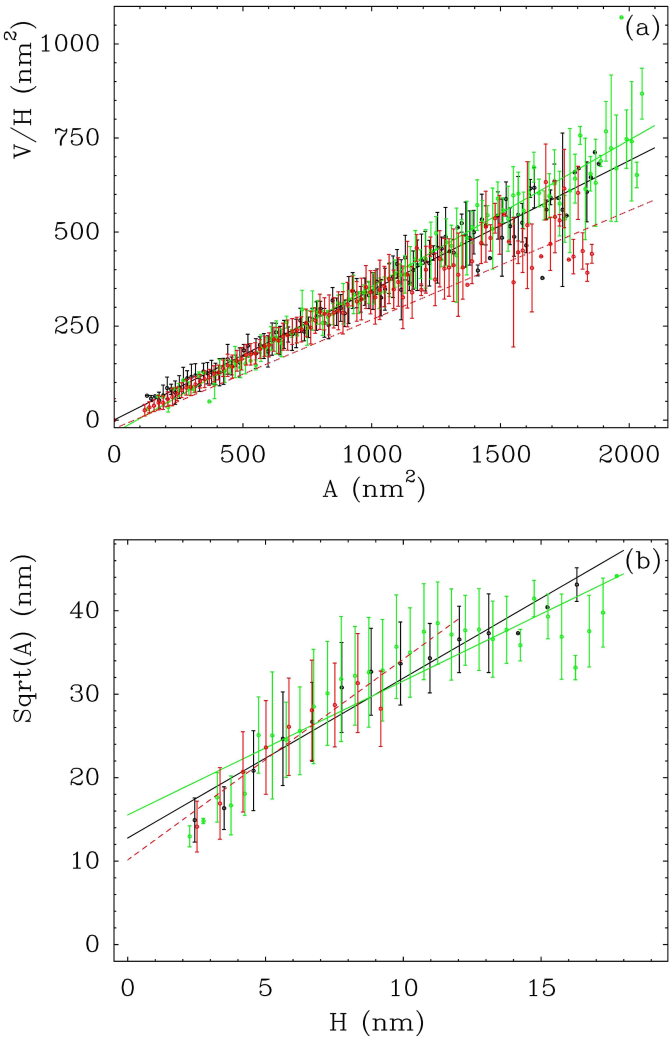

Figure 2.15 Determination of the gold objects 3D-shape after segmentation using the WTMM algorithm. (a) plot of $V/H = f(A)$. (b) plot of $\sqrt{A} = f(H)$. H, A, and V correspond respectively to the height, area and volume presented in Figure 2.14. For clarity reasons, objects of the same area (resp. height) have been averaged in (a) (resp. (b)) and the errorbars have been computed using a mean square deviation algorithm. A linear fit is done for each set of concentration, and the corresponding coefficient is reported in Table 2.5.Same set of surfaces and same color coding as in Figure 2.12.

determined and found pyramidal or conical, with a summit angle $2\alpha = (132 \pm 4)°$. Therefore, the metal layer is found relatively smooth, and even smoother when the glass substrates have been chemically treated with $[10^{-2}\text{mg.ml}^{-1}]$ of $11\text{MUD(MeO)}_3\text{Si}$.

B.2 Surface structure analysis of the chemically treated samples before deposition of gold

B.2.1 AFM images of the treated glass substrates

We saw in the previous section that the surface structure after deposition of gold can be dramatically improved on samples treated with $[10^{-2}\text{mg.ml}^{-1}]$ of $11\text{MUD(MeO)}_3\text{Si}$. In this

section, we focus on the glass substrates just after treatment with 11MUD$(MeO)_3$Si (*i.e.* before the gold deposition).
Figure 2.16 presents topography (left panel) and phase (right panel) AFM images of treated glass substrates. The samples are imaged with tapping mode AFM, before deposition of gold, and for the same concentrations of molecules as in the previous section: an untreated substrate is shown in (a) and (a'), and samples treated with [10^{-3}mg.ml^{-1}] or [10^{-2}mg.ml^{-1}] of 11MUD$(MeO)_3$Si in (b) and (b') or (c) and (c') respectively.

Topography images

We can see in Figure 2.16 that the range of the topographic images (Δz) is higher for a concentration of [10^{-2}mg.ml^{-1}]: Δz =10.2 nm (c), to be compared with Δz =5.3 nm for untreated coverslips (a) and Δz =6.4 nm for a treatment with [10^{-3}mg.ml^{-1}] of molecules (b). This observation can be explained by the presence of a large number of small size objects (∼10-30nm of diameter) in the image presented in Figure 2.16(c) that tends to increase artificially the maximum value of the heights.

The topography dynamics of these images are relatively close to each other, and for any concentration of treatment, they are not strictly homogeneous. The presence of higher domains in some locations of the coverslips, including those that have not been treated, leads to the conclusion that this roughness is intrinsic to the glass. As presented in Figure 2.17, the larger domains are about 0.5-1.5 nm high. Since the expected height of a 11MUD$(MeO)_3$Si monolayer is about 1.5 nm[116], these surface variations are going to prevent a precise determination of the number of layers formed at the surface from the topography images.
Moreover, comparing first the dynamics of the topography images and second the modifications in the sizes of the objects on gold and on glass respectively in figures 2.11 and 2.16, it is clear that the roughness of the substrates after deposition of gold is not simply the reflection of the glass or SAM surface structures. Indeed, non-treated or chemically modified glass presents an overall roughness that is about 4 times lower before the deposition of gold. In consequence, the dramatic changes in the gold structure seen for samples treated with [10^{-2}mg.ml^{-1}] of 11MUD$(MeO)_3$Si (comparison between figures 2.11(a) to (c) and (a") to (c")) cannot be explained solely by the slight modifications in the glass roughness that is due to the formation of a SAM (see Figure 2.16(a) and (c)). A detailed discussion can be found in section B.6.2 about the modifications induced by the SAM in the physical properties that influence the deposition processes during the thermal evaporation.

Phase images

AFM phase imaging has proven to be a powerful tool to probe local modifications in sample composition in several studies.[117–119] Indeed, phase images actually reflect less the topography structure of the surface than local variations in friction, or even in the composition of the objects. This point is very well illustrated in Figure 2.16 where the variations due to the surface topography presented in (a), (b) and (c) have been lost in the phase images (a'), (b') and (c').

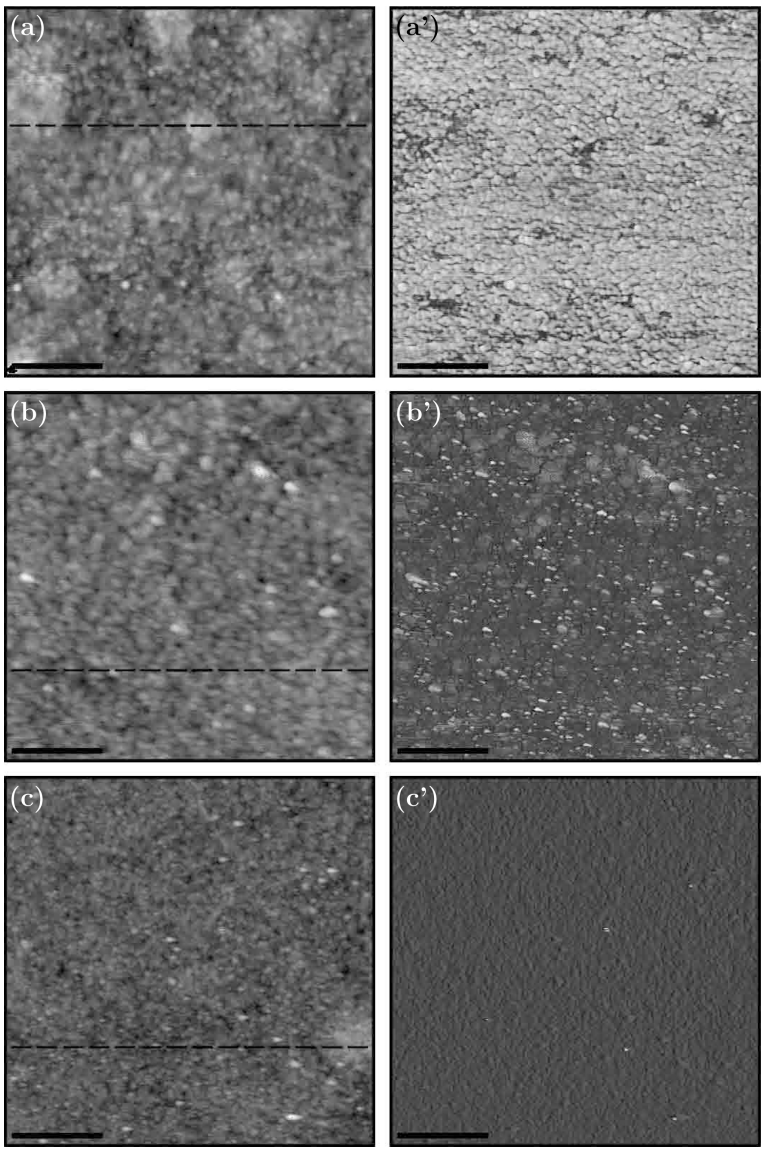

Figure 2.16 Topography of the glass surfaces obtained by AFM tapping mode imaging, without treatment (a), after treatment with[10^{-3}mg.ml^{-1}] of 11MUD(MeO)$_3$Si (b), and after treatment with [10^{-2}mg.ml^{-1}] of molecules (c). Dashed lines in (a), (b) and (c) correspond to the cross-sections shown in figures 2.16(a), (b) and (c) respectively. (a'), (b') and (c') show the corresponding dissipation images obtained by AFM. Brighter regions indicate topmost part of the glass surface. The scale bar corresponds to 250 nm. The minimum (black) and maximum (white) height of the images respectively correspond to: (a) -1.7 nm and 3.6 nm; (b) -1.9 nm and 4.5 nm; (c) -2.4 nm and 7.8 nm; (a') -90 ° and 82 °; (b') -26 ° and 90 °; (c') -20 ° and 90 °.

It has been demonstrated that the phase lag in the oscillation of the AFM tip is often related to local changes in the surface stiffness,[120] *i.e.* the viscoelasticity[118].
Indeed, depending on the strength and type of the forces exerted between the AFM tip and the sample, a phase lag φ in the oscillation of the cantilever occurs. In other words, if the excitation signal is of the type $s(t) = s_0\ cos(\omega t + \varphi_0)$, then the oscillation of the cantilever will be $s_d(t, \varphi_d) = s_{0,d}\ cos(\omega t + \varphi_0 + \varphi_d)$, where φ contains all the information about the

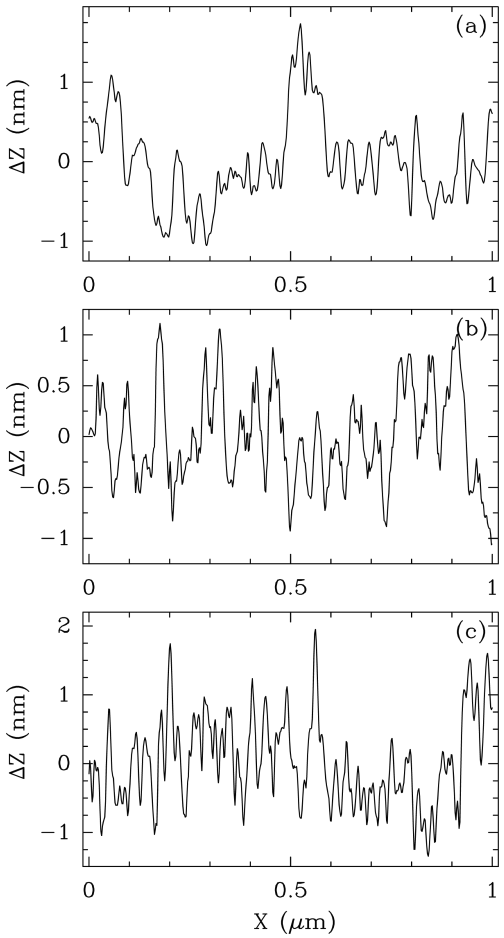

Figure 2.17 Cross-sections of the AFM topography images presented in Figure 2.16 for untreated glass substrates (a), or after treatment with [10^{-3}mg.ml^{-1}] of 11MUD(MeO)$_3$Si (b), or with [10^{-2}mg.ml^{-1}] of molecules (c).

types of interaction experienced by the surface/tip system. Note that the phase lag can either correspond to a delay or an advance in the oscillation with respect to the signal of excitation of the cantilever.

Therefore, we have acquired phase images of the samples (with about the same contact force intensity between the tip and the surface) so as to try and determine the quality of the SAM formation with respect to the concentration of chemicals used during the treatment, see Figure 2.16 (a'), (b') and (c').
The contrast and the dynamics of the phase images depends on the chemistry of the surface. The phase spans over a range $\Delta\varphi \sim 120°$, 40 ° and 20 ° for untreated samples, slides treated with [10^{-3}mg.ml^{-1}] or [10^{-2}mg.ml^{-1}] of 11MUD(MeO)$_3$Si respectively. We also observe that the proportion of domains where the phase is very high tends to disappear when the concentration of chemicals is increased. Indeed, most of the surface presents high values of phase for untreated substrates, whereas only small white dots appear on substrates treated with [10^{-3}mg.ml^{-1}] of molecules. The most obvious effect is that for [10^{-2}mg.ml^{-1}] chemically treated samples, the surface is almost free from high phase value domains.

Moreover, we observe that increasing the concentration of treatment also tends to create local variations in the phase images. Those relatively smooth variations present a ripple-like pattern in the range of scales $\sim$ 10 nm to $\sim$ 50 nm.

In conclusion, it has been shown in this section that the roughness of the gold layers is not a simple reflection of the glass structure before or after treatment. We have also seen that even if no obvious modifications could be observed in the topography of the glass substrates after treatment with 11MUD$(MeO)_3$Si, phase imaging is likely a good tool to discriminate bare glass from glass treated by 11MUD$(MeO)_3$Si. We also observed that phase images not only seem to be more homogeneous when the concentration of molecules is increased, but that wave-like pattern variations appear in presence of more chemicals.

B.2.2 Power spectral analysis and histogram of heights of the AFM images

Topography images

In order to determine more accurately the differences induced by the chemical treatment on the glass substrates, the averaged 1D power spectra (along the x direction) and histograms of heights are computed from about 20 AFM topography images (1x1 μm^2) for each situation. They are presented in figures 2.18(a) and (b) respectively. The averaging for both the power spectra and the histograms of height has been carried out over the 512 lines in the image, and for the whole set of images.

The same way as for gold surfaces, the averaged 1D power spectra of the AFM topography images show several domains in Figure 2.18(a). However, it would seem that no matter the concentration of 11MUD$(MeO)_3$Si, all coverslips behave the same way.

First, the saturation at small frequencies (below $f \sim 30\ \mu m^{-1}$) accounts for the absence of structures at large scales.

Then, a very small domain corresponding to intermediate scales can be seen from $f \sim 30\ \mu m^{-1}$ to $f \sim 100\ \mu m^{-1}$. This range of distances is linked to the roughness of the glass substrates at small scales, meaning that this should be the scales where we might see a change in the structure of the substrates because of the chemical treatment. However, the slope of the curves does not seem to vary much from untreated to treated coverslips. It appears then that the extra layer of 11MUD$(MeO)_3$Si does not change radically the surface structure, even for the highest concentration.

Figure 2.18(b) shows the histograms of heights computed from the same AFM topography images as those used for Figure 2.18(a).

We can see here that the FWHM of the histograms present a very slight increase as the chemical treatment is enhanced : 1.15 $\pm$ 0.05 nm for untreated substrates, 1.25 $\pm$ 0.05 nm for the samples treated with [10^{-3}mg.ml^{-1}] of molecules, and 1.35 $\pm$ 0.05 nm for a treatment with [10^{-2}mg.ml^{-1}] of 11MUD$(MeO)_3$Si. This enhancement of 0.2 nm is less than the expected $\sim$ 1.5 nm thickness of a 11MUD$(MeO)_3$Si monolayer[116]. This confirms then that the intrinsic glass roughness prevents the determination of the number of layers adsorbed on the surface. However, highly ordered domains can still be present in some locations of the substrates,

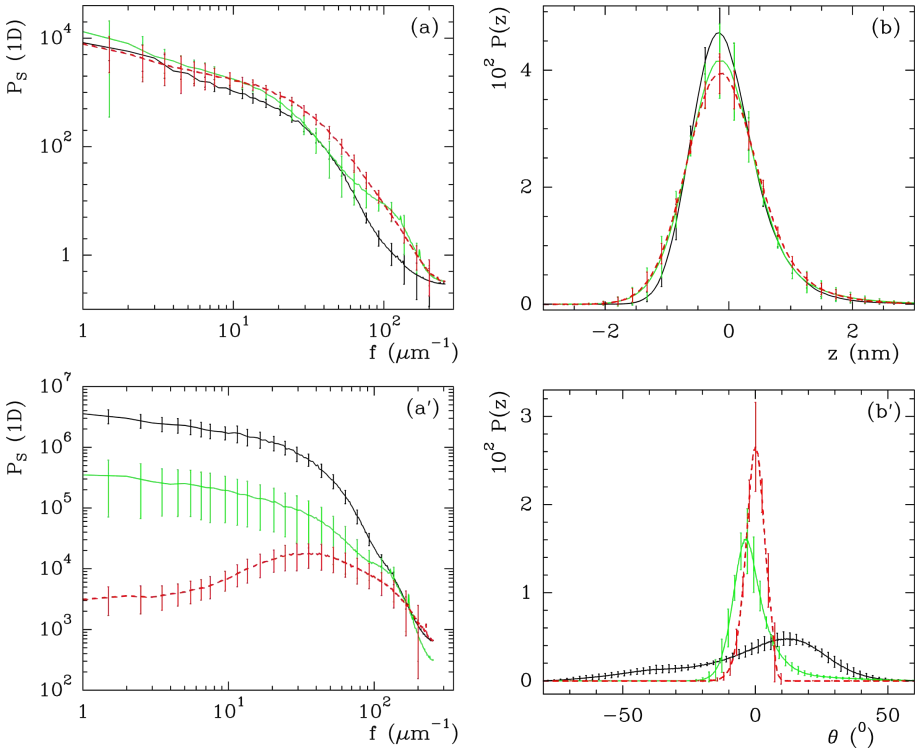

Figure 2.18 Averaged 1D power spectra (along the x direction) computed respectively from 1 μm^2 AFM topography (a) and phase (a') images of glass surfaces. Black line: 1D spectrum averaged over 17 images of untreated glass samples. Green line: 1D spectrum averaged over 22 images of glass treated by (11MUD(MeO)$_3$Si) [10^{-3}mg.ml^{-1}] in cyclohexane. Dashed red line: 1D spectrum averaged over 23 images of glass treated by (11MUD(MeO)$_3$Si) [10^{-2}mg.ml^{-1}] in cyclohexane. Histogram of gold surface topography (b) and phase (b') images computed from the same set as (a) and (a'), are presented with the same color coding.

especially after a treatment with [10^{-2}mg.ml^{-1}] of 11MUD(MeO)$_3$Si: several layers can be formed (via chemical bonds between the thiol or even the silane ends[121–124]) and interpenetrate, eventually decreasing their effective thickness.

Phase images

We saw previously that chemically treated glass surfaces cannot be distinguished from untreated samples by solely imaging the topography with AFM. However, AFM phase imaging should be able to probe variations in the tip/sample interactions and can give insights on local composition modifications of the samples[117–120].

The power spectra and histograms of height of the phase images have been computed and the averaged curves are presented in Figure 2.18(a') and (b'). The same set of images as for the topography study shown previously has been used, and the averaging has been done over the 512 lines for each image and for the whole set of images, that is about 20 for each

concentration. Note that no flattening was used for phase images.
The first remark we can make is that the power spectra of the phase images (Figure 2.18(a')) are clearly not equivalent when the concentration of molecules used to treat the samples is increased. It can be seen that [10^{-3}mg.ml^{-1}] treated samples behave intermediately between untreated and [10^{-2}mg.ml^{-1}] treated coverslips. This point is even more striking given the fact that it was not possible to distinguish the concentration of treatment from the topography images.
There is a larger dispersion in the power spectra of treated glass surfaces and thus, some of the curves have been excluded from the computation of the curves in Figure 2.18(a') for clarity reasons: four power spectra (out of 22) corresponding to samples treated with [10^{-3}mg.ml^{-1}] of molecules behave like those of untreated coverslips, 3 (out of 24) of [10^{-2}mg.ml^{-1}] treated coverslips are similar to those of [10^{-3}mg.ml^{-1}], and one of [10^{-2}mg.ml^{-1}] treated coverslips is similar to the untreated samples.
The power spectra can again be divided into three domains (as seen in Section B.1.2). The first one at large scales, below $\sim$45 μm^{-1}, where no matter the concentration of treatment, no specific size seems to be detected. At high frequency (small scales), another saturation appears above f $\sim$200 μm^{-1}, where the limitation is a consequence of the size of the AFM cantilever tip ($\sim$10-15 nm). Note that even if the behavior of the intermediate regime for each type of sample is clearly different, the non linearity and the narrowness of the range of scales make the estimation of a scaling coefficient impossible.

The histograms of heights computed from the same set of AFM phase images as in Figure 2.18(a') are presented in Figure 2.18(b'). Note that no flattening has been done on the AFM phase images prior to the computation of these histograms of height. In consequence, the phase values presented in this section are not relative, but absolute, and contrary to the histograms calculated from the topography images, they are not centered around the mean value of the pixels in the whole image.

Figure 2.18(b') clearly confirms that the interaction between the tip and the surface depends on the concentration of molecules used to treat the samples.
At first glance samples treated with [10^{-3}mg.ml^{-1}] of 11MUD(MeO)$_3$Si (Figure 2.16(b')) may appear similar to samples treated with [10^{-2}mg.ml^{-1}] of molecules (Figure 2.16(c')). However, a careful analysis of the phase values distribution of the three samples (Figure 2.17(b')) leads to a different conclusion.
The distribution of phase values for untreated samples (black line) is very wide, ranging from about -70° to 50°. It presents two maxima, the main one around 15°, and a satellite one around -40°, corresponding respectively to the numerous light gray pixels and to the rare dark gray pixels in Figure 2.16(a'). In contrast, the histogram of heights for glass samples treated with [10^{-3}mg.ml^{-1}] of molecules displays a single higher and narrower peak (green line), with a FWHM = 12.2 ± 0.3°, indicating that the distribution of heights is less dispersed than for untreated samples. This peak is also slightly asymmetric (with a longer tail for higher φ values), because of the presence of two types of brighter pixels in Figure 2.16(b') corresponding to numerous very small (diameter $\sim$ 10-30 nm) white spots and to light gray domains with larger size (diameter $\sim$ 30-100 nm). Finally, the histogram of phase heights

for the glass substrates treated with [10^{-2}mg.ml^{-1}] of 11MUD(MeO)$_3$Si displays an even narrower and higher peak with FWHM $8.5 \pm 0.3°$. This histogram is no longer anisotropic, confirming the disappearance of the brightest spots from the AFM phase image in Figure 2.16(c').
Moreover, the errorbars of the histograms of height tend to increase with the concentration of treatment. As noticed for the power spectra before averaging, there is a dispersion in the distributions of heights that very likely corresponds to inhomogeneities in the organization of SAM on the glass substrates (this can be seen for the [10^{-3}mg.ml^{-1}] and even more for the [10^{-2}mg.ml^{-1}]) treated samples).

In conclusion, it has been shown in this section that the roughness of the gold layers is not a simple reflection of the glass structure before or after treatment. To summarize, whereas the topography of untreated glass samples or coverslips treated with [10^{-3}mg.ml^{-1}] or [10^{-2}mg.ml^{-1}] of 11MUD(MeO)$_3$Si can barely be distinguished by AFM topography images (Figure 2.16(a), (b) and (c)), AFM phase images (Figure 2.16(a'), (b') and (c')) show that a concentration of molecules of 10^{-2} mg.ml^{-1} is necessary to achieve a complete coverage of glass.

B.2.3 2D Wavelet Transform Modulus Maxima (WTMM) analysis of the AFM images

The 2D WTMM segmentation was also used to compare the surface structure of the bare glass coverslips with the topography of the chemically treated samples before deposition of gold.
Figure 2.19 presents the 3D geometrical parameters (the area A, diameter D, perimeter P, filament index F, volume V, and height H) of the objects segmented by the WTMM algorithm.

As expected, the histograms presenting all the parameters of the detected objects are very similar looking. In other words, it appears that those objects are very much alike. More precisely, it would seem from Figure 2.19(d) that the detected objects have a rather circular contour (F close to 1).
However, the only slight difference comes from the relative height H of the objects (see Figure 2.19(f)) that gets higher when the concentration of 11MUD(MeO)$_3$Si reaches [10^{-2}mg.ml^{-1}]. We also notice that the distribution of this parameter is wider, hence confirming the inhomogeneity of the surface structure, that can be enhanced by the chemical treatment itself.

To finish with the AFM and the WTMM analyses, we have shown that no change could be seen in the surface structure of the coverslips after treating them with 11MUD(MeO)$_3$Si. However, AFM phase imaging proved effective to differentiate from the concentration of treatment, mainly because of the local variations of the surface chemical properties.

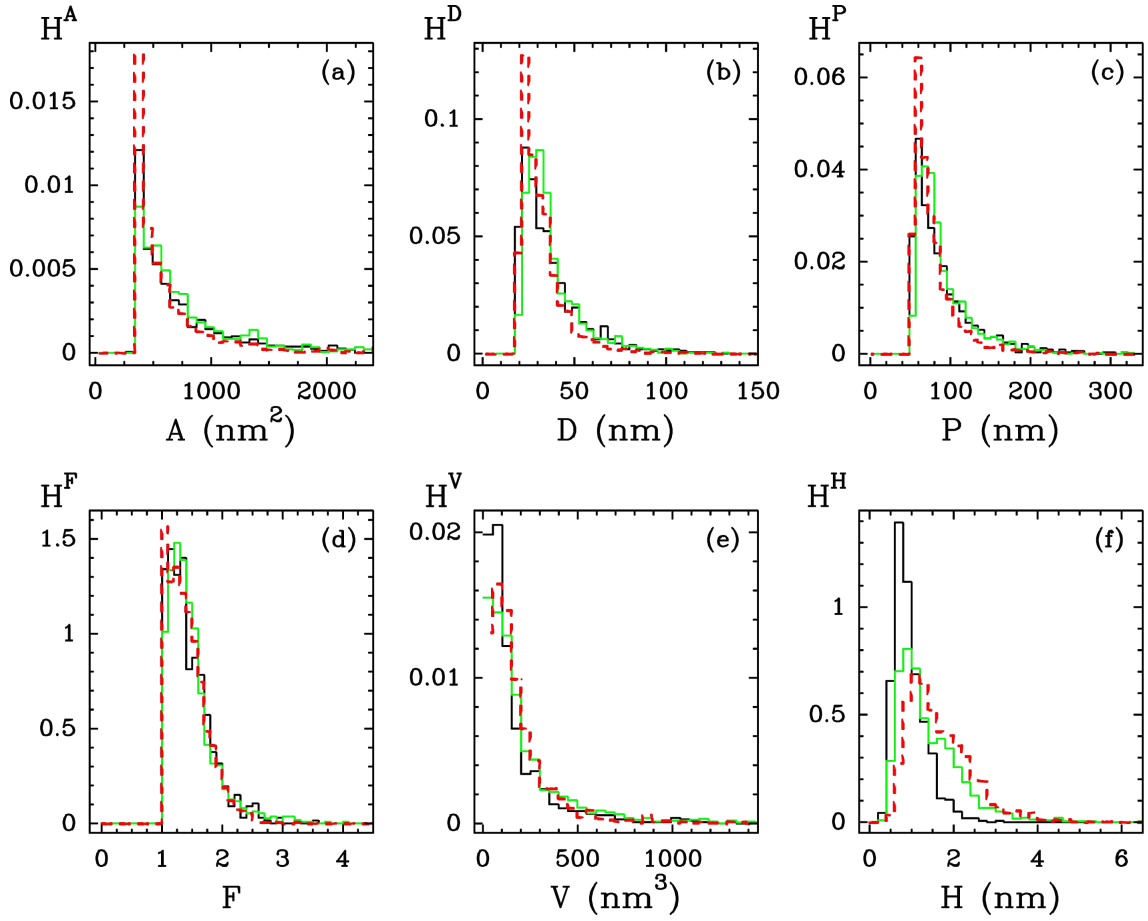

Figure 2.19 Histograms of the 2D and 3D geometrical parameters computed with WTMM method from glass surface topography images reconstructed by tapping mode AFM. The parameters correspond respectively to the area A (a), diameter D (b), perimeter P (c), filament index F (d), volume V (e), and height H (f). Same surfaces as those analysed in Fig. 2.18, and same color coding.

B.3 Chemical analysis by X-ray Photoelectron Spectroscopy (XPS) of the treated substrates before and after deposition of gold

X-ray Photoelectron Spectroscopy (XPS)[125] experiments were carried out in collaboration with Pierre Delichère from the Institut de recherches sur la Catalyse et l'Environnement de Lyon (UMR5256). The main objective of this section is to obtain more information about the composition of the SAMs formed on the glass samples. XPS is a powerful tool to probe the topmost ($\lesssim$10 nm) layer of a sample. It has been proven effective to characterize qualitatively and semi-quantitatively the chemistry of surfaces, and more precisely the study of SAM formation[126].

This technique relies on the illumination of an area of the sample by a monochromated X-ray beam and the collection of both the number and energy of the electrons extracted

from the surface. Using these two parameters, it is then possible to determine the elemental composition of the samples and even their proportion[127].
The contribution to the detected signal of a layer of thickness z is given by:

$$I_d = 1 - \exp[-z\ /(\lambda\ \cos\theta_d)] \tag{2.6}$$

with λ the mean free path of the extracted photoelectrons, and θ_d the angle of detection (with respect to the normal of the surface).
It is then obvious that the detected signal is going to depend strongly on the angle θ_d. Typically, the electrons extracted from the sample for a depth $z < 3\ \lambda cos\theta_d$ are going to contribute to 95% of the whole signal. Consequently, we see that detecting the energy of the electrons for $\theta_d = 60°$ is going to decrease by a factor two the thickness of the probed layer (compared to $\theta_d = 0°$).

XPS experiments have been realized on two glass samples: A, treated with [10^{-3}mg.ml^{-1}] of 11MUD(MeO)$_3$Si; B, treated with [10^{-2}mg.ml^{-1}] of 11MUD(MeO)$_3$Si; and two gold samples: C, prepared from an untreated glass substrate; D, prepared from glass treated with [10^{-2}mg.ml^{-1}] of 11MUD(MeO)$_3$Si.

The surface characterization experiments have been carried out with a KRATOS Axis Ultra DLD XPS set-up, and the vacuum in the analysis chamber was about 5 10^{-10} mbar. The Al Kα X-ray source used here is monochromated and the analyzed surface of the sample is about 300 x 700 μm^2. For each coverslip, a general spectrum is acquired with an energy window of 160 eV. High resolution spectra are also acquired for the different elements detected either for the glass or gold layers, with an energy window of 20 eV. Experiments have been done at normal incident angle ($\theta_d = 0°$), or for an angle $\theta_d = 60°$.

Figure 2.20 presents the wide scan energy XPS spectrum acquired for each type of sample, and Figure 2.21 shows the high resolution peak corresponding to 2s S.

Regardless the concentration of molecules used during the chemical treatment, the energy spectra (at normal incidence, *i.e.* $z \sim 10$ nm) of glass samples are roughly similar (only one is shown in figure 2.21 for convenience), whereas they clearly do not behave the same way as those where a metal layer is present. More precisely, we note the presence of a higher number of pikes for samples without gold, corresponding to different energy values.

Table 2.6 presents the main energy peaks and the corresponding proportion of the chemical elements at the surface for each sample.

Elements corresponding to the glass substrates composition[128] have only been detected for samples A and B (*i.e.* before deposition of gold). Those elements are not presented in Table 2.6, but correspond to the glass composition shown in Table 2.7[128].

Comparing the glass substrates treated with [10^{-3}mg.ml^{-1}] (sample A) or [10^{-2}mg.ml^{-1}] (sample B) of molecules, we observe that the proportion of several chemical elements increases with the concentration (the angle of detection is kept normal to the surface): Si, S, O and C. All these elements except S, can be attributed either to the glass or to the chemicals used to treat the surface. In consequence, the presence of S ($\sim$0.2% for a glass substrate treated

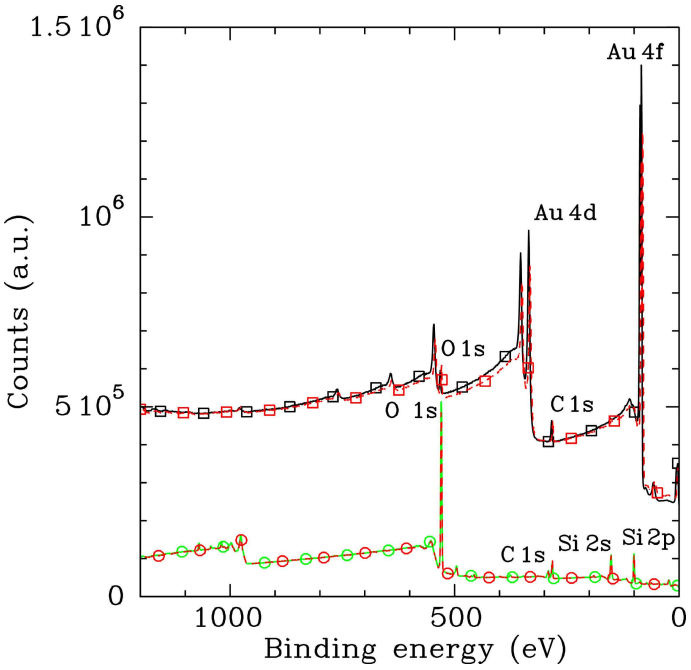

Figure 2.20 Wide scan XPS spectra of: glass substrates chemically treated with [10^{-3}mg.ml^{-1}] (sample A, green solid line and circles) or [10^{-2}mg.ml^{-1}] (sample B, red dashed line and circles) of 11MUD(MeO)$_3$Si before deposition of gold; gold-coated samples with no treatment (sample C, black solid line with plain squares) or chemical treatment with [10^{-2}mg.ml^{-1}] of molecules prior to the deposition (sample D, red dashed line and plain squares). Surveys done at normal incidence ($\theta_d = 0°$).

Sample	Au	Si	S	O	C
A	*n.d.*	21.1	*n.d.*	63.9	15.0
B	*n.d.*	20.7	0.41	62.1	16.7
B (60°)	*n.d.*	19.91	0.84	57.38	20.83
C	45.65	7.17*	*n.d.*	13.92	33.27
D	37.22	8.03*	*n.d.*	18.78	35.97
D (60°)	36.35	7.46*	*n.d.*	21.75	34.44

Table 2.6 Proportion of the chemical elements at the surface (in %) detected at normal incidence ($\theta_d = 0°$) or razing incidence ($\theta_d = 60°$) for: glass substrates chemically treated with [10^{-3}mg.ml^{-1}] (sample A) or [10^{-2}mg.ml^{-1}] (sample B) of 11MUD(MeO)$_3$Si before deposition of gold; gold-coated samples with no treatment (sample C) or chemical treatment with [10^{-2}mg.ml^{-1}] (sample D) of molecules prior to the deposition. Note that *n.d.* stands for not detected. * the quantitative analysis was done on the ray 2s for Si.

with [10^{-2}mg.ml^{-1}] of molecules) is the confirmation that a SAM of 11MUD(MeO)$_3$Si has been formed on sample B. However, the fact that no S has been detected on sample A (where molecules are ten times less concentrated), does not necessarily mean that no molecule is linked to the glass surface, but that the proportion of S on the surface is below the detection limit which is about 0.1% for this accumulation time length. Note that the presence of only

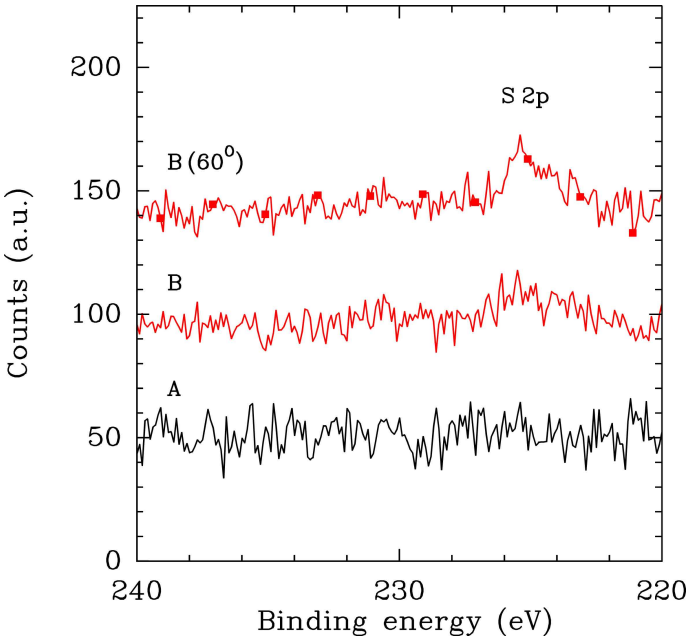

Figure 2.21 XPS high resolution energy pike of 2s S: glass substrates chemically treated with $[10^{-3}\text{mg.ml}^{-1}]$ (sample A, green solid line and circles) or $[10^{-2}\text{mg.ml}^{-1}]$ (sample B, red dashed line and circles) of 11MUD$(\text{MeO})_3$Si before deposition of gold. Pikes recorded at normal incidence ($\theta_d = 0°$) for samples A and B ($\theta_d = 0°$) or at razing angle ($\theta_d = 60°$) for sample B.

	SiO_2	B_2O_3	Al_2O_3	NaO	TiO	ZnO	K_2O
wt%	64.1	8.4	4.2	6.4	4.0	5.9	6.9

Table 2.7 Chemical composition of the glass surface (BK7, *i.e.* D 263) in wt%.

one atom of S per molecule linked to the surface explains why the ratio of S with respect to Si or O is so small: the quantity of SiO_2 in the probed layer is much more important than that of S (even when $\theta_d = 60°$).
XPS scan survey is repeated for the glass surface treated with $[10^{-2}\text{mg.ml}^{-1}]$ (sample B) and an angle of incidence $\theta_d = 60°$. As explained previously, the thickness of the probed layer is then decreased by a factor two: $z \sim 5$ nm, and the weight of the elements present at the surface is going to be more important in the detected signal. We observe from Table 2.6 that the proportion of S and C significantly increase, whereas the fraction of Si and O decrease. This observation tends to show that S and C are mainly located at the surface of the samples, and Si and O mostly in the bulk. This is confirmed by the fact that decreasing the probed thickness by a factor two leads to an enhancement by twice of the S fraction.

We are now focusing our attention on the treated substrates after deposition of the gold layer. Note that for samples C and D, the estimation of S is done by detecting the 2s peak. This is explained by the presence of phonons due to the gold layer for which the photoelectron's energy corresponds to the same as the 1s peak of S.

Our first remark is that besides Au (∼40%), other elements are detected (at normal incidence $\theta_d = 0°$) on both samples C and D by the XPS apparatus: Si (∼8%), O (∼15%) and C (∼35%). Although detecting Au is easily understandable, the detection of Si, O and C on both surfaces can seem surprising. Those elements are all constitutive of the molecule 11MUD$(MeO)_3$Si that is used to treat the surface. However, it seems hard to conceive a process explaining how those molecules eventually end up at the upper surface of the gold layers. It is even more striking that sample C presents almost the same proportion of those elements, whereas no treatment was done on the glass substrate prior to the gold deposition. Another XPS survey was carried out for $\theta_d = 60°$ on sample D. We notice from the results that the proportion of all detected elements does not vary much from the measurements at normal incidence.
This last observation tends to show that Si, O and C are not segregated at the surface, but diffused into the gold layer itself. This presence of extra chemical elements is rather consistent with pollution during the deposition of gold (presence of contaminants due to the vacuum grease, or even to previous depositions of other metals).

In conclusion, even if we cannot confirm the presence of molecules linked to the glass substrate treated with a concentration of [10^{-3}mg.ml^{-1}], the [10^{-2}mg.ml^{-1}] treated coverslip shows clearly that 11MUD$(MeO)_3$Si is located at the surface. However, we were not able with the XPS analysis to differentiate the untreated from the treated coverslips after deposition of gold, and no direct information on the quality or organization of the SAM or gold structures could be obtained.

B.4 SPR analysis of the treated glass substrates after gold deposition

B.4.1 Parametrization of SPR data with variable gold indices

Figure 2.22 presents the experimental and fitted SPR curves obtained for samples without treatment (a), or treated with [10^{-3}mg.ml^{-1}] (b) or with [10^{-2}mg.ml^{-1}] (c) of 11MUD$(MeO)_3$Si. The estimation of the parameters has been done by using the same algorithm as in section A.1. The fitted SPR curves have been computed by using a three layer model with adjustable gold indices: as in section A.2.1, the averaged thickness H_e is first determined for each sample, and afterwards the gold indices.

We can see from Figure 2.22 that the determination of both the Attenuated Total Reflection (ATR) angle and the angle of resonance are in good agreement with the experimental data, and especially for the untreated sample. However, the fits do not account accurately for the global shapes of the curves after the SPR angle.
The estimated heights of the gold films are respectively $H_e = 45.2\pm1.4$ nm, $H_e = 45.9\pm1.1$ nm and $H_e = 45.6\pm1.9$ nm respectively for untreated substrates, and coverslips treated with [10^{-3}mg.ml^{-1}], or [10^{-2}mg.ml^{-1}] of 11MUD$(MeO)_3$Si. This shows that no matter the concentration of chemicals used to treat the samples, the gold layers eventually present the same

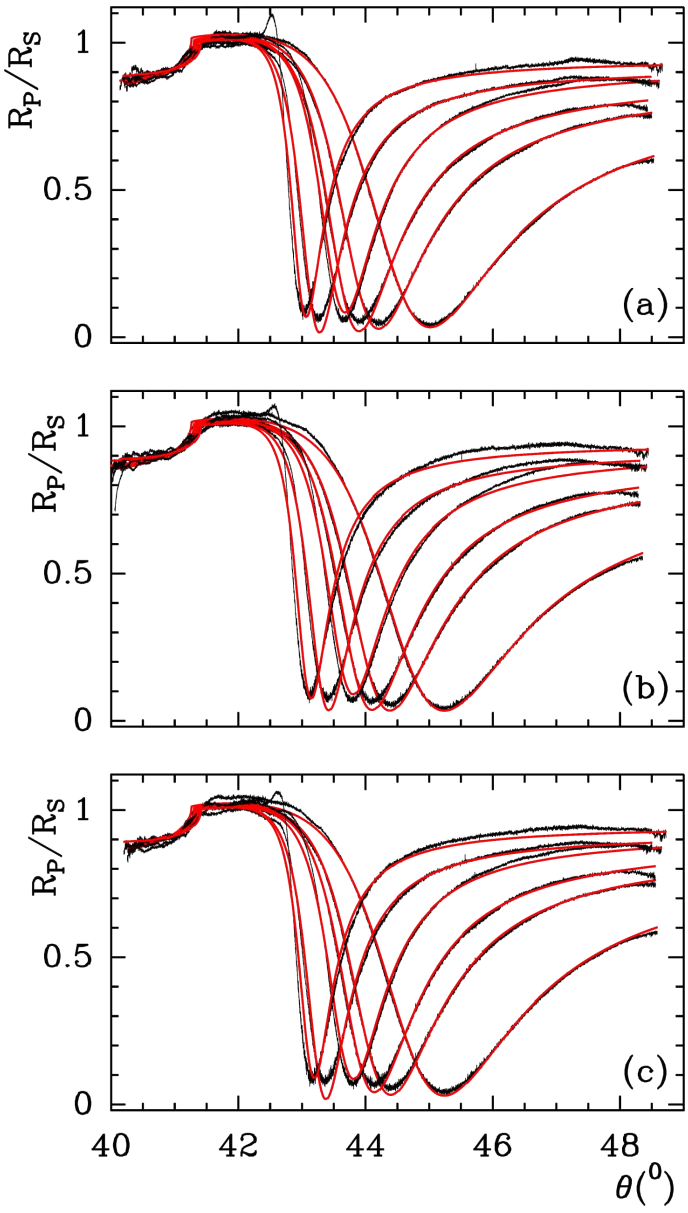

Figure 2.22 Experimental (black) and fitted (red) SPR curves (R_p/R_s) obtained for (a) untreated glass coverslips, or samples treated with [10^{-3}mg.ml^{-1}] (b) or [10^{-2}mg.ml^{-1}] (c) of 11MUD(MeO)$_3$Si. Fits have been done by using a three layer model with adjustable gold indices. The SPR curves presented here have been recorded for λ = 600, 647, 676, 700 and 750 nm (from right to left).

thickness.
After determining the layer's thickness, the algorithm is set to estimate the dielectric indices of the gold films. Those indices are reported in Table 2.8 for each type of chemical treatment.

No treatment

λ (nm)	ε'	ε''
600	-7.80 ± 0.80	1.12 ± 0.11
633	-9.83 ± 0.98	1.14 ± 0.11
647	-10.92 ± 1.09	1.19 ± 0.12
676	-12.21 ± 1.22	0.98 ± 0.10
700	-14.49 ± 1.45	1.26 ± 0.13
750	-16.85 ± 1.69	1.10 ± 0.11

[10^{-3}mg.ml^{-1}]

λ (nm)	ε'	ε''
600	-7.80 ± 0.78	1.08 ± 0.11
633	-9.90 ± 0.99	1.11 ± 0.11
647	-10.88 ± 1.09	1.10 ± 0.11
676	-12.26 ± 1.23	0.92 ± 0.09
700	-14.48 ± 1.45	1.14 ± 0.11
750	-17.06 ± 1.70	1.03 ± 0.10

[10^{-2}mg.ml^{-1}]

λ (nm)	ε'	ε''
600	-7.83 ± 0.78	1.11 ± 0.11
633	-10.32 ± 1.03	1.12 ± 0.11
647	-10.08 ± 1.01	1.09 ± 0.11
676	-12.23 ± 1.22	0.93 ± 0.09
700	-14.63 ± 1.46	1.21 ± 0.12
750	-16.74 ± 1.67	1.02 ± 0.10

Table 2.8 Table of gold indices estimated from the parametrization of experimental SPR curves with a three layer model. The global gold thickness is estimated to $H_e = 45.2 \pm 1.4$ nm, $H_e = 45.9 \pm 1.1$ nm and $H_e = 45.6 \pm 1.9$ nm for untreated samples, coverslips treated with [10^{-3}mg.ml^{-1}], or [10^{-2}mg.ml^{-1}] of 11MUD(MeO)$_3$Si respectively. The mean square deviation between the experimental and the fitted SPR curves is also reported in each case.

The first and most remarkable conclusion we can draw from Table 2.8 is that no difference can be seen in the dielectric indices whether the substrates have been chemically treated or not.
No matter what type of treatment, the proportion of vacuum included into the metal films is kept constant (see next section for the estimation of this parameter), even if the size of the inclusions varies.

To conclude this section, we saw that the fits of the SPR curves lead to the estimation of the same layer thickness $H_e = 45.6 \pm 1.9$ nm, no matter the type of chemical treatment. By using a three layer model with adjustable indices of gold, we were also able to determine that gold indices are also constant with the concentration of treatment, which accounts for the same fraction of gold and hence the same proportion of vacuum inclusions in the layers.

B.4.2 Comparison of our gold index estimations with previously reported data

In Figure 2.23, we compare our predicted values for the gold index of the chemical layers with the reference data reported respectively by Thèye[41] and from the Handbook of Physics[109].

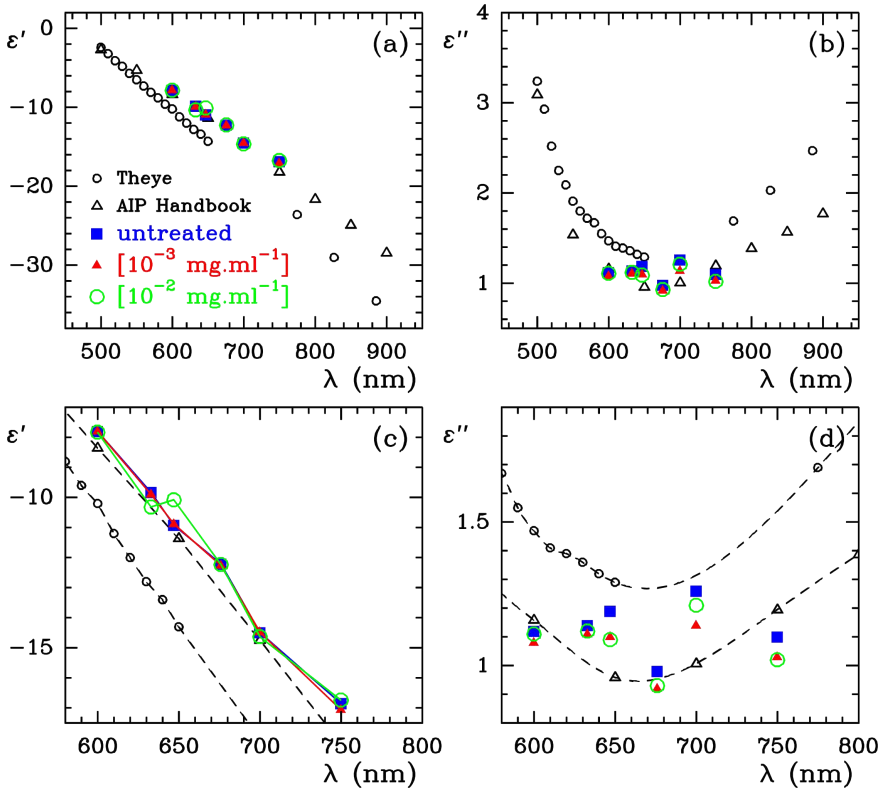

Figure 2.23 Comparison of the dielectric constants of the gold layers after chemical treatment (predicted by using a three layer model and free index of the metal), with literature data of Thèye[41] (black circles) and Handbook of Physics[109] (black triangle). Untreated substrates, coverslips chemically treated with $[10^{-3}\text{mg.ml}^{-1}]$, or $[10^{-2}\text{mg.ml}^{-1}]$ of $11\text{MUD(MeO)}_3\text{Si}$ are labelled with blue squares, red triangles, and green circles respectively. (a) and (b) give the real and imaginary part of the dielectric constant. In (c) and (d) we have zoomed on the wavelength range used in our SPR measures.

We see from Figure 2.23 that the dielectric constants (both the real and the imaginary parts) estimated from our fitting of the gold layers deposited on either bare glass or substrates treated

chemically are very close to the literature references. Indeed, even if our computed ε' values are slightly above the data from Handbook of Physics, our estimations of ε'' fall in the same interval as literature data from Thèye and the Handbook of Physics. Also, the difference with the gold indices determined in section A.2.2 is significant: the real part of the dielectric indices of the gold layers prepared after treating the glass surfaces are globally above the ones of the slow or fast deposition modes presented in section A.2.2, whereas their imaginary part get closer to each other.

To determine the volume fraction of gold in the layers from their dielectric indices with respect to Thèye data (considered as plain gold), we use the model of Bruggeman (see equation (2.5) and Figure 2.6). The values at $\lambda = 633$ nm of the real and imaginary parts of the dielectric constants averaged over the samples (chemically treated or not) presented in Table 2.8 are $\varepsilon' = -10.01 \pm 1.00$ and $\varepsilon'' = 1.12 \pm 0.11$. From these values and Figure 2.6, we obtain the fraction of gold inside the layers: $\eta_1 = 0.90 \pm 0.04$.
This value needs to be compared with those obtained (by a three layer model with adjustable gold indices) for slow or fast deposited gold layers, that is respectively $\eta_1 = 0.9292 \pm 0.0093$, and $\eta_1 = 0.9714 \pm 0.0086$ (see section 2 A.2.2). Therefore, there appears to be a diminution of the fraction of gold for the substrates prepared with or without a chemical treatment of the glass. They are also globally less homogeneous and composed of more inclusions of vacuum than the coverslips used for the study on the influence of the deposition rate. We attribute this non negligible difference to the change in the type of crucible used to heat the gold wire during the evaporation step.

In conclusion, that the dielectric index values of the gold layers prepared after chemically treating the glass substrates are very close to the data found in the literature[41,109]. We also estimated the fraction of gold inside the layers as being $\eta_1 = 0.90 \pm 0.04$, which is smaller than the proportion of gold present in the layers presented in section 2 A.2.2.

B.5 SSPM analysis of the treated substrates

B.5.1 SSPM images of the treated substrates

After characterizing the gold layers deposited on chemically treated glass coverslips, in this section we are going to image directly the spatial variations of the plasmon resonance by the use of our high resolution SSPM. As we try to improve the quality of our samples in order to image single molecular assemblies, we need to characterize the impact of such a treatment, and therefore the layer structure modifications, on the optical response of the microscope.

The SSPM images shown in this section have been reconstructed with a 0^{th}order flattening, normalized with the maximum of the $I(z)/I_0$ curve like previously explained in section A.2.3, and finally filtered with a sliding box averaging.

Figure 2.24 presents SSPM images of untreated samples (left panel) or coverslips treated

with with [10^{-2}mg.ml^{-1}] of 11MUD(MeO)$_3$Si (right panel) that have been acquired in air for two values of defocalization: $z = 0$ and $z = 1$ μm. The dynamics of the images have been kept constant so as to compare more easily the influence of the chemical treatment, and 2x2 μm^2 AFM topography images in tapping mode are also presented as a reminder.

Let us also recall that images acquired at $z = 0$ reflect both the bulk and surface structures of the layers, whereas those acquired at $z = 1$ μm are rather influenced by their surface roughness.

Previous studies[129,130] have demonstrated that the image of a thin metal layer illuminated by a polarized monochromatic light presents subwavelength variations in its intensity distribution. This phenomenon is called "speckle", and has been demonstrated to be due to the inhomogeneities of the metal film. Therefore, we can interpret the variations present in figures 2.24 to 2.27, no matter the concentration of treatment, to be due to the gold structure.

The most striking point in these figures consists in the drastic difference between the global contrast of the untreated sample and the glass substrate treated with [10^{-2}mg.ml^{-1}] of 11MUD(MeO)$_3$Si. Indeed, we clearly see that treating the glass surface leads to a dramatic decrease in the contrast of the image at a given defocalization value. This not only confirms that the surface roughness has been lowered (as presented in Figure 2.24(c) and (c')), but also that the organization in bulk is more homogeneous.

We present in figures 2.25, 2.26, and 2.27 the SSPM images of the two last surfaces, reconstructed for defocalization values ranging from $z = -2$ μm to $z = 2.5$ μm. Note that the dynamics of each image has been chosen separately in such a way that the intensity variations can be clearly compared.

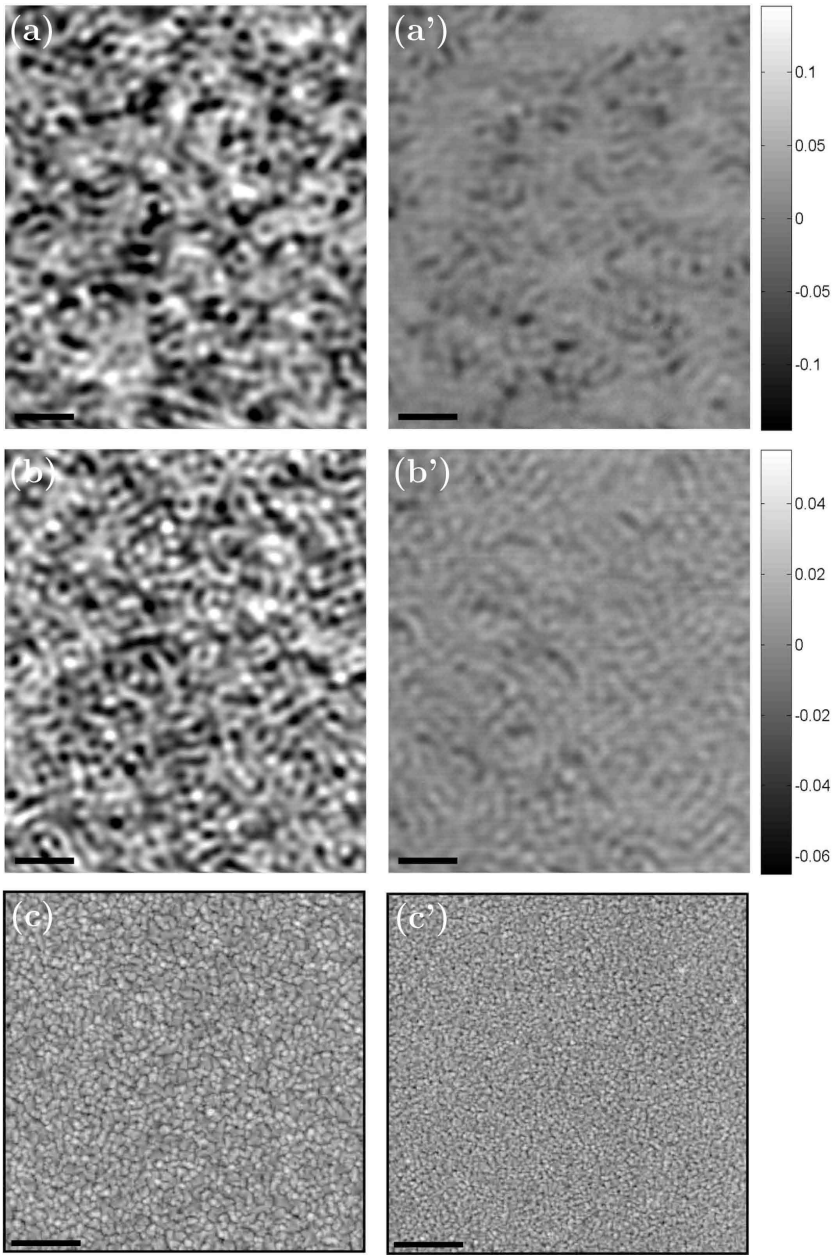

Figure 2.24 SSPM imaging of gold films. (a) and (b) Speckle-like patterns obtained from gold films evaporated on untreated glass, corresponding to defocusing positions $z = 0$, and $z = 1\ \mu m$ respectively. (a') and (b') Speckle-like patterns obtained from gold films evaporated on glass treated with (11MUD(MeO)$_3$Si) [10^{-2}mg.ml^{-1}] in cyclohexane, corresponding to defocusing position $z = 0$, and $z = 1\ \mu m$ respectively. The image dynamics of (a) and (a') (resp. (b) and (b')) are the same so as to simplify the comparisons. (c) and (c') show the corresponding gold topography 5x5 μm^2 images obtained by tapping mode AFM. The minimum (black) and maximum (white) height of these images respectively correspond to: (c) -25.6 nm and 25.3 nm; (c') -11.7 nm and 14.3 nm; Scale bars: 1 μm.

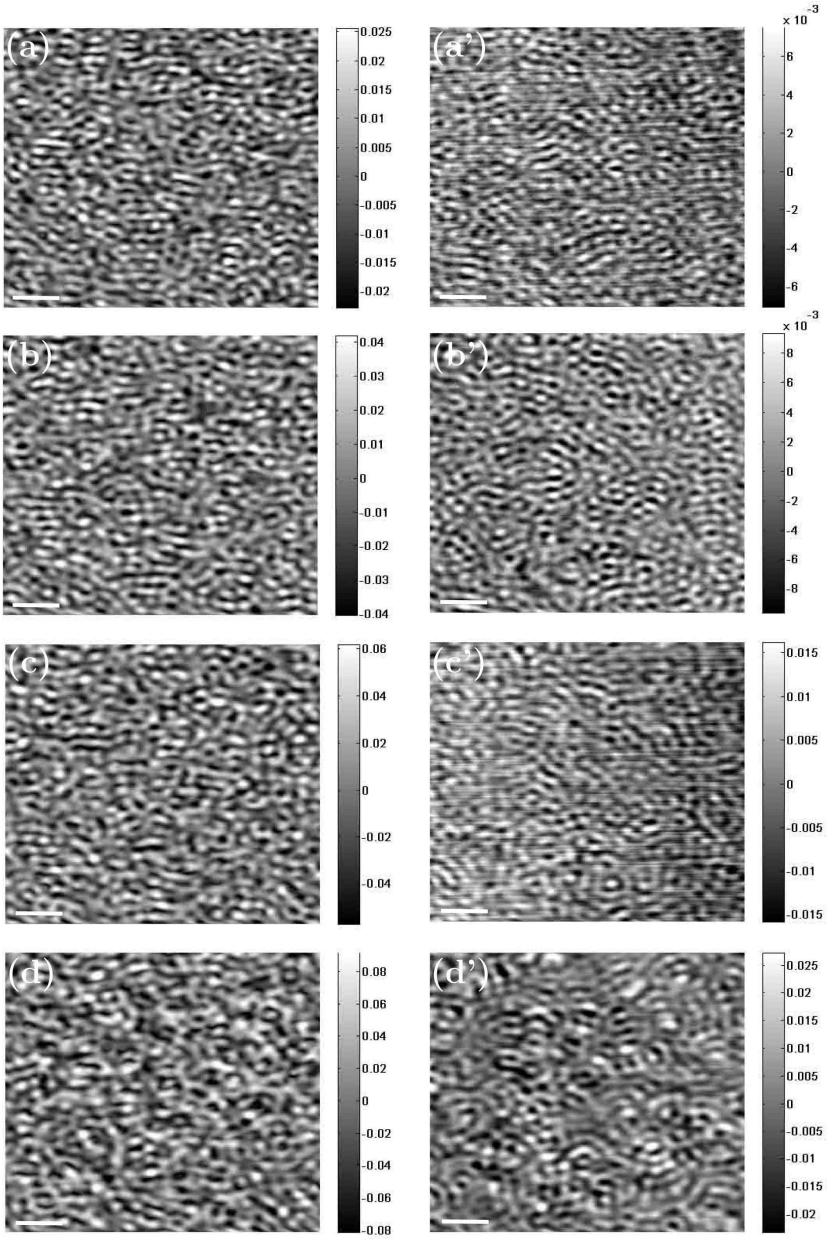

Figure 2.25 SSPM images of an untreated sample (left panel) or a coverslip chemically treated with [10^{-2}mg.ml^{-1}] of 11MUD(MeO)$_3$Si (right panel). The images have been acquired for defocalization values: (a) and (a') $z = -2$ μm, (b) and (b') $z = -1.5$ μm, (c) and (c') $z = -1$ μm, (d) and (d') $z = -0.5$ μm. Scale bars are 1 μm.

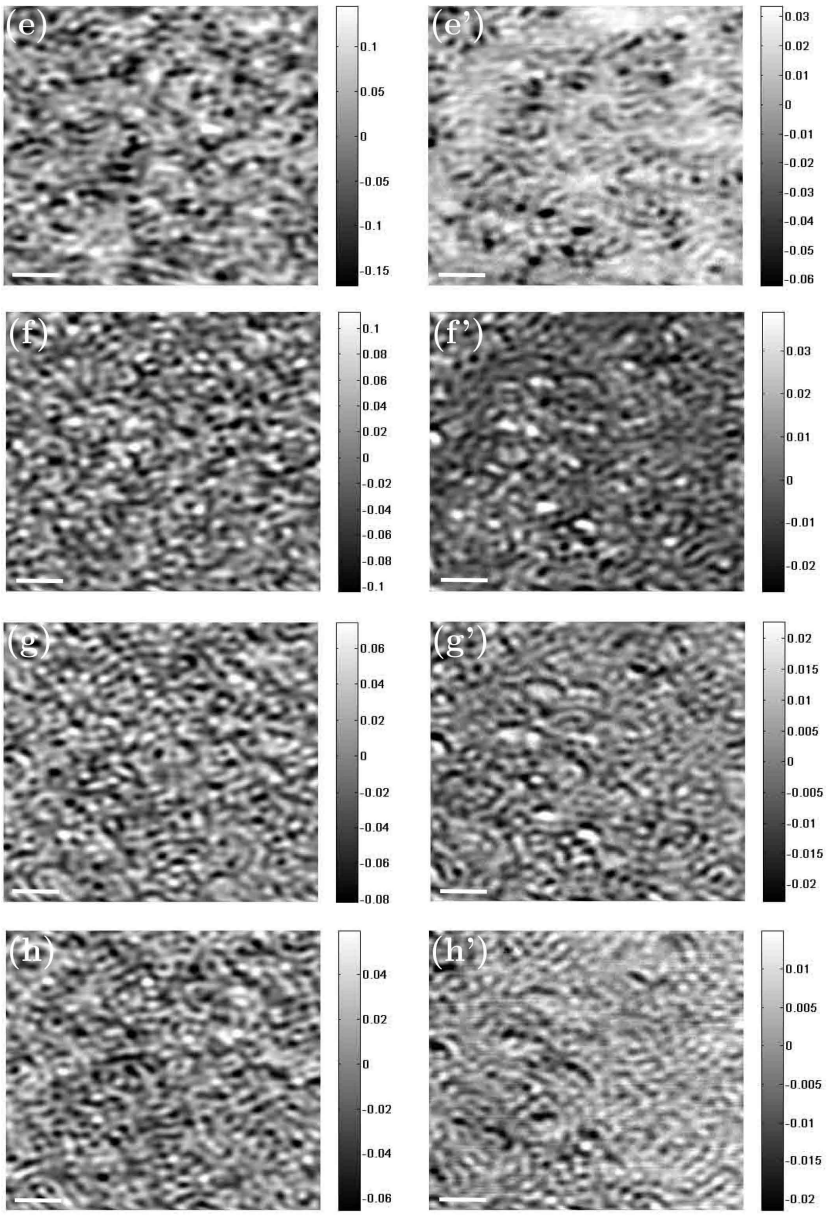

Figure 2.26 SSPM images of an untreated sample (left panel) or a coverslip chemically treated with [10^{-2}mg.ml^{-1}] of 11MUD(MeO)$_3$Si (right panel). The images have been acquired for defocalization values: (e) and (e') $z = 0$ μm, (f) and (f') $z = 0.5$ μm, (g) and (g') $z = 0.75$ μm, (h) and (h') $z = 1$ μm. Scale bars are 1 μm.

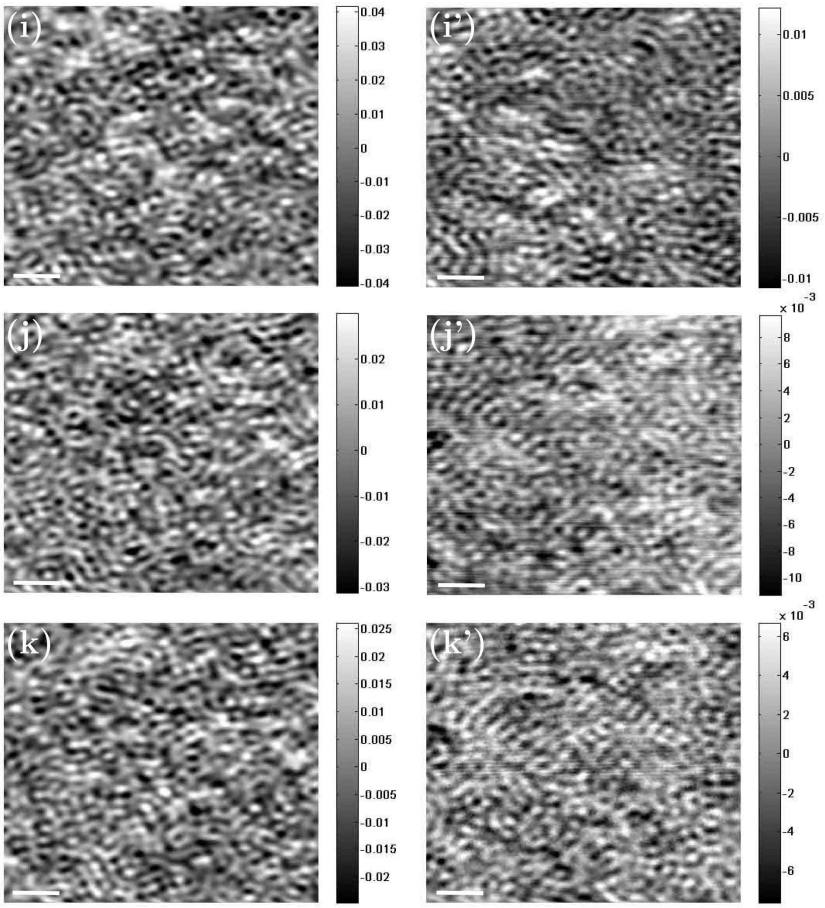

Figure 2.27 SSPM images of an untreated sample (left panel) or a coverslip chemically treated with $[10^{-2}\text{mg.ml}^{-1}]$ of 11MUD(MeO)$_3$Si (right panel). The images have been acquired for defocalization values: (i) and (i') $z = 1.5$ μm, (j) and (j') $z = 2$ μm, (k) and (k') $z = 2.5$ μm. Scale bars are 1 μm.

As for Figure 2.24, we notice that the global contrast of the images (no matter the concentration of molecules) follows the evolution of the $I(z)/I_0$ curve (see section C.4 and more precisely Figure 1.30). In other words, the contrast is maximum when the focus is at the gold/air interface and decreases with the defocalization z.
By comparing for each defocalization the images corresponding to untreated or treated sample, we can see that in presence of the chemicals at the surface, the contrast dynamics is lowered by a factor three to four. This means that the gold layer deposited on glass pretreated with the chemicals is structurally more homogeneous. If we look more closely at the variations in the images, we notice that just like for the fast/slow deposition SSPM study in section A.2.3, some black grains (of about 200-500 nm of diameter) are also present for the two types of coverslips. However, the two sets of samples do not behave strictly the same way: the structures seem to be more regularly distributed over the surface of the coverslips treated with $[10^{-2}\text{mg.ml}^{-1}]$ of 11MUD(MeO)$_3$Si. As said previously, we interpret these black grains as domains where the amount of gold is lower. This consideration can also be reversed with the white grains corresponding to domains of the layer where more gold is present in volume

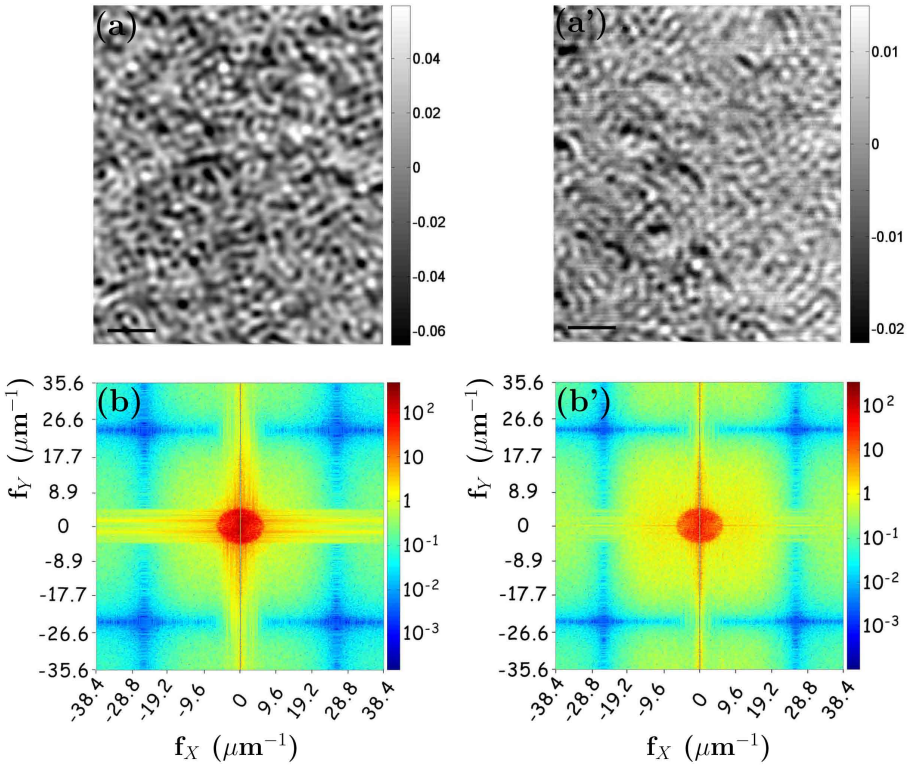

Figure 2.28 SSPM images of gold films deposited on (a) untreated substrates or on (a') glass coverslips treated with [10^{-2}mg.ml^{-1}] of 11MUD(MeO)$_3$Si The defocalization value is $z = 1\mu$m for both images. (b) and (b') are the logarithm of the 2D Fourier Transforms of (a) and (a') respectively.

(and in consequence where light is more reflected), or in surface (creation of "hot spots" where the plasmon resonance fluctuations are maximum).

In conclusion, we have shown in this section that SSPM helped us once again to probe the bulk properties of the gold layers. The structure of the film (both in surface and in bulk) is more heterogeneous in the case of untreated glass substrates. We achieved our aim, which was to improve the quality of the gold deposits in such a way that the background was lowered in order to image single molecular assemblies.

B.5.2 Fourier Transform of the SSPM images

Figure 2.28 presents the logarithm of the 2D Fourier Transforms in (b) and (b') of the SSPM images of an untreated glass surface (a) or a sample treated with [10^{-2}mg.ml^{-1}] of chemicals (a') for a defocalization value of z =1 μm.

First of all, we observe that the global aspects of the 2D Fourier Transforms of the SSPM images corresponding either to untreated samples of coverlips treated chemically are relatively similar. Indeed, the two show a yellow cross-like shape at the center, which represents the

highest scales, and blue cross-like shapes situated for highest frequencies that are likely to be caused by the pixelization effect of the image. We also notice the presence of a very intense spot in the center of the 2D FT image. This spot corresponds to a size that is almost the same in the X and Y directions: $\sim 150 - 170$ nm. We believe this scale actually corresponds to the periodicity of the contrast variations between two domains of either positive or negative values, which is about the size of the point spread function of the SSPM apparatus in air (~ 200 nm).
However, slight differences can be seen when looking more closely at the central spot and the surrounding area. The central spot is indeed less intense (the red is lighter) for the treated sample, and the surrounding area more intense (yellow is brighter) and more homogeneously distributed. We interpret these two observations as a more homogeneous distribution of the scales of the plasmon phase variations, but also as an increase of their isotropy.

In conclusion, we have shown in this section that the typical distance between two consecutive bright or dark spots are about 160 nm, no matter the type of sample. However, we have observed that the distance scales of those variations are more evenly and isotropically distributed for coverslips treated with [10^{-2}mg.ml^{-1}] of 11MUD(MeO)$_3$Si.

B.6 Results and discussion

In this section, we first sum up the results obtained about the effects of the chemical treatment on the glass samples and on the structure of the metal films. In the second part, we present the important physical processes that rule the deposition of gold by thermal evaporation on glass substrates. Finally, we propose a model explaining the formation of the gold layer on the treated coverslips.

B.6.1 Results

Thanks to AFM imaging in tapping mode, we have seen in section B.1.1 that chemically treating the glass substrates with [10^{-2}mg.ml^{-1}] of 11MUD(MeO)$_3$Si has a dramatic effect on the surface structure of the gold layers. However, we also observed that the gold structure of the samples treated with [10^{-3} mg.ml^{-1}] of 11MUD(MeO)$_3$Si behaves the same way as the untreated coverslips.
By computing the power spectra of those AFM topographic images, we observed in section B.1.2 that the range of scales of the objects corresponding to the untreated substrates or to the samples treated with [10^{-3} mg.ml^{-1}] of molecules is larger than the one for the highest concentration of chemicals. We also saw that the full width at half maximum of the histograms of heights is two times narrower in case of the highest treatment. Taken together, these results mean that the gold clusters seem to be smaller not only in size, but also in height after treating the glass with [10^{-2} mg.ml^{-1}] of 11MUD(MeO)$_3$Si. As a consequence, the gold roughness of those coverslips is drastically decreased.

Using the 2D WTMM segmentation approach in section B.1.3, we looked more closely at the individual objects composing the gold films. First, we confirmed that treating the glass with [10^{-2} mg.ml^{-1}] of 11MUD(MeO)$_3$Si leads to the presence of smaller metal clusters at the surface (smaller values of their diameter, perimeter, height, and volume). Moreover, we determined that their overall 3D shape does not depend on the chemical concentration, since they all show a conical or pyramidal geometrical aspect, with an angle at the summit of $(132 \pm 4)^\circ$.
We have also noted that treating the surfaces with a concentration of chemicals of [10^{-3} mg.ml^{-1}] does not seem to induce noticeable variations in the surface structure of the gold layer. To further investigate this observation, we carried out AFM topography and phase experiments (in tapping mode) in section B.2.1 on the treated glass substrates before deposition of gold. From those experiments, we have determined that the roughness of the gold layers is not directly linked to the glass structure. We have also demonstrated in sections B.2.2 and B.2.3 that the computation of the power spectra, histograms of heights, and detection of the objects at the surface could not reveal topological modifications of the glass samples after treatment. This showed that the variations in the gold layer structure must be a consequence of changes in the physical properties of the glass surface because of a 11MUD(MeO)$_3$Si layer.
However, we were able to discriminate from the types of treatment by using AFM phase imaging. We observed that the image contrast was dramatically different when the concentration of molecules used to treat the samples is raised, which accounts for drastic modifications in the interaction forces between the AFM tip and the sample. Therefore, the physical properties of the glass surface are certainly ruled by the presence of the 11MUD(MeO)$_3$Si layer. Another point is that even if the treated glass surfaces are not definitely homogeneous (due to variations in the organization or in the density of the SAM), they tend to be more organized as the concentration of chemicals is raised. Furthermore, when we look more closely at the phase images of samples treated with [10^{-3} mg.ml^{-1}] of chemicals, we observe the presence of numerous small domains where the contrast is relatively high. The fact that most of these are present on untreated coverslips and that almost none of them can be seen on substrates treated with the highest concentration of molecules, suggests that they are likely to correspond to areas where no molecule is present.

Section B.3 presents the chemical analysis by X-ray Photoelectron Spectroscopy that has been carried out on the treated coverslips before and after deposition of gold. Even if we have been able to confirm the presence of the molecules from the high resolution S energy spectrum of the sample treated with [10^{-2} mg.ml^{-1}] of 11MUD(MeO)$_3$Si, we were not able to detect this element neither on the sample treated more lightly, nor after deposition of gold. However, this does not means that no molecule is present on the surfaces, but that they were below the detection limit. Therefore, no information on the quality or the organization of the SAM could be determined with this technique.

On the other hand, we used surface plasmon techniques to have more insights about the internal structure of the gold layers deposited on treated glass substrates.
We have presented in section B.4 the SPR experiments (R_P/R_S curves) and their fits using

a three layer model with adjustable dielectric indices. Thanks to those fits, we were able to estimate that no matter the concentration of molecules to treat the glass substrates, both the thickness of the metal layers and the fraction of vacuum inclusions inside them were the same: $H_e = 45.6 \pm 1.9$ nm and $\eta_1 = 0.90 \pm 0.04$ respectively. However, it does not mean that the layers are strictly equivalent.
In order to check on the local variations of the metal film structure (both in surface and and in bulk), we did SSPM experiments (see section B.5). By comparing the images of untreated surfaces with those of samples treated with [10^{-2} mg.ml^{-1}] of 11MUD$(MeO)_3$Si (and for several values of defocalization), we have noticed local modifications both in the surface plasmon resonance, and in the reflectivity of the layer: these variations are more regularly distributed and the image contrast is lowered for samples treated with the chemicals.

B.6.2 Physical processes involved in the thermal evaporation and the deposition of the metal layer

Extraction of the gold particles from the source and travel through the vacuum chamber

The first stage of the thermal evaporation[131] process is the heating up to fusion of the gold wire and the extraction of the charged[99] metal particles from the source. We suspect that the size of these particles depend mainly on the temperature of the source which controls the speed of the evaporation. Note that the more spatially and temporally homogeneous the evaporation rate is, the less dispersed the size distribution of the gold particles are going to be. According to Barns *et al.*[99], the clusters nucleate during their travel through the vacuum chamber because of successive impacts with other metallic particles. In other words, the size of the clusters would depend on the mean free path λ_{fp} of a gold particle (ranging from one to several hundreds of gold atoms) after extraction from the source:

$$\lambda_{fp} = (n\sigma)^{-1} \tag{2.7}$$

where n is the number of metal particles (atoms or group of atoms) per unit volume, and σ the effective cross section of collision .

If we assume that the velocities of the metal particles follow a Maxwell-Boltzmann distribution, the mean free path reads:

$$\lambda_{fp} = \frac{k_B T}{\sqrt{2}\pi \ {D_p}^2 \ P} \tag{2.8}$$

with k_B the Boltzmann constant, T and P respectively the temperature and pressure, and D_p the diameter of the metal particles in the vacuum chamber.

We can evaluate the order of magnitude of the mean free path for particles ranging from one atom ($D_p \sim 0.1$ nm) to several hundreds or few thousands of them ($D_p \sim$10 nm). When considering the experimental pressure during the evaporation process $P \sim 5\ 10^{-5}$ mbar, and

using the temperature of evaporation of gold $T_{gold} \sim 1600$ K, we obtain: $\lambda_{fp,atom} \sim 50$ m and $\lambda_{fp,cluster} \sim 0.5$ cm.

Therefore, we believe that even if some nucleation can happen in the vacuum chamber for the smallest clusters, the very narrow dispersion of the gold nuclei sizes (see section B.1) tends to show that most of them are likely to come directly from the metal source.

Moreover, we think that the size of the nuclei (with $\sim$ 5-10 nm of diameter) extracted from the metal source is ruled by the temperature of the gold source.

Wettability of gold with respect to the glass substrate

After traveling all the way to the substrates (considering an untreated glass substrate), the first nuclei arrive to the surface with a very high kinetic energy, and depending on their size and the wettability of gold for the surface, they adopt a shape that is intermediate between the disk and the half sphere (or a spherical cap). This, of course, happens before the layer covers the whole surface (meaning when its thickness is less than 5-10 nm).

The addition of an intermediate metal layer (often made of chromium) between glass and gold is often needed in order for the metal to increase the adherence of gold to the glass substrate. This shows that the bonds between the gold clusters and the glass coverslips are weak, and their wettability is relatively bad. As a consequence, it is then very probable that the gold nuclei diffusion on the surface is increased, as well as the coalescence of those particles. On the opposite, if the wettability of gold for the substrate is improved, the interactions between the two materials are globally stronger, and thus both the diffusion and coalescence of the metal clusters are disfavored.
Moreover, the clusters extracted from the metal source are electrically charged and the Coulombic repulsion between those nuclei counterbalances this coalescence phenomenon[99].

In conclusion, as the wettability worsens, the coalescence increases.

Thermal exchanges at the glass surface

Thermal exchanges at the substrate surface are a critical aspect of the deposition process, and are directly ruled by the thermal conductivity of the present materials. However, two situations have to be considered with respect to the evaporation.

First, let us focus on the early times of the deposition, that is before the formation of a complete gold layer (when the glass surface is not entirely covered yet). At this stage, the very hot ($\sim$1600 K) gold clusters arrive with a high kinetic energy on the glass coverslip, which has a temperature of about 300 K (at the beginning) and is not regulated as the deposition

goes on. Therefore, we not only expect on the glass coverslip the presence of a very strong gradient of temperature, but also changes in the physical properties of the surface with time. Table 2.9 presents the thermal conductivity of the materials used in this chapter.

	thermal conductivity ($W.m^{-1}.K^{-1}$)
water (bulk)[132]	∼0.6
glass (BK7, bulk)[133]	∼1
gold (bulk)[132]	317
carbon chains (bulk)[132]	∼0.1
carbon chains (2D)[134]	∼100

Table 2.9 Thermal conductivity of the materials used in this chapter (and water as a reference) at ambient temperature.

We observe from Table 2.9 that the thermal conductivity of the glass layer is very low (close to the one of water, presented here as a reference). This actually means that the heat relaxation is very bad when the hot metal clusters hit the bare glass surface. The heat is then trapped inside the gold particles, and as the number of objects arriving at the surface increases with the time, it is very likely that both the diffusion and the coalescence of the particles are favored.
However, even if we see that the thermal conductivity of carbon chains in volume is very low (∼0.1 $W.m^{-1}.K^{-1}$, which is even less than the one for water) it dramatically increases and gets closer to that of bulk gold (∼100 $W.m^{-1}.K^{-1}$) when they are organized as an intermediate layer between two dielectric media[134]. Indeed, the collective movements[134] (phonons) of the molecules help to dissipate the extra energy, and lead to a faster decrease of the particle temperature.
Another possibility is that the high temperature of the clusters hitting the surface induce the vaporization of some of the chemicals. However, this would also lead to a decrease in the local temperature since a lot of energy would be needed to ionize the elements of the molecules.
The consequence of these two possibilities is that both diffusion and coalescence events become less favorable.

The second stage of the deposition process happens after the first (almost) complete gold layer is formed at the surface. This step is harder to assess, since the substrate temperature is not controlled nor measured.
In the case of untreated glass substrates, we believe it is very likely that as the clusters hit the already hot surface, they do not transfer much of their internal energy to the surroundings but rather diffuse and coalesce more easily.
On the contrary, we think that the glass coverslips with a complete layer of $11MUD(MeO)_3Si$ do not behave the same way since the temperature of the first metal layer is probably lower (due to a better dissipation of the energy thanks to the molecules). As the thermal conductivity of gold is very high (see Table 2.9, ∼320 $W.m^{-1}.K^{-1}$), we think that the transfer of temperature to the first layer of metal is very fast, and then that the nuclei are less prone to either diffuse or coalesce at the surface.

In conclusion, the dissipation of heat at the surface is a very important aspect of the deposition process, which is very likely to change as the evaporation goes on. We believe that the increase of the thermal conductivity at the surface leads to a better dissipation of the energy, and *via* a decrease of the temperature gradient intensity, to a lowering of both the diffusion and the coalescence of the gold clusters.

B.6.3 Interpretation of our observations

From the experiments carried out on the chemically treated glass samples before and after evaporation of gold, together with the remarks made on the physical properties ruling the deposition by thermal evaporation, we propose in Figure 2.29 a model explaining the process of the metal layer formation on a 11MUD$(MeO)_3$Si SAM.

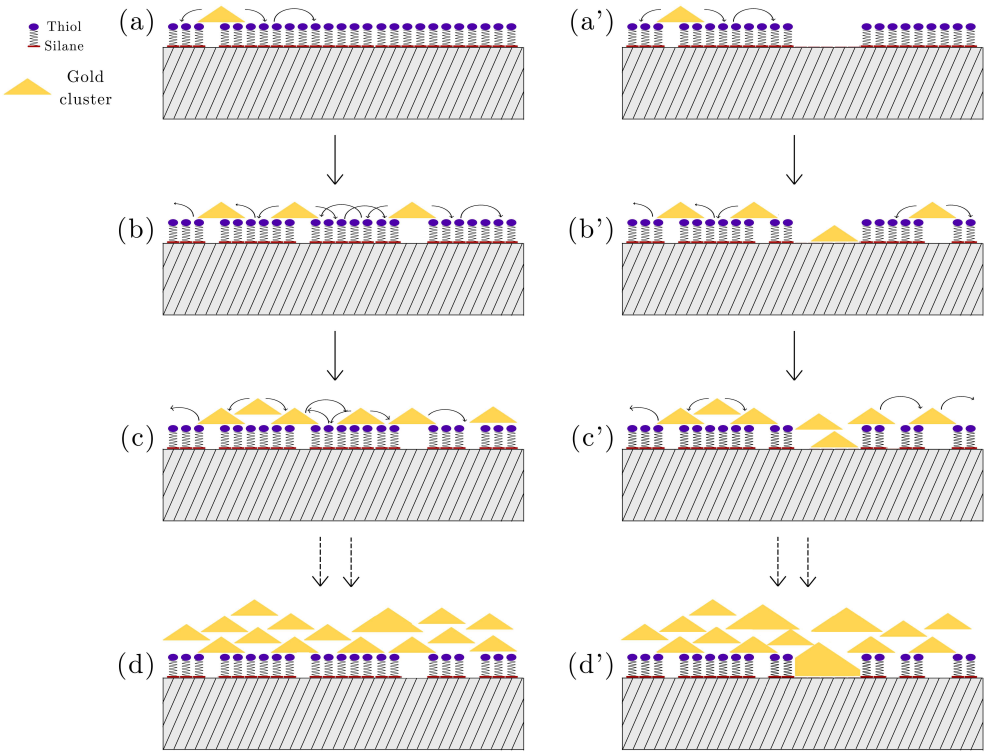

Figure 2.29 Deposition of the gold clusters on a glass substrate treated chemically with 11MUD$(MeO)_3$Si. In the left panel, the SAM is very well organized, whereas many defects are present in the right panel. The curved arrows show the dissipation of heat at the surface thanks to the high thermal conductivity of the chemicals. The deposition evolution is represented from (a) to (d) and (a') to (d').

We saw in section B.6.2 that the size of the gold clusters hitting the glass sample is mainly ruled by the temperature of the gold wire during the evaporation process. Since the deposition occurs for all coverslips at the same time, the properties (and particularly their size) of the

gold particles hitting the surfaces is very likely to be identical, no matter the type of treatment. It is then very probable that the smallest objects seen in the AFM images correspond to the ones extracted from the source (maybe after some nucleation events in the vacuum chamber, and after convolution by the AFM tip). As a consequence, the almost absence of bigger clusters on samples treated with [10^{-2} mg.ml^{-1}] of chemicals can be explained by the decrease of both the diffusion and coalescence events of the metal clusters (see section B.6.2).

The first step during the deposition process is the arrival of a few gold nuclei on the surface. They may hit either the highly ordered SAM (left panel), and be "trapped" (a) by the thiols (no diffusion), or arrive in a zone without chemicals (right panel), where they can diffuse (a') on a very short distance.
We saw previously that the presence of the molecules linked to the surface leads to a better dissipation of the heat in (b) with respect to (b'). This is likely to be a consequence of the collective oscillations (phonons) of the chemicals that propagate in all directions around the hot gold object. Moreover, we also note that some of the chemicals may be vaporized because of the very high temperature of the gold nuclei. However, this should also lead to a decrease in the local temperature since a lot of energy would be needed to ionize the elements of the molecules. Therefore, as the deposition goes on, we expect to see a lower number of coalescence events where glass has been treated (c) to (d), whereas a higher number of clusters should merge (c') to (d') in the vicinity of the untreated domains (since the heat cannot leak as easily).
Afterwards, other gold nuclei hit the surface, transfer relatively rapidly their heat to the surrounding clusters, and probably diffuse over short distances. We also believe that as deposition continues, some coalescence still takes place at the surface (with a higher rate for the domains where no molecules were present since the local temperature is likely higher), see (d) and (d'), and eventually form a continuous layer of about 45 nm thick.

From the considerations of the heat dissipation in presence of the molecules, we believe that treating the glass substrates with a concentration of [10^{-3} mg.ml^{-1}] of 11MUD(MeO)$_3$Si is probably not enough to form a complete and well organized SAM. In consequence, the heat is not dissipated as efficiently as for a [10^{-2} mg.ml^{-1}] treated coverslip, and coalescence events are very likely to happen at about the same rate as untreated samples.

In conclusion, we strongly believe that the enhancement of the gold films' homogeneity, both in bulk and in surface, is ruled by the formation of a complete and relatively well ordered layer of 11MUD(MeO)$_3$Si on the glass samples. It appears also very likely that the most important effect of the SAM on the deposition process by thermal evaporation is rather the increase in the heat dissipation at the surface, and not the improvement of the compatibility of the glass substrates for gold. Therefore, we expect to see a similar effect on the gold film quality in the absence of the thiol end of the molecules used to treat the glass surfaces. Finally, note that the quality of the gold layers prepared by thermal evaporation should be even higher when the chemical treatment of the glass surfaces is combined with a precise control of their temperature during the deposition.

Chapter 3

Application of SSPM to NanoParticles (NPs) imaging

Before imaging unlabeled biological samples, we study in this chapter the SSPM imaging of NanoParticles (NPs). Their optical response should be simpler than biological objects since their properties such as hydration, shape or even composition, in other words their dielectric index can be expected to vary less from one sample to another one. The optical properties of NPs behave intermediately between bulk materials and proteins, and they depend not only on their composition and size but also on their shape[135].

In previous studies, two types of optical methods have been applied on NPs using either near field[136] or far field[137] detection. Since the scattered light intensity of a NP varies versus the particle diameter as D^6, the discrimination of a single particle from other scatterers requires long integration times. Interferometric methods pushed down this size limitation by decreasing the exponent of the scattered light intensity versus particle diameter ($\sim D^3$). Recently, Photothermal Heterodyne Imaging (PHI) was proposed for gold NPs with diameters as small as 1.4 nm with an integration time of a few ms[138]. Imaging low index dielectric particles is mainly limited by the contrast difference with the surrounding medium. Very few studies afford the detection of unlabeled particles with sizes much smaller than the wavelength. Ignatovich and Novotny[139] have proposed an interferometric device that pushes the detection limit down to 20 nm diameter for polymer particles within a few milliseconds.

In this chapter, we show that SSPM can be used to image unlabelled NPs of different materials (metal and dielectric) for diameters ranging from 10 nm to 200 nm in air and in water. We present the optical SSPM response of unlabelled NPs adsorbed on gold films. We show first the SSPM images of the NPs in air, and we address the question of differentiating their size and dielectric index, both experimentally and theoretically thanks to the model based on the multipolar expansion of the Maxwell equations (see Chapter 1, Section D). Then, we present SSPM images of the NPs in water and finally we consider the influence of the laser beam polarization on the contrast of NPs and on the resolution of the SSPM apparatus.

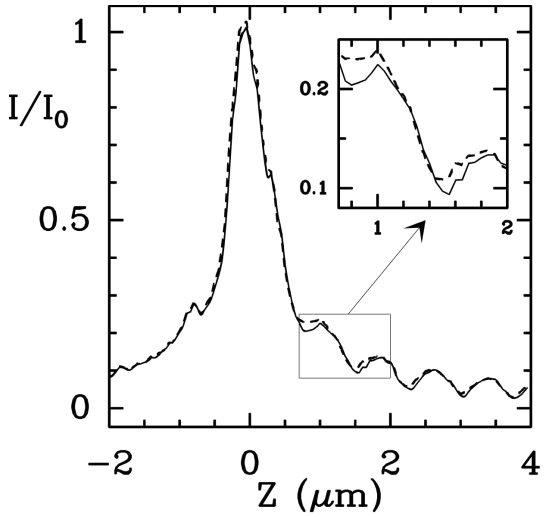

Figure 3.1 Experimental I(Z)/I$_0$ curve in air and for a linear polarization for a fixed location (X,Y) corresponding to: bare gold (plain line), or an isolated 30 nm gold NP adsorbed at the surface (dashed curve).

A SSPM imaging of NPs in air

We present in this section the SSPM images and cross-sections of gold and latex NPs with diameter ranging from 10 nm to 200 nm, in air and for a linear polarization of the light. All experiments reported in this chapter have been carried out on 45 nm thick gold films deposited on top of glass substrate supporting an adhesive layer of chromium (1.5 nm thick).

A.1 Size criterion (gold NPs)

A.1.1 Experimental I(Z)/I$_0$ curve on the background or on a gold NP

We present in Figure 3.1 the experimental I(Z)/I$_0$ curves (see Chapter 1, Section C.4) corresponding either to bare gold (plain line) or to an isolated 30 nm calibrated (C) gold NP (dashed line). The I(Z)/I$_0$ experimental curves were reconstructed from a set of 140 SSPM images (see Figure 3.3) that were filtered but not flattened, and by plotting the evolution of the normalized pixel value I/I$_0$ versus the defocalization value Z (the pixel position is fixed along the defocus) of the objective for a point (X, Y) located on the bare gold surface or on a 30 nm gold NP. Before each image, a quick I(Z) curve is recorded, and its maximum value I$_0$ is used to both normalize the optical signal, and determine the reference $Z_0 = 0$ (see Chapter 1, Section C.5). Z was stepped by 50 nm from -2 μm to 4 μm.

In Figure 3.1, the experimental I(Z)/I$_0$ curves show SPPs oscillations for positive values of Z. We observe that their period is the same (and compatible with the theoretical value from Equation 1.27), Δz =0.80±0.05 μm, in absence or in presence of a 30 nm gold NP. However, the phase and the amplitude of these oscillations change when a NP is adsorbed on the gold film. As we explained in Chapter 1, Section C.5, this difference of I/I_0 for a

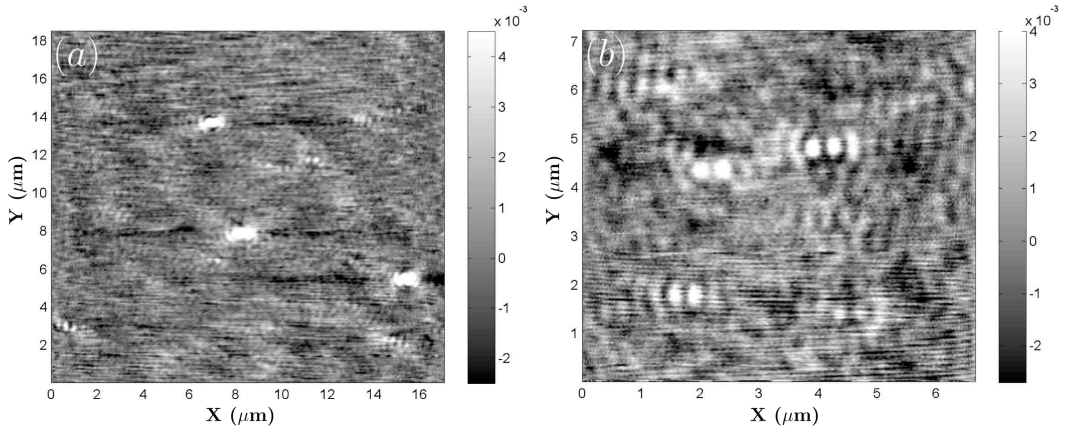

Figure 3.2 SSPM images of NPs dispersed on the gold surface ($Z \sim 0.8$ μm): (a) 200 nm gold NPs, and (b) 50 nm gold NPs. These images have been obtained with a linear polarization of the laser beam. The dielectric medium embedding the NPs is air.

fixed defocalization value Z, rules the contrast of the image, when the sample is scanned in the X and Y directions. We expect then the contrast of the NP (difference between the two I(Z)/I$_0$ curves for a given Z value) to behave periodically (ΔZ =0.80±0.05 μm) for $Z > 0$. This means that the optical response of the NP varies with Z and follows the same oscillatory behavior as the global response of the gold film.

A.1.2 SSPM images of gold NPs

We present in Figure 3.2 the SSPM images of two sets ofNPs (respectively 200 nm (a) and 50 nm (b)) dispersed on the metal surface. The defocalization value is $Z \sim 0.8$ μm for (a) and (b). The SSPM images shown in this section are filtered with a 3×3 pixel sliding box and flattened with a second order polynomial function. As explained previously, the modulus of the optical response I is normalized by the maximal value I_0 of $I(Z)$ at $(X, Y) = (0, 0)$. The Z value corresponding to this maximal value I_0 is chosen as the origin $Z_0 = 0$.

We see from this figure that NPs of various sizes, lying on the surface of a gold film can be detected. The two-lobe shape of their image is mainly ruled by the linear polarization of the light (see Chapter 1, Section D.3). The axis of this linear polarization is along the X direction. The contrast of the NPs (defined as the difference between the value of the pixel corresponding the a lobe maximum and the average value of the pixels from the background) seems to be higher for larger (200 nm) NPs.

Figure 3.3 shows the evolution of the contrast of a 30 nm gold NP lying on the bare gold surface, when defocalization Z is changed. Note that the dynamics of the images shown in Figure 3.3 (filtered with the 3×3 pixel box and flattened with a 0^{th} order polynomial) varies with the defocalization Z, whereas the scale is fixed for the whole set of cross-sections.

First of all, we can see from Figure 3.3 that as expect, the contrast of the NP depends on the defocalization value Z. When the focus is located in the glass medium ($Z < 0$, see Figure

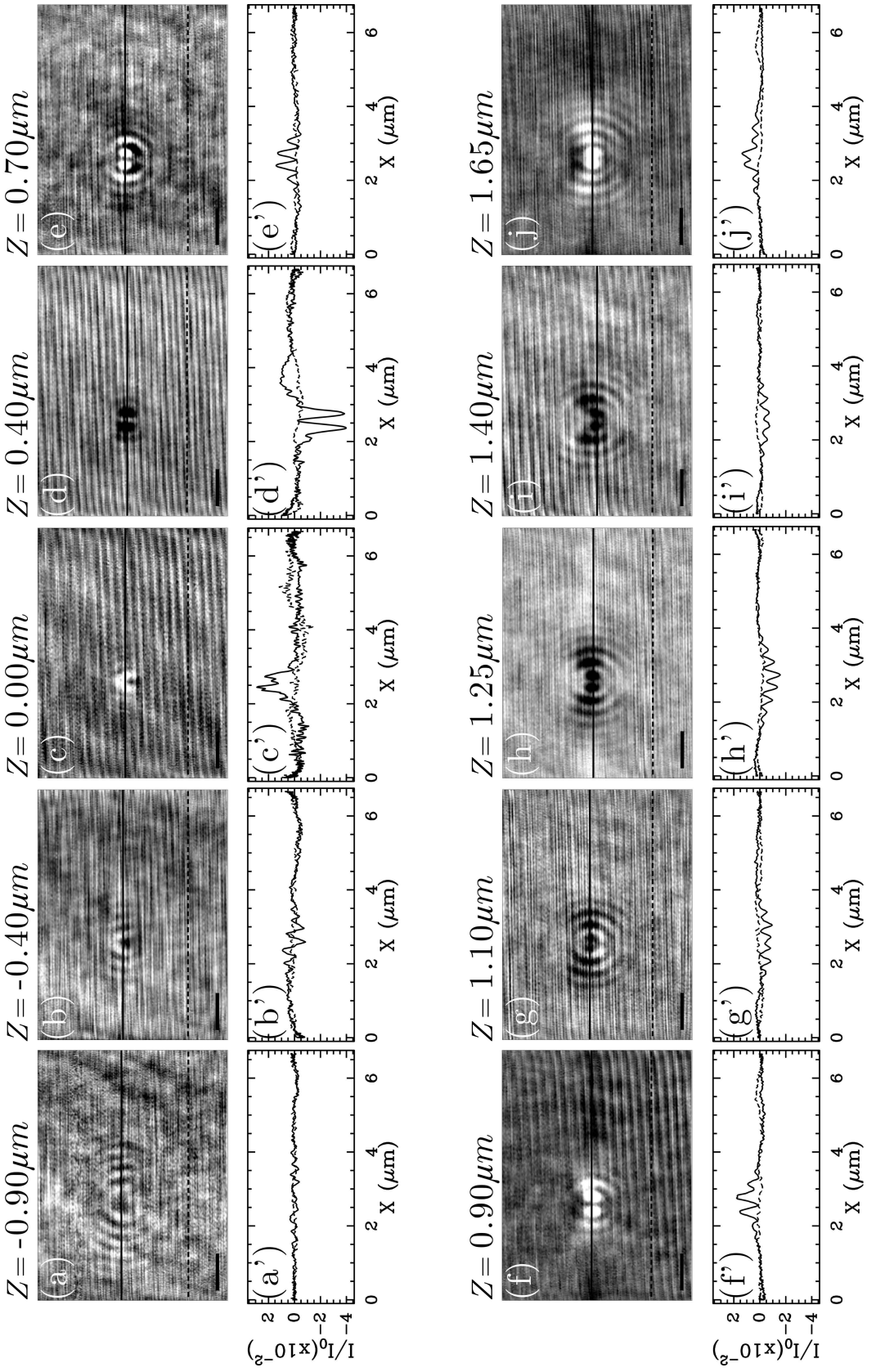

Figure 3.3 SSPM images and cross-sections of a 30 nm gold NP in air for different defocalization values (linear polarization): (a) and (a') $Z = -0.90$ μm, (b) and (b') $Z = -0.40$ μm, (c) and (c') $Z = 0.00$ μm, (d) and (d') $Z = 0.40$ μm, (e) and (e') $Z = 0.70$ μm, (f) and (f') $Z = 0.90$ μm, (g) and (g') $Z = 1.10$ μm, (h) and (h') $Z = 1.25$ μm, (i) and (i') $Z = 1.40$ μm and (j) and (j') $Z = 1.65$ μm. Black plain and dashed lines on the images correspond to the cross-sections below (respectively in plain and dashed line). Scale bars are 1 μm.

1.28(b)), the SPPs no longer converge to the beam axis, and the two lobe pattern is shrinked. However, we still can see a diffraction-like pattern. Reminding that the intensity of a pixel (for a given location (X, Y) then) is related to the back reflected light from the objective, the diffraction pattern seen for $Z < 0$ can be understood as a consequence of the reflection induced by the NP of some of the SPPs that moved away from the axis of the objective and have been collected back by the objective. Since we do not put any angular diaphragm in the optical set-up which has been used to obtain this set of images, we cannot discriminate these back reflected beams.

On the other hand, we notice that the double spot corresponding to the NP signature appears only for $Z \geq 0$. This situation corresponds to the conditions where the surface plasmon waves are converging towards the center of the illuminated area (see Figure 1.28(c)), which occurs only when the objective is focused into the dielectric medium (in the air here). As explained from the $I(Z)/I_0$ curves in Figure 3.1, the contrast of the 30 nm gold NP presents a periodicity $\Delta Z \sim 0.8$ μm, see Figure 3.3 (c), (c'), (f), (f') and (j), (j'). Furthermore, we see from these images and the corresponding cross-sections that no matter the defocalization value (for $Z > O$), the shape and size of the NP image are the same: a two-lobed pattern in the direction of the laser polarization[65] (since the SPPs can only be excited by P-polarized light) with a separation of ∼350 nm in air. We also notice the presence of an increasing number of wavelets, separated from each other by ∼330 nm, around the central lobes as the defocalization parameter Z is increased. We believe that the number of fringes produced by the self-interference of the evanescent wave (propagating laterally along the metal-observation medium interface) increases with Z. The path of the SPPs propagating at the gold surface is enhanced progressively, and the distance between these wavelets is likely to depend on the frequency of these self-interferences (∼330 nm here).
This figure shows well the importance of the defocalization value chosen to image the surface.

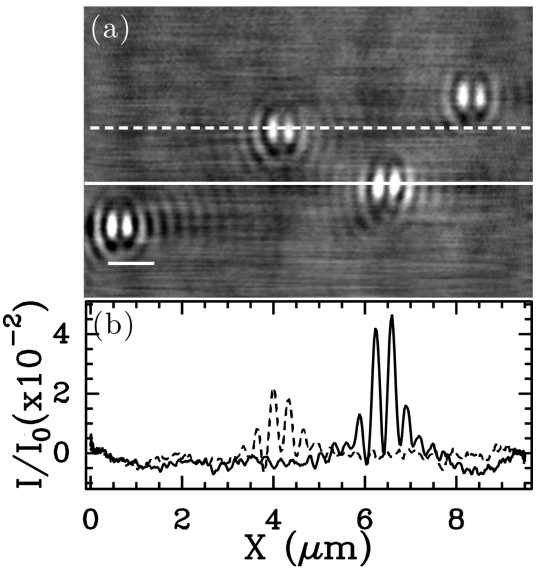

Figure 3.4 (a) SSPM image of 100 nm gold NPs in air and for a linear polarization at Z =0.9 μm. Scale bar is 1 μm. (b) black (resp. red) cross-section corresponds to the plain (resp. dashed) line in (a).

Indeed, depending on Z, the contrast of the spot is either positive, negative or null, and its intensity tends to decrease with the defocalization value.

Moreover, it has to be noted that the reproducibility of the SSPM apparatus has been tested on such NPs. It has been found that scanning the same NP over time ($>$ 4h) for the same defocalization Z, gives the same contrast values (the dispersity of the measurements is less than 5%).

We present in Figure 3.4 an SSPM image of several 100 nm gold NPs lying on the thin gold surface.

We see that the cross-sections in Figure 3.4(b) do not behave the same way. Indeed, the maximum intensity of the object corresponding to the black line (resp. the plain line in 3.4(a)) is about twice higher than for the object represented by the red line (resp. the dashed line in 3.4(a)). Scanning this area several times produces the same ratio in the particle lobe intensities, showing that these amplitude variations cannot be simply due to optical or electronic fluctuations. Three reasons may explain this quantitative difference: (i) a change of size of the particle, or the aggregation of two particles at the same location; (ii) the influence of the surface roughness that may enhance locally the electric field, and as a consequence the effect of the local dielectric index; (iii) a difference in the vertical position (Z direction) of the particle with respect to the gold surface.

Let us now consider the effect of the NPs size on their SSPM images. Figure 3.5 shows the SSPM images and corresponding cross-sections of 200 nm and 50 nm gold NPs in air for positive ((a) and (a')) or negative ((b) and (b')) contrast.

The comparison of the NPs cross-sections shows that the optical response of the 200 nm colloid is about 4 times more intense than that of the 50 nm one for the first positive contrast, and about twice as much for the second negative contrast. The asymmetry of the two-lobed pattern depends on the optical adjustments of the SSPM apparatus. We indeed suspect that shifting slightly the axis of the objective with respect to the laser axis is responsible for the imbalance of the pattern.

Figure 3.6 presents the profiles derived from a set of gold NPs with different sizes, at defocalization Z corresponding to their maximum positive contrast (around $Z \sim 0.8-0.9$ μm). The cross-sections have been averaged over several colloids for each size. Again, SSPM imaging is performed in air and for a linear polarization.

We notice from Figure 3.6 that the distance between the two lobes, as well as their width, do not depend on the size of the particle as long as it is smaller than the width of the PSF (see Chapter 1, Section D.3). This PSF width can be estimated from the FWHM of each lobe, leading to a mean value of 220 nm$\pm$30 nm in air. The corresponding mean distances between the two lobes are 340 nm$\pm$30 nm. As shown in Figure 3.6, when the particle size reaches 200 nm, the two lobes are no longer separated and their intensities overlap, consistently with our estimation of the PSF width. In consequence, we believe that 350 nm is roughly the resolution limit of our apparatus in air. Finally, the intensity of the NP SSPM response increases with their diameter. However, this intensity saturates as the colloids get smaller and even if we can still detect them, we suspect the discrimination of NPs sizes to be difficult, when they are single and very small ($\sim$ 5-20 nm).

To conclude this section, we have shown that (i) gold NPs (down to 10 nm in diameter) can be detected by SSPM imaging, (ii) the intensity of the detected objects oscillates with

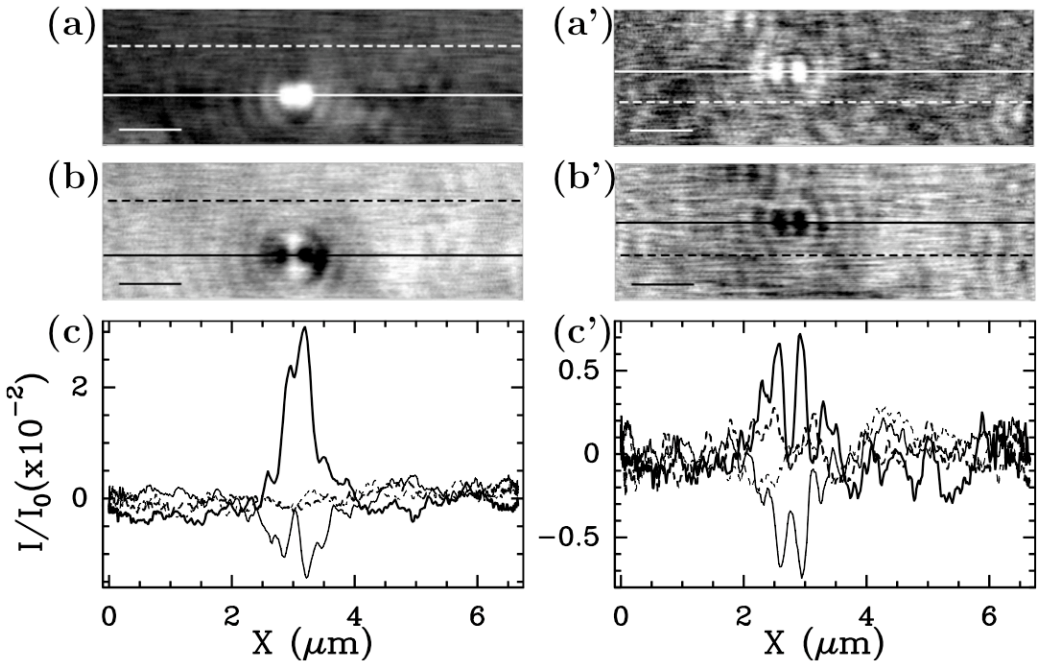

Figure 3.5 SSPM images of NPs in air and for a linear polarization. Left panel: 200 nm gold NP. Grey coded images constructed for a fixed defocus $Z = 0.825$ μm (a) and 1.150 μm (b). In (c) are shown some sections of (a) and (b) obtained at $Y = 0.84$ μm (white dashed line), 1.63 μm (white solid line) and $Y = 0.74$ μm (black dashed line), 1.61 μm (black solid line) respectively. Right panel: 50 nm gold NP. Grey coded images constructed for a fixed defocus $Z = 0.925$ μm (a') and 1.330 μm (b'). In (c') are shown sections of (a') and (b') obtained at $Y = 1.54$ μm (white dashed line), 1.02 μm (white solid line) and $Y = 1.51$ μm (black dashed line), 1.00 μm (black solid line) respectively. White (resp. black) section lines in (a) and (a') (resp. (b) and (b')) correspond to thick (resp. thin) curves in (c) and (c'). Scale bars are 1 μm.

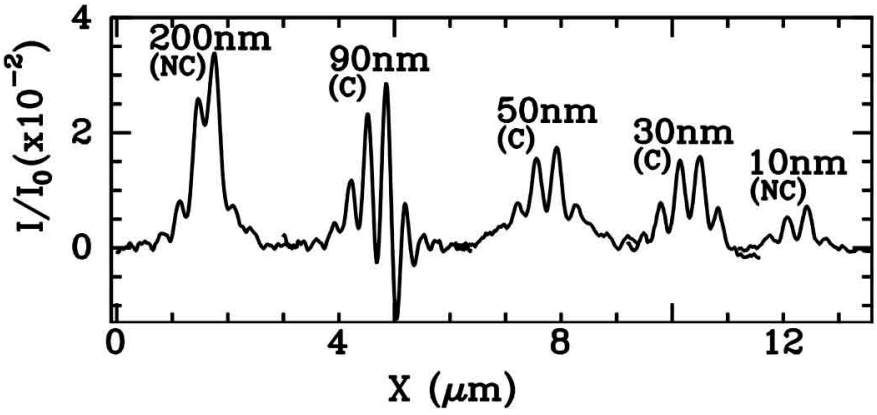

Figure 3.6 Comparison of SSPM image cross-sections in air and for a linear polarization of gold NPs of different sizes (for $Z \sim 0.8 - 0.9$ μm, corresponding to the first maximum positive contrast). The 200 nm and 10 nm profiles have been averaged over 3 and 6 NPs respectively, whereas the 90 nm, 50 nm and 30 nm profiles have all been averaged over 4 NPs. NC (resp. C) stands for Non Calibrated (resp. Calibrated) NP (in size).

the objective defocalization Z, with a period of about 0.8 μm (see Figure 3.3) and (iii) the images of the smallest NPs (<100 nm of diameter) give the PSF of the SSPM apparatus: 220 nm±30 nm (defined as the FWHM of a lobe) and the distance between the two lobes: 340 nm±30 nm (see Figures 3.4, 3.5, and 3.6). The contrast of the objects at the surface depends on the size of the NP (when it is isolated) and the number of colloids present at the same location in the case of an aggregate. Particles with diameter greater than 20 nm can be discriminated as long as they are more than 300 nm apart. Their contrast saturates when their size gets smaller. We believe we can improve this differentiation by either chemically treating the glass surfaces before depositing the gold layer (see Chapter 2, Section B), or by modifying the thickness of the metal film itself. Indeed, we have shown theoretically[140] (see Section 3.23) that the thickness of the gold layer influences drastically the NP contrast and that this optimum value of thickness also depends on the dielectric index of the colloid.

A.2 Dielectric index criterion (gold/latex NPs)

Let us now address the question of the influence of the dielectric index of the NPs on the SSPM response. This aspect is very important since we want to image biological samples. In this section, we adsorb on the gold substrates latex NPs of different sizes, whose dielectric index is real and closer to the one expected for biological objects.

A.2.1 I(Z)/I$_0$ curve on the NPs

We present in Figure 3.7 the theoretical (a) and experimental (b) I(Z)/I$_0$ curves obtained on either bare gold, or a 100 nm gold ($\epsilon_{NP} = -12.8 + j1.36$) or latex ($n_{NP} = 2.56$) NP lying on the metal surface. These particles are observed in air and a linear polarization of the laser beam is used. These curves are reconstructed from 100 SSPM images (some of them are shown in Figure 3.8) acquired for a set of defocalization values ranging from -2 μm to 3 μm (with a step of 50 nm). We note that the theoretical I(Z)/I$_0$ curve (Fig. 3.7(a)) computed from the full solution of Maxwell equations described in chapter 1 with a 45 nm thick gold film show strong similarities with the experimental ones. However, we note also some differences: the central peak of I(Z)/I$_0$ is narrower in the theoretical calculations than in the experiments, the difference of I(Z)/I$_0$ curves on naked gold and gold with a latex NP are smaller in the theory than in the experiment. Although the reason of this discrepancy is not yet completely elucidated, we suspect that the finite size of the focus point in the experiment may produce such an effect, making this central peak less sharp.

We saw in the previous section that the I(z)/I$_0$ curves corresponding to bare gold, or to a gold NP are different. We notice in Figure 3.7(a) that the presence of a latex NP induces also variations in the condition of resonance of the SPPs. More precisely, we see that the normalized intensities for a fixed defocalization value are slightly different for each situation. However, from these experimental curves we cannot conclude about the modification in the oscillation periods in absence or in presence of either a gold or a latex NP: $\Delta Z \sim 0.80 \pm 0.05$ μm. We believe this is due mostly to the error made in the determination of the $Z_0 = 0$ position before each image, and also because of the tilt of the sample as it is scanned by the objective (discrepancy in Z between the point (X,y)=(0,0) and (X,y)=(500,500) for instance). Never-

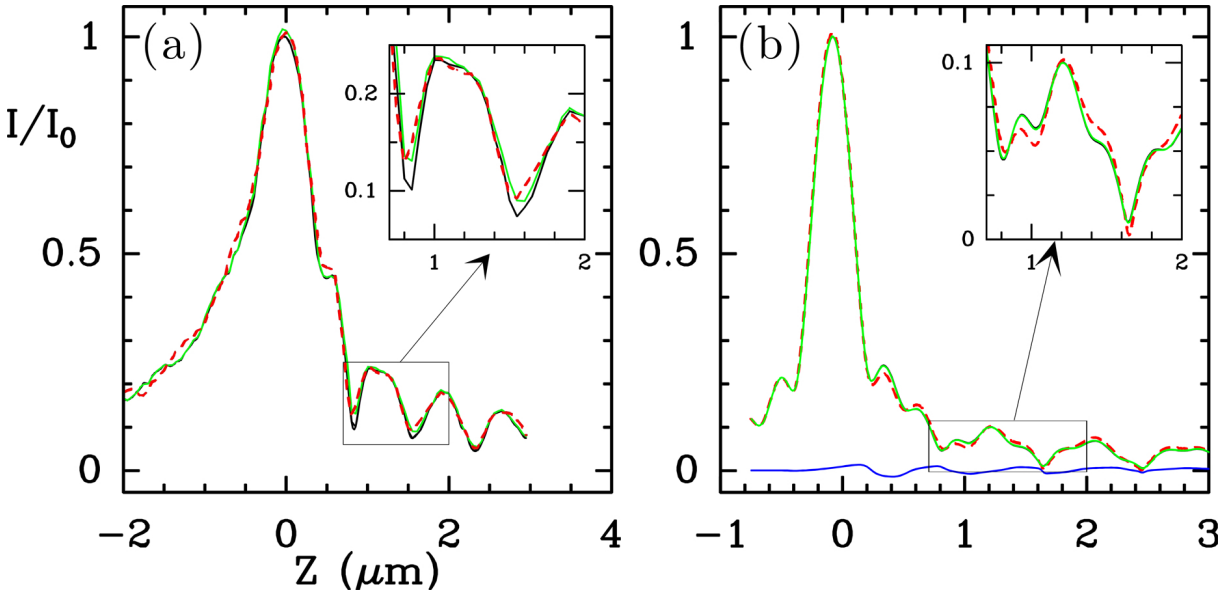

Figure 3.7 Experimental (a) and theoretical (b) I(z)/I_0 curves in air and for a linear polarization: the plain black line corresponds to bare gold, and the red dashed (resp. green plain) one to a 100 nm gold (resp. latex) NP lying on the surface. The blue curve in (b) corresponds to the difference between the I(z)/I_0 curves in case of a 100 nm latex NP and the bare surface (this difference has been magnified by a factor 10 for clarity reasons). The theoretical curves have been computed with the 3D-ME model presented in Chapter 1, Section D, for a 45 nm thick gold film and $\epsilon_{NP} = -12.8 + j1.36$ (resp. $n_{NP} = 2.56$) for the gold (resp. latex) NP.

theless, we think that after improving both the positioning in defocus and the parallelism of the samples, it should be possible to determine the dielectric properties of the materials thanks to the oscillations periods of the I(Z)/I_0 curves that are given by $\Delta z = \lambda/[2n_c(1 - cos\theta_p)]$, with $n_c \sin\theta_p = \sqrt{\frac{\epsilon_m \epsilon_d}{\epsilon_m + \epsilon_d}}$, n_c is the optical index of the coupling medium (glass), and ϵ_m, ϵ_d the dielectric permittivity of gold and the observation medium (air) respectively.
On the other hand, we see from Figure 3.7(b) that even if variations of the SSPM signal are predicted by the 3D-ME model when a 100 nm gold NP is present, the modification of the signal induced by a 100 nm latex NP is not as important (blue curves in (b)), which is in contradiction with the experimental data. This difference is not entirely clear to us, but we believe that the surface roughness is partly responsible for it, since it enhances locally the EM field[43,44] (see Chapter 1, Section A.2.3), and consequently increases the variation of the SPPs excitation when the latex NP is present.

In conclusion, we have seen that the presence of a 100 nm latex NP adsorbed at the metal surface appears to modify as well the SPPs excitation. Therefore, we expect the SSPM apparatus to be able to detect, and more precisely, to image such structures. However, it has to be noted that their dielectric index ($n_{NP} = 2.56$) is closer to that of air ($n_d = 1$), as compared with gold ($\epsilon_{NP} = -12.8 + j1.36$), which suggests that the contrast of the latex NP should be lower than their gold counterparts.

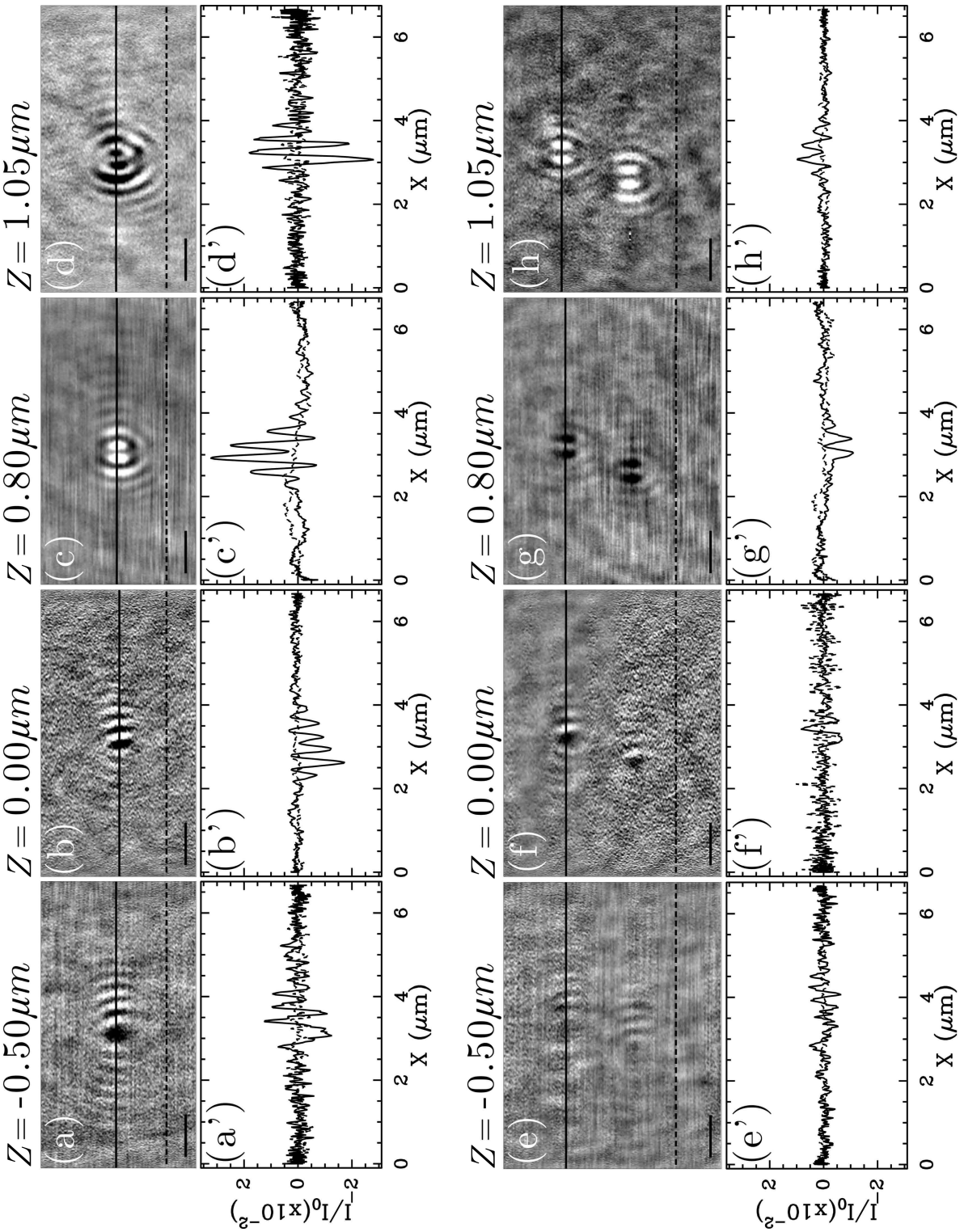

Figure 3.8 SSPM images and cross-sections of 100 nm NPs made either of gold (a-d) or latex (e-h). Experiments were carried out in air and for different defocalization values (linear polarization): (a), (a'), (e) and (e') $Z = -0.50$ μm, (b), (b'), (f) and (f') $Z = 0.00$ μm, (c), (c'), (g) and (g') $Z = 0.80$ μm, (d), (d'), (h) and (h') $Z = 1.05$ μm. Plain (resp. dashed) line on the images corresponds to the plain (resp. dashed) line in the cross-sections below. Scale bars are 1 μm. Note that the dynamics of the images (filtered with the 3×3 pixel box and flattened with a 0^{th} order polynomial) varies with the defocalization Z, whereas the scale is fixed for the whole set of cross-sections.

A.2.2 SSPM images of latex NPs

In Figure 3.8, we present SSPM images of 100 nm gold and latex NPs acquired for several defocalization values Z. Note that these images are part of the set of 140 images used to reconstruct the experimental $I(z)/I_0$ curves from Figure 3.7(a).

Several observations can be made from Figure 3.8. First of all, we confirm here that non--metallic (latex) NPs can be detected by the SSPM apparatus, which is very promising for the detection of small biological samples such as nucleosomes. When comparing the images of 100 nm gold or latex NPs, we see no drastic difference in the intensities or the patterns for $Z \leq 0$, because as explained previously, the SPPs do not converge to the center of the illuminated area. However, we clearly see variations in the contrast of the NPs for $Z > 0$ when the dielectric index is changed: the contrast of the latex (resp. gold) NP is negative (resp. positive) at Z=0.8μm, whereas it is reversed at Z=1.05μm. Moreover, we notice that even if the maximum contrast of the latex NPs is of the same order of magnitude as that of the gold colloids ($\sim 10^{-2}$), it is as expected from the previous section, smaller by a factor $\sim$2.5.

We show in Figure 3.9 the averaged cross-sections of the SSPM images (in air and for a linear polarization) of 50 nm and 20 nm latex NPs for the defocalization value corresponding to their maximum of contrast.

We see that the optical response I/I_0 of 50 nm or 20 nm latex NPs are not the same: $\sim$ 1.5 10^{-2} and $\sim$ 1.15 10^{-2} respectively. We also estimate from Figure 3.9 that the PSF of the set-up (FWHM of the lobes) and the mean distance between the two lobes are the same as for the gold NPs: 220 nm$\pm$10 nm and 350 nm$\pm$10 nm respectively in air. Moreover, by comparing figures 3.9 and 3.6, we notice that the optical responses of metallic and dielectric particles are very similar in shape, and that consequently their PSF width is independent of their nature or size, as long as they are smaller than about 100 nm. On the other hand, changing the dielectric properties of the NPs does not seem to modify drastically the lobe intensities: they are all of the same order of magnitude. This is a puzzling result, and we

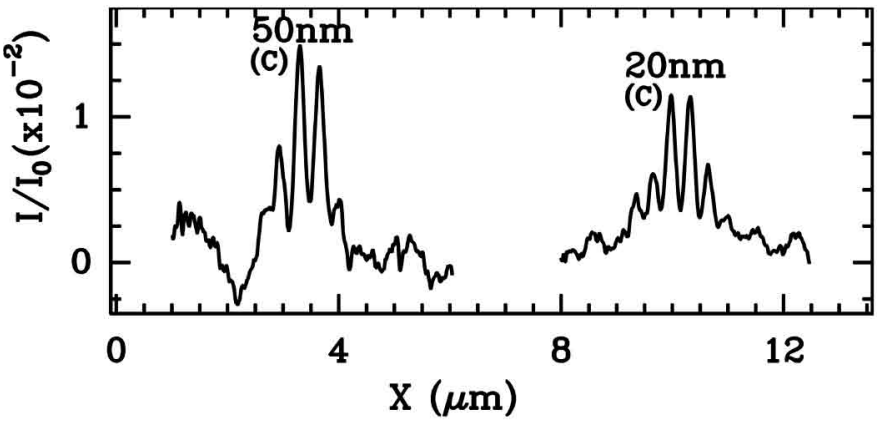

Figure 3.9 Comparison of SSPM image cross-sections in air and for a linear polarization of latex NPs of different sizes. The 50 nm and 20 nm NP profiles have been averaged over 2 and 6 NPs respectively.

therefore need the support of theoretical modeling to conclude about that observation.

A.2.3 Contrast of a 100 nm gold or latex NP with respect to the defocalization Z

Let us now consider more precisely the evolution of the contrast of gold and a latex NPs of the same size (100 nm), with respect to the defocalization Z of the objective. To reconstruct the evolution presented in Figure 3.10, we have plotted the averaged intensity of the lobes corresponding to the NP, after filtering the images (from a set of 140 of them, acquired for varying Z values) with a 3×3 pixels sliding box and subtracting from each line n its mean value I_n (0^{th} order flattening). The errorbars correspond to the mean square deviation computed for the 8 gold or latex NPs.

We notice from the experimental figure in (a) that as expected, there is almost no contrast for a 100 nm colloid (no matter its material) imaged for a defocalization value $Z < 0$. This is also predicted by the theoretical modeling in (b). For $Z > 0$ the NP contrast changes drastically with the dielectric property of the NP. The first experimental maximum of contrast for the gold or latex NPs are $(I\text{-}I_n)/I_0$=3.75 10^{-2} at Z ∼0.8μm and $(I\text{-}I_n)/I_0$=1.25 10^{-2} at Z ∼0.35μm respectively. This point is very important since it means that the images of gold or latex colloids can be distinguished. Indeed, even if we saw in section A.1 that varying the size of the NP changes only the intensity of their image, Figure 3.10 shows also that the extremal values of their contrast are not obtained for the same defocus Z. This point is corroborated by the theoretical curves presented in (b), for which the position of the maxima is also slightly shifted (by ∼ 100 nm) when considering the two types of NPs. However, it has to be noted first, that this shift is more pronounced for experimental curves (∼200 nm),

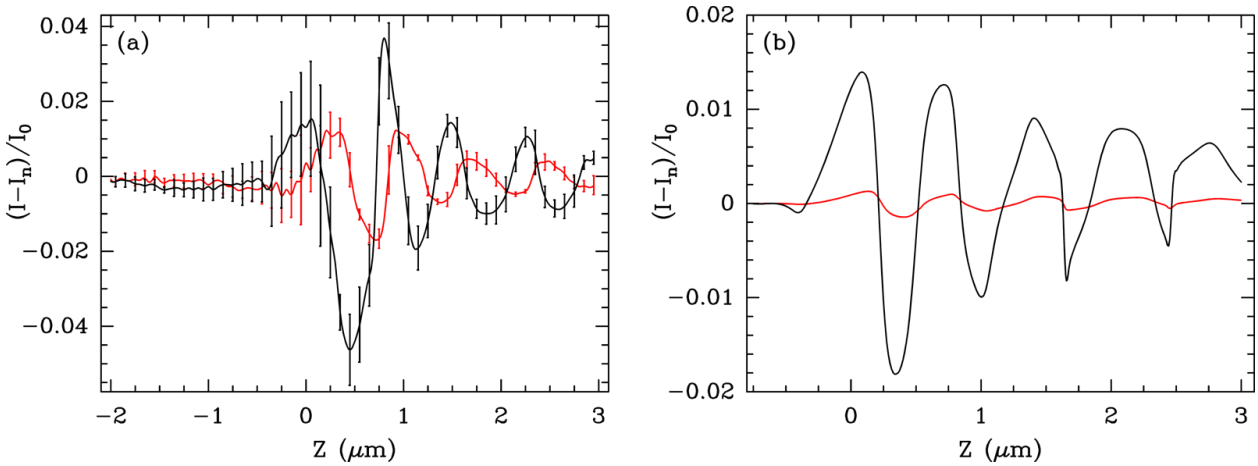

Figure 3.10 Experimental (a) and theoretical (b) contrasts of a 100 nm gold (black line) or latex (red line) NP, imaged in air and for a linear polarization, with respect to the defocalization Z of the objective lens. The experimental contrasts have been computed by averaging the optical signals over 8 NPs for both materials. Theoretical data have been computed with the 3D-ME model presented in Chapter 1, Section D, for a 45 nm thick gold film and $\epsilon_{NP} = -12.8 + j1.36$ (resp. $n_{NP} = 2.56$) for the gold (resp. latex) NP.

and second, that even if the order of magnitude of the NPs contrast is correctly estimated by the model, there is a difference between theoretical and experimental measures: a factor $\sim$ 2.5 for gold NPs, and almost a factor 10 for latex colloids. The difference between theoretical and experimental values of gold NPs can be attributed to the surface roughness that is not taken into account by the 3D-ME model. However, when considering the important difference we observe for dielectric NPs, it seems likely that the roughness parameter is only a partial explanation of this parameter. We believe that a more careful study of this difference will lead to a better understanding of the physical mechanisms ruling the excitation of the SPPs, and as a consequence the contrast formation of the SSPM images.

To conclude, we have seen in these sections that latex NPs can also be imaged by SSPM (see Figure 3.8), and that similarly to gold NPs (see Figure 3.6), their optical response varies slowly with their size (Figure 3.9). Moreover, we have determined from these figures that their image is very similar in shape and size to that of gold colloids, and that the PSF of the apparatus and the distance between the lobes are 220 nm$\pm$10 nm and 350 nm$\pm$10 nm respectively. In consequence, we see that the distance between the two lobes as well as their width, do not depend on the size and the nature of the particle if it is smaller than the PSF. Finally, we have also demonstrated in Figure 3.10 that, at fixed size, the evolution of the NP intensity with the defocalization depends on their dielectric index. In consequence, it should be possible to discriminate experimentally between NPs of different sizes (see Figure 3.9), but also between NPs of different dielectric indices (see Figure 3.10).

A.3 Modeling the NPs optical response in air

In order to master the optical response of the SSPM to the size and the nature of NPs, the optical near field interaction between SPPs and the NP needs to be considered. A quantitative understanding of the above clues was achieved by Juan Elezgaray who developed the theoretical model based on the multipolar expansion of the Maxwell equations[80,84] presented in Chapter 1, Section D. As explained previously, this calculation considers the ideal case of a gold or latex sphere of diameter D, lying on a perfectly flat gold surface that separates the coupling medium (coverslip and oil) and the observation medium (air or liquid medium). More precisely, in the theoretical computations presented in this section, the NP is embedded in air and separated by 0.1 nm of air from the 50 nm gold layer.

Figure 3.11(a) shows the theoretical SSPM image of a 50 nm gold NP illuminated in air by a linearly polarized light, and for a defocalization value of Z=0.8μm. We present in (b) the theoretical cross-section of the SSPM image (a) at $Y = 0$ (solid line), and an experimental section for comparison (black dots). The absolute value of the I($Z = 0.8$ μm)/I$_0$ intensity of the colloid lobes is presented in (c) for gold (black curve) and $n_{NP} = 2.56$ dielectric NPs (grey curve) versus their diameter D. The symbols correspond to the experimental estimations from SSPM image cross-sections of the several gold (black dots) and latex (grey circles) NPs of various sizes shown in the previous sections (typically 5 to 10 NPs for each dot).

We see in figures 3.11(a) and particularly in the cross-sections (b) that the computation of the NP optical response is remarkably similar to the experimental data for a 50 nm gold

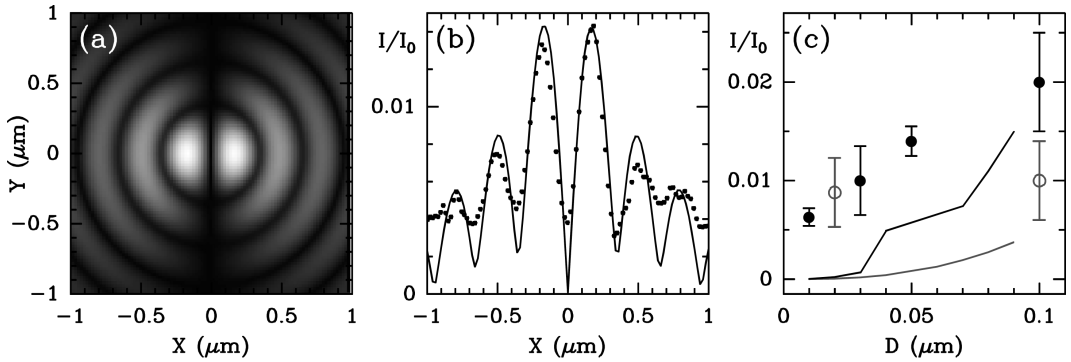

Figure 3.11 (a) Theoretical grey coded intensity I(X,Y,$Z = 0.8$ μm)/I$_0$ computed for a $D = 50$ nm gold NP in air (linear polarization). (b) Cross-section of (a) at $Y = 0$ (solid line), compared to the corresponding experimental section (black dots). (c) I(Z=0.8 μm)/I$_0$ intensity at the maxima of the lobes computed for gold (black curve) and $n = 1.5$ dielectric NPs (grey curve) versus their diameter D. The symbols correspond to the experimental data obtained by averaging the SSPM images of the gold (black dots) and latex (grey circles) NPs of various sizes. In the theoretical model, the particles are embedded in air and separated by 0.1 nm from the 50 nm gold layer ($\epsilon_1 = -12 + i\ 1.2$) coated on a glass coverslip. Theoretical data have been computed with the 3D-ME model presented in Chapter 1, Section D, for a 45 nm thick gold film.

NP in air. We also notice from these computations that the predictions of the PSF FWHM (240 nm in air) and of the distance of the lobes (340 nm in air) compare very well with the experimental values determined in Sections A.1.2 and A.2.2. Moreover, the model predicts that the contrast of the NPs for Z=0.8 μm (around the first maximum of contrast, see Figure 3.10) increases with their diameter D (see Figure 3.11(c)).
As supposed previously, we believe that the high contrast (as compared to the predictions) of the small ($D < 50$ nm) particles detected experimentally can be explained by the the effect of the surface roughness which, as we saw in Chapter 1, Section A.2.2, can induce the creation of "hot spots" where the EM field is locally enhanced.

As D gets higher, the intensity of the maximum of the SSPM image lobes increases similarly in the theoretical one and the experimental data for the gold NPs. Moreover, we have already seen in the previous section that the model underestimates the contrast of the latex NPs, no matter their size.

However, experimental data and theoretical prediction for the SPPM images of NPs do not coincide precisely for three reasons:
(i) for very small D values $\leq$ 5-10 nm, the roughness of the gold surface should be taken into account in the model. Indeed, since the surface inhomogeneities are the same order of magnitude as the NP size, we expect the position on the layer to be of great importance. As mentioned previously, we believe that "hot spots" may appear at locations where the gold interface is locally higher than its vicinity (clusters of gold which are studied in Chapter 2, that as a consequence enhance the contrast of the nanoobjet (because the evanescent field is locally stronger and the dielectric variation due to the NP is more important);
(ii) the finite size resolution of the computation may not allow the computation of very sharp electric field gradient which may arise for very small particles, moreover the interplay of the near field generated by the SP with the near field produced by the surface requires a very fine

tuning of the spatial variables, which is very consuming in terms of computation time;
(iii) the number of multipoles used to calculate accurately the optical response of the NPs increases with the particle diameter and again, tests have been done to ensure that this decomposition converges. However, as the number of poles increases the computation time diverges also.

In conclusion, we have shown in this section that for a fixed defocalization value, the evolution of the NPs contrast with their size and nature (dielectric index) can be relatively accurately predicted by the full solution of Maxwell equations for the interaction of a single NP with a flat gold coated coverslip. The reradiation of the field scattered by the NPs is of great importance in the local modification of the plasmon excitation, and as a consequence in the contrast in the image. However, the predicted and measured contrasts diverge for the latex NPs and the smallest gold colloids. We believe it is due partly to the roughness of the gold surface, and to the coupling of the surface polaritons of the layer with the localized plasmons of the metallic NPs.

In addition to these observations, the modeling also corroborates the fact that the PSF along the p-polarization axis does not vary much with the material properties of the NP. Actually, the information about the size and dielectric properties of the NP is mainly contained in the amplitude of the PSF of this microscope. The good agreement between experiments and computations enlightens the fundamental role of SPPs in the detection of the NPs: (i) the SPPs concentrate the incoming radiation in a manner that varies quite periodically with the defocus Z, allowing to improve the image contrast and (ii) the SPPs due to gold roughness strongly enhance the coupling of evanescent waves scattered from the NPs with the gold film, leading to a slow increase of I/I_0 versus D that allows the detection of NPs as small as 10 nm (see Figure 3.11(c)). Finally, the detection of even smaller NPs should be possible by SSPM imaging by a modification of the gold film roughness via either a thermal (by annealing for instance) or a chemical treatment of the samples[7,111] (see Chapter 2).

B SSPM imaging of NPs in aqueous medium

Our ultimate goal being to image unlabeled biological samples (such as nucleosomes or larger systems) by the mean of our SSPM apparatus, we have to make sure that nanomaterials can be imaged in aqueous medium and we have to study their optical response as well. We present in this section the same study as the one carried out for the NPs in air.

B.1 SSPM imaging in air/water

We compare in this section the optical response of the SSPM in air and in aqueous medium ($I(Z)/I_0$ curves and images of NPs). Note that for aqueous experiments, the coupling medium (objective, immersion oil and the glass coverslips) must be changed because the angle of resonance in water of the SPPs on gold is to high for a 1.45 NA objective lens: $\sim 71°$, see Section A.3.1. Hence, by changing the coupling configuration, it is possible to decrease θ_P (see Equation 1.21) in such a way that experiments in water can be carried out. The optical

indices of the material, as well as the preparation protocols of the samples can be found in Appendix A, Section B.4. This configuration was used by Berguiga *et al.*[79] to obtain the first images of 200 nm gold NPs in water.

B.1.1 I(Z)/I$_0$ curves

Figure 3.12 presents the experimental I(Z)/I$_0$ curves for a linear polarization of (a) a bare gold film in air or in water.

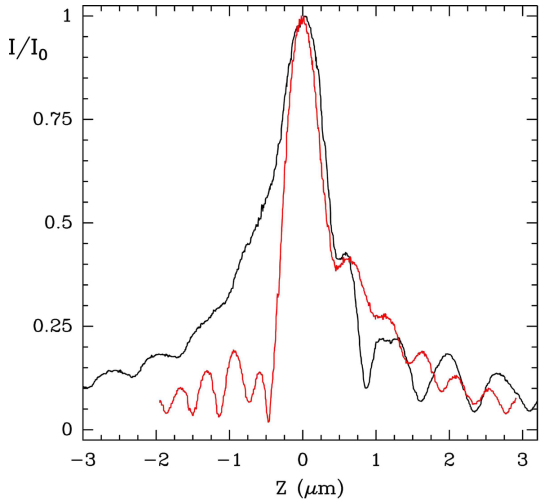

Figure 3.12 (a) I(Z)/I$_0$ curves of a bare gold film in air (black line) or in water (red line) for a linear polarization.

We notice from Figure 3.12 that changing the coupling configuration (thus, its optical index n_c) and the medium of observation from air to water not only changes the width of the center peak of I/I_0 curves, but has also a strong influence on the conditions of excitation of the SPPs, *i.e.* the period of the oscillations corresponding to the plasmon resonance (for $Z > 0$): Δz_{air} =0.75±0.05 μm and Δz_{water} =0.48±0.05 μm. This observation can be explained by the increase of both the refractive index of the coupling medium n_c (see Appendix A, Section B.4), and the angle of resonance θ_p (from 43.3° in air to 53.6° in water), that lead eventually to a decrease in the oscillations period given by $\Delta z = \lambda/[2n_0(1 - cos\theta_p)]$ (Equation 1.27): Δz_{air} = 765 nm and Δz_{water} = 440 nm, which is remarkably close to the experimental measurements.
We can also estimate the diffraction oscillations from the part of the I(Z)/I$_0$ curves of Figure 3.12 for which Z is negative: 0.62±0.05 μm in air and 0.39±0.05 μm in water. As mentioned previously, these oscillations only modulate the SPPs oscillations and do not change much their intensity or period of oscillation from the theoretical values.

In consequence, we expect the contrast of the NPs versus the defocalization Z to be different in water medium than in air. Moreover, the decrease in the period of the oscillations is likely to make the NPs contrast oscillate with a higher periodicity (with respect to Z).

B.1.2 Comparison of the SSPM images of 30 nm gold NPs in air/aqueous medium

We compare in Figure 3.13 the images and cross-sections in air (upper panel) and in water (lower panel) of a 30 nm gold NP lying on a gold coated substrate and for a linear polarization of the light. Two images for each observation medium are presented here: the defocalization value $Z \sim 0.95$ μm of the first ones, in (a) and (c), corresponds approximately to the maximum (positive) contrast of the NP in air, whereas in (b) and (d) $Z \sim 1.25$ μm corresponds to the minimum (negative) contrast in air.

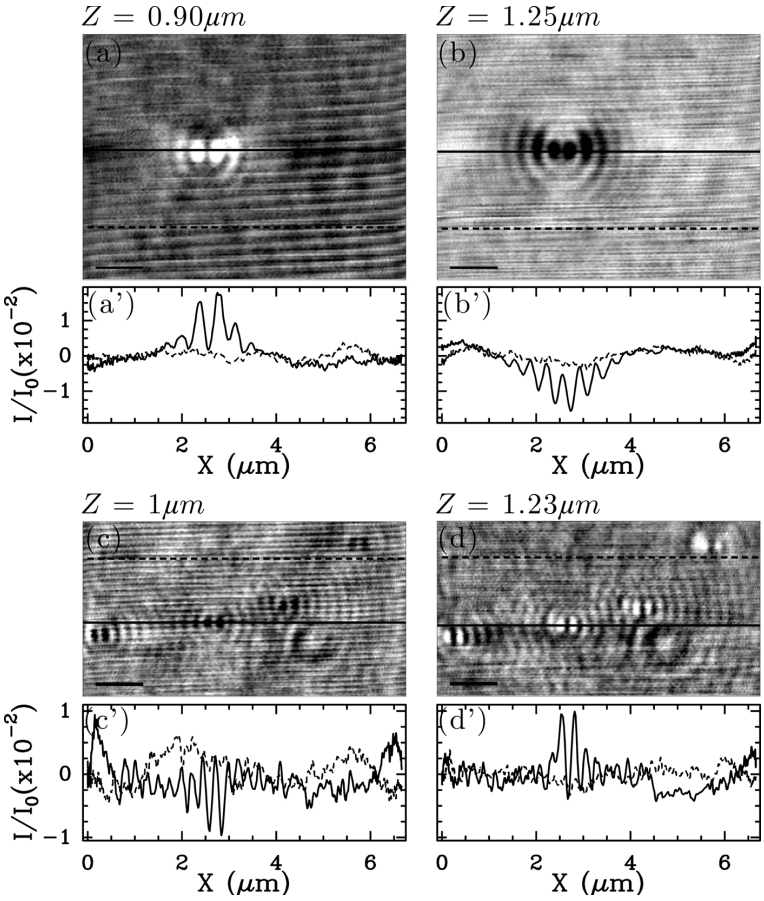

Figure 3.13 SSPM images and cross-sections of a 30 nm gold NP in air (upper panel) or in water (bottom panel) for different defocalization values (linear polarization): (a) and (a') $z = 0.90$ μm, (b) and (b') $z = 1.25$ μm, (c) and (c') $z = 1.00$ μm, (d) and (d') $z = 1.23$ μm. Plain (resp. dashed) line on the images correspond to the plain (resp. dashed) line in the cross-sections below. Scale bars are 1 μm.

We observe in Figure 3.13 that as expected from the previous section, the contrast of a 30 nm gold NP at a given defocalization value changes when imaged in air or in water. Indeed, the NP in air presents a positive (resp. negative) contrast for $Z \sim 1$ μm (resp. $Z \sim 1.25$ μm),

whereas it is the opposite for water imaging. However, no matter the medium of observation, the order of magnitude of the gold NP contrast does not change: $\sim 10^{-2}$, the contrast of gold NPs in water being about half their contrast in water. Moreover, by comparing the cross-sections of the 30 nm gold NPs in air (upper panel of Figure 3.13) with those in water (lower panel of Figure 3.13), we see that the distance of the two lobes, as well as their width (and as a consequence, the PSF of the apparatus), shrink by a factor about 2/3 when the observation medium is changed. Indeed, the mean value of the PSF and the mean distance between the lobes were respectively 220 nm±20 nm and 350 nm±20 nm in air (as determined in section A) whereas it seems to be respectively ∼145 nm and ∼230 nm nm in water.

B.2 SSPM images of gold and latex NPs in aqueous medium

We present in Figure 3.13 the SSPM images and cross-sections of a 30 nm gold NP (for a linear polarization) observed in water, with respect to the defocalization Z of the objective. Just like we saw in Section A.2.3, Figure 3.15 shows the behavior of the NP contrast $I - I_n/I_0$ with respect to the defocalization Z. To plot this evolution, the 140 SSPM images of the NP have been filtered with a 3×3 pixel sliding box, and flattened with a 0^{th} order polynomial. This was done for 4 calibrated gold NPs of 30 nm of diameter, and the individual $I - I_n/I_0$ curves were averaged and their mean square deviation computed to determine the errorbars.

As suspected from the comparison of the I(z)/I_0 curves in air and in water, presented in Figure 3.12 (section B.1.1), we notice in Figures 3.14 and 3.15 that the contrast of the 30 nm gold NPs imaged in water behaves differently than in air, and more precisely it oscillates with a smaller period $\Delta z = 450 \pm 50$ nm that corresponds to the period Δz_{water} of the I(z)/I_0 curve in water presented in Figure 3.12. We also notice that the first positive (resp. negative) contrast is given for $Z \sim 0.35$ μm (resp. $Z \sim 0.10$ μm) in water, whereas we found $Z \sim 0.80$ μm (resp. $Z \sim 0.40$ μm) in air. Note that the uncertainty on the determination of the reference value $Z_0 = 0$, and as a consequence of the position Z of the first maximum/minimum is a crucial problem for SSPM imaging in water, since the oscillation period is smaller than in air. Furthermore, we confirm here that the contrast dynamics in air is about twice as much as in water, no matter the defocalization value, which is understandable since the variation of dielectric index is higher in the case of air imaging.
Finally, we observe that for a fixed defocalization value, the gold NPs imaged in water present a higher number of wavelets around the main spot than in air: the period of these wavelets is ∼230 nm in water, and ∼330 nm in air (see Section A.1.2).

We compare in Figure 3.16 images in water and for a linear polarization of 30 nm gold (a) to (c) or latex (a') to (c') NPs.

To conclude, we saw in these sections that the distance between the two lobes as well as their width, do not depend on the size nor the nature of the particle as long as its diameter is smaller than the PSF. This PSF width was estimated from the FWHM of the NP lobes (made either of gold or latex), and we determined its mean value to be 220 nm±20 nm in air and 135±20 nm in water. The corresponding mean distance between the two lobes is 350 nm±20 nm in air and 245 nm±15 nm in water. However, when the particle size reaches

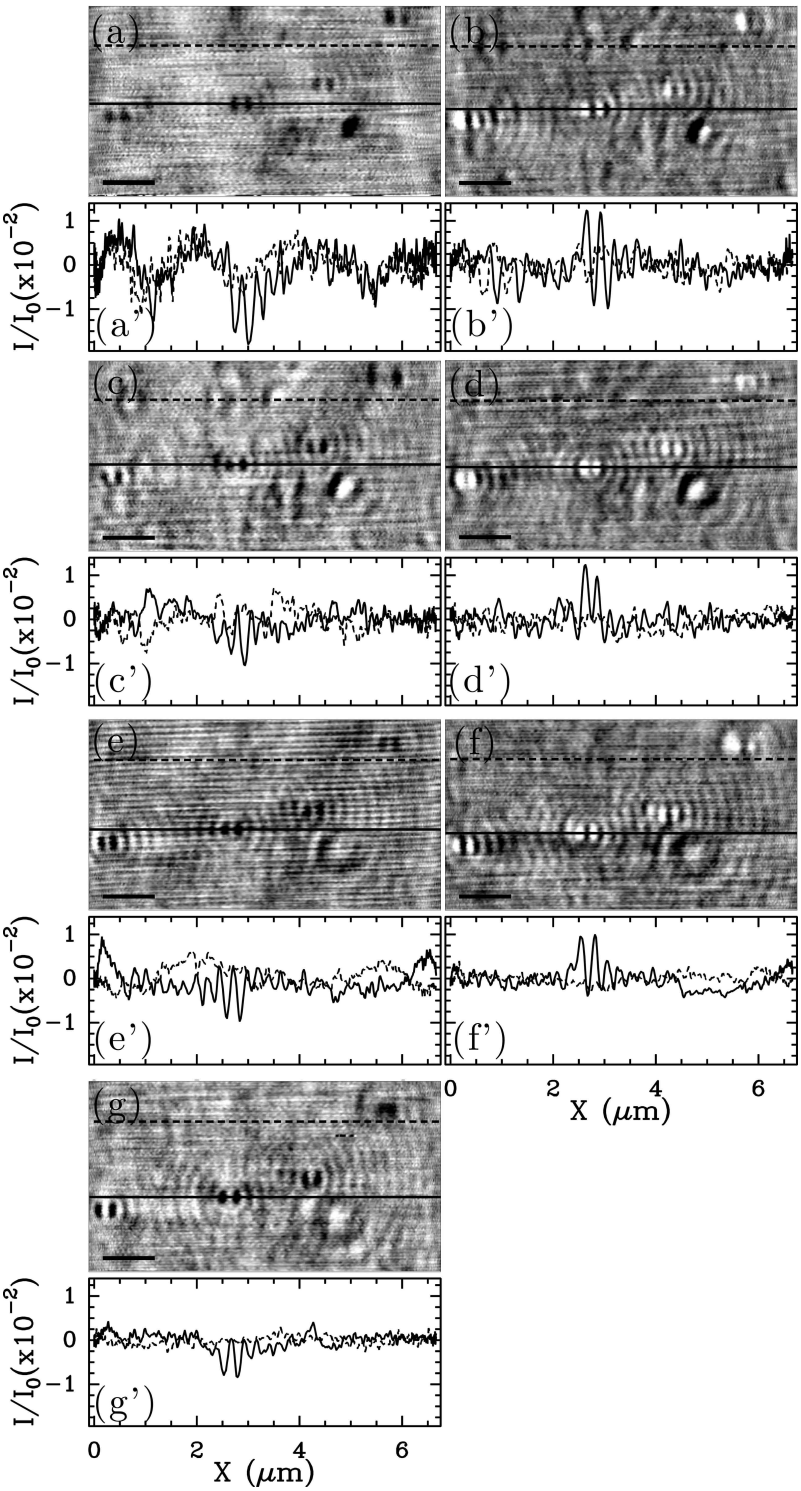

Figure 3.14 SSPM images and cross-sections of a 30 nm gold NP in water for different defocalization values (linear polarization): (a) and (a') $Z = 0.00$ μm, (b) and (b') $Z = 0.33$ μm, (c) and (c') $Z = 0.50$ μm, (d) and (d') $Z = 0.77$ μm, (e) and (e') $Z = 1.00$ μm, (f) and (f') $Z = 1.23$ μm, (g) and (g') $Z = 1.50$ μm. Plain (resp. dashed) line on the images correspond to the plain (resp. dashed) line in the cross-sections below. Scale bars are 1 μm.

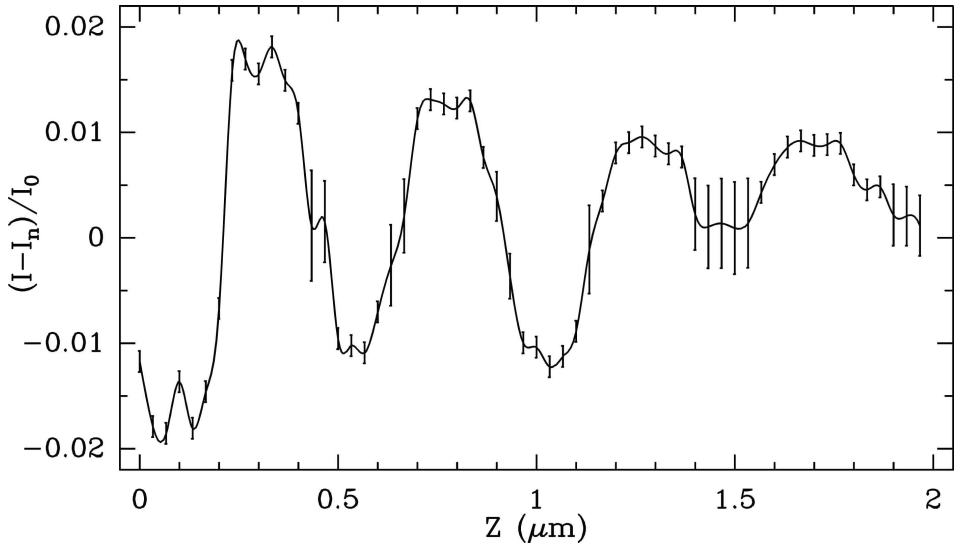

Figure 3.15 Contrast of a 30 nm gold NP, imaged in water and for a linear polarization, with respect to the defocalization of the objective lens. The contrasts have been computed by averaging over 4 calibrated NPs.

200 nm (see Figure 3.6), the two lobes are no longer separated and their intensities overlap, consistently with our estimation of the PSF width. Moreover, going from air to water, the PSF width decreases by a factor 2/3, independently from the nature of the NPs.
In addition to that, we have seen that changing the type of material (and in consequence its dielectric index) does not change radically the contrast of the NPs when they are observed in water ($\sim 1\ 10^{-2}$ for the positive contrast, and $\sim -1\ 10^{-2}$ for the negative contrast). The same way as for SSPM imaging in air (see Section A.3), this may seem surprising, since the variation of the dielectric permittivity between the observation medium ($\epsilon_d = 1.77$) and the latex NP ($\epsilon_{NP} \sim 2.56$) lying at the surface is lower than for a gold NP ($\epsilon_{NP} = -12.8 + j1.36$). Once again, we believe that the surface roughness plays a major role in the enhancement of the NP response, even when they are dielectric. On the other hand, we saw from Equation 1.13 in Section A.2.2 that the penetration depth $\delta_{z,d}$ in water is smaller ($\sim$ 190 nm) than in air ($\sim$ 350 nm). We also note that since the coupling configuration ($n_c \sim 1.78$) is changed for imaging in water, and in particular the the objective lens (which NA goes from 1.45 to 1.65 and thus focalizes more the light), the lateral distribution of the evanescent field at the interface is likely to be modified. Therefore, the amplification of the EM field is probably stronger at the interface, which might also explain this little difference in the NPs contrast between air and water imaging.
Finally, we want to emphasize that the SSPM apparatus can detect and image in water nanomaterials made of polymers (latex), which dielectric index is very close to the one expected for biological samples ($n_{biol\ samp}$ ~1.6-1.7). In consequence, this observation strongly suggests that this technique is also able to image biological samples in aqueous medium.

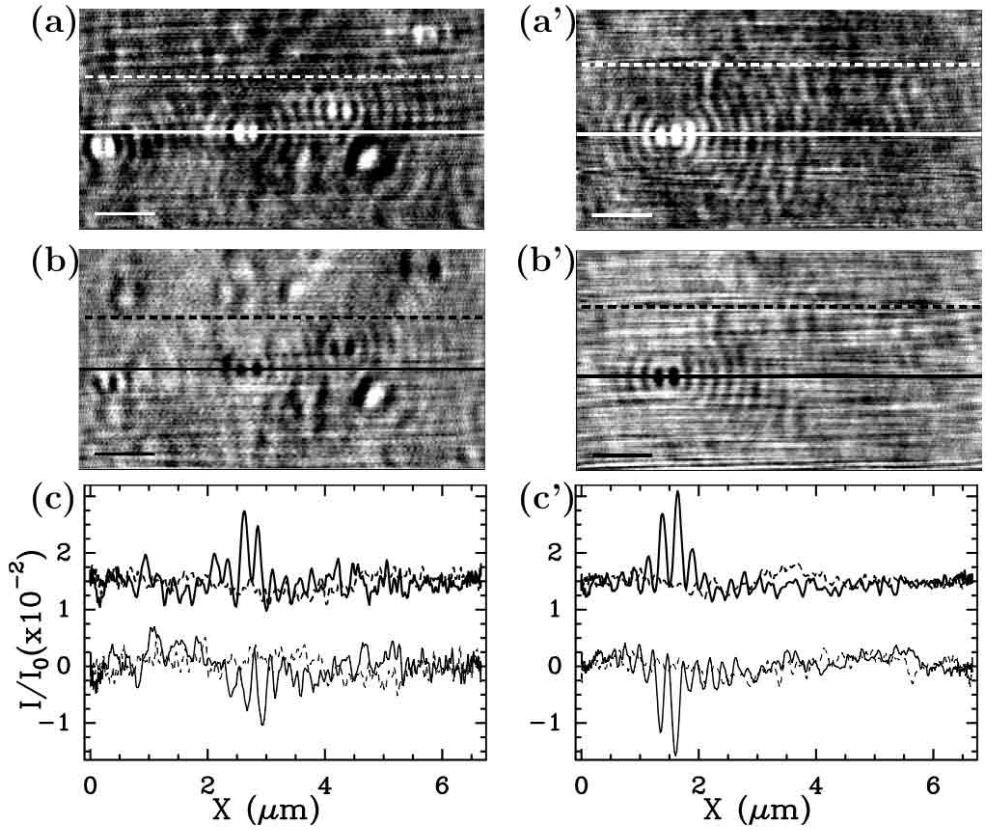

Figure 3.16 SSPM images of calibrated NPs in water for a linear polarization. (a-c) 30 nm gold NP. (a) $Z = 1.270$ μm (b) $Z = 1.100$ μm. (a'-c') 30 nm latex NP. (a') $Z = 0.767$ μm. (b) $Z = 0.500$ μm. White (resp. black) section lines in (a) and (a') (resp. (b) and (b')) correspond to thick (resp. thin) curves in (c) and (c'). Scale bar is 1 μm. Intensity profiles corresponding to positive contrast in (a) and (a') have been artificially shifted upward in (c) and (c').

C SSPM images of NPs in radial polarization

As explained in Chapter 1, Sections C.1 and D.3, the polarization of the light used to excite the SPPs plays a major role in the SPR excitation and consequently in the SSPM imaging technique. In the previous sections, the PSF of the apparatus consisted in a two lobe shape which direction is ruled by that of the linear polarization of the laser beam[65,79]. In a linear polarization configuration, only a part of the incident light participates to the creation of the surface plasmon waves since the electric field is not in the plane of incidence for all rays (see Chapter 1, Sections C.1 and D.3). To overcome this problem, Zhan[86] proposed theoretically an improvement by using a radially polarized beam. The consequence of illuminating the whole surface with a purely P-polarized light is that the evanescent beam presents a Bessel like pattern that is used as a virtual probe to image surfaces.[74,78,141] In this section, we give the experimental $I(Z)/I_0$ curves of bare gold in air for a radial or an azimuthal polarization of light, and present the influence of such polarizations on the images of a 50 nm latex NP. Finally, the evolution of the contrast of a 30 nm gold NP is presented as function of the

defocalization value.

C.1 Radial and azimuthal polarizations

C.1.1 I(z)/I_0 curves

We compare in Figure 3.17 the theoretical (a) and experimental (b) I(Z)/I_0 curves of bare gold surface in air and for radial and azimuthal polarizations. The theoretical curves in (a) have been computed with the mean field model, and the set of parameters used here is: $\epsilon_m = \epsilon_{NP} = -12.8 + j1.36$, $\epsilon_d = 1$, and $n_c = 1.515$ (1.45 objective lens).

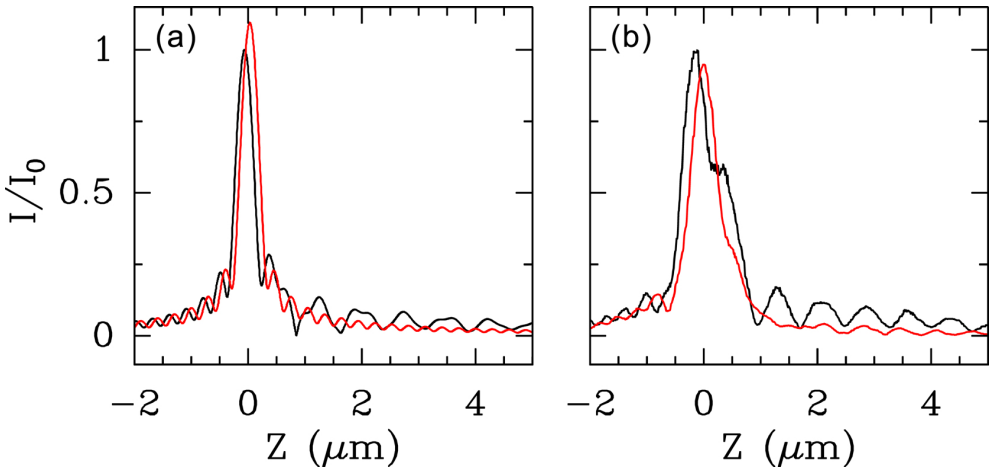

Figure 3.17 (a) theoretical and (b) experimental I(z)/I_0 curves for a bare gold film in air using a radially (plain line) or azimuthally (dashed line) polarized light. Computation done from Equations 1.25 and 1.26, and by using the Fresnel equations (see Chapter 1, Section C.4.2)

First of all, we observe from this figure that both theoretically and experimentally, the I(Z)/I_0 curves corresponding to radial or azimuthal polarizations are not the same: as explained previously in Chapter 1, Section C.4 the oscillations for $Z > 0$ corresponding to the presence of SPPs only appear when the light is p-polarized, that is for radial polarization in Figure 3.17. However, the azimuthal experimental I(Z)/I_0 curve still presents some very small SPPs oscillations that are mainly due the finite size of the beam waist when it enters the back side of the objective lens[79]. We determine from these curves that the theoretical and experimental oscillations present a periodicity which is the same: ΔZ =0.78 μm and ΔZ =0.77±0.035 μm respectively.

We can also notice that the maximum of the I(Z)/I_0 curves for radial and azimuthal polarization are not at the same defocalization value Z for both the theoretical and experimental data. This shift is slightly more important for the experimental curves (170 nm ±50 nm as compared to 100 nm), and its existence can be understood as being due to a difference in the optical path of the light when it is radially or azimuthally polarized (mainly because the total internal reflection of the light[68] at the interface and the excitation of SPPs induce an extra phase shifts).

Finally, by comparing the I(Z)/I_0 curves acquired for a linear polarization (Figures 3.1 and

3.7) with those done for a purely p-polarized light (Figure 3.17(b)) we see that as expected (since the observation medium and conditions of excitation of the SPPs at the interface are unchanged), the period of the oscillations is the same: $\Delta z \sim 0.78$ μm (see Chapter 1, Section C.4, were Equation 1.27 is valid for linear and radial polarizations).

C.1.2 SSPM images of a 50 nm latex NP for a linear or a radial polarization

Figure 3.18 illustrates the consequences of switching the polarization from linear to radial: the same 50 nm latex NP was imaged in air, for a linear (horizontal) polarization (left) and a radial polarization (right).

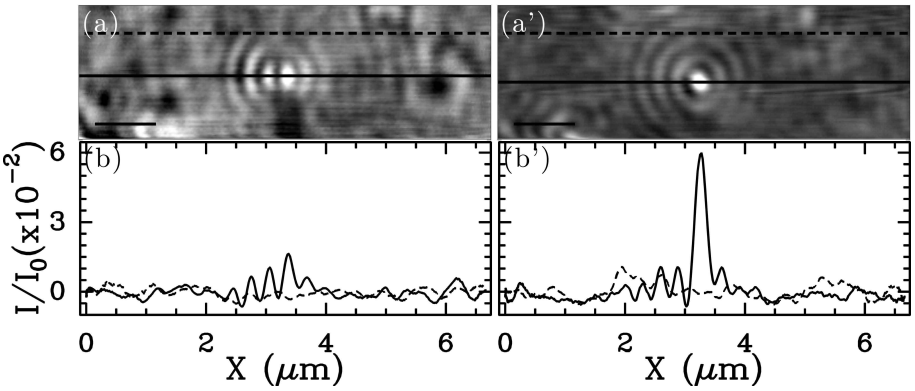

Figure 3.18 SSPM images and cross-sections of the same aggregate of 50 nm latex NPs in air, for (a) and (b) a linear or (a') and (b') a radial polarization, and for a defocalization value of $Z = 0.85$ μm and $Z = 0.90$ μm respectively.

We notice that as expected from Chapter 1, Sections C.1 and D.3, the two lobe structure (Figure 3.18(a)) of the PSF is converted into a single peak (Figure 3.18(a')) with a FWHM of 220±10 nm in air. In consequence, we expect the lateral resolution of the SSPM apparatus to be improved when using a radially polarized light. Moreover, as shown from the cross-sections (b) and (b'), the contrast of the nanoobject is increased by a factor ∼3.6 when going from a linear to a radial polarization. This enhancement of the contrast can be explained by two factors: (i) the surface plasmon waves have a radial symmetry (contrary to the linear polarization for which the SPPs are only excited on two crescents along its direction), and in consequence, the EM field at the interface is expected to increase by a factor close to 2, which improves the sensitivity of the apparatus to local modifications of the dielectric index, (ii) to explain the 3.6 factor, a more quantitative computation is necessary; as said previously, the E_Z component of the electric field is the major contributor to the the excitation of the SPP waves[1,65,78], and the radial symmetry of the polarization of the incoming light enhances the plasmon localization even further than in linear polarization (see Figure 1.26).

We present in Figure 3.19 the effect of switching the polarization from radial in (a) and (b) to azimuthal in (a') and (b').

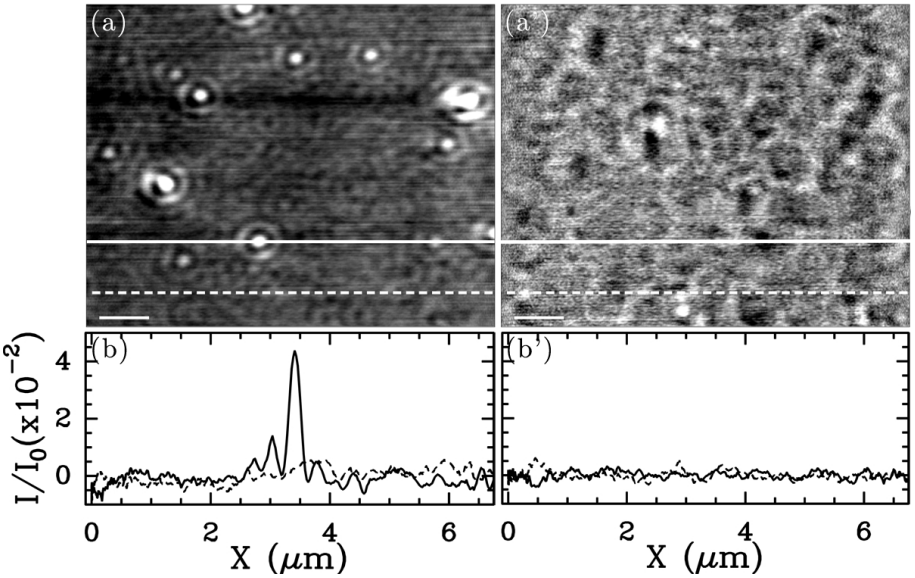

Figure 3.19 SSPM images and cross-sections of the same 50 nm latex NP in air, for (a) and (b) a radial or (a') and (b') an azimuthal polarization, and for a defocalization value of $Z = 0.90$ μm for both.

This figure illustrates perfectly that this is thanks to the variation of the SPPs excitation that nanoobjects can be observed at the gold surface: when light is purely s-polarized, no plasmon waves are excited, and then nothing can be detected. Therefore, we see that even if small oscillations are still present at $Z > 0$ for the red $I(Z)/I_0$ curve in Figure 3.17(b), the polarization of the incident light is nevertheless well tuned.

C.2 SSPM images of 30 nm gold NPs illuminated in air by a radially polarized light

We present in Figure 3.20 SSPM images and cross-sections of 30 nm gold NPs for different values of defocalization and for a radial polarization. Note that thanks to its FWHM and maximum of contrast, the spot situated at the bottom of the image has been identified to be an aggregate of several NPs.

We see from this figure that the same way as with a linear polarization, the contrast of the NP changes with the defocalization. However, the first maximum of the contrast versus Z curves occurs for smaller $Z \sim 0.4$ μm value. We note also that for this defocalization value, the lateral waves around the central spot are strongly damped. We also believe that because the symmetry of the exciting field is the same as the particle, there is a stronger interplay between the delocalized SPPs of the gold film and the scattered field of the NP.

We present in Figure 3.21 the contrast $(I_0\text{-}I_n)/I_0$ of a 30 nm gold NP imaged in air as function of the defocalization Z and for either a linear (dashed line) or a radial (plain line)

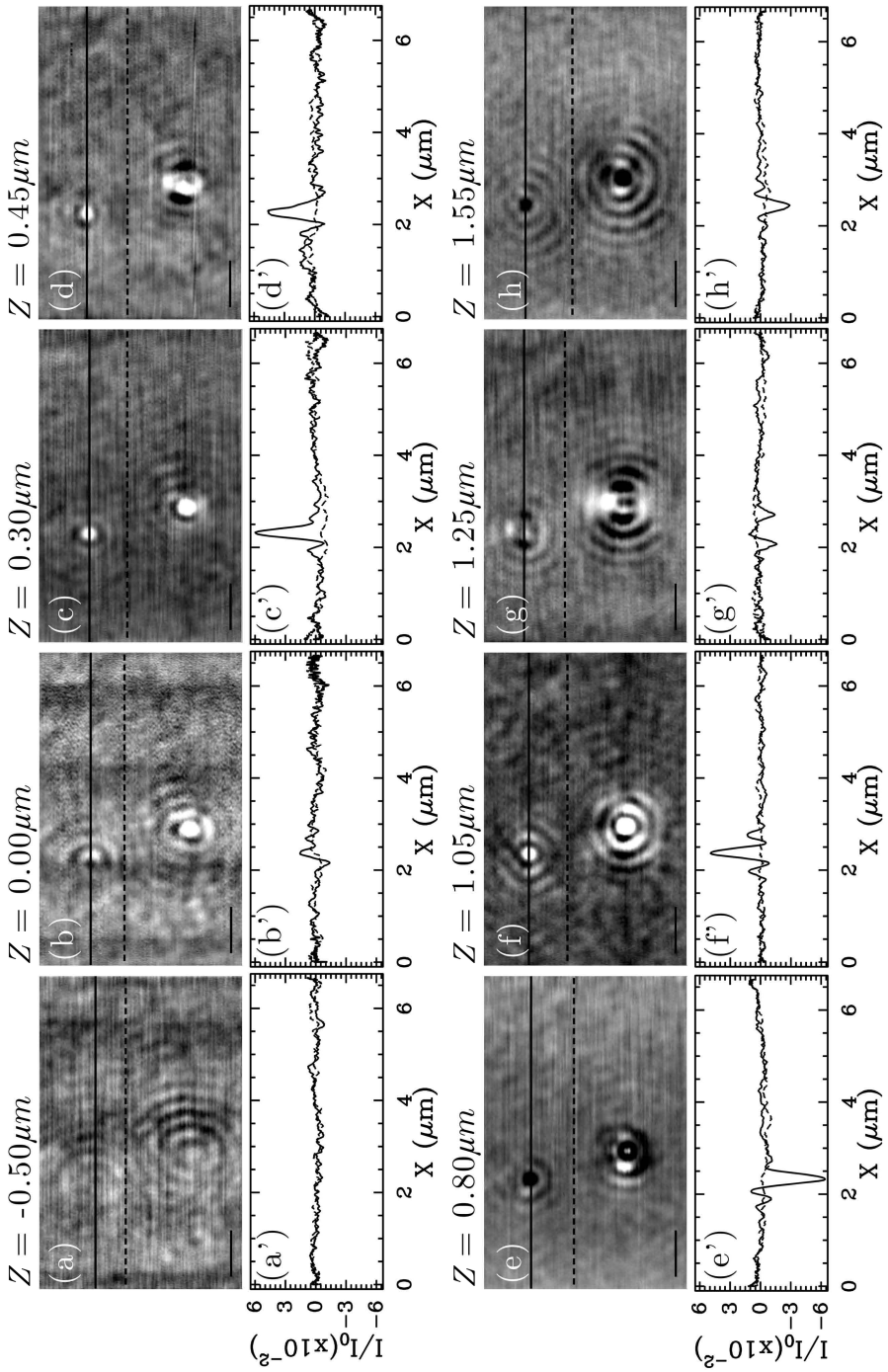

Figure 3.20 SSPM images and cross-sections of 30 nm gold NPs in air for different defocalization values and a radial polarization: (a) and (a') $Z = -0.50$ μm, (b) and (b') $Z = 0.00$ μm, (c) and (c') $Z = 0.30$ μm, (d) and (d') $Z = 0.45$ μm, (e) and (e') $Z = 0.80$ μm, (f) and (f') $Z = 1.05$ μm, (g) and (g') $Z = 1.25$ μm, (h) and (h') $Z = 1.55$ μm. Plain (resp. dashed) line on the images correspond to the plain (resp. dashed) line in the cross-sections below. Scale bars are 1 μm. The color coding of the images is different, but the dynamics of the cross-sections is fixed.

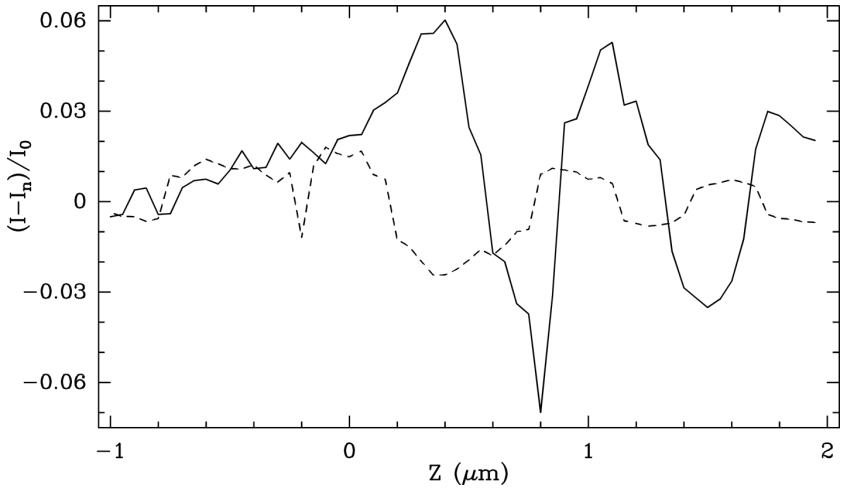

Figure 3.21 Contrast $(I_0\text{-}I_n)/I_0$ of the same 30 nm gold NP (corresponding to the NP imaged in Figure 3.20) in air imaged for a linear (dashed line) or a radial (plain line) polarization, with respect to the defocalization Z of the objective.

polarization. The computation of these curves have been done from a set of 60 images, treated the same way as as those of in Figures 3.10(a) and 3.15.

We confirm here that the evolution of the contrast for the same NP is not exactly the same when it is illuminated by a linearly or a purely polarized light. Indeed, even if the estimation of the oscillations period is compatible (0.65±0.07 μm and 0.7±0.07 μm for the linear and radial polarizations respectively), the position of the first maximum of contrast does not occur at the same defocalization value: 0.40±0.05 μm and 1.075±0.05 μm, for a linearly or a radially polarized beam respectively. We interpret this shift as being due partly to the presence of s-polarized light in the case of an illumination with a linear polarization (see Section C.1.1), since this shift depends strongly on the polarization, a mixture of S and P polarization will give a different result than the pure p-polarization obtained with the radial symmetry.

C.3 SSPM images of a 30 nm gold NP illuminated in water by a radially polarized light

We present in Figure 3.22 the SSPM images of the same 30 nm gold NP, illuminated by a radially polarized light, and when the observation medium is water.

Several observations can be made from these images. First of all, the 30 nm gold NPs are still detected in water and for a radial polarization. However, even if their contrast is of the same order of magnitude than in air ($\sim 10^{-2}$), they are about twice to three-fold less contrasted (see Section C.2, Figures 3.20 and 3.21): $\sim 210^{-2}$ in water and $\sim 410^{-2}$ in air for the maximum of positive contrast, and $\sim -210^{-2}$ in water and $\sim -610^{-2}$ in air for the minimum of negative contrast. Moreover, we notice that the contrast of the NPs oscillates quicker in water than in

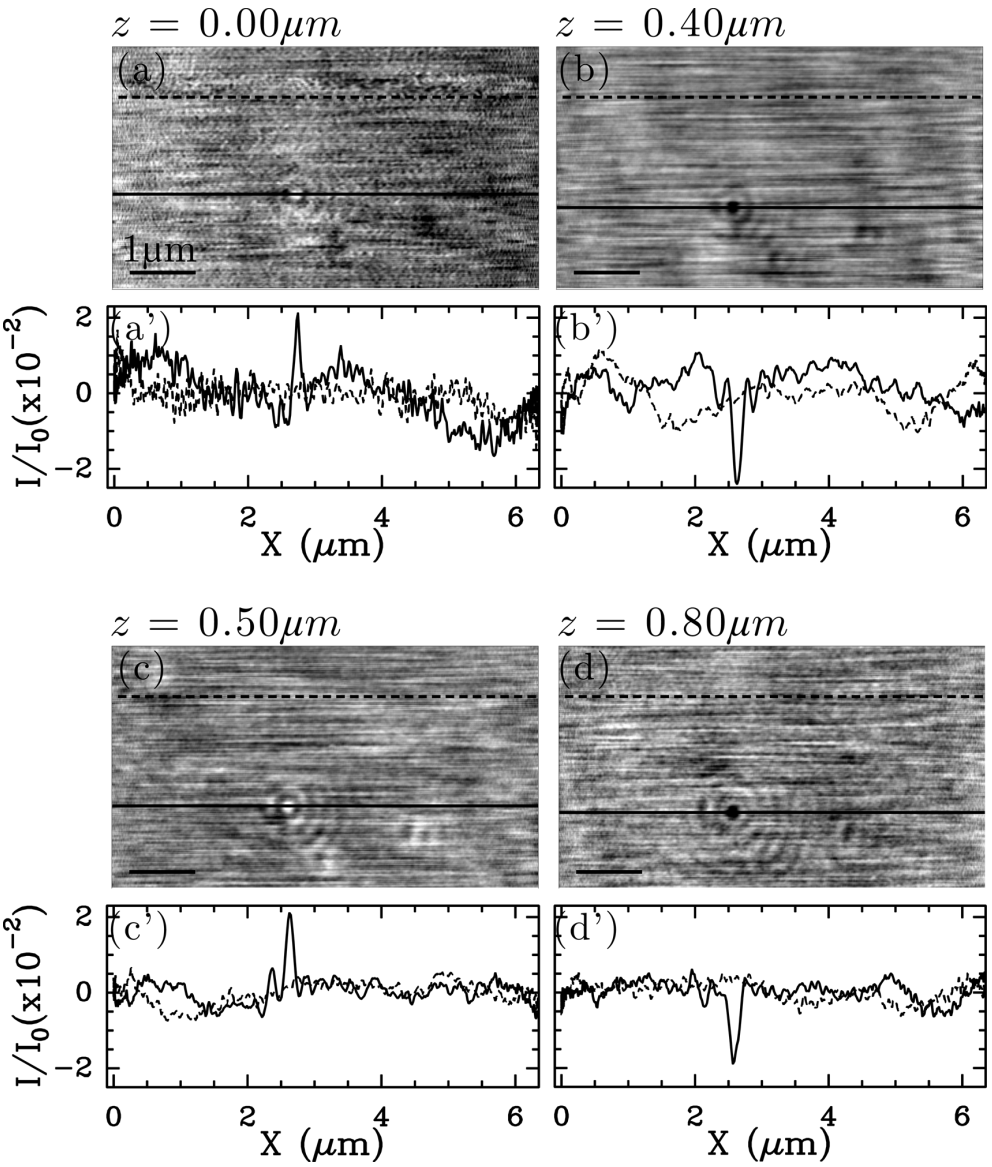

Figure 3.22 SSPM images and cross-sections of a 30 nm gold NP in water for different defocalization values and a radial polarization: (a) and (a') $Z = 0.00$ μm, (b) and (b') $Z = 0.40$ μm, (c) and (c') $Z = 0.50$ μm, (d) and (d') $Z = 0.80$ μm. Plain (resp. dashed) line on the images correspond to the plain (resp. dashed) line in the cross-sections below. Scale bars are 1 μm. The color coding of the images is different, but the dynamics of the cross-sections is fixed.

air, which is in good agreement with what was observed for a linear polarization (see Section B.2, Figure 3.15). Finally, the PSF of the microscope can be determined from the FWHM of the NPs, and more particularly from the cross-sections of the NPs in (a') to (d'), that it is 110 ± 20 nm.

In conclusion, we have seen in this section that using a radial polarization to illuminate the samples is a good way to improve not only the resolution, but also the image contrast by a factor about 3.6 (see Figure 3.18). In consequence, the sensitivity of the SSPM apparatus is also increased, in such a way that we should be able to detect even smaller variations of the local dielectric index (as seen in Chapter 2, Section B.5 about the surface roughness variations). Moreover, we have observed that imaging a quasi-punctual object (a 30 nm gold NP), in water and for a radial polarization, has allowed us to determine that the PSF of the SSPM set-up has shrinked to about 110 nm in these conditions. This last point is particularly interesting since it suggests we should be able to visualize biological samples in an aqueous medium with a higher resolution than what will be obtained in air.

C.4 Perspectives

In this section, we present some perspectives for future studies on nanomaterials with the SSPM apparatus. These perspectives are based on several clues that either our experiments or modeling provided.

C.4.1 Variation of the gold layer thickness and restriction of the incident angles to a small window around the angle of resonance

As already mentioned in Section A.3, we have seen[80] that the thickness of the gold film influences the SPR excitation and therefore changes the global contrast of the NPs (for a fixed defocalization value). We present in Figure 3.23 the contrast as predicted by the 3D--ME model, of a 20 nm NP made either of (a) gold ($\epsilon_{NP} = -12.8 + j1.36$) or (b) latex ($n_{NP} = 2.56$) and separated from the gold film by 1 nm. Note that the computations have been done for the whole set of incident angles (dashed lines, $0° < \theta < 60°$), or restricted to angles close to the angle of resonance (plain lines, $40° < \theta < 50°$). It has to be noted that the absolute value of the contrast presented here is less important than its evolution with respect to the film thickness.

This figure illustrates well the influence of the gold thickness on the contrast of the nanomaterials. Indeed, the optimal values of contrast for gold and dielectric NPs are predicted for thinner layers than those corresponding to the minimum of the SPR curves ($\sim 48\ nm$ in air). Typically, we observe a gain in contrast by a factor ~ 2 when going from 45 nm to $\sim$ 20-25 nm thickness for the gold film (for the whole set of incident angles).

Moreover, we observe from the plain lines in Figure 3.23 that decreasing the amount of incident light illuminating the surface to a small window around the angle of resonance ($40°$ $< \theta < 50°$) improves the contrast of the particle. All these evidences suggest that the metal film should be thinner ($\sim$30 nm) than what was used during the experiments shown in this chapter ($\sim$45 nm); an optimum thickness should therefore be $\sim$ 20-30 nm. Confining the incident rays around the SPR resonance angle ($40° < \theta < 50°$) leads also to an increase of the NP contrast in the case of the latex colloid. However, it is the opposite for the gold NP, and we believe this can be caused by variations in the energy transfers between the surface and the NP.

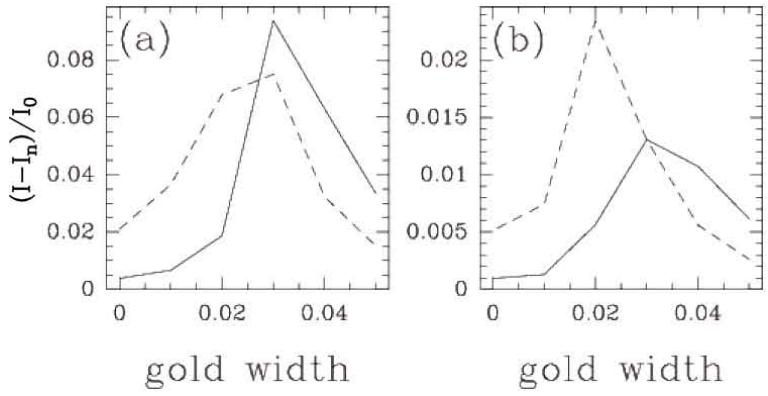

Figure 3.23 Contrast of a (a) gold or (b) latex 20 nm NP adsorbed at the surface of a metal layer as function of its thickness, for a radial polarization. Plain lines (resp. dashed lines) are such that the incoming rays are limited to $40° < \theta < 50°$ (resp. $0° < \theta < 60°$). The dielectric index of the latex and gold NP used in the 3D-ME model are $\epsilon_{NP} = 2.7$ and $-12.8 + j1.36$. Figure extracted from Elezgaray *et al.*[80]. The computation was done using the multipolar expansion model presented in Chapter 1, Section D.

C.4.2 Surface roughness modelization

We have observed in the SSPM images of the bare gold surfaces in figures 2.10 and 2.24 (see Chapter 2) that the variations of the surface inhomogeneities lead to a dramatic change in the contrast of the speckle-like patterns. We confirm then here that this surface roughness induces local modifications of the evanescent field distribution at the interface,[43,44] and in particular the creation of "hot spots", where the image contrast of an adsorbed object may eventually be increased.

We believe that modeling this aspect is of great importance to understand more precisely the effect of the surface roughness on the visualization of samples, and especially synthetic nanomaterials and eventually biological systems. To do so, we propose to add to the flat gold film ($\sim$ 20 nm thick) an additional layer composed of randomly distributed spherical gold NPs or spherical gold caps of varying sizes (in such a way that the average thickness of the effective metal structure is $\sim$ 45 nm thick), as inspired from the mean field model used in Chapter 2, Section A.1.5.[54] First of all, we hope this model could account for the speckle-like effect we see when imaging the bare metal surfaces, and eventually help us understanding more precisely the physical processes ruling this phenomenon and the local enhancement of the EM field at the surface. On the other hand, we believe that adding a NP at different locations on the surface (at the top of a cluster, or in the groove between them) could serve as a local probe of the local field. This may also explain the dispersion of the NP contrast values that we observed experimentally and which was stronger than what was expected when considering the deviation in size of the calibrated NPs.

C.4.3 Normalization of the SSPM images, and estimation of the reference value Z_0

For all experiments presented in this thesis, the SSPM images have been normalized by the maximum value I_0 of the $I(Z)$ curves, that defined also the reference value $Z_0 = 0$. However, we believe that the contrast of the images can be improved by comparing the optical signal detected for a radial polarization (I_p) with the signal acquired for an azimuthally polarized light (I_s).

We actually want to take advantage of the sample scanning to detect first (trace) the radial optical signal, and then (retrace) the azimuthal signal. Thanks to these two signals, it is very likely that making the difference of $I(Z)$ values in s- and p- polarization for each pixel of the SSPM images could increase the sensitivity of the apparatus by improving the signal to noise ratio. In other words, we would like to keep only the information induced by the plasmon waves excitation, and decrease the noise due to the substrates (as well as eventually getting rid of the misalignement or planeity defaults of the coverslips). We believe that future work should focus on the computation of I_P/I_S or $(I_P\text{-}I_S)/(I_P+jI_S)$ to improve the normalization.

We also believe strongly that the problem of the determination of the reference value Z_0 should be dealt with, since this is a key point to the reproducibility of this technique when considering the imaging of uncalibrated samples such as biological systems.

C.4.4 SSPM imaging anisotropic nanomaterials

We saw in section C that switching from linear to radial polarization both increases the resolution and contrast of the images. It seems then likely that most of the SSPM users will tend to use the technique with a purely p-polarized light.

However, we believe that linear polarization may prove useful to study anisotropic nanomaterials. Indeed, we think that changing the direction of the linearly polarized light may help determining the orientation of such objects, even if they are smaller than the PSF of the apparatus (the contrast of the two lobes should be higher when the polarization coincides with the object anisotropy axis).

C.4.5 SSPM phase imaging

Finally, as explained in Chapter 1, Section C.4.1, besides using the amplitude of the detected optical signal, the SSPM set-up has been constructed to recover its phase counterpart. Hence, we would like to take advantage of this extra information to get more insights on the local variations of the dielectric index (the phase is more sensitive to its modification than the amplitude alone). Some figures presenting the SSPM phase images of biological samples (such as nucleosomes) can be found in the next chapter.

C.5 Conclusions

We have seen in this chapter that SSPM imaging is not only a good tool to detect and visualize in air or in liquid medium nanoobjects adsorbed at a metal surface, but is also potentially a powerful technique to discriminate between their size (even if their contrast tends to saturate for small diameters). We have observed that, no matter the observation medium, the contrast of the gold NPs is globally higher than that of latex NPs (for a given size), and also that the decrease in the intensity of the NP SSPM images is relatively low when changing the medium from air to water.

Moreover, by imaging the smallest NPs, we have shown that the PSF of the apparatus and the mean distance between the lobes depend on the medium of observation: respectively $\sim$220 nm and $\sim$350 nm in air and $\sim$150 nm and $\sim$230 nm in water.

In addition to this, we have confirmed that the contrast of the SSPM images oscillates with the defocalization of the objective lens, and that its period of oscillation is ruled by the observation and hence the coupling media (Δz_{air} $\sim$0.8 μm in air, and Δz_{water} $\sim$0.45 μm in water). Thanks to this study, we have demonstrated that the contrast of the NPs at a fixed defocalization value depends on their dielectric index, which gives the opportunity to differentiate them from the type of material they are made from.

We also demonstrated that a model relying on the multipolar expansion of the Maxwell equations (presented in Chapter 1, Section D) can account relatively accurately for the SSPM images of simple nanomaterials. Furthermore, we showed that switching the polarization of the light from linear to radial is a good way to improve the resolution, contrast and sensitivity of the SSPM apparatus. Finally, from a practical point of view, the results reported in this work demonstrate that SSPM is a very promising non intrusive optical technique for visualizing soft nanomaterials like polymers, gels, macromolecular objects and biological molecular assemblies, with no need of fluorescent probes as commonly used in classical microscopy techniques (such as Total Internal Reflection Fluorescence Microscopy, confocal microscopy, fluorescence PhotoActivation Localization Microscopy[142,143], Fluorescence Recovery After Photobleaching microscopy...).

Chapter 4

Application of SSPM to nucleosomes and cells imaging

We have seen in Chapter 3 that NPs made either of metal (gold), or a dielectric medium (latex) can be visualized at a metal (gold) surface with the SSPM apparatus. More precisely, we have demonstrated that such objects can be detected in air or in liquid and differentiated from their size or material. Moreover, we noted that changing the light polarization to radial is an effective way to enhance both the resolution and the sensitivity of the set-up.
In this chapter, we address the question of detecting and imaging biological samples without labeling, in air and with a radially polarized light. We show first SSPM amplitude and phase images of nucleoproteic complexes (nucleosomes), and in the last part we apply the SSPM system to the imaging of whole cells (IMR-90 and 293T lines).

A SSPM imaging of IL2RA nucleosomal particles

A.1 Introduction: the nucleosome structure

DeoxyriboNucleic acid (DNA) is a 2 nm thick molecule[144] that contains the genetic information used in the development and functioning of all organisms. Figure 4.1 presents a schematic view of the DNA molecule, which length and composition varies with the species considered. This molecule is structured as a double-helix composed of two complementary strands that consist in a sugar phosphate backbone on the outside and a sequence of base pairs from a set of four possibilities (adenine Ö.) on the inside, stabilizing the whole structure *via* hydrogen bonds. It is actually the sequence of these base pairs that codes for the proteins.
To fit inside a nucleus of $\sim$10 μm in diameter (see Figure 4.11 for a sketch of the structures and organelles of a typical eukaryotic cell), human DNA ($\sim$2 m long) is highly compacted. Figure 4.2 shows the levels of this compaction, from the naked DNA helix to the well-known mitotic chromosome. Even if several structures can be found on intermediate length scales, we focus in this chapter on the nucleosome (see Figure 4.3), a cylindrical nucleo-proteic complex

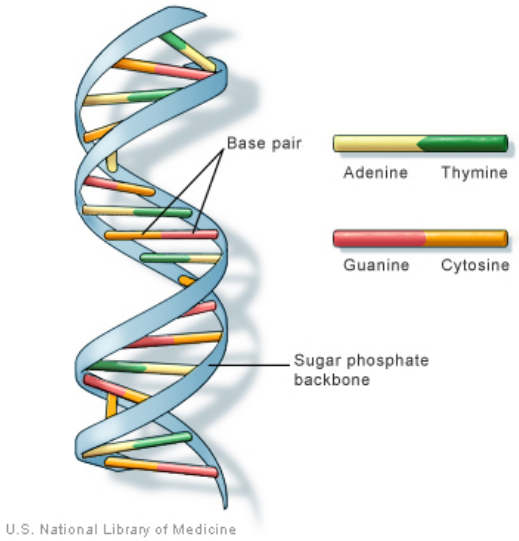

Figure 4.1 Sketch of a DNA molecule.

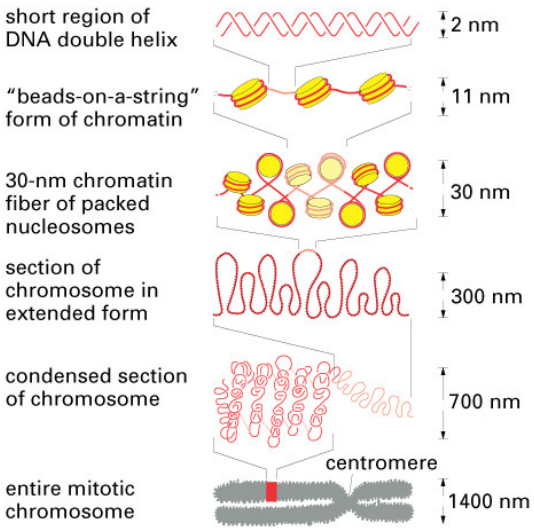

Figure 4.2 Levels of DNA compaction in eucaryotic cells, from the naked molecule to the mitotic chromosome.

whose size is about 11 nm in diameter and 5 nm in width. This biological particle consists of 8 positively charged core proteins called histones[145] (2×[H3, H4, H2A, H2B]), around which the negatively charged ds-DNA molecule is stabilized by forming about two loops (147 base pairs (bp)).

In this section, we address the question of imaging nucleosomes at the surface of the gold film with the SSPM apparatus. Such samples were reconstituted *in vitro* from 898 bp (∼300 nm long if straight) IL2RA sequences[147] (see Figure 4.4 for an AFM illustration of the nucleosomes, and Appendix A, Section E for the reconstitution protocol).

Figure 4.3 Crystal structure of the nucleosome core particle. The DNA strands are presented by the brown and turquoise ribbon structures surrounding the eight histone proteins (blue: H3; green: H4; yellow: H2A; red: H2B). The views are down the DNA superhelix axis for the left particle and perpendicular to it for the right particle. Figure extracted from Lüger *et al.*[146].

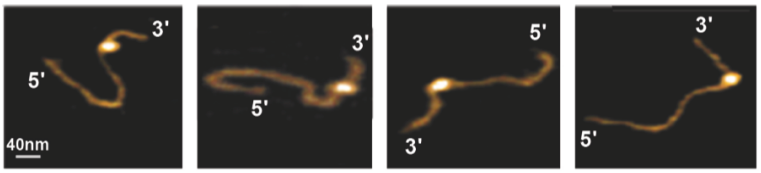

Figure 4.4 AFM images in liquid of IL2RA nucleosomes adsorbed on a freshly cleaved mica surface. Figure extracted and modified from Milani *et al.*[147].

A.2 Amplitude images

A.2.1 From latex NPs to nucleosomes

Figure 4.5 presents SSPM images and corresponding cross-sections of IL2RA nucleosomes (right panel) adsorbed at the metal/air interface, and 50 nm latex NPs (left panel) as a reference. The first remark we can make from Figure 4.5(b) is that we detect nucleosomes at the metal surface. This point is very important since it validates the technique for detecting and imaging biological samples with no need for labeling.

When comparing (a) and (b), we observe that the contrast values of the 50 nm latex NP and the nucleosomes are relatively close: $\sim 4.4\ 10^{-2}$ and $\sim 6.3\ 10^{-2}$ respectively, for values of defocalization ($Z = 0.90\ \mu$m and $Z = 0.45\ \mu$m respectively) corresponding to the first maximum of contrast for each nanomaterial (data not shown here for the 50 nm latex NP, see Figure 4.7 for the nucleosome). However, the DNA strands projecting out of the nucleosome ($\sim$ 750 bp) are likely to counterbalance the fact that the core particle is smaller than the 50 nm NP: indeed, the nucleosome (*i.e.* all histones plus 147 bp of DNA) amounts for $\sim$260 kDa,[148] whereas the extra DNA corresponds to $\sim$500 kDa (750$\times$0.66 kDa), therefore multiplying the overall mass by a factor three. On the other side, the FWHM of the image of the nucleosome is almost the same as that of the NP: $\sim$ 240 nm and $\sim$ 220 nm respectively.

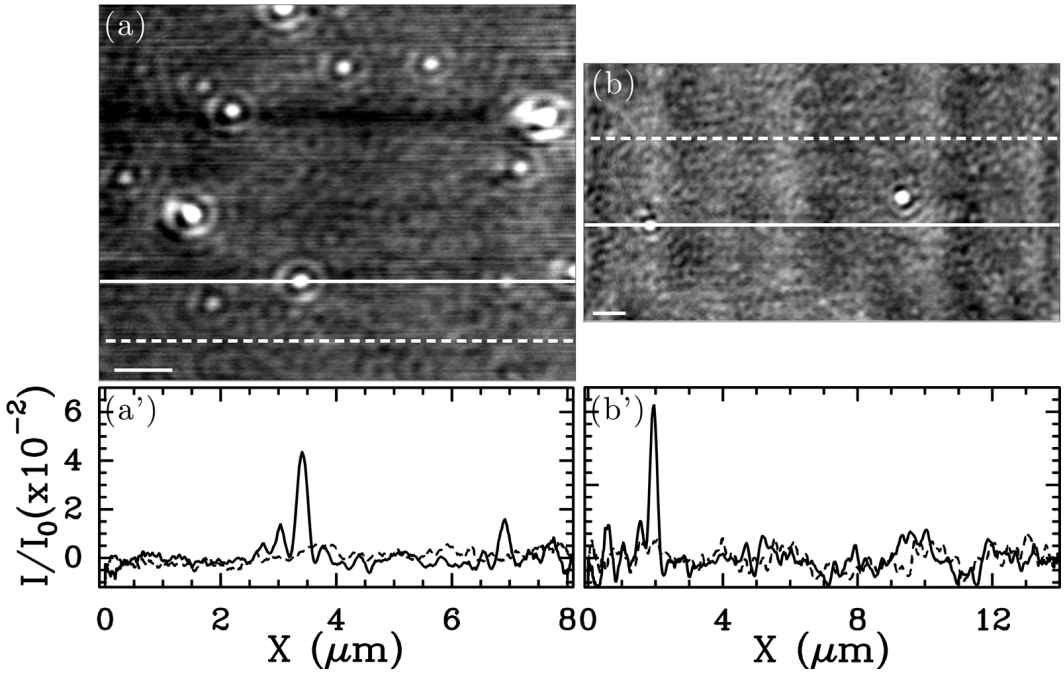

Figure 4.5 SSPM amplitude images in air of (a) 50 nm latex NPs and (b) IL2RA nucleosomes dispersed on the gold surface for a defocalization value of $Z = 0.90$ μm and $Z = 0.45$ μm respectively, and a radial polarization. (a') and (b'): cross-sections of (a) and (b). Scale bars are 1 μm. Images are filtered with a 3×3 pixel sliding box, and flattened with a O^{th} order polynomial.

A.2.2 Nucleosome image contrast versus the defocalization Z

In this section, we present the SSPM images of the same nucleosome for increasing defocalization values. Similarly to the metal or latex NPs (see Chapter 3), we observe that the contrast of the nucleosome varies with Z: nothing can be seen for $Z < 0$, whereas the contrast goes from positive to negative when $Z > 0$. We note however that contrary to what is seen for the latex NPs imaged in radial polarization (see Chapter 3), the contrast is almost never positive when $Z > 0.5$ μm. Figure 4.7 shows the evolution of the nucleosome image contrast (computed as explained in Chapter 3, Section A.2.1), after averaging over 5 of them.

The same way as for the 50 nm latex NPs, we observe that the contrast of the nucleosomes oscillates with Z: it is minimum (resp. maximum) at $Z = 0$ (resp. $Z = 0.45$ μm), and goes on with a period of ~ 0.9 μm. The minimum (resp. maximum) value of contrast is (-3 ± 1) 10^{-2} (resp. (3 ± 1) 10^{-2}). On the other hand, we observe that the first maximum value is higher in the case of the NPs, (5 ± 1) 10^{-2} , and that the oscillations are shifted by $\sim$ 500 nm, which suggests that the dielectric indices of the nucleosomes and latex NPs are different (see Chapter 1, Section C.4). However, we expect both the contrast and the FWHM of the biological samples to increase with the length of the DNA molecule.

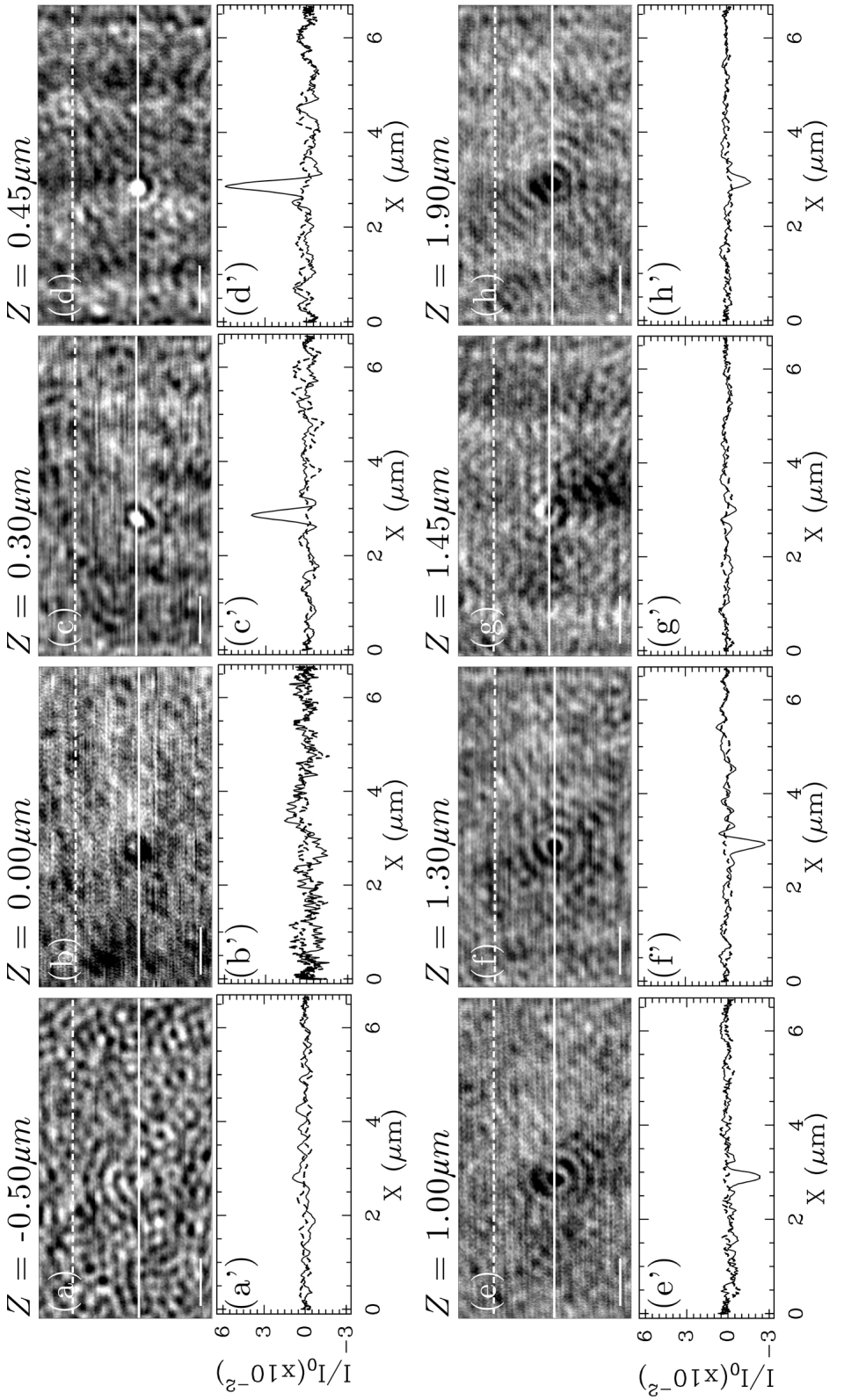

Figure 4.6 SSPM amplitude images in air and cross-sections of the same IL2RA nucleosome for various defocalization values: (a) and (a') $Z = -0.50$ μm, (b) and (b') $Z = 0.00$ μm, (c) and (c') $Z = 0.30$ μm, (d) and (d') $Z = 0.45$ μm, (e) and (e') $Z = 1.00$ μm, (f) and (f') $Z = 1.30$ μm, (g) and (g') $Z = 1.45$ μm, (h) and (h') $Z = 1.90$ μm. Images acquired for a radially polarized light. White plain and dashed lines on the images correspond to the cross-sections below (respectively in plain and dashed line). Scale bars are 1 μm. Images are filtered with a 3×3 pixel sliding box, and flattened with a O^{th} order polynomial.

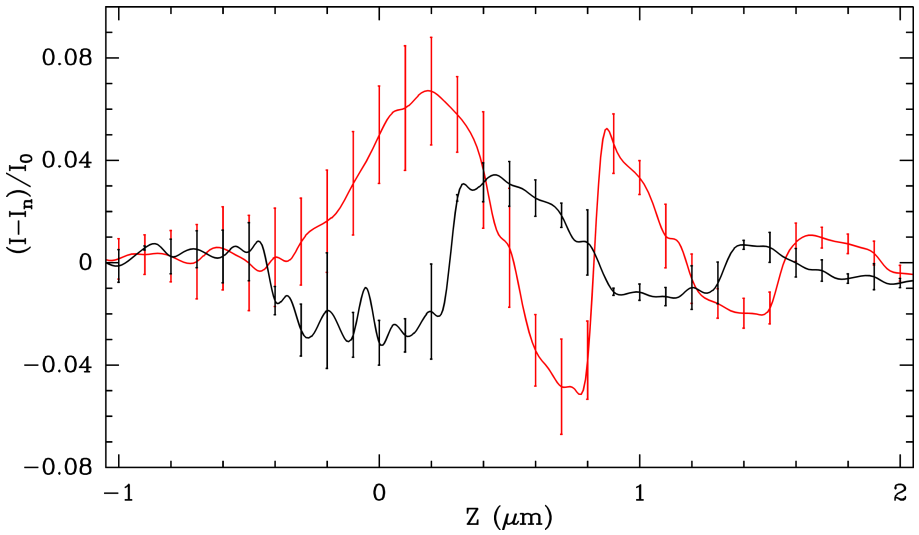

Figure 4.7 Mean amplitude contrast of IL2RA nucleosomes (black curve) and 50 nm latex NP (red curve) with respect to the defocalization of the objective lens. The contrasts have been computed by averaging the amplitude of the optical signals over 5 nucleosomes. The errorbars correspond to the mean square deviation of the set.

A.3 Phase images

A.3.1 From the I(Z)/I$_0$ curves to the variations in the phase contrast

We saw in Chapter 1, Section C.4.1 that the optical response of the SSPM apparatus for a fixed (X,Y) lateral direction is given by $V(Z)$, see Equation 1.25. Thanks to the heterodyne interferometer, it is possible to detect both the real and imaginary parts of the $V(Z)$ signal: $Re[V(Z)]$ and $Im[V(Z)]$ respectively. In the previous chapters we focused on the amplitude $I(Z) = |V(Z)| = \sqrt{Re[V(Z)]^2 \pm Im[V(Z)]^2}$ of the optical response, but it is also possible to look at its phase counterpart $\phi(Z) = \arctan\left(Im[V(Z)]/Re[V(Z)]\right)$. Therefore, we present in Figure 4.8 the theoretical $I(Z)/I_0$ curve (black line), and the corresponding real (red line) and imaginary (blue line) parts of the $V(Z)$ signal (normalized by I_0), for a bare gold film ($\epsilon_m = -12.8 + j1.36$; plain lines), or with an extra 5 nm thick layer of lipids ($\epsilon_d = 2.56$; dashed lines). (b) shows a zoomed view of (a).

The black curves (that is I(Z)/I$_0$) in Figures (a), and more particularly (b) confirm that the amplitude contrast is changed by the presence at the interface of an additional layer of lipid (see Chapter 1, Section C.5). Now, we observe from the real (red) and imaginary (blue) curves that they are modified as well by the 5 nm thick layer of lipids, and as a consequence, so will the phase $\phi(Z) = \arctan\left(Im[V(Z)]/Re[V(Z)]\right)$. Therefore, it is possible to reconstruct a phase contrast map of the samples by scanning laterally the substrates, and by computing $\arctan\left(Im[V(Z)]/Re[V(Z)]\right)$. It has to be noted that the computation of the theoretical $\phi(Z)$ curves is not straightforward since the real and imaginary parts of the optical signal do not oscillate like simple cosine functions (see Figure 4.8(b)). A deeper analysis of $Re[V(Z)/I_0]$ and $Im[V(Z)/I_0]$ shows subharmonic modulations of the oscillations introduced by SPR, that are currently under investigation in collaboration with J. Elezgaray (see Chapter 1, Section D).

As a conclusion, in the same way as for the amplitude $I(Z)$, the phase signal will be modified accordingly to the variations of the local dielectric index when scanning the sample for a fixed

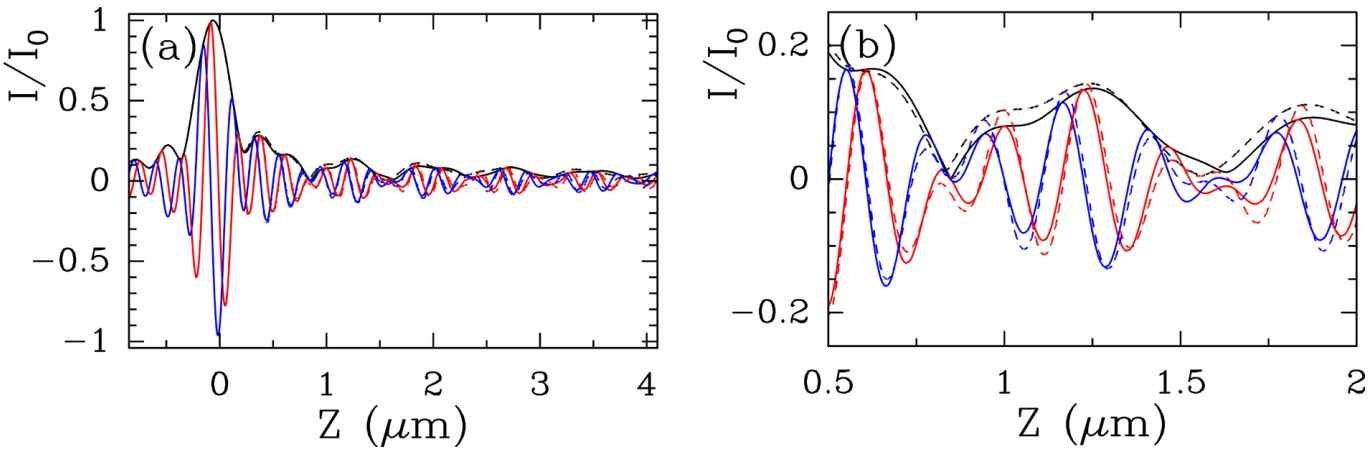

Figure 4.8 Theoretical SSPM optical response in air computed from Equation 1.25 and the Fresnel equations (see Chapter 1, Section C.4.2), for a radially polarized light. (a) In black: $I(Z)/I_0$ curve for a 45 nm gold film ($\epsilon_m = -12.8 + j1.36$); in red: $Re[V(Z)/I_0]$; in blue: $Im[V(Z)/I_0]$. Plain curves correspond to a bare gold surface, dashed curves to a gold film with an extra 5 nm thick layer of lipids ($\epsilon_d = 2.56$). (b) Zoom of the curves in (a), same color coding.

defocalization Z, thus enabling the detection of samples at the metal surface.

A.3.2 Phase images of the nucleosomes

We present in Figure 4.9 the phase images and corresponding cross-sections of the same 50 nm latex NPs (left panel) or IL2RA nucleosomes (right panel) as those shown in Figure 4.5(a) and (b) respectively, for a defocalization value Z corresponding approximately to their best (minimum here) contrast: (a) $Z = 0.90$ μm and (b) $Z = 0.45$ μm.

These images illustrate the influence of changing locally the dielectric constant at the interface: both the 50 nm latex NPs and the nucleosomes can be detected, with a signal about twice as much as the experimental noise for the two situations. We can estimate from the cross-sections both the value of the contrast of the object, and its FWHM: $\sim$ -18° and $\sim$ 260 nm respectively for the NP, and $\sim$ -16° and $\sim$ 220 nm respectively for the nucleosome. Therefore, we note that the first minimum of contrast of the nucleosomes is relatively close to that of a 50 nm latex NP (however for different values of defocalization), and that the phase image of a punctual object (PSF of the apparatus) in air is $\sim$ 240 nm, hence compatible with what was found for amplitude visualization (220$\pm$10 nm see Chapter 3, Section C.1.2).

A.3.3 Phase images of the nucleosomes with respect to the defocalization Z

Figure 4.10 presents the SSPM phase images of the same nucleosome for increasing values of defocalization Z. The nucleosome shown in this figure corresponds to that of Figure 4.6.

We observe from this figure that the contrast of the phase images varies also with the defocalization value Z: no contrast can be seen for $Z \leq 0$, and goes from positive at $Z = 0.35$ μm to negative for $Z > 0.35$ μm.

In conclusion, we have seen in this section that phase imaging can also be used to probe the presence of biological samples such as unmarked nucleosomes. The same way as for amplitude

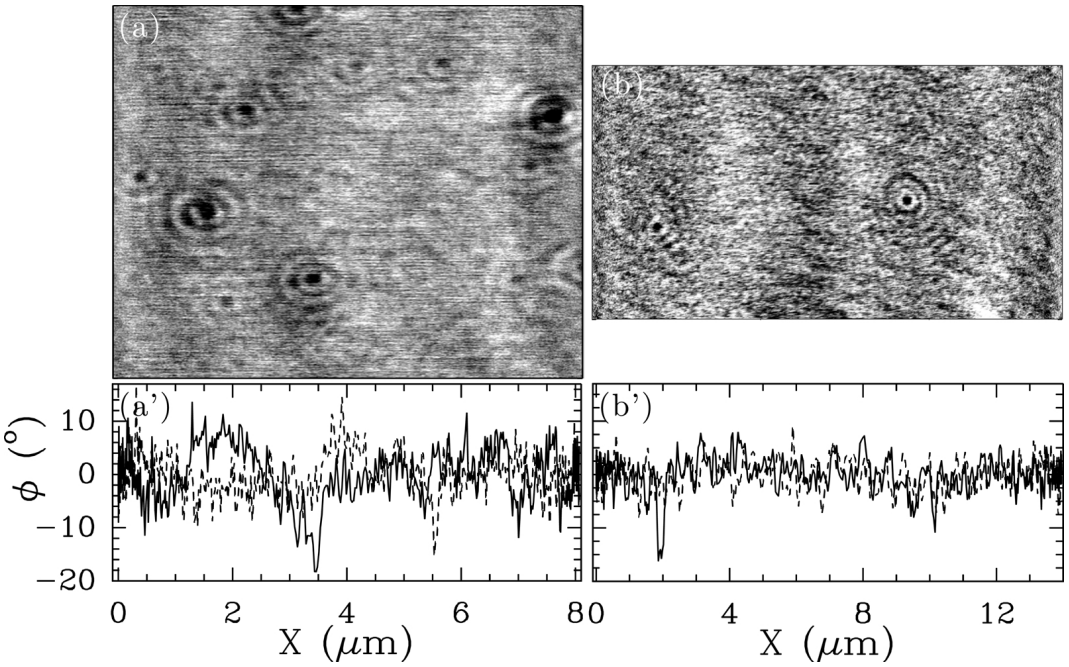

Figure 4.9 SSPM amplitude images in air of (a) 50 nm latex NPs and (b) IL2RA nucleosomes dispersed on the gold surface for a defocalization value of $Z = 0.90$ μm and $Z = 1.45$ μm respectively, and a radial polarization. Images are filtered with a 3×3 pixel sliding box, and flattened with a O^{th} order polynomial.

imaging, we have noticed that the phase contrast of the samples varies with the defocalization of the objective, and that for the appropriate value Z, the signal is twice as much as the noise. However, it has to be noted that even if theoretically the SSPM phase signal should be stable in time, we observe in the experiments important temporal phase fluctuations (data not shown here). We believe that this phenomenon might come from several origins: (i) electrical noise in the power supply of the acousto-optic modulators; (ii) noise in the detection system (photomultiplier or the electronics). Moreover, the phase optical signal has also been found to dependent highly on the settings of the optical bench. These two points tend to show that for the moment it might be tedious to exploit the phase information provided by the SSPM apparatus, and even more difficult to compare experiments carried out with different settings.

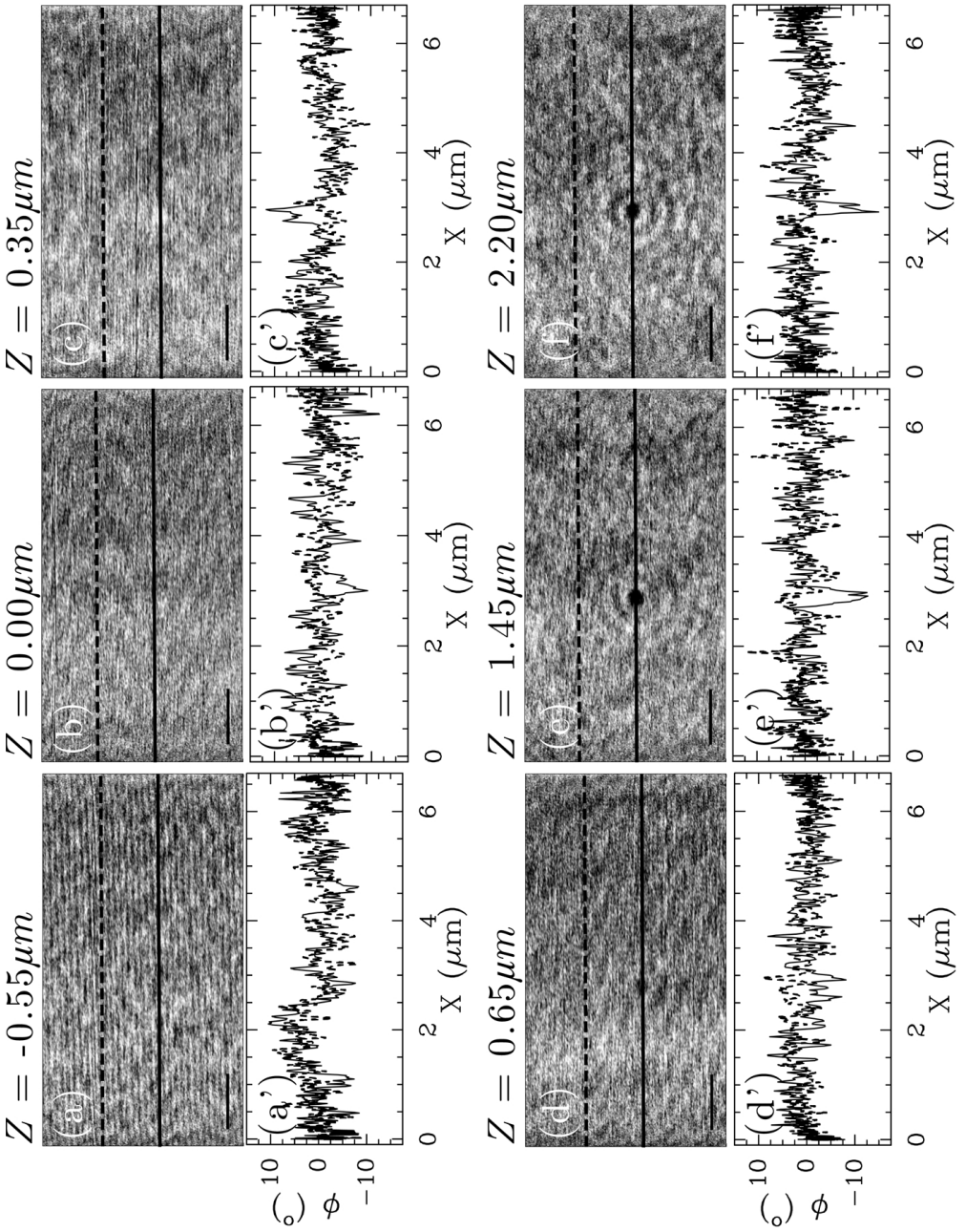

Figure 4.10 SSPM phase images in air and cross-sections of the same IL2RA nucleosome for various defocalization values: (a) and (a') $Z = -0.55$ μm, (b) and (b') $Z = 0.00$ μm, (c) and (c') $Z = 0.35$ μm, (d) and (d') $Z = 0.65$ μm, (e) and (e') $Z = 1.45$ μm, (f) and (f') $Z = 2.20$ μm. Images acquired for a radially polarized light. White plain and dashed lines on the images correspond to the cross-sections below (respectively in plain and dashed line). Scale bars are 1 μ. The nucleosome presented here corresponds to that in Figure 4.6. Images are filtered with a 3×3 pixel sliding box, and flattened with a O^{th} order polynomial.

B SSPM imaging of whole cells

After considering the optical response of synthetic nanomaterials (gold and latex NPs, see Chapter 3) or unmarked nucleo-proteic molecules (see Section A), we have chosen to adress the question of imaging much larger systems: whole cells.

B.1 Introduction: 293T and IMR-90 cells

The objective of this section is to determine to which extend it is possible to visualize and differentiate the inner structures of single cells adsorbed on a flat support. Figure 4.11 presents a schematic view of the organelles usually found in eukaryotic cells, and their main role.

Two lines of cells have been chosen for imaging in air: (i) 293T cells (extracted from human fetal kidney) and (ii) IMR–90 cells (primary culture of fibroblasts of human fetal lung).

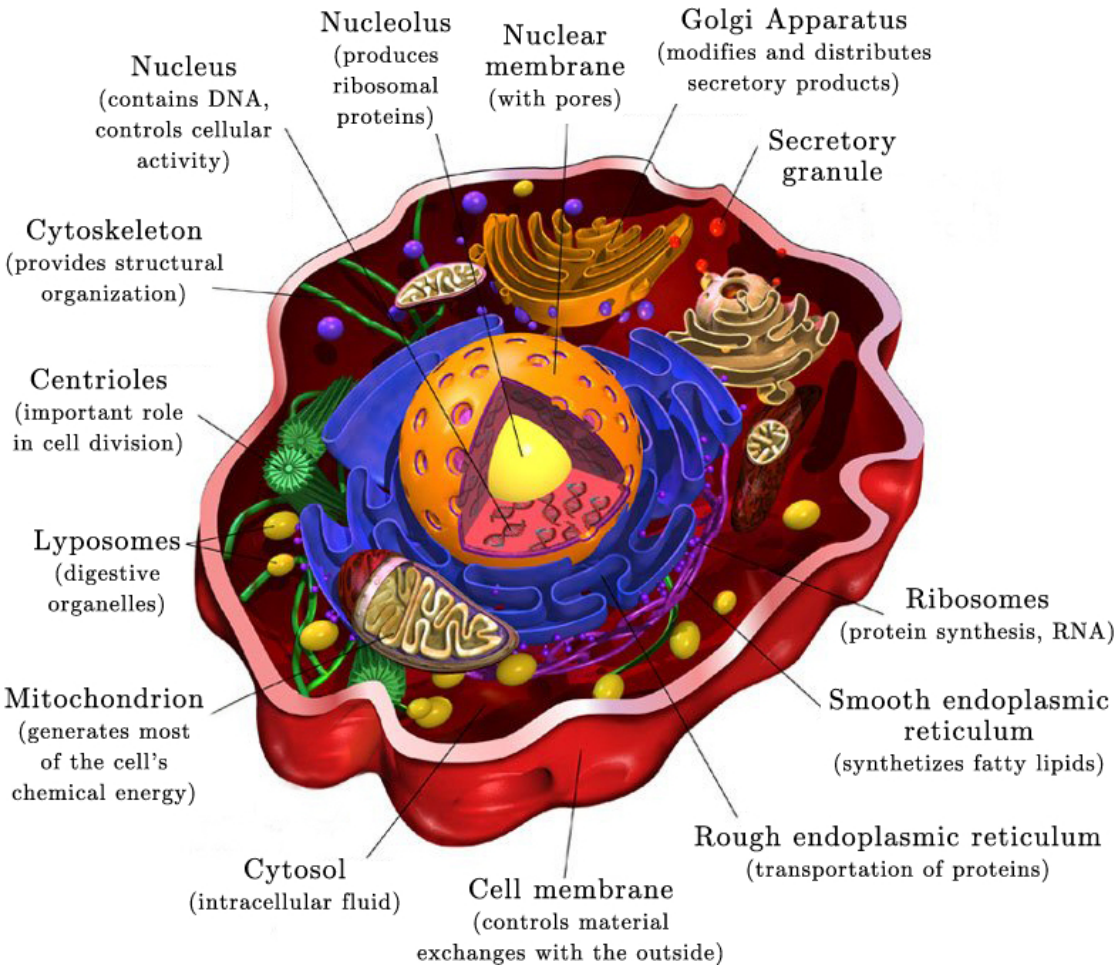

Figure 4.11 Sketch of the structures and organelles of a typical eukaryotic cell, and main role they play in its functioning.

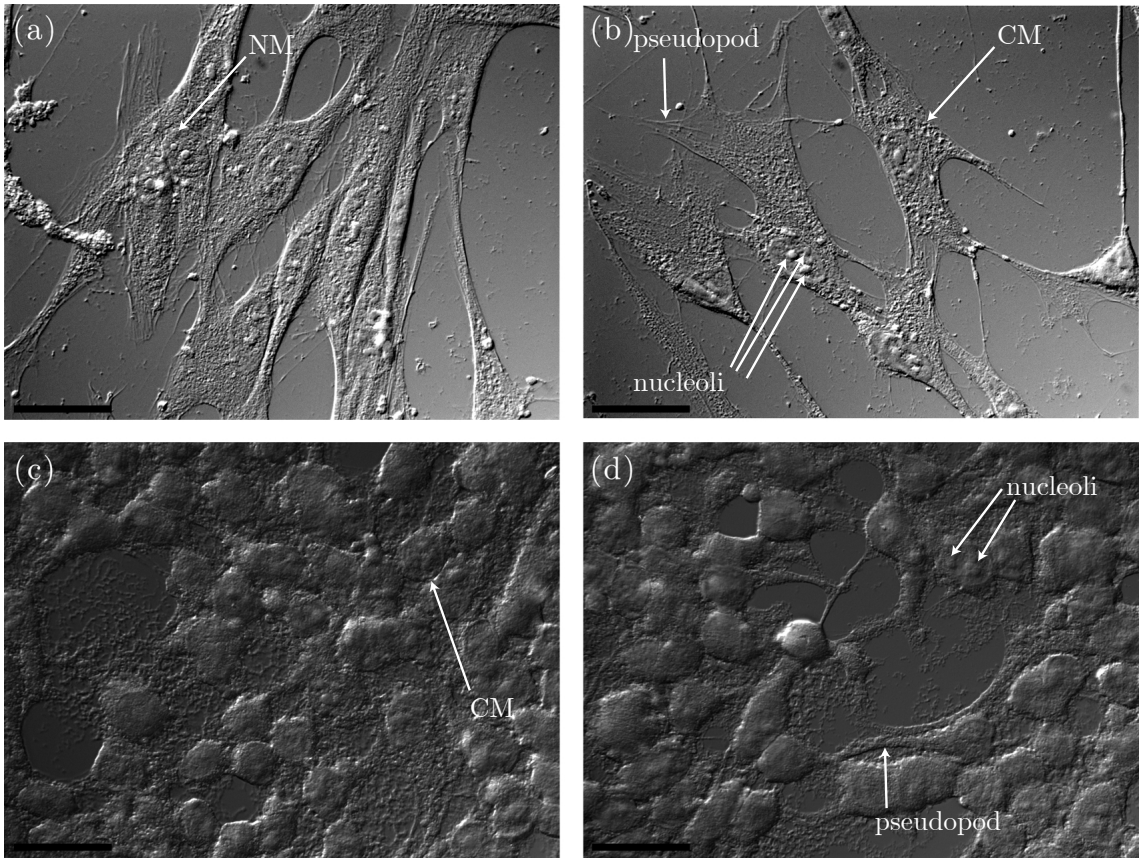

Figure 4.12 Differential Interference Contrast (DIC) microscopy images of two locations of the glass substrate where (a) and (b) IMR-90, or (c) and (d) 293T cells are adsorbed. CM: cellular membrane; NM: nucleus membrane. Scale bars are 25 μm.

We present in Figure 4.12 reference images of (a) and (b) IMR-90, and (c) and (d) 293T cells adsorbed on a glass substrate obtained by Differential Interference Contrast (DIC) microscopy. Several structures can be distinguished: cellular and nucleus membranes, pseudopods (extensions of the cytoskeleton proteins), and nucleoli (often several of them in each nucleus). We note that IMR-90 cells are larger than 293T cells, and because of they spread more over the glass surface, they also seem to adhere more strongly to it.

As a reminder, we present in Figure 4.13 a few images of cells recorded by the SPR-based techniques mentioned in Chapter 1, Section B.

B.2 Amplitude images

B.2.1 SSPM images of 293T and IMR-90 cells

The preparation protocol of the cells can be found in Appendix A, Section F. We present in Figure 4.14 large ($\sim$40$\times$40 μm^2) SSPM images in air of fixed cells for a radial polarization: (a) 293T ($Z = 0.85$ μm) and (b) IMR-90 ($Z = 0.45$ μm).

We observe from (a) that the 293T cells are near confluence (high density) in the left part of the images, whereas the gold surface is bare in the right part. Looking more closely at the top right hand corner of Figure 4.14(a), we can even see what we believe to be a pseudopod

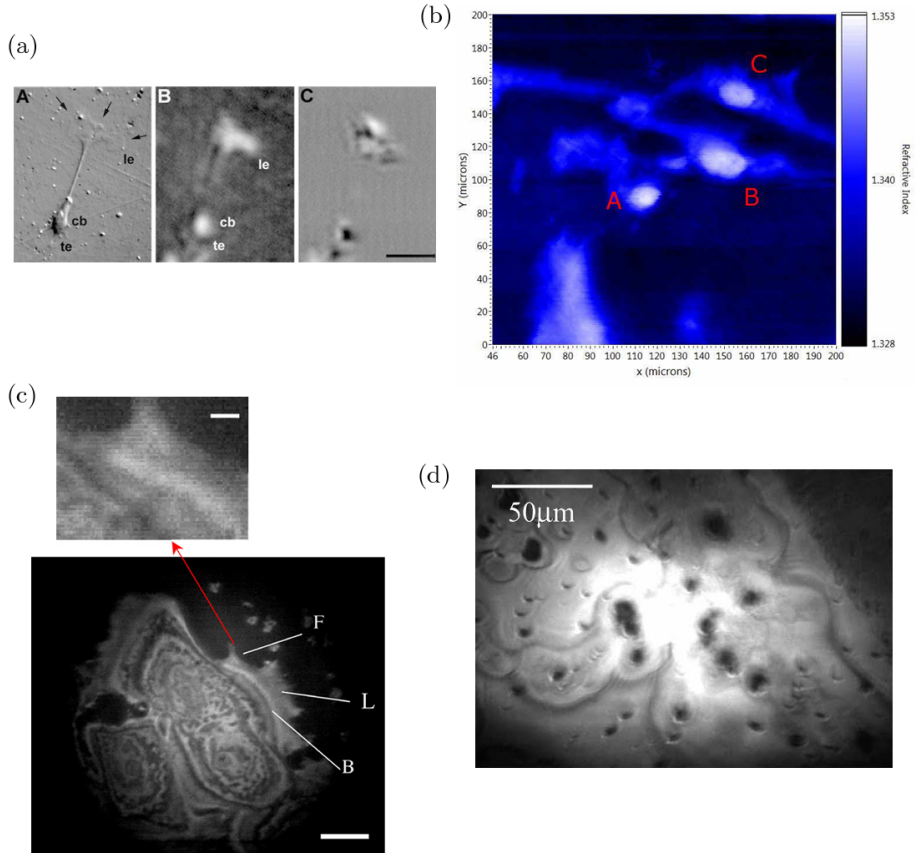

Figure 4.13 (a) Images of a goldfish glial cell in liquid medium and deposited onto an aluminum substrate. The cells are imaged in epi-illumination (A) and SPR microscopy (B). Scale bar is 100 μm. Figure extracted from Giebel *et al.*[55] (b) Refractive index image of fixed 3T3 fibroblast cells in aqueous medium[71]. (c) HaCaT cells imaged in air[69,73]. Scale bar is 12 μm (scale bar of the exert is 2 μm). (d) Image of a blood smear[74].

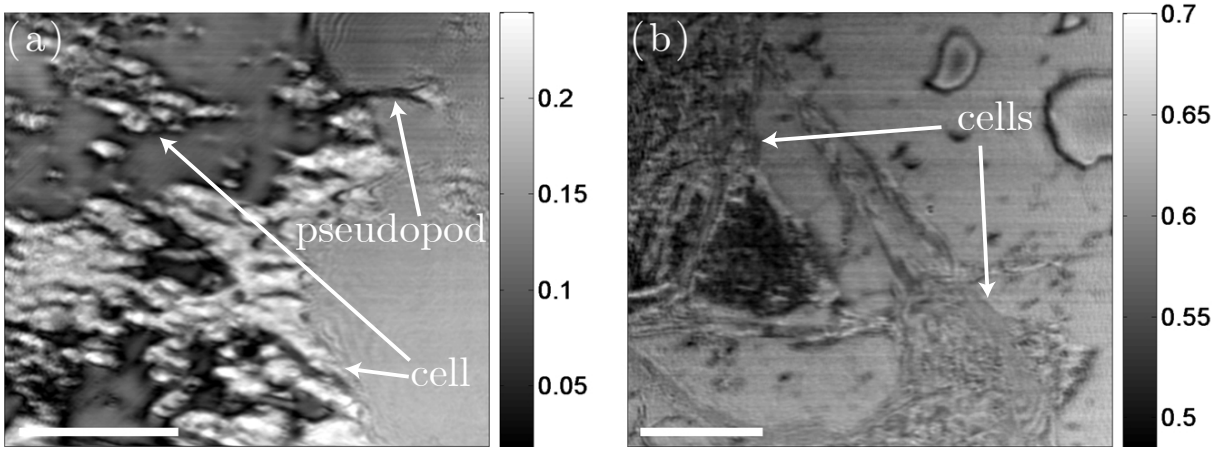

Figure 4.14 SSPM amplitude images in air of fixed cells for a radial polarization: (a) 293T ($Z = 0.85$ μm) and (b) IMR-90 ($Z = 0.45$ μm). Scale bars are 10 μm. Images are filtered with a 3×3 pixel sliding box, but not flattened.

(cell spreading over the metal surface).
On the other hand, Figure 4.14(b) confirms that the IMR-90 cells are larger than the 293T, and that their size seems to be comparable with what is seen in Figure 4.12. In this case, the IMR-90 cells seem also to spread more on (and closer to) the metal surface than the 293T ones, allowing then the inner structures to be detected, with a much better resolution than that obtained with the SPR-based techniques presented in Chapter 1, Section B (see Figure 4.13).

B.2.2 Images of 293T and IMR-90 cells with respect to the defocalization Z

We consider in this section image contrast of the cells as a function of the defocalization parameter Z. Let us first focus on the 293T cells. Figure 4.15 presents the SSPM images in air of these cells, after fixation with methanol and for Z going from -0.50 μm to 1.50 μm.
First of all, Figure 4.15 confirms that no matter the value of defocalization, the inner structures of 293T cells is hardly distinguishable with this (X,Y) range ($\sim 6 \times 6.5$ μm^2).
Moreover, we notice from Figure 4.15(a) that even for $Z = -0.50$ μm, the cells can be detected. We believe this is because these cells are massive objects (even after the fixation with methanol) that change locally the reflection coefficients r_P, and as a consequence the field amplitude of the light reflected by the metal surface as well. However, we also observe that the contrast of the images changes with the defocalization. From (b) to (f), the objects detected tend to get larger as Z increases. The inner structures of the cells are not resolved here, and contrary to what could be seen in Figure 4.14(a) (see CS), we do not observe cell spreading over the surface. Therefore, we believe that this cell line adheres relatively weakly to the gold surface, in such a way that they present a rather spherical shape. We saw in Chapter 1, Section D.2.2 that the penetration depth of the electric field in the medium of observation is very likely to increase with the defocalization parameter to a certain extent. As a consequence, we hypothesize that the evanescent field probes a larger volume of these cells (less prone to spread over the surface than the IMR-90 ones), as the defocalization is increased. To increase the adhesion of the cells during the proliferation phase, we believe that functionalizing the metal surface with lipid-like molecules composed of a carbon chain linking thiols on one side and a polar head on the other side might be a good candidate.

We present in Figures 4.16, 4.17 and 4.18 the SSPM images in air of the same IMR-90 cell, for different enlargements.
We see from Figure 4.16(a) that the same way as for Figure 4.15(a), the global shape of the cells can be distinguished even for $Z < 0$, but not its details.
When focusing on (b), we note that for $Z = 0$, the SSPM image is more contrasted, and that even if it is hard to distinguish the inner structure of the IMR-90 cell, it is easy to detect the cellular membrane (CM in the figure), and even the numerous and small white spots that we believe to be the focal adhesion sites (FAS in the figure), which could not be detected by the DIC microscopy images presented in Figure 4.12. Moreover, we note that the IMR-90 cell contrast is positive at $Z = 0$, contrarily to that of 293T cells in Figure 4.15(b). We attribute this difference to the estimation of the defocalization reference $Z_0 = 0$ of the $I(Z)/I_0$ curve (see Chapter 1, Section C.5), that might be shifted at (X,Y)=(0,0), *i.e.* in presence or absence

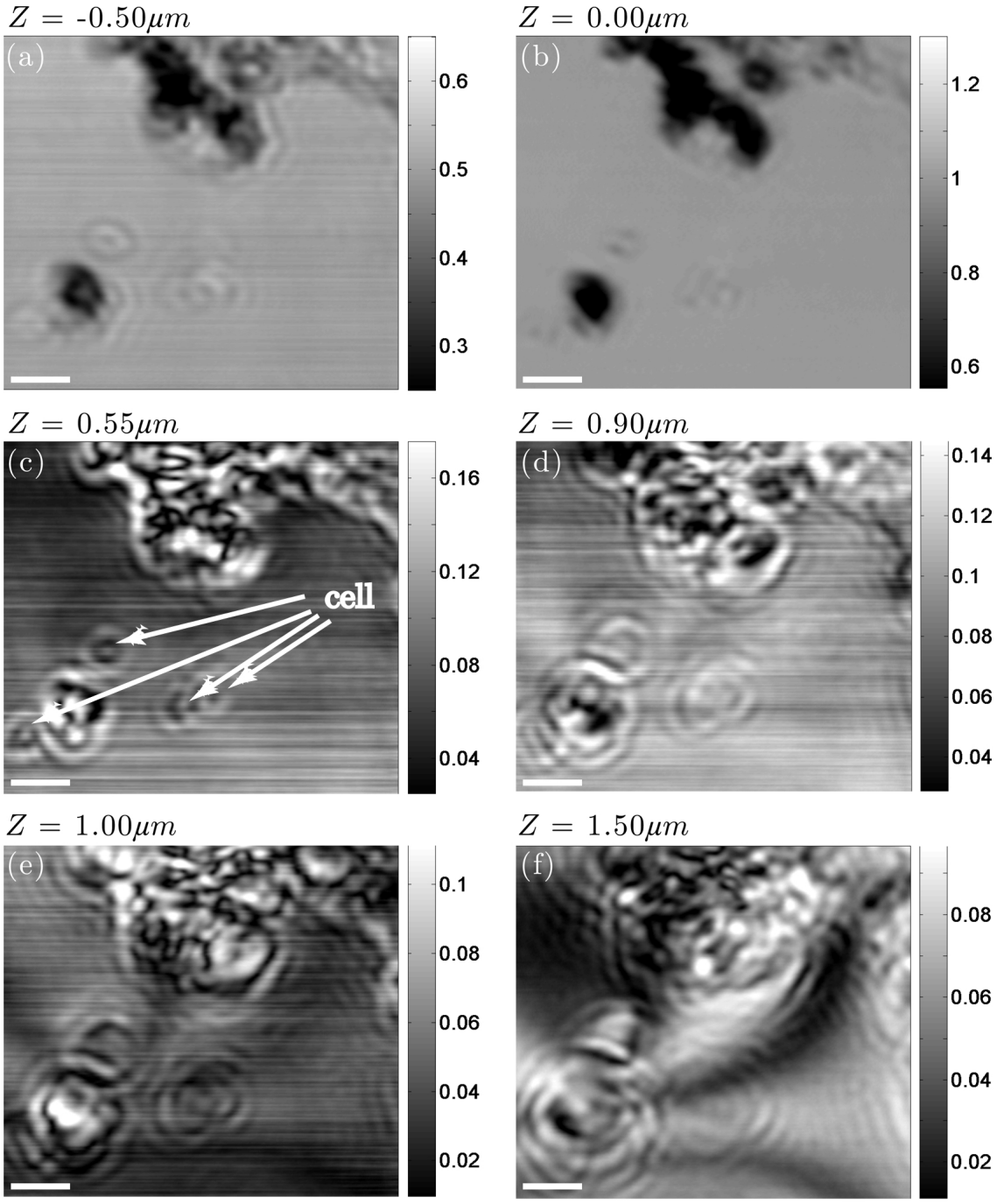

Figure 4.15 SSPM amplitude images in air of fixed 293T cells lying at the surface of the gold film. The defocalization values are: (a) $Z = -0.50$ μm; (b) $Z = 0.00$ μm; (c) $Z = 0.55$ μm; (d) $Z = 0.90$ μm; (e) $Z = 1.00$ μm; (f) $Z = 1.50$ μm. Scale bars are 1 μm. Images are filtered with a 3×3 pixel sliding box, but not flattened.

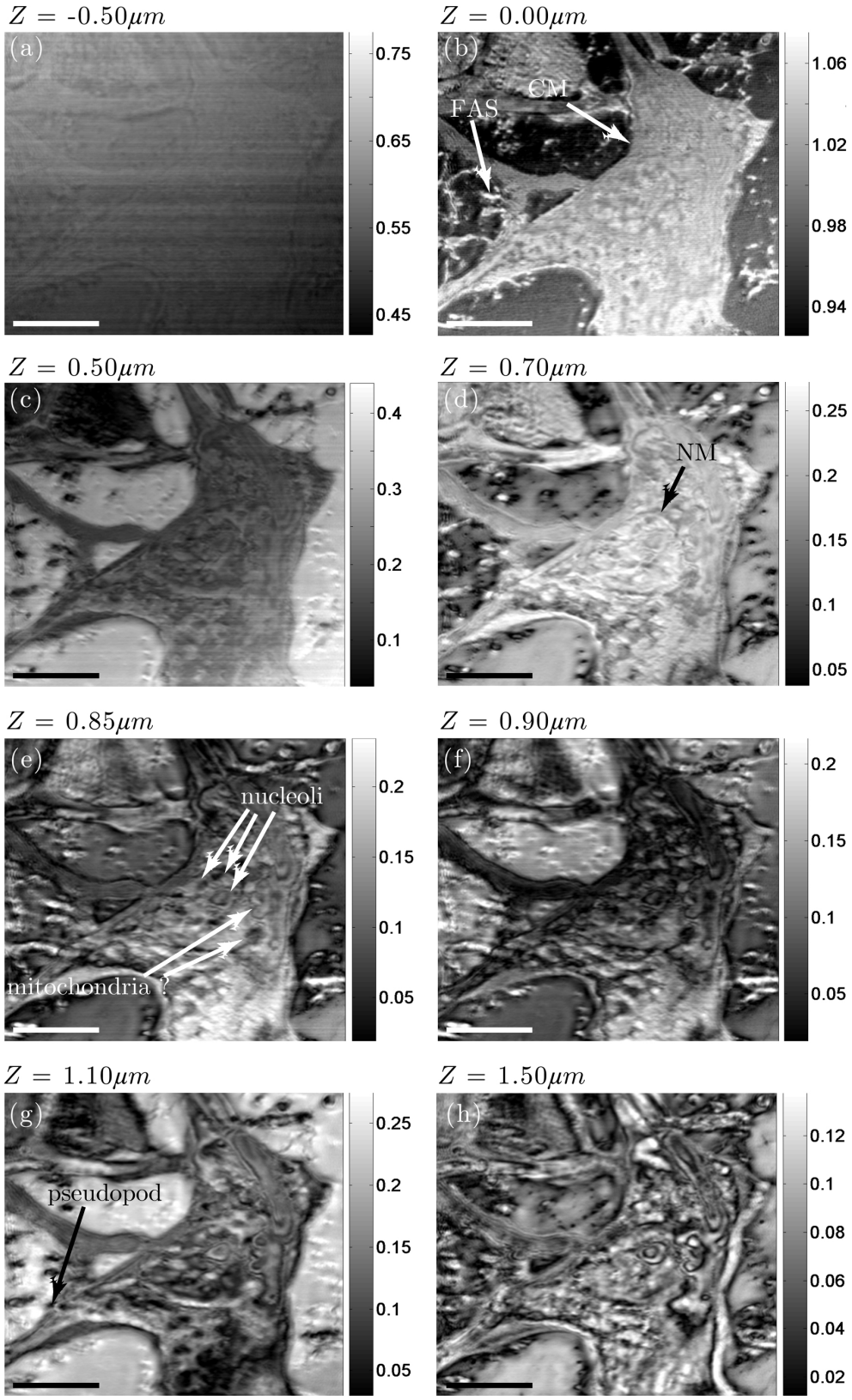

Figure 4.16 SSPM amplitude images in air of a fixed IMR-90 cell lying at the surface of the gold film. The defocalization values are: (a) $Z = -0.50$ μm; (b) $Z = 0.00$ μm; (c) $Z = 0.50$ μm; (d) $Z = 0.70$ μm; (e) $Z = 0.85$ μm; (f) $Z = 0.90$ μm; (g) $Z = 1.10$ μm; (h) $Z = 1.50$ μm. Arrows point at several cellular structures: cellular membrane (CM); nuclear membrane (NM); focal adhesion site (FAS); pseudopod; nucleoli; mitochondria. Scale bars are 10 μm. Images are filtered with a 3×3 pixel sliding box, but not flattened.

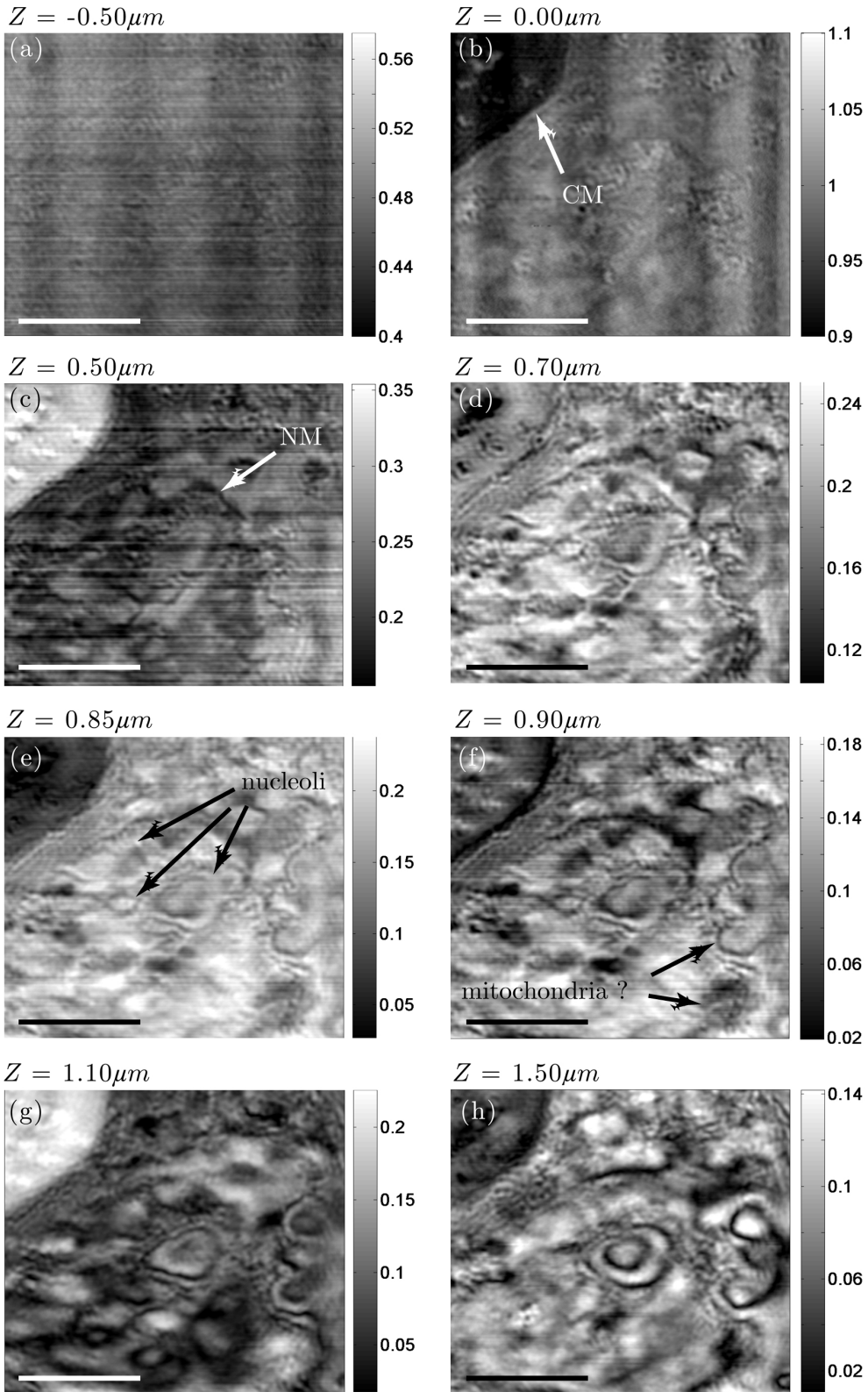

Figure 4.17 SSPM amplitude images in air of the fixed IMR-90 cell presented in Figure 4.16. The defocalization values are: (a) $Z = -0.50$ μm; (b) $Z = 0.00$ μm; (c) $Z = 0.50$ μm; (d) $Z = 0.70$ μm; (e) $Z = 0.85$ μm; (f) $Z = 0.90$ μm; (g) $Z = 1.10$ μm; (h) $Z = 1.50$ μm. Arrows point at several cellular structures: cellular membrane (CM); nuclear membrane (NM); nucleoli; mitochondria. Scale bars are 5 μm. Images are filtered with a 3×3 pixel sliding box, but not flattened.

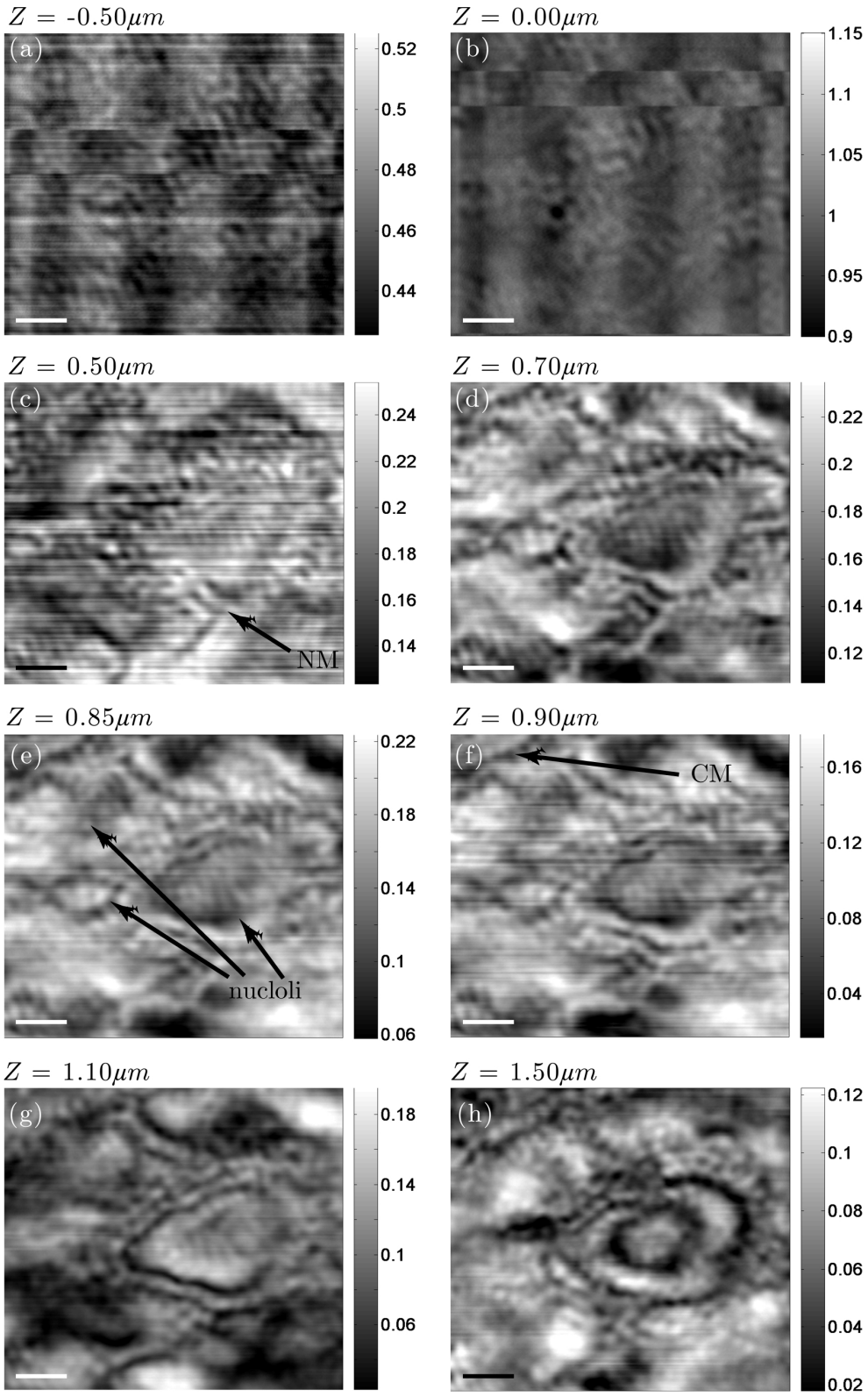

Figure 4.18 SSPM amplitude images in air of the fixed IMR-90 cell presented in Figure 4.16. The defocalization values are: (a) $Z = -0.50$ μm; (b) $Z = 0.00$ μm; (c) $Z = 0.50$ μm; (d) $Z = 0.70$ μm; (e) $Z = 0.85$ μm; (f) $Z = 0.90$ μm; (g) $Z = 1.10$ μm; (h) $Z = 1.50$ μm. Arrows point at several cellular structures: cellular membrane (CM); nuclear membrane (NM); nucleoli. Scale bars are 1 μm. Images are filtered with a 3×3 pixel sliding box, but not flattened.

of a cell or an aggregate of them at this point.
By increasing the defocalization of the objective with respect to the interface or by zooming into the cell (see Figures 4.17 and 4.18), one can distinguish relatively easily some of the inner structures of the cell: the nucleus membrane (NM), the nucleoli, and even what we believe to be the mitochondria (that cannot be seen in DIC microscopy, see Figure 4.12). Other variations of the dielectric index can be observed in the cytoplasm, but we cannot elaborate further on these because combined fluorescence and SSPM imaging should be used to demonstrate which cellular compartment is actually recognized by SSPM. We want to emphasize that increasing the defocus to $Z \sim 0.9$ μm reveals a few structures that could not be observed for $Z = 0$. We believe this can be explained by two reasons. First, as explained in Chapters 1 and 2, the optical response is more sensitive to the variations at the surface when the objective is focused in the observation medium than when it is focused at the interface. Therefore, the presence of cell structures is likely to have a larger impact on the contrast when $Z > 0$. Second, we have seen in Chapter 1, Section D.2.2 that the 3D-ME model predicts that the penetration depth of the evanescent field increases with the defocalization. It is then possible that the SSPM images reveal structures further away from the surface when Z is enhanced.
On the other hand, we also note that increasing Z around 1.5 μm makes the largest structures easier to identify (see for instance what we believe to be the mitochondrion in Figure 4.16(h)), but the smaller variations of contrast disappear.
Therefore, we believe that the defocalization parameter must be tuned during the SSPM imaging to resolve the smaller and larger structures, as well as those further away from the surface.

B.2.3 Evolution of the cells' contrast with respect to the defocalization Z

We present in Figures 4.19(b) and 4.20(b) the evolution of the amplitude contrast of 293T and IMR-90 cells respectively, for different locations at the surface, represented by the crosses in Figures 4.19(a) and 4.20(a). The curves in (b) have been reconstituted from the stack of 100 SSPM images recorded for increasing values of defocalization (with a step of 50 nm; see Chapter 3, Section A.2.1).

First of all, we note that the evolution of the contrast is different according to the lateral position considered. By comparing the black and red curves, we see that the oscillations (characteristic of the plasmon resonance) are significantly modified when going from a location corresponding to bare gold (black curve) to that of a biological object (red curve), and that they even tend to disappear when considering an aggregate of cells (blue curve). This huge variation could be expected since the departure from the conditions of resonance of the SPPs increases with the variation of local dielectric index, and therefore with the amount of biological material present at the metal surface.
On the other hand, we notice the same behavior from Figure 4.20: the oscillations are well defined for bare gold, whereas they vary drastically when following the evolution of the contrast inside the cell. However, it has to be noted that without a detailed theoretical study of the behavior of the contrast with Z, it is hard to extrapolate much information from the comparison of the curves corresponding to the different positions inside the cell.

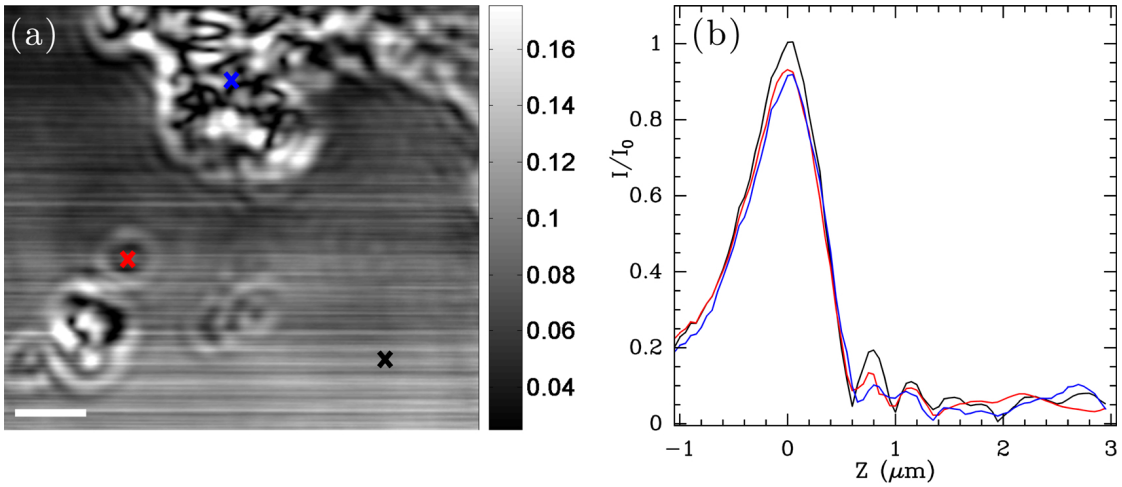

Figure 4.19 (a) SSPM amplitude image in air of a fixed 293T cell for $Z = 0.55$ μm. Scale bar is 1 μm. (b) evolution of the contrast at several locations: black curve and cross for naked gold; red curve and cross for what we believe to be a biological object; blue curve and cross for an aggregate of cells. The image series corresponds to those shown in Figure 4.15.

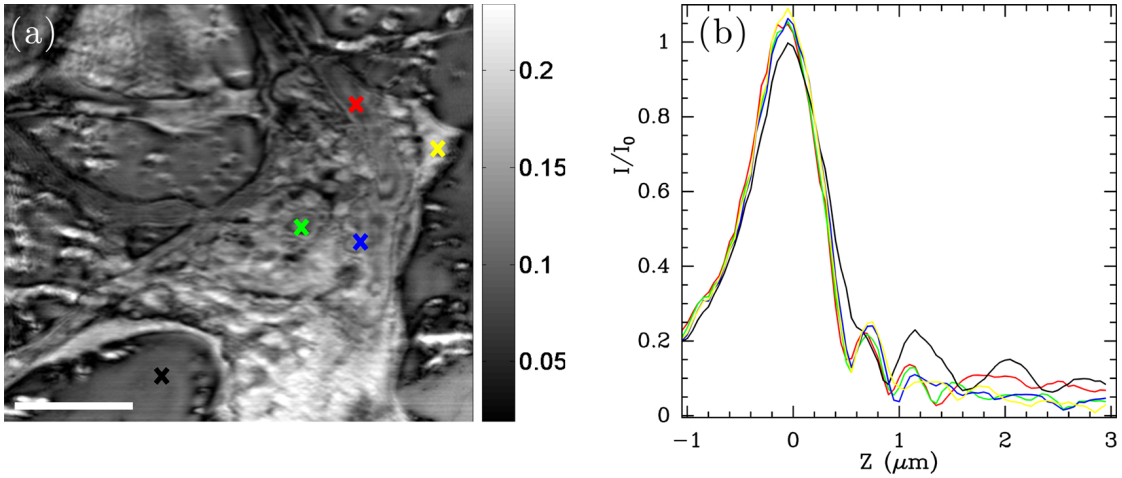

Figure 4.20 (a) SSPM amplitude image in air of a fixed IMR-90 cell for $Z = 0.85$ μm. Scale bar is 10 μm. (b) evolution of the contrast at several locations: black curve and cross for naked gold; green curve and cross for a nucleolus; red curve and cross for the cytoplasm; blue curve and cross for what we believe to be a mitochondrion; yellow curve and cross for a specific point corresponding to a ruffle (folding of the membrane onto the cell body). The image series corresponds to those shown in Figure 4.16.

B.3 Phase images of 293T and IMR-90 cells

We present in this section the SSPM phase images of the same cells considered in the previous section. All phase images shown here have been filtered with a 3×3 pixel sliding box, and flattened with a 2^{nd} order polynomial because contrary to the amplitude images, large temporal variations of the phase are present. However, it has to be noted that this flattening induces white and black artefactual stripes at locations where the phase jumps to high/low values.

Figure 4.21 shows SSPM phase images of (a) 293T and (b) IMR-90 cells, for $Z = 0.85$ μm $Z = 0.45$ μm respectively, and a radially polarized light.

We observe from this figure that the same way as for the nucleosomes in Section A.3, 293T and IMR-90 cells can also be detected by phase imaging. Figures 4.22 to 4.25 show the evo-

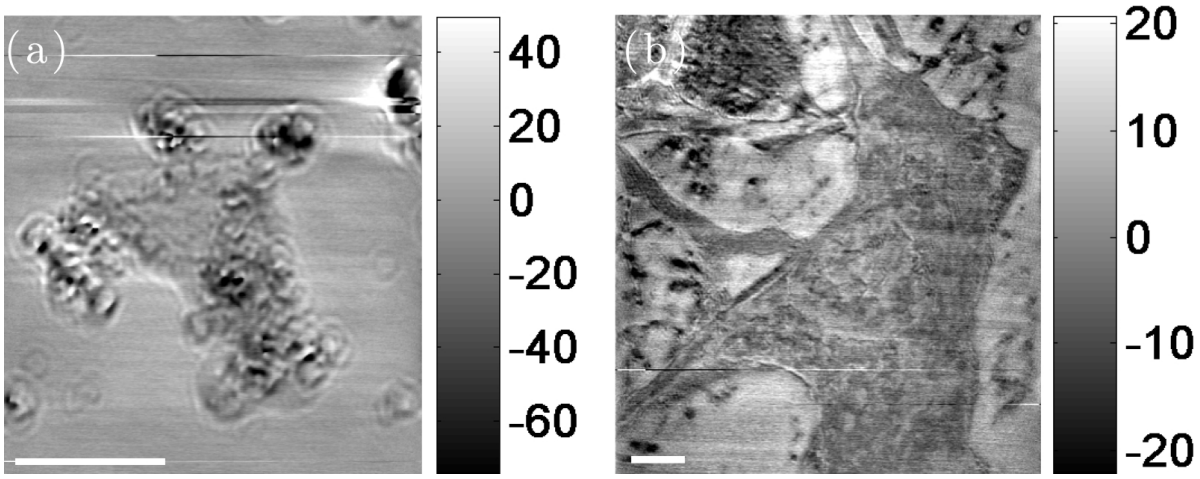

Figure 4.21 SSPM phase images in air of fixed cells for a radial polarization: (a) 293T ($Z = 0.85$ μm) and (b) IMR-90 ($Z = 0.40$ μm). Scale bars are 5 μm. Images are filtered with a 3×3 pixel sliding box, and flattened with a 2^{nd} order polynomial.

lution of the phase contrast with respect to the defocalization Z for the same cells as those presented in Figures 4.15 to 4.18.
We observe from Figure 4.22 that the 293T cells can also be detected even when the objective is focused in the coupling medium ($Z = -0.5$ μm). However, even if the contrast of the phase images increases with Z, we see that the same way as for the amplitude images shown in Figure 4.15, the inner structures of the cells cannot be resolved.

Let us now focus on the IMR-90 cells and Figures from 4.23 to 4.25. The same way as for the 293T, the contour (cellular membrane) of the cell can be detected when the image size is large enough (*i.e.* for Fig. 4.23) and for $Z = -0.5$ μm. This can be explained by the fact that even if no plasmon information is contained into the optical signal detected, the large variation of the local dielectric index at the cellular membrane (and not inside the cell) induce a large change in the reflection of light by the metal film. However, when the objective is at focus nothing can be detected**,** even the shape of the cell. This can be explained by the fact that it is where the phase variations are the smallest, and therefore more difficult to discriminate from the background phase noise. On the other hand, as Z increases, the contrast of the cell varies about the same way as for the amplitude contrast (*i.e.* with an oscillatory behavior, data not shown here) and the inner structures of the cell can be resolved.

We compare in Figure 4.26 the SSPM amplitude (left panel) and phase (right panel) images of the IMR-90 cells, for the same values of defocalization: (a) and (a') $Z = -0.55$ μm; (b) and (b') $Z = 0.65$ μm; (c) and (c') $Z = 0.70$ μm.
If we forget about the white and black scratches that are a consequence of the image treatment (flattening with a 2^{nd} order polynomial), we observe that no matter their size, the phase images are sharper than the amplitude ones. For instance, the mitochondrion in (a'), or the nucleus membrane, as well as the nucleoli are easier to resolve in (b') than in (a) and (b) respectively. This believe that this is due to the fact that a variation of the local dielectric index leads to a larger modification in the phase signal than in the amplitude response (see Figures 1.31 and 4.8). As a consequence, the edges of the inner structures appear to be better contrasted, in other words better detected.

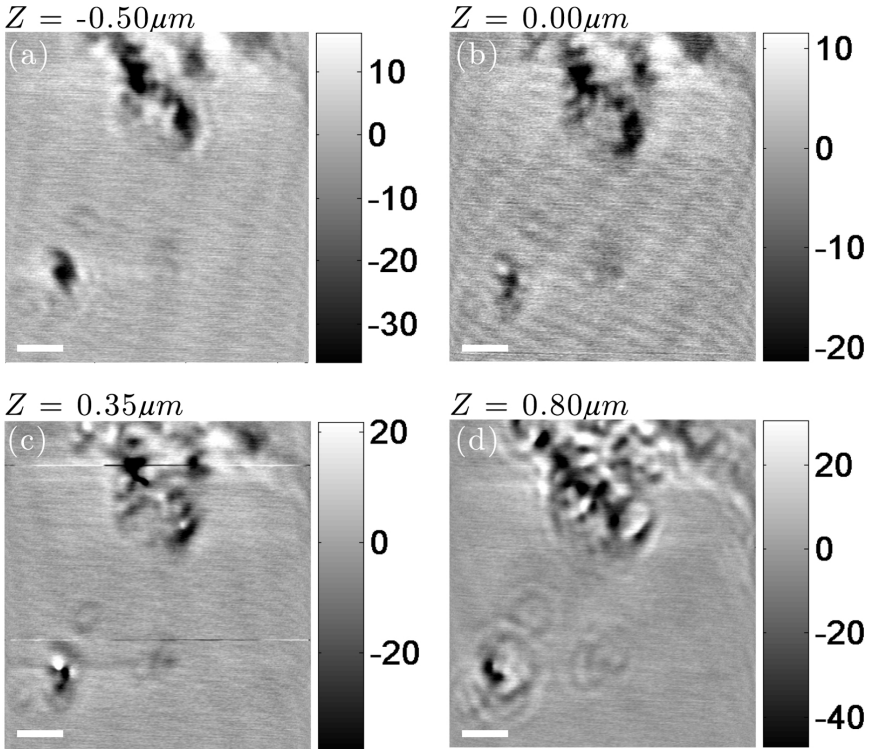

Figure 4.22 SSPM phase images in air of fixed 293T cells (same ones as in Figure 4.15) lying at the surface of the gold film. The defocalization values are: (a) $Z = -0.50$ μm; (b) $Z = 0.00$ μm; (c) $Z = 0.35$ μm; (d) $Z = 0.80$ μm. Scale bars are 1 μm. Images are filtered with a 3×3 pixel sliding box, and flattened with a 2^{nd} order polynomial.

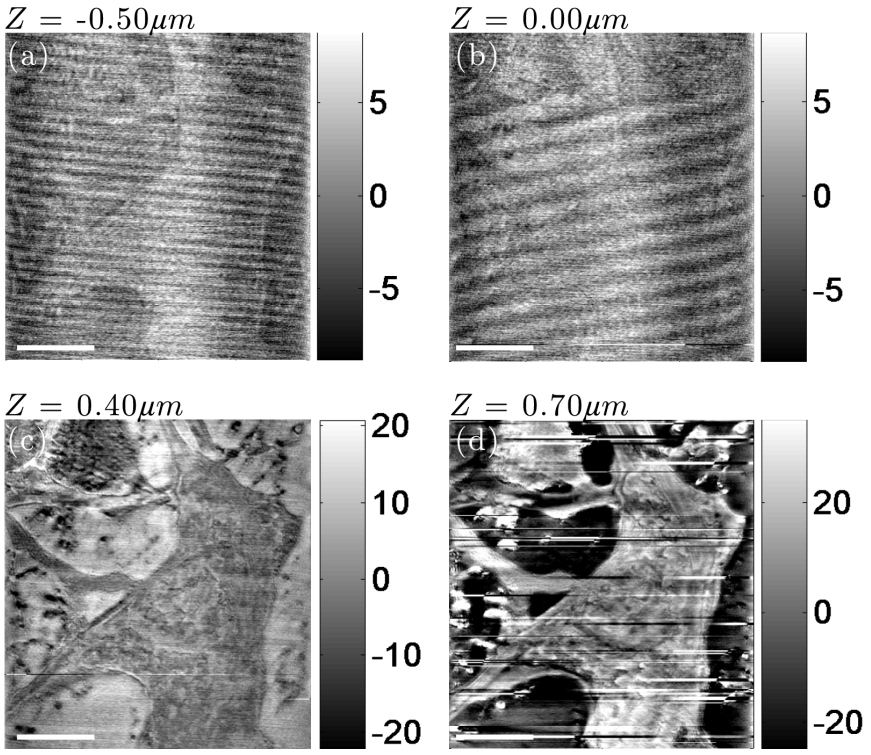

Figure 4.23 SSPM phase images in air of a fixed IMR-90 cell (same one as in Figure 4.16) lying at the surface of the gold film. The defocalization values are: (a) $Z = -0.50$ μm; (b) $Z = 0.00$ μm; (c) $Z = 0.40$ μm; (d) $Z = 0.70$ μm. Scale bars are 10 μm. Images are filtered with a 3×3 pixel sliding box, and flattened with a 2^{nd} order polynomial.

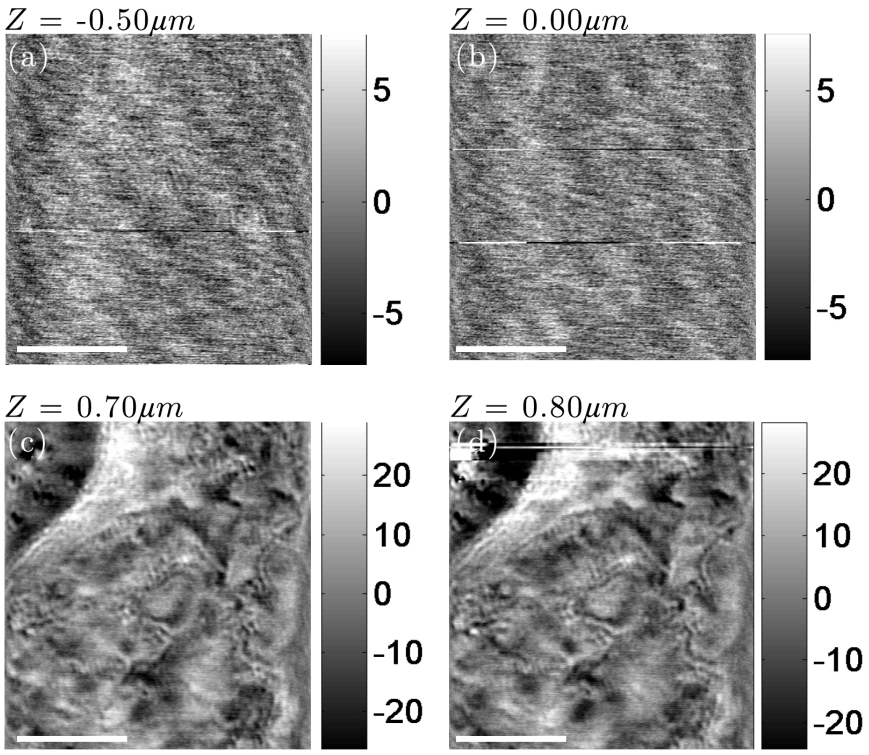

Figure 4.24 SSPM phase images in air of the fixed IMR-90 cell presented in Figure 4.23. The defocalization values are: (a) $Z = -0.50$ μm; (b) $Z = 0.00$ μm; (c) $Z = 0.70$ μm; (d) $Z = 0.80$ μm. Scale bars are 5 μm. Images are filtered with a 3×3 pixel sliding box, and flattened with a 2^{nd} order polynomial.

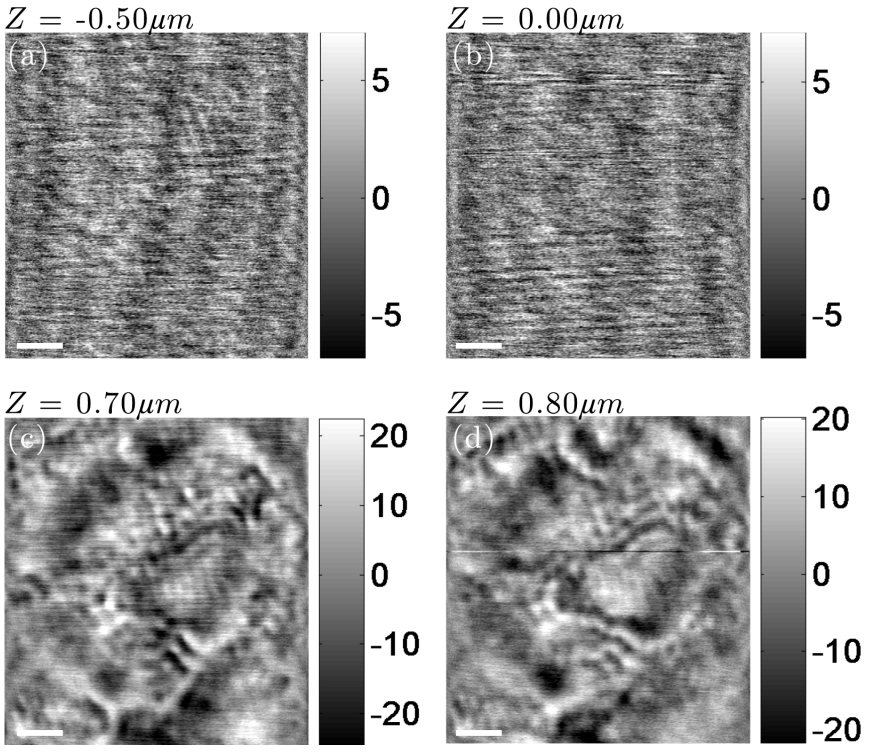

Figure 4.25 SSPM phase images in air of the fixed IMR-90 cell presented in Figure 4.23. The defocalization values are: (a) $Z = -0.50$ μm; (b) $Z = 0.00$ μm; (c) $Z = 0.70$ μm; (d) $Z = 0.80$ μm. Images are filtered with a 3×3 pixel sliding box, and flattened with a 2^{nd} order polynomial.

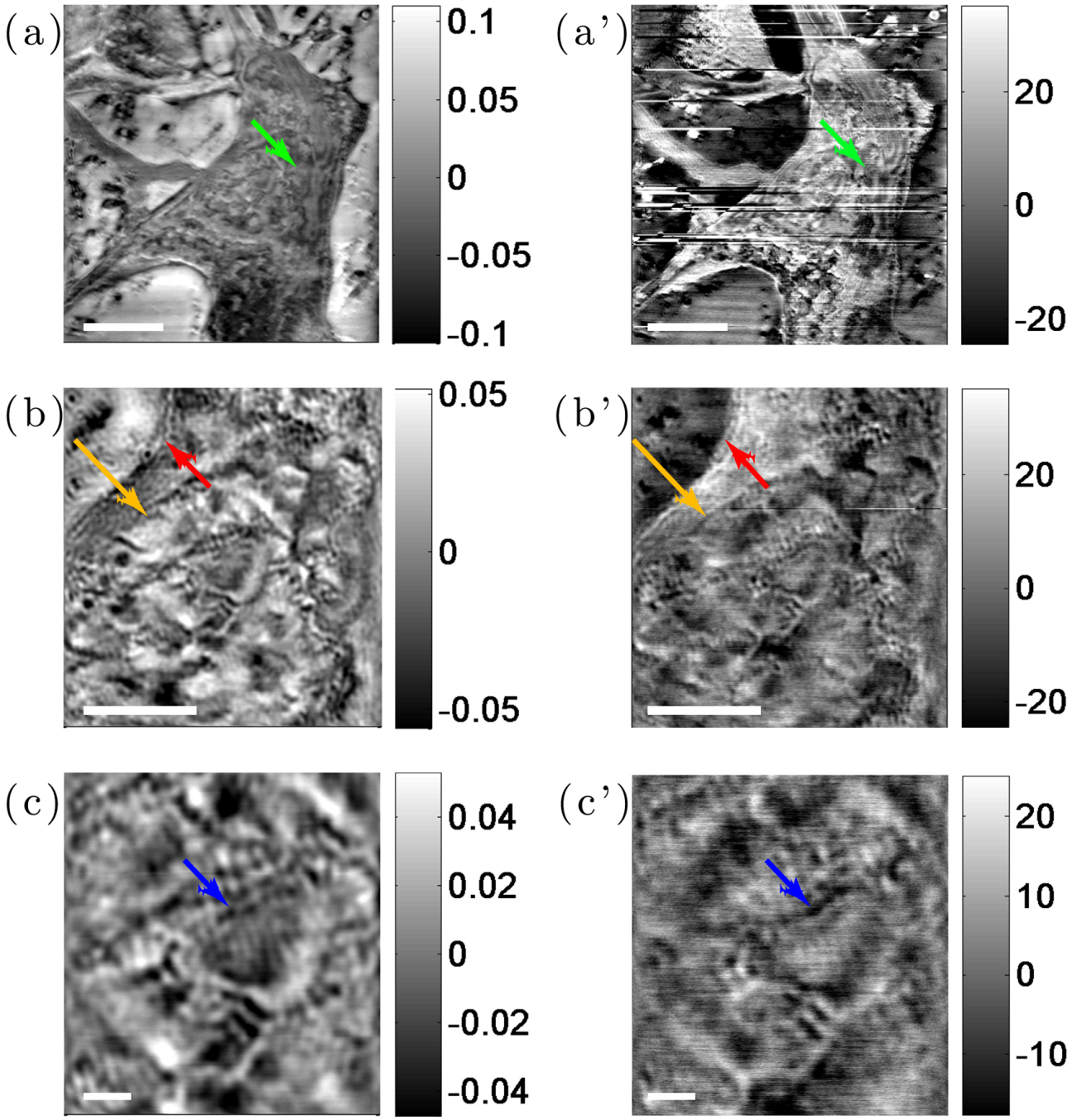

Figure 4.26 Comparison of the SSPM amplitude (left panel) and phase (right panel) images of the fixed IMR-90 cell presented in Figures 4.23, 4.24 and 4.25. (a) and (a') $Z = 0.55$ μm; (b) and (b') $Z = 0.65$ μm; (c) and (c') $Z = 0.70$ μm. The colored arrows show examples of structures that are easier to observe in phase images than in amplitude images. Scale bars are: (a) and (a') 10 μm; (b) and (b') 5 μm; (c) and (c') 1 μm. Amplitude and phase images are filtered with a 3×3 pixel sliding box. Amplitude images are not flattened, contrarily to phase images that are flattened with a 2^{nd} order polynomial.

C Conclusions

As a conclusion, we have seen in this section that SSPM imaging is a very promising technique to image in air unmarked and isolated macromolecular complexes (nucleosomes, see Section A) and cells (see Section B) that makes it complementary to other microscopies such as fluorescence microscopy and a good alternate to other SPR-based imaging techniques because of its higher resolution (see Figure 4.13). This is, to our knowledge, the first evidence for a single technique which can offer a fast, direct, versatile and non intrusive imaging of nanosize objects.
We have also noted in Section B.2.2 that 293T cells are probably less adherent than IMR-90 cells, and that depending on the defocalization of the objective with respect to the metal/observation medium interface, the amplitude contrast of the biological samples changes. We observed from the SSPM amplitude images that the best contrast is given for $0 < Z \lesssim 1.5$ μm, and we hypothesized that depending on this value of defocalization Z, the penetration depth of the evanescent field can be to a certain extent modified, and as a consequence more or fewer structures can be probed.
Moreover, we have noticed that both nucleosomes and cells can be detected by phase imaging (see Sections A.3 and B.3), and that the cellular structures appear more contrasted than for amplitude imaging (see Figure 4.26).
This first attempt is quite encouraging and it confirms that imaging biological samples with the SSPM apparatus needs to be developed, and in particular by changing the observation medium to thermally controlled aqueous buffers, so that macromolecules and cells are no more fixed. This way, such samples and their evolution will be observed with the time in a quasi--physiological environment. Another challenge would be to couple SSPM with fluorescence microscopy. Indeed, by expressing recombinant fluorescent proteins that are characteristic from certain organelles, we could precisely identify the cellular structures resolved by the SSPM apparatus.

Conclusions and perspectives

Conclusions

We have presented in this manuscript a new microscopy technique dedicated to the study of unmarked biological samples, scaling from a few tens of nanometers to a few tens of micrometers. This technique is of course not aimed at replacing the ones that have already been developed and used for tens of years for some of them, but rather to complement them, and avoid as much as possible to affect the samples or the processes that are studied because of the use of any type of markers.

We introduced in Chapter 1 Surface Plasmon Resonance from a physical point of view (see Section A), and presented in Section B some of the techniques relying on this phenomenon to study biological samples. In Section C, we demonstrated that the local variation of the dielectric index of a sample can be detected with a very high sensitivity and a resolution ($\sim$200 nm in air and for radially polarized light) several orders of magnitude smaller than the propagation length ($\sim$10 μm in air) of the SPPs thanks to the use of a high numerical aperture objective lens (NA= 1.45) coupled with both piezoelectric stages (in the Z and (X,Y) directions) and an heterodyne interferometer.
Thanks to a full resolution of the Maxwell equations presented in Section D.1 (3D-ME model), we also computed the electric field at the interface, and could derive from it the optical response of the SSPM apparatus. Moreover, we saw that the electric field at the interface changes (in shape and amplitude) with the polarization of the incident light, and that the image of a point source (the PSF) consists either of two lobes (in the direction of the linear polarization), or a single and more contrasted (by a factor $\sim$5) spot. Finally, we have also observed that the response $I(Z)$ of the SSPM apparatus varies with the defocalization Z of the objective with respect to the metal/observation medium interface. The maximum value I_0 of $I(Z)$ is taken as a reference $Z_0 = 0$ (light is focused at the interface), and the maps of the variation of the local dielectric index are recorded by scanning the sample in the lateral (X,Y) directions, for a fixed value Z.

We considered in Chapter 2 the preparation of the thin ($\sim$45 nm) metal films used to carry out the experiments with the SSPM apparatus, and more precisely the influence of some physical parameters on the deposition of the gold layers *via* thermal evaporation.
Thanks to AFM and SPR-based assays, we first demonstrated in Section A that increasing the deposition rate of the metal is a good way to enhance the quality of the layers: the gold

roughness decreases by a factor of ∼1.5 when the evaporation rate is 20 times larger. We also demonstrated *via* the modeling of the SPR reflectivity curves (the metal film is considered as a layer of adjustable dielectric index), that contrary to what is usually considered, such thin metal films are not only rough in surface, they also present defects in bulk (small inclusions of vacuum).
The second step was to treat chemically the glass surfaces with a self-assembled layer of molecules compatible both with glass and gold (see Section B): a silane head linked to a thiol head by a rather long carbon chain (a dozen of C atoms). Again, we investigated the surface and volume structures mainly by AFM imaging and SPR-based experiments. A careful study of the AFM images with a 2D Wavelet Transform Modulus Maxima analysis enabled us to identify the overall shape of the gold clusters after chemical treatment of the surfaces (no matter the concentration of molecules): a relatively flat cone or pyramid (with a half summit angle of ∼66°). We concluded that a concentration of [10^{-2} mg.ml^{-1}] of 11MUD(MeO)$_3$Si is optimal to increase the homogeneity of the layers: the metal clusters are smaller and homogeneously distributed all over the substrates, leading to a global decrease of the surface roughness by a factor ∼2.
Finally, we proposed a model based on diffusion and coalescence events, together with the dissipation of heat at the surface, so as to explain the processes ruling the metal film formation, and the consequences of the chemicals presence after treatment.

Before addressing the complex problem of visualizing biological samples, we considered in Chapter 3 the SSPM response in air and in water of synthetic NPs. We started by imaging in air metallic (gold) and dielectric (latex) NPs of diameters ranging from 10 to 200 nm (see Section A), and observed in Section A.2 that the contrast of gold and latex NPs of the same size behaves differently as function of the defocalization Z. We demonstrated in Section A.3 that the experimental SSPM response of such NPs coincides relatively well with the prediction of the 3D-ME model (see Chapter 1, Section D.1), and we confirmed that it is possible to differentiate these nanomaterials because their dielectric index is different.
Moreover, we have shown in Section B that both gold and latex NPs can also be detected in aqueous environment, and that first, their contrast is almost as important as for air visualization, and second that no matter the medium of observation the contrast of gold NPs is globally higher than that of latex NPs for a given size. By imaging the smallest NPs, we also confirmed the size of the SSPM PSF (determined as the FWHM of one of the two spots) and the mean distance between the lobes in case of a linearly polarized light: respectively ∼220 nm and ∼350 nm in air and ∼150 nm and ∼230 nm in water.
Finally, we confirmed experimentally in Section C that the polarization of light changes the SSPM response, that is the PSF shape and the contrast value of the NP: the FWHM of the single spot is ∼220 nm, and the contrast is increased by a factor ∼3.5.

In the last Chapter of this manuscript, we have applied the SSPM technique to the visualization of unmarked biological samples in air and with a radial polarization.
We have demonstrated in Section A that SSPM can detect nucleoproteic macromolecules lying at the metal surface, with almost the same contrast as a 50 nm latex NP. We also noticed that the same way as for the NPs, the contrast of the nucleosomes oscillates with the defocalization of the objective. Moreover, we saw that phase imaging is an alternate possibility to amplitude visualization in order to detect nucleosomes.

In addition to nucleosome imaging, we reconstructed in Section B the amplitude images of whole cells (IMR-90 and 293T lines) and determined that the 293T cells are probably less adherent than IMR-90 cells. Considering the IMR-90 cells, we noticed that several structures could be observed: the cellular and nucleus membranes, the nucleoli, pseudopods, some of the focal adhesion sites, and even what we believe to be mitochondria. Again we saw that the contrast of the samples changes with the defocalization Z, and we suspected the penetration depth of the evanescent field in the observation medium to be likely modified by this value of defocus. Finally, we noted that cellular structures seem to be easier to detect by phase imaging, since the SPPs phase information is more sensitive to local variations of the dielectric index.

As a conclusion, SSPM imaging is, to our knowledge, the first evidence for a single technique which can offer a fast, direct, versatile and non intrusive imaging of biological objects ranging from the nanoscale of macromolecular complexes to the micron scale of a whole cell. Moreover, we have seen throughout this manuscript that the SSPM technique has no pretention at replacing other microscopies that have proven very effective and convenient at studying many biological samples, but rather to propose a new tool to answer questions that could not be addressed another way, or by a whole set of other methods harder to carry out.

Perspectives

We saw in Chapter 3 that even if the 3D-ME model predicts relatively well the optical response of simple objects such as spherical dielectric and metallic NPs, few discrepancies are observed: little differences in the values of contrasts for NPs of diameter D>50 nm, and NPs of smaller diameters are still detected experimentally whereas the model suggests we should not be able to visualize NPs with diameter < 50 nm.
These discrepancies are due to the roughness of gold which induces an enhancement of the surface electric field. The 3D-ME model should therefore be improved to match more closely the response of very small objects, by including the gold inhomogeneities. The first idea is to implement in the model the surface and volume inhomogeneities (evidenced in Chapter 2) of the gold layers. Indeed, we expect the distribution of the evanescent field to be inhomogeneous over the surface, with locations at the surface where the field is stronger. Another point we believe to be of great importance is the thickness of the metal layer, as presented in Chapter 3, Section C.4.1: the model suggest that the contrast of the samples could be enhanced by simply decreasing the amount of gold deposited on the glass substrates. The same way (same section), it appears that limiting the incident angles around the angle of plasmon resonance θ_P is a good way to once again increase the contrast of the samples.
In addition to these aspects, we also recommend to address theoretically the problem of SSPM phase imaging. Indeed, as we explained in Chapters 1 and 4, the detection of the phase variation is more pronounced than that of the amplitude. Therefore, it is very likely that phase imaging would be a better candidate to discriminate more easily objects with different dielec-

tric index (such as the gold/latex NPs considered in Chapter 3).
Therefore, a careful theoretical study of these parameters, in parallel to experiments, is likely to improve both the understanding of the SSPM apparatus and the sensitivity of the technique.

Even if the SSPM imaging system is devoted to the study of unmarked biological samples, we would like to implement the possibility of detecting fluorescence emitted by the samples. This way, we could combine the two techniques, and get more information (especially about the dynamics and structure of the system). Indeed, by expressing for instance recombinant fluorescent proteins that are characteristic from specific cellular structures, we could confirm the organelles detected by the SSPM set-up in Chapter 4.

Another very important point is the imaging of the samples, and in particular biological, in an aqueous environment with temperature control, so that they can be observed within a few hours. Again, the 3D-ME model is probably an asset for such studies. As a consequence, we expect to follow the evolution of samples such as cells, and address questions that require a quasi-physiological environment (such as the study of dynamical events: entry of a NP inside the cell body, spreading of a cell...).

Finally, we would like to take advantage of the experiments carried out on both the NPs' visualization (Chapter 3) and the observation of the biological samples (Chapter 4), and more particularly the IMR-90 cells, to study the vectorization of NPs that are functionalized with drugs inside the cell body, and ultimately in the nucleus.
As explained previously, the first step would be to visualize such cells in a controlled aqueous environment, for a relatively long period of time (a couple of hours).
A good candidate to use as a biocompatible (glucose) NP would be that developed by the group of T.K. Kundu[149]. It has in particular been demonstrated that their vectorization depends on their functionalization (they can even be integrated into the nucleus), and are not toxic to the host cell. Therefore, a possible application to our SSPM system would be to study the cellular mechanisms as well as the physical processes implicated in the vectorization of the NPs inside the cell and possibly their nucleus. We also believe we could follow the evolution of the system in real time and identify specific cellular structures where the colloids aggregate. Finally, we expect the fluorescence of recombinant proteins of interest (such as assembling or remodeling factors of the chromatin, transcription factors of genes coding for target proteins of the molecules grafted at the surface of the NPs...) to be enhanced because of the surface plasmon waves. This way, we propose to follow in real time the travel of a NP or an assembly of NPs through the cytoplasm, the nuclear membrane and in the end inside the nucleus. The drug delivery aspect could also be studied, by testing the vectorization of small therapeutic molecules on isolated cells, and follow their effect in real time.

Bibliography

1. H. Raether. Surface plasmons on smooth and rough surfaces and on gratings. In *Springer tracts in modern physics*, volume 111. Springer Verlag, Berlin, Heidelberg, 1988.

2. S. Zhang. *Surface Plasmon Resonance and its applications to the probing of macromolecules on gold surfaces.* PhD thesis, Ecole Normale Supérieure de Lyon, 2008.

3. D.W. Lubbers and Opitz. Eine neue pco2–bzw: po2–essonde zur messung des pco2 oder po2 von gasen une flussigikeiten. *Zeitschrift Fur Naturforschung C*, 30:532–533, 1975.

4. J. Homola, S.S. Yee, and G. Gauglitz. Surface plasmon resonance sensors: review. *Sensors and Actuators B*, 54:3–15, 1999.

5. R. J. Green, R. A. Frazier, K. M. Shakesheff, M.C. Davies, C.J. Robert, and S.J.B. Tendle. Surface plasmon resonance analysis of dynamic biological interactions with biomaterials. *Biomaterials*, 21:1823–1835, 2000.

6. I. Pockrand, J.D. Swalen, J.G. Gordon, and M.R. Philpott. Surface plasmon spectroscopy or organic monolayer assemblies. *Surface Science*, 74:237–244, 1978.

7. S. Zhang, N. Hugo, W. Li, T. Roland, L. Berguiga, J. Elezgaray, and F. Argoul. Impedance spectroscopy of the potential response of MUO and AUT self-assembled monolayers on polycrystalline thin gold films. *Journal of Electroanalytical Chemistry*, 629 (1-2):138–146, 2009.

8. R.W. Wood. On a remarkable case of uneven distribution of light in a diffraction grating spectrum. *Phil. Magm.*, 4:396–402, 1902.

9. E. Kretschmann and H. Raether. Radiative decay of non radiative surface plasmons excited by light. *Zeitschrift fur naturforschung A*, 23:2135–2136, 1968.

10. A. Otto. Excitation of nonradiative surface plasma waves in silver by the method of frustrated total reflection. *Zeitschrift fur Physik*, 216:398–410, 1968.

11. P. K. Jain, X. Huang, I. H. El-Sayed, and M. A. El-Sayed. Review of some interesting surface plasmon resonance-enhanced properties of noble metal nanoparticles and their applications to biosystems. *Plasmonics*, 2:107–118, 2007.

12. C.M. Feldherr and J.M. Marshall. The use of colloidal gold for studies of intracellular exchanges in the ameba chaos. *Journal of Biophysical and Biochemical Cytology*, 12:640–645, 1952.

13. C. G. Harford, A. Hamlin, and E. Parker. Electron microscopy of hela cells after the ingestion of colloidal gold. *Journal of Biophysical and Biochemical Cytology*, 3:749–756, 1957.

14. S. Link and M.A. El-Sayed. Shape and size dependence of radiative, nonradiative, and photothermal properties of gold nanocrystals. *International Reviews in Physical Chemistry*, 19 (3):409–453, 2000.

15. I. H. El-Sayed, X. Huang, and M. A. El-Sayed. Surface plasmon resonance scattering and absorption of anti-egfr antibody conjugated gold nanoparticles in cancer diagnostics: applications in oral cancer. *Nano Letters*, 5 (5):829–834, 2005.

16. K. Aslan, J.R. Lakowicz, and C.D. Geddes. Plasmon light scattering in biology and medicine: new sensing approaches, visions, and perspectives. *Current Opinion in Chemical Biology*, 9:538–544, 2005.

17. E. Fort and S. Gresillon. Surface enhanced fluorescence. *Journal of Physics D: Applied Physics*, 41:013001, 2008.

18. C.K. Chen, T.F. Heinz, D. Ricard, and Y.R.Shen. Surface-enhanced second-harmonic generation and raman scattering. *Physical Review B*, 27:1965–1979, 1983.

19. C.F. Bohren and D.R. Huffman. *Absorption and Scattering of Light by Small Particles*. Wiley Science Paperback Series, 1998.

20. Y. Goulam Houssen. *Plasmonique appliquee a l'ingenierie des processus de fluorescence en biophotonique*. PhD thesis, Universite Paris Diderot - Paris7, 2009.

21. H. Frohlich. *Theory of dielectrics*. Oxford University Press, 1949.

22. C. Sonnichsen. *Plasmons in metal nanostructures*. PhD thesis, Ludwig-Maximilians Universitat, Munich, 2001.

23. L.M. Liz-Marzan. Nanometals : Formation and color. *Materials Today*, 7 (2):26–31, 2004.

24. U. Kreibig and L. Genzel. Optical absorption of small metallic particles. *Surf. Sci.*, 156:678–700, 1985.

25. U. Kreibig and M. Vollmer. *Optical properties of metal clusters*. Springer, Berlin, 1995.

26. C. Burda, Z. Chen, R. Narayanan, and M.A. El-Sayed. The chemistry and properties of nanocrystals of different shapes. *Chemical Reviews*, 105 (4):1025–1102, 2005.

27. E. Katz and I. Willner. Integrated nanoparticle-biomolecule hybrid systems: Synthesis, properties, and applications. *Angewandte Chemie*, 43 (45):6042–6108, 2004.

28. S. Underwood and P. Mulvaney. Effect of the solution refractive index on the color of gold colloids. *Langmuir*, 10:3427–3430, 1994.

29. K.L. Kelly, E. Coronado, L.L. Zhao, and G.C. Schatz. The optical properties of metal nanoparticles: The influence of size, shape, and dielectric environment. *Journal of Physical Chemistry B*, 107 (3):668–677, 2003.

30. J.N. Anker, W.P. Hall, O. Lyandres, N.C. Shah, J. Zhao, and R.P. Van Duyne. Biosensing with plasmonic nanosensors. *Nature Materials*, 7 (6):442–453, 2008.

31. J.J. Storhoff, A.A. Lazarides, R.C. Mucic, C.A. Mirkin, R.L. Letsinger, and G.C. Schatz. What controls the optical properties of dna-linked gold nanoparticle assemblies? *Journal of American Chemical Society*, 122 (19):4640–4650, 2000.

32. K.H. Su, Q.H. Wei, X. Zhang, J.J. Mock, D.R. Smith, and S. Schultz. Interparticle coupling effects on plasmon resonances of nanogold particles. *Nano Letters*, 3:1087–1090, 2003.

33. W. Rechberger, A. Hohenau, A. Leitner, J.R. Krenn, B. Lamprecht, and F.R. Aussenegg. Optical properties of two interacting gold nanoparticles. *Optics Communications*, 220:137–141, 2003.

34. P.K. Jain, W. Qian, and M.A. El-Sayed. Ultrafast electron relaxation dynamics in coupled metal nanoparticles in aggregates. *Journal of Physical Chemistry B*, 110 (1):136–142, 2006.

35. P.K. Jain, S. Eustis, and M.A. El-Sayed. Plasmon coupling in nanorod assemblies: Optical absorption, discrete dipole approximation simulation, and exciton-coupling model. *Journal of Physical Chemistry B*, 110 (1):18243–18253, 2006.

36. J. Zenneck. Uber die fortpflanzung ebener elektromagnetischer wellen langs einer ebenen leiterache und ihre beziehung zur drahtlosen telegraphie. *Annalen der Physik*, 328:846–866, 1907.

37. A. Sommerfeld. Uber dir ausbreitung der wellen in der drahtlosen telegraphie. *Ann. Physik*, 28:665–736, 1909.

38. R. Bruns and H. Raether. Plasma resonance radiation from non radiative plasmons. *Zeitschrift Fur Physik A*, 237 (1):98–106, 1970.

39. H. Raether. *Physics of thin films*, volume 9, chapter III, pages 145–261. Academic Press, New York, 1977.

40. H. Raether. *Excitation of plasmons and interband transitions by electrons*. Springer Verlag, Berlin, 1980.

41. M.L. Thèye. Investigation of the optical properties of Au by means of thin semitransparent films. *Phys. Rev. B*, 2:3060–3078, 1970.

42. H. Kapitza. Influence of surface roughness on the reflection of gold films in the region osf surface plasmon excitation. *Optics Communications*, 16 (1):73–75, 1976.

43. K. Arya, Z.B. Su, and J.L. Birman. Localization of the surface plasmon polariton caused by random roughness and its role in surface-enhanced optical phenomena. *Physical Review Letters*, 54 (14):1559–1562, 1985.

44. S.I. Bozhevolnyi, B. Vohnsen, I.I. Smolyaninov, and A.V. Zayats. Direct observation of surface polariton localization caused by surface roughness. *Optics Communications*, 117:417–423, 1995.

45. C.S. West and K.A. O'Donnell. Backscattering enhancement from plasmon polaritons on a deterministic metal surface. *Optics Communications*, 123:109–114, 1996.

46. J. Homola. Present and future of surface plasmon resonance biosensors. *Analytical and Bioanalytical Chemistry*, 377 (3):528–539, 2003.

47. R. Slavik, J. Homola, and J. Ctyroky. Novel spectral fiber optic sensor based on surface plasmon resonance. *Sensors and Actuators B Chemical*, 74:106–111, 2001.

48. A. Leung, P.M. Shankar, and R. Mutharasan. A review of fiber-optic biosensors. *Sensors and Actuators B*, 125:688–703, 2007.

49. M. Kanso, S. Cuenot, and G. Louarn. Sensitivity of optical fiber sensor based on surface plasmon resonance: modeling and experiments. *Plasmonics*, 3:49–57, 2008.

50. X. Fan, I.M. White, S.I. Shopova, H. Zhu, J.D. Suter, and Y. Sun. Sensitive optical biosensors for unlabeled targets: a review. *Analytica Chimica Acta*, 620:8–26, 2008.

51. M.N. Velasco-Garcia. Optical biosensors for probing at the cellular level: A review of recent progress and future prospects. *Seminars in Cell & Developmental Biology*, 20:27–33, 2009.

52. M. Born and E. Wolf. *Principles of optics: electromagnetic theory of propagation, interference and diffraction of light*. Cambridge University Press, 1999.

53. H.P. Chiang, J.L. Lin, R. Chang, S.Y. Su, and P.T. Leung. High-resolution angular measurement using surface-plasmon-resonance via phase interrogation at optimal incident wavelengths. *Optics Letters*, 30 (20):2727, 2005.

54. S. J. Zhang, L. Berguiga, J. Elezgaray, T. Roland, C. Faivre-Moskalenko, and F. Argoul. Surface plasmon resonance characterization of thermally evaporated thin gold films. *Surface Science*, 601:5445–5458, 2007.

55. K. Giebel, C. Bechinger, S. Herminghaus, M. Riedel, P. Leidererand U. Weiland, and M. Bastmeyer. Imaging of cell/substrate contacts of living cells with surface plasmon resonance microscopy. *Biophysical Journal*, 78 (1):509–516, 1999.

56. B. Rothenhausler and W. Knoll. Surface plasmon microscopy. *Nature*, 332:615–617, 1988.

57. E. Fu, J. Folay, and P. Yager. Wavelength-tunable surface plasmon resonance microscope. *Review of Scientific Instruments*, 74:3182–3184, 2003.

58. E.M. Yeatman. Resolution and sensitivity in surface plasmon microscopy and sensing. *Biosensors and Bioelectronics*, 11(6–7):635–649, 1996.

59. C. Boozer, G. Kim, S. Cong, H. Guan, and T. Londergan. Looking towards label-free biomolecular interaction analysis in a high-thoughput format: a review of new surface plasmon resonance technologies. *Current Opinion of Biotechnology*, 17:400–405, 2006.

60. C. Qian, T.S. Velinov, M.C. Pitter, and M.G. Somekh. Surface plasmon-assisted wide-field non-linear imaging of gold structures. *Journal of Microscopy*, 229:6–11, 2007.

61. K.J. Moh, X.C. Yuan, J. Bu, S.W. Zhu, and B.Z. Gao. Radial polarization induced surface plasmon virtual probe for two-photon fluorescence microscopy. *Optics Letters*, 34 (7):971–973, 2009.

62. C.L. Wong, H.P. Ho, Y.K. Suen, S.K. Kong, Q.L. Chen, W. Yuan, and S.Y. Wu. Real-time protein biosensor arrays based on surface plasmon resonance differential phase imaging. *Biosensors and Bioelectronics*, 24 (4):606–612, 2008.

63. C.L. Wong, H.P. Ho, T.T. Yu, Y.K. Suen, W.W.Y. Chow, S.Y. Wu, W.C. Law, W. Yuan, W.J. Li, S.K. Kong, and C. Lin. Two-dimensional biosensor arrays based on surface plasmon resonance phase imaging. *Applied Optics*, 46 (12):2325–2332, 2007.

64. P.I. Nikitin, A.N. Grigorenko, A.A. Beloglazov, M.V. Valeiko, A.I. Savchuk, O.A. Savchuk, G. Steiner, C. Kuhne, A. Huebner, and R. Salzer. Surface plasmon resonance interferometry for micro-array biosensing. *Sensors and Actuators A*, 85:189–193, 2000.

65. H. Kano, S. Mizuguchi, and S. Kawata. Excitation of surface plasmon polaritons by a focused laser beam. *J. Opt. Soc. Am. B*, 15(4):1381–1386, 1998.

66. H. Kano and W. Knoll. Locally excited surface-plasmon-polaritons for thickness measurement of lbk films. *Optics Communications*, 153(4):235–239, 1998.

67. H. Kano and W. Knoll. A scanning microscope employing localized surface-plasmon-polaritons as a sensing probe. *Optics Communications*, 182:11–15, 2000.

68. L. Novotny, R. D. Grober, and K. Karrai. Reflected image of a strongly focused spot. *Optics Letters*, 26:789–791, 2001.

69. M.M. Jamil, M.C. Denyer, M. Youseffi, S.T. Britland, S. Liu, C.W. See, M.G. Somekh, and J. Zhang. Imaging of the cell surface interface using objective coupled widefield surface plasmon microscopy. *Journal of Structural Biology*, 164 (1):75–80, 2008.

70. K. Karrai, X. Lorenz, and L. Novotny. Enhanced reflectivity contrast in confocal solid immersion lens microscopy. *Applied Physics Letters*, 77 (21):3459–3461, 2000.

71. K.J. Moh, X.C. Yuan, J. Bu, S.W. Zhu, and B.Z. Gao. Surface plasmon resonance imaging of cell-substrate contacts with radially polarized beams. *Optics Express*, 16 (25):20734–20741, 2008.

72. B. Huang, F. Yu, and R.N. Zare. Surface plasmon resonance imaging using a high numerical aperture microscope objective. *Analytical Chemistry*, 79:2979–2983, 2007.

73. M.M. Jamil, M. Youseffi, P.C. Twigg, S.T. Britland, S. Liu, C.W. See, J. Zhang, M.G. Somekh, and M.C. Denyer. High resolution imaging of bio-molecular binding studies using a widefield surface plasmon microscope. *Sensors and Actuators B*, 129 (2):566–574, 2007.

74. R. Vander and S. G. Lipson. High-resolution surface-plasmon resonance real-time imaging. *Optics Letters*, 34:37–39, 2009.

75. H.K. Wickramasinghe. *Journal of Microscopy*, 129, 1982.

76. M. G. Somekh, S. G. Liu, T. S. Velinov, and C. W. See. Optical v(z) for high resolution 2π surface plasmon miscroscopy. *Optics Letters*, 25(11):823–825, 2000.

77. M. G. Somekh, S. G. Liu, T. S. Velinov, and C. W. See. High resolution scanning surface plasmon microscopy. *Applied optics*, 39:6279–6287, 2000.

78. K. Watanabe, N. Horiguchi, and H. Kano. Optimized measurement probe of the localized surface plasmon microscope by using radially polarized illumination. *Applied Optics*, 46 (22):4985–4990, 2007.

79. L. Berguiga, S.-J. Zhang, F. Argoul, and J. Elezgaray. High-resolution surface-plasmon imaging in air and in water: V(z) curve and operating conditions. *Optics Letters*, 32(5):509–511, 2007.

80. J. Elezgaray, T. Roland, L. Berguiga, A. Fahys, and F. Argoul. Modellization of the surface scanning plasmon microscope optical response with a full solution of maxwell equations. *submitted to Journal of the Optical Society of America A*, 2009.

81. B. Richards and E. Wolf. Electromagnetic diffraction in optical systems. ii. structure of the image field in an aplanatic system. *Proceedings of the Royal Society A*, 253 (1274):358–379, 1959.

82. B.R. Johnson. Calculation of light scattering from a spherical particle on a surface by the multipole expansion method. *Journal of Optical Society of America A*, 13 (2):326–337, 1996.

83. A. Doicu, Y.A. Eremin, and T. Wriedt. Convergence of the t-matrix method for light scattering from a particle on or near a surface. *Optics Communications*, 159:266–277, 1999.

84. T. Roland, L. Berguiga, J. Elezgaray, and F. Argoul. High resolution scanning surface plasmon imaging of nanoparticles. *submitted to Physical Review Letters*, 2009.

85. R. Dorn, S. Quabis, and G. Leuchs. Sharper focus for a radially polarized light beam. *Physical Review Letters*, 91:233901, 2003.

86. Q. Zhan. Evanescent bessel beam generation via surface plasmon resonance excitation by a radially polarized beam. *Optics Letters*, 31 (11):1726–1728, 2006.

87. P.S. Tan, X.C. Yuan, J. Lin, Q Wang, and E. Burge. Analysis of surface plasmon interference pattern formed by optical vortex beams. *Optics Express*, 16 (22):18451–18455, 2008.

88. K. Watanabe, G. Terakado, and H. Kano. Localized surface plasmon microscope with an illumination system employing a radially polarized zeroth-order bessel beam. *Optics Letters*, 34 (8):1180–1182, 2009.

89. M.J. Heller. Dna microarray technology: Devices, systems, and applications. *Annual Review of Biomedical Engineering*, 4:129–153, 2002.

90. G.H.W. Sanders and A. Manz. Chip-based microsystems for genomic and proteomic analysis. *Trac-Trends in Analytical Chemistry*, 19 (6):364–378, 2000.

91. M. Cretich, F. Damin, G. Pirri, and M. Chiari. Protein and peptide arrays: Recent trends and new directions. *Biomolecular Engineering*, 23 (2-3):77–88, 2006.

92. R.A. Ferrell. Predicted radiation of plasmon oscillations in metal films. *Physical Review*, 111(5):1214–1222, 1958.

93. H. Raether. Solid state excitations by electrons (plasma state excitations by electrons). *Springer Tracts in Mod. Phys.*, 38:84–157, 1965.

94. R.H. Doremus. Optical properties of thin metallic films in island form. *Journal of Applied Physics*, 37(7):2775–2781, 1966.

95. A. Sentenac, G. Toso, and M. Saillard. Study of coherent scattering from one-dimensional rough surfaces with a mean-field theory. *Optical Society of America*, 15 (4):924–931, 1998.

96. A. Sentenac and J.J. Greffet. Mean-field theory of light scattering by onedimensional rough surfaces. *Journal of Optical Society of America A*, 15 (2):528–532, 1998.

97. C.A. Guérin and A. Sentenac. Second-order perturbation theory for scattering from heterogeneous rough surfaces. *Journal of Optical Society of America A*, 21 (7):1251–1260, 2004.

98. W. Mahoney, S.T. Lin, and R.P. Andres. . In *Material Research Symposium Proceedings*, volume 355, page 83. MRS, 1995.

99. M.C. Barnes, D.-Y. Kim, and N.M. Hwang. The mechanism of gold deposition by thermal evaporation. *Journal of Ceramic Processing Research*, 1(1):45–52, 2000.

100. G. Binnig, C.-F. Quate, and C. Gerber. Atomic force microscope. *Phys. Rev. Lett.*, 56(9):930–933, Mar 1986.

101. A.L. Barabasi and H.E. Stanley. *Fractal concepts in surface growth*. Cambrigde University Press, Cambridge, USA, 1995.

102. J. Lekner. *Theory of reflection of electromagnetic and particle waves*. Martinus Nijhoff publishers, Dordrecht, 1987.

103. Edward D. Palik. *Handbook of optical constants of solids*, volume I. Academic Press, 1985.

104. J. C. Maxwell-Garnett. Colours in metal glasses and in metallic films. *Phil. Trans. Roy. Soc. A*, 203:385–420, 1904.

105. D.A.G. Bruggeman. Berechnung verschiedener physikalischer konstanten von heterogenen substanzen. i. dielektrizitatskonstanten und leitfahigkeiten der mischkorper aus isotropen substanzen. *Ann. Phys. Lpz.*, 24:636–679, 1935.

106. T.C. Choy. *Effective Medium Theory. Principles and Applications*. Clarendon Press, Oxford, New York, 1999.

107. L. Ward. *The optical constants of bulk materials and films*. Optics and Optoelectronic Series. Institute of Physics Publishing, Bristol, England, 2nd edition, 1994.

108. P.B. Johnson and R.W. Christy. Optical constants of the noble metals. *Phys. Rev. B*, 6(12):4370–4379, 1972.

109. Dwight E. Gray, editor. *American Institute of Physics (AIP) Handbook*. McGraw-Hill, 3rd edition edition, 1972.

110. C.-E. Berger, R.P.H. Kooyman, and J. Greve. Resolution in surface plasmon microscopy. *Rev. Sci. Instrum.*, 65(9):2829–2836, 1994.

111. T. Roland, A. Khalil, L. Berguiga, L. Bonneviot, J. Elezgaray, A. Arneodo, and F. Argoul. The role of chemical glass treatment on the morphology of thermally evaporated thin gold films: an afm and spr study. *In preparation*, 2009.

112. A. Arnedo, N. Decoster, and S.G. Roux. A wavelet-based method for multifractal image analysis. i. methodology and test applications on isotropic and anisotropic random rough surfaces. *European Physical Journal B*, 15:567–600, 2000.

113. A. Khalil, G. Joncas, F. Nekka, P. Kestener, and A. Arneodo. Morphological analysis of h i features. ii. wavelet-based multifractal formalism. *The Astrophysical Journal Supplement Series*, 165 (2):512–550, 2006.

114. A. Khalil, J.L. Grant, L.B. Caddle, E. Atzema, K. Mills, and A. Arneodo. Chromosome territories have a highly nonspherical morphology and nonrandom positioning. *Chromosome Research*, 15:899–916, 2007.

115. A. Khalil, G. Joncas, and F. Nekka. Morphological analysis of h i features. i. metric space technique. *The Astrophysical Journal*, 601 (2):352–364, 2004.

116. Z. X. Xie, X. Xu, B. W. Mao, and K. Tanaka. Self-assembled binary monolayers of n-alkanes on reconstructed au(111) and hopg surfaces. *Langmuir*, 18 (8):3113–3116, 2002.

117. M. Argaman, R. Golan, N.H. Thomson, and H.G. Hansma. Phase imaging of moving dna molecules and dna molecules replicated in the atomic force microscope. *Nucleic Acids Research*, 25 (21):4379–4384, 1997.

118. J. Tamayo and R. Garca. Deformation, contact time, and phase contrast in tapping mode scanning force microscopy. *Langmuir*, 12 (18):4430–4435, 1996.

119. T. Aytun, O.F. Mutaf, O.J. el Atwani, and C.W. Ow-Yang. Nanoscale composition mapping of segregation in micelles with tapping-mode atomic force microscopy. *Langmuir*, 24 (24):14183–14187, 2008.

120. S.N. Magonov, V. Elings, and M.H. Whangbo. Phase imaging and stiffness in tapping-mode atomic force microscopy. *Surface Science*, 375 (2–3):L385–L391, 1997.

121. D. L. Angst and G. W.Simmons. Moisture absorption characteristics of organosiloxane self-assembled monolayers. *Langmuir*, 7 (10):2236–2242, 1991.

122. P. Silberzan, L. Leger, D. Ausserre, and J. J. Benattar. Silanation of silica surfaces. a new method of constructing pure or mixed monolayers. *Langmuir*, 7 (8):1647–1651, 1991.

123. K. M. R. Kallury, M. Thompson, C. P. Tripp, and M. L. Hair. Interaction of silicon surfaces silanized with octadecylchlorosilanes with octadecanoic acid and octadecanamine studied by ellipsometry, x-ray photoelectron spectroscopy, and reflectance fourier transform infrared spectroscopy. *Langmuir*, 8 (3):947–954, 1992.

124. S. Pillai and R. K. Pai. Controlled growth and formation of sams investigated by atomic force microscopy. *Ultramicroscopy*, 109 (2):161–166, 2009.

125. R.K. Wild. Surface analytical techniques. *Advanced Materials for Optics and Electronics*, 5:53–70, 1995.

126. A.-S. Duwez. Exploiting electron spectroscopies to probe the structure and organization of self-assembled monolayers: a review. *Journal of Electron Spectroscopy and Related Phenomena*, 134:97–138, 2004.

127. S. Gunther, B. Kaulich, L. Gregoratti, and M. Kiskinova. Photoelectron microscopy and applications in surface and materials science. *Progress in Surface Science*, 70:187–260, 2002.

128. L. Lallement, C. Gosse, A. Rhallabi, and Ch. Cardinaud. *Plasma diagnostics and surface characterisation for the etching of silica glass in inductively coupled fluorine based plasmas*. Journees Nationales sur les Technologies Emergentes en Micro–nanofabrication.

129. J.W. Goodman. Some fundamental properties of speckle. *Journal of the Optical Society of America*, 66 (11):1145–1150, 1976.

130. J. Laverdant, S. Buil, B. Berini, and X. Quelin. Polarization dependent near-field speckle of random gold films. *Physical Review B*, 77:165406, 2008.

131. D. M. Mattox. *Handbook of Physical Vapor Deposition (PVD) processing.* Noyes Publications, 1998.

132. David R. Lide, editor. *Handbook of Chemistry and Physics 89th Revised edition.* CRC Press Inc, 2008.

133. M.J. Assael, S. Botsios, K. Gialou, and I.N. Metaxa. Thermal conductivity of polymethyl methacrylate (pmma) and borosilicate crown glass bk7. *International Journal of Thermophysics*, 26 (5):1595–1605, 2005.

134. A. Henry and G. Chen. High thermal conductivity of single polyethylene chains using molecular dynamics simulations. *Physical Review Letters*, 101:235502, 2008.

135. M.A. El-Sayed. Small is different: Shape-, size-, and composition- dependent properties of some colloidal semiconductor nanocrystals. *Accounts of Chemical Research*, 37 (5):326–333, 2004.

136. G.P. Wiederrecht. Near-field optical imaging of noble metal nanoparticles. *The European Physical Journal Applied Physics*, 28:3–18, 2004.

137. M.A. van Dijk, M. Lippitz, and M. Orrit. Far-field optical microscopy of single metal nanoparticles. *Accounts of Chemical Research*, 38:594–601, 2005.

138. S. Berciaud, D. Lasne, G.A. Blab, L. Cognet, and B. Lounis. Photothermal heterodyne imaging of individual metallic nanoparticles: theory versus experiments. *Physical Review B*, 73:045424, 2006.

139. F.V. Ignatovich and L. Novotny. Real-time and background free detection of nanoscale particles. *Phys. Rev. Lett.*, 96:013901(1–4), 2006.

140. J Elezgaray, L. Berguiga, T. Roland, and F. Argoul. Optical characterization of decorated nanostructures. *In preparation*, 2009.

141. T. Grosjean, D. Courjon, and D. Van Labeke. Bessel beams as virtual tips for near-field optics. *Journal of Microscopy*, 210 (3):319–323, 2003.

142. M.F. Juette, T.J. Gould, M.D. Lessard, M.J. Mlodzianoski, B.S. Nagpure, B.T. Bennett, S.T. Hess, and J. Bewersdorf. Three-dimensional sub-100 nm resolution fluorescence microscopy of thick samples. *Nature Methods*, 5:527–529, 2008.

143. S.T. Hess, T.P.K. Girirajan, and M.D. Mason. Ultra-high resolution imaging by fluorescence photoactivation localization microscopy. *Biophysical Journal*, 91:4258–4272, 2006.

144. J.D. Watson and F.H. Crick. The structure of DNA. *Cold Spring Harbor Symposia on Quantitative Biology*, 18:123–131, 1953.

145. F. Montel. *Dynamique à l'équilibre et hors-équilibre de la chromatine visualisée par Microscopie à Force Atomique : effet des variants d'histone et des facteurs de remodelage.* PhD thesis, Ecole Normale Supérieure de Lyon, 2009.

146. K. Lüger, A.W. Mäder, R.K. Richmond, D.F. Sargent, and T.J. Richmond. Crystal structure of the nucleosome core particle at 2.8a resolution. *Nature*, 389:251–260, 1997.

147. P. Milani, G. Chevereau, C. Vaillant, B. Audit, Z. Haftek-Terreau, M. Marilley, P. Bouvet, F. Argoul, and A. Arneodo. Nucleosome positioning by excluding genomic energy barriers. *submitted to Proceedings of the National Academy of Sciences*, 2009.

148. B. Lewin, editor. *Cells*. Jones & Bartlett Publishers, 2006.

149. B.R. Selvi, D. Jagadeesan, B.S. Suma, G. Nagashankar, M. Arif, K. Balasubramanyam, M. Eswaramoorthy, and T.K. Kundu. Intrinsically fluorescent carbon nanospheres as a nuclear targeting vector: delivery of membrane-impermeable molecule to modulate gene expression in vivo. *Nano Letters*, 8 (10):3182–3188, 2008.

150. E. Metwalli, D. Haines, O. Becker, S. Conzone, and C.G. Pantano. Surface characterizations of mono-, di-, and tri-aminosilane treated glass substrates. *Journal of Colloid and Interface Science*, 298:825–831, 2006.

151. C.A. Goss, D.H. Charych, and M. Madja. Application of (3-mercaptopropyl)trimethoxysilane as a molecular adhesive in the fabrication of vapor deposited gold electrodes on glass substrates. *Analytical Chemistry*, 63:85–88, 1991.

152. K. Luger, T.J. Rechsteiner, and T.J. Richmond. Expression and purification of recombinant histones and nucleosome reconstitution. *Methods in Molecular Biology*, 119:1–16, 1999.

153. V. Mutskov, D. Gerber, D. Angelov, J. Ausio, J. Workman, and S. Dimitrov. Persistent interactions of core histone tails with nucleosomal dna following acetylation and transcription factor binding. *Molecular and Cellular Biology*, 18:6293–6304, 1998.

154. S. Mallat and S. Zhong. Characterization of signals from multiscale edges. *IEEE Transactions on Pattern Analysis and Machine Intelligence*, 14 (7):710–732, 1992.

155. S. Mallat and W.L. Hwang. Singularity detection and processing with wavelets. *IEEE Transactions on Information Theory*, 38 (2):617–643, 1992.

Appendices

Appendix A

Materials and methods

A Cleansing of the substrates

A.1 Glass coverslips

Prior to the chemical treatment of the glass surfaces[111] or the deposition of gold[54,111], the coverslips were cleaned in a caustic detergent (Decon 90 from Decon, Sussex, England) for 2 to 3 hours at $50°C$, and then rinsed two times in distilled water (at least 2 hours each) at room temperature. After this, the coverslips were quickly rinsed with ultrapure water (18 $M\Omega.cm^{-1}$), absolute ethanol (Merck, Darmstadt, Germany) and finally dried under a nitrogen flow.

A.2 Gold surfaces

Before doing the experiments shown in chapter 2, the gold surfaces are thoroughly rinsed with absolute ethanol, and dried under a nitrogen flow.
The substrates used in the other chapters are afterwards cleaned by O_3, in a UV/O_3 chamber (for 20-30 minutes). They are then, either deposited for 30 minutes in absolute ethanol in order their reactivity to get back to normal, or immersed into the SAM solution.

B Deposition of the thin gold films

B.1 Preparation of the films used in the deposition rate study from chapter 2, section A

22x22 mm BK7 coverslips (n_c=1.51509 at 632.8 nm) purchased from Menzel-Gläser (Braunschweig, Germany) are cleansed as presented in section A.1.
Two sets of gold films are prepared using a thermal evaporation[131] system (MS300, Plassys S.A.), at different rates, respectively 0.02 nm/s (slow deposition mode) and 0.4 nm/s (fast deposition mode). Evaporation was performed under high vacuum ($\sim$ 8 10^{-6} mbar at the

beginning). It was afforded by ohmic heating of a gold wire up to fusion. The deposited gold weight, monitored in real time by a quartz microbalance, is fixed (with a relative accuracy of 0.1%) and corresponds to an effective thickness of 45 nm for plain gold.

B.2 Deposition of the gold films on the chemically glass substrates from chapter 2, section B

Just after the chemical treatment (see section C.1), gold was deposited onto all substrates at the same time, no matter the concentration of chemicals. The protocol from section B.1 has been improved as follows. Prior to the evaporation, $\sim$ 1 cm of the gold wire was sonicated into absolute ethanol for 10 minutes, thoroughly rinsed with absolute ethanol, dried under a nitrogen flow, and finally deposited into the alumina coated hearth of the thermal evaporation[131] system. Before the evaporation process, all Cs were deposited close to each other in such a way the evaporation parameters (speed, time, thickness...) were identical regardless of the 11MUD$(MeO)_3$Si concentration treatment.
To ensure a good homogeneity of gold in the hearth and avoid depositing impurities during the evaporation stage, the wire was heated for 30 minutes at a temperature of about 1800°C in the vacuum chamber ($P \sim 4\ 10^{-6}$ mbar at the beginning of the evaporation, and $P \sim 5\ 10^{-5}$ mbar when gold is deposited). Afterwards, heat was gently increased, and when the rate of evaporation reached 0.4 nm.s^{-1} (with a relative accuracy of 5%), the shutter was opened and gold was deposited onto the substrates (as explained previously, its temperature was not controlled during deposition). After the deposition of a 45 nm gold layer, the shutter was closed, heating stopped, and a break of 20 minutes was made. Finally, the pressure was progressively elevated back to ambient conditions.
If not used immediately, gold-Cs were stored into individual closed vessels filled with absolute ethanol to prevent pollution with impurities.

Moreover, other 11MUD$(MeO)_3$Si treated Cs (without a gold film) were stored into individual closed vessels filled with degased ethanol until being imaged by AFM.

B.3 Deposition of the gold films by cathodic pulverization

The gold films used in the study on the NPs detection from chapter 3 were prepared by ACM (Villiers Saint Frederic, France) by cathodic pulverizing.[131] First, a layer of chromium (<2 nm) and then a gold layer of 45 nm were deposited on 22x22 mm BK7 coverslips heated at 264°C and under vacuum (7.4 10^{-9} bar). Prior to the deposition of the metal layers, the glass substrates were cleansed as in section A.1.

B.4 Preparation of the substrates used in the liquid experiments

20 mm round coverslips (n_c=1.7845 at 632.8 nm) purchased from Olympus are cleansed as explained in section A.1. The substrates are prepared by depositing first, a $\sim$2 nm chromium layer, and then a 45 nm gold film, by thermal evaporation, and at a rate of $\sim$0.04 nm/s for

both.

The SSPM experiments done in liquid have been carried out with a 1.65 NA objective lens (100x) from Olympus and a matching index oil n_0=1.7845 (at λ=632.8 nm). It has to be noted that the adaptation oil has to be changed every ∼45 min because it evaporates and crystalizes with time, and the image series are in consequence done for a smaller scale of defocalization values.

C Self-assembled monolayer preparation

C.1 Chemical treatment of the glass substrates by 11MUD(MeO)$_3$Si

The experiments presented in chapter 2, section B were carried out on 12 mm circular BK7 glass Cs also purchased from Menzel-Gläser.
After cleansing with Decon, the coverslips were arranged inside a glass Petri dish (up to eight substrates per dish) so as to be treated with the molecules.
Cyclohexane (99.8% for HPLC, Fisher Scientific, France) was degased with argon during one hour, and 11MUD(MeO)$_3$Si molecules (Prochimia, Poland) were diluted into it at a final concentration of 10 mg.ml^{-1}. In order to ensure the absence of aggregates in solution, the solution was vortexed for 15 minutes at maximum speed (beforehand, the atmosphere of the tube was saturated with argon to prevent air from getting back into the mixture). 11MUD(MeO)$_3$Si molecules in cyclohexane were subsequently diluted to reach a final concentration (0 mg.ml^{-1}, 0.001 mg.ml^{-1} or 0.01 mg.ml^{-1}) into degased cyclohexane and vortexed for 10 minutes (again at maximum speed) so that the emulsion was homogeneous.
Then, this emulsion was poured into (5 ml into a 6-cm-diameter dish) and then stored under argon atmosphere for 20 hours. The molecules then linked to the surface and rearranged into a compact and highly ordered monolayer[150] that shows thiol heads, increasing the wettability of gold for the Cs and improving its adhesion to it[151] (see figure A.1).
Finally, the SAM coated glass substrates were thoroughly rinsed with cyclohexane and dried under a nitrogen flow.

C.2 1-Mercaptoundecanol (MUO) and 11-Amino-1-undecanethiol (AUT) SAM preparation on gold substrates

First, Phosphate Buffer (abbreviated as PB; pH 7 and 100 mM ionic strength) was prepared and degased with argon during one hour. AUT or MUO molecules[54] were then diluted into degased ethanol (they are not soluble in aqueous buffers) at a final concentration of 10 mg.ml^{-1} each, with a 15 minutes vortexing at maximum speed to ensure there was no aggregate in solution (the atmosphere was saturated with argon). AUT and MUO molecules in ethanol were subsequently mixed at a given ratio and diluted to a final concentration of 0.1 mg.ml^{-1} into PB and vortexed 10 minutes (at maximum speed) so that the emulsion was

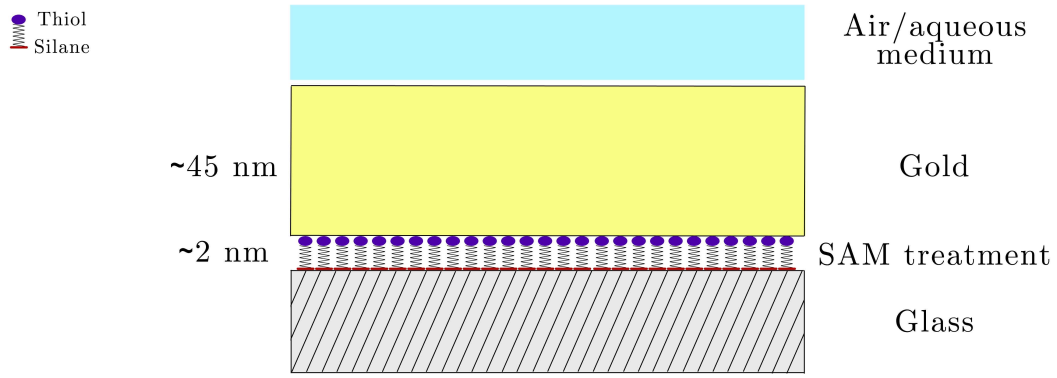

Figure A.1 Sketch representation of the SPR chips after treatment with 11-mercapto-undecyl-methoxysilane molecules and deposition of a 45 nm gold layer. Thanks to their silane groups, 11MUD$(MeO)_3$Si molecules form a self-assembled monolayer onto the glass coverslip, and thiol heads enhance the affinity of gold with respect to the substrate.

homogeneous.
Just after the O_3 treatment, the coverslips were immersed into Ar degazed the mixture (PB/ethanol or PB/ethanol/AUT) which was stored under argon atmosphere for 20 hours. Finally, the SAM coated gold layer samples were first thoroughly rinsed with ultrapure water and then quickly rinsed with absolute ethanol and dried with nitrogen gas before use. If not used immediately, the SAM-coated samples were stored for a maximum of seven days in absolute ethanol in individual closed vessels.

D Adsorption of the NPs onto the samples and SSPM imaging

Calibrated (C) and non-calibrated (NC) gold or latex NP have been purchased from Ted Pella Inc. (USA) and stored at room temperature until being used.

A uniform deposition of isolated NPs on gold surface was optimized as follows. For all experiments carried out in air and water, C or NC gold NP were dispersed in ultrapure water (18 M$\Omega.cm^{-1}$) to a final concentration ranging from 10^7 to 10^9 particles.ml^{-1}. A drop of $\sim$150 μl of the NPs dispersion was then deposited on a cleaned bare gold surface, and stored in an air oven at 60°C for about one hour.

After diluting the C and NC latex to a final concentration ranging from 10^5 to 10^9 p.ml^{-1} in PB (pH 8 and 100 mM ionic strength), a droplet of 150 μl of NPs solution was deposited onto the SAM coated gold surface (20% MUO, 80% AUT) and stored for one hour in an air oven at 80°C.
To avoid the formation of salt crystals upon drying on samples with latex NPs, they were rinsed with 1 ml of ultrapure water and dried under nitrogen gas before running the experi-

ments in air or water.

For experiments carried out in water, the NPs were first imaged in air and 20-50 μl of water were afterwards injected in the flow cell (which volume is 5 μl).

E Preparation of the nucleosomes

DNA fragments amplification

The human IL2RA promoter sequence (898 bp) on chromosome 10: 4433-5331 (NCBI, locus n° NG007403), was amplified by PCR with Taq polymerase (Sigma) from human genomic DNA.

E.1 Protein purification and nucleosome reconstitution

Recombinant full-length histone proteins of *Xenopus laevis* were overexpressed in bacteria and purified as previously described.[152] Nucleosome reconstitution was performed by the salt dialysis procedure.[153] The reaction was stopped in TE buffer (10 mM Tris-HCl, pH 7.4, 1mM EDTA) and 10 mM NaCl. Nucleosomes were reconstituted with histone/DNA ratio 1/0.8.

E.2 Deposition of the nucleosomes on the gold surfaces

10 μl of a $\sim$2 nM reconstitution solution in imaging buffer (10 mM Tris-HCl, pH 7.9) were deposited onto cleaned gold surfaces for about two minutes before rinsing with a 100 μl drop of water, and drying under nitrogen flow.

F Preparation of the IMR-90 and 293T cells for SSPM imaging

Two cell lines were observed in this thesis: (i) 293T cells (originated from human fetal kidney) and (ii) IMR–90 cells (primary culture of fibroblasts of human fetal lung).
The cells were cultivated at 37° in the growth buffer (EMEM, 10% SVF, NEaa) and an atmosphere saturated with 5% of CO_2. They were peeled off by addition of trypsin, counted, and resuspended in the growth buffer at a concentration of 100 000 cells/ml. The gold coated glass substrates were deposited inside tissue culture plates and a volume of 3 ml of cell suspension was poured into each well (*i.e.* $\sim$300 000 cells). Cells were incubated during 48 h so that the cells are dense enough and still, not at confluence. Each coverslip was subsequently rinsed with PBS 1X, treated with absolute methanol (at -20°) and incubated 30 min on ice. Methanol was eliminated and the samples were then incubated 2$\times$ 5 min in PBS 1X, 0.1% Triton, before a series of 5 min dehydration steps (70%, 90% and 100%) in

absolute ethanol. Finally, the coverslips were dried under nitrogen flow and stored in vacuum at ambient temperature.

Appendix B

Object segmentation with the 2D WTMM method

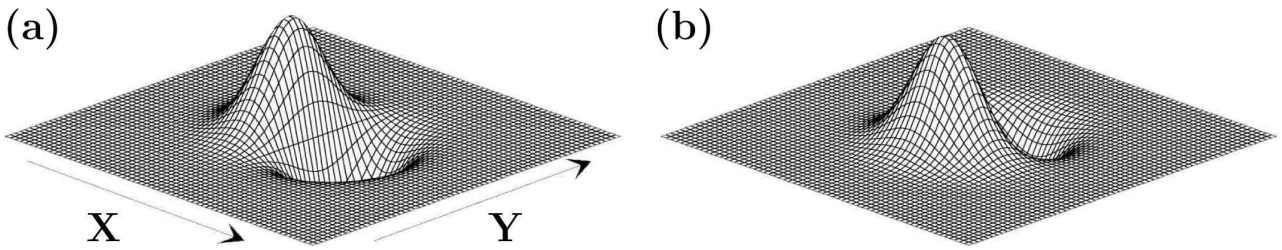

Figure B.1 3D plot of the derivative of the 2D Gaussian wavelet function used for the WTMM method, along the two axis X (a) and Y (b).

The 2D WTMM (wavelet transform modulus maxima) method[112,113] is primordially a multifractal analysis tool that was adapted to perform accurate and objective object segmentation.[114]

Image segmentation with continuous wavelets is based on the derivative of a 2D smoothing function (filter) acting as an "edge detectorïí. Let us consider two wavelets that are, respectively, the partial derivatives with respect to x and y of a 2D smoothing (Gaussian) function,

$$\phi_{\mathrm{Gau}}(x,y) = e^{-(x^2+y^2)/2} = e^{-|\mathbf{x}|^2/2}, \tag{B.1}$$

namely

$$\begin{gathered} \psi_1(x,y) = \partial\phi_{\mathrm{Gau}}(x,y)/\partial x \\ \text{and} \\ \psi_2(x,y) = \partial\phi_{\mathrm{Gau}}(x,y)/\partial y. \end{gathered} \tag{B.2}$$

For any function $f(x,y) \in L^2(\mathbf{R})$ (where $L^2(\mathbf{R})$ consists of all square integrable functions), the continuous wavelet transform of f with respect to ψ_1 and ψ_2 is expressed as a vector:[154,155]

$$\mathbf{T}_\psi[f](\mathbf{b},a) = \begin{pmatrix} T_{\psi_1}[f] = a^{-2}\int d^2\mathbf{x}\ \psi_1\big(a^{-1}(\mathbf{x}-\mathbf{b})\big) f(\mathbf{x}) \\ T_{\psi_2}[f] = a^{-2}\int d^2\mathbf{x}\ \psi_2\big(a^{-1}(\mathbf{x}-\mathbf{b})\big) f(\mathbf{x}) \end{pmatrix} = \nabla\{T_{\phi_{\mathrm{Gau}}}[f](\mathbf{b},a)\} = \nabla\{\phi_{\mathrm{Gau},\mathbf{b},a} * f\}. \tag{B.3}$$

Thus, Eq. (B.3) amounts to define the 2D wavelet transform as the gradient vector of $f(\mathbf{x})$ smoothed by dilated versions of $\phi_{\mathrm{Gau}}(a^{-1}\mathbf{x})$ of the Gaussian filter.

The wavelet transform can be written in terms of its modulus and argument

$$\mathbf{T}_\psi[f](\mathbf{b},a) = \big(\mathcal{M}_\psi[f](\mathbf{b},a), \mathcal{A}_\psi[f](\mathbf{b},a)\big), \tag{B.4}$$

where

$$\mathcal{M}_\psi[f](\mathbf{b},a) = \sqrt{\big(T_{\psi 1}[f](\mathbf{b},a)\big)^2 + \big(T_{\psi 2}[f](\mathbf{b},a)\big)^2}, \tag{B.5}$$

and

$$\mathcal{A}_\psi[f](\mathbf{b},a) = \mathbf{Arg}\big(T_{\psi 1}[f](\mathbf{b},a) + iT_{\psi 2}[f](\mathbf{b},a)\big). \tag{B.6}$$

The wavelet-transform modulus maxima (WTMM), or intensity gradient maxima are defined by the positions where the modulus of the WT, $\mathcal{M}_\psi[f](\mathbf{b},a)$, i.e., the gradient, is locally maximum. These WTMM are automatically organized as maxima chains which act as contour lines of the smoothed image at the considered scales. At a given scale, the algorithm scans all the boundary lines that correspond to the highest values of the gradient, i.e. the maxima chains. The algorithm then keeps only those maxima chains that are connected. This process is repeated at all scales, from large to small. The algorithm expects to detect large objects at very large scales, but it is instructed to look for those large objects to become smaller objects at smaller scales. The algorithm goes through a loop in order to make sure that the gold blobs are detected at the smallest possible scale, where most details on the boundary of the segmented objects will be obtained. No subjectivity is introduced. As the algorithm performs the segmentation on smaller and smaller scales, it stops when the boundary lines are no longer connected, i.e. at a scale where the WT starts resolving the noisy component in the image. For a detailed description, the reader is referred to Khalil *et al.*[114]

The segmented gold blobs can be rigorously defined and characterized mathematically. Let $\mathbf{B} \subset \mathbf{R^2}$ denote the domain in the real plane where the gold object is circumscribed. Several geometrical parameters can therefore be defined.

2D Geometrical Parameters

→ The *area*, A, of the domain $\mathbf{B}$ in the real plane is

$$A = \int\int_{\mathbf{B}} dxdy. \tag{B.7}$$

→ The *diameter*, D, of the domain $\mathbf{B}$ is

$$D = \sup_{(x,y)\ \in\ \mathbf{B}} d\Big((x,y),\mathbf{B}\Big), \text{ where } d\Big((x,y),\mathbf{B}\Big) = \sup_{(x',y')\ \in\ \mathbf{B}} d\Big((x,y),(x',y')\Big), \tag{B.8}$$

and where d is the standard Euclidean metric, i.e.,
$d\Big((x,y),(x',y')\Big) = \sqrt{(y'-y)^2 + (x'-x)^2}$.

→ If the boundary of $\mathbf{B}$, γ, has the parameter form $\mathbf{r}(t) = \Big(x(t), y(t)\Big)$, then the *perimeter*, P, is given by

$$P = \int_{\gamma} \sqrt{x'(t)^2 + y'(t)^2} dt. \tag{B.9}$$

→ The *filament index*, F,[113,114] is a measure of non-circularity:

$$F = \frac{PD}{4A}, \tag{B.10}$$

where P, D, and A denote respectively the perimeter, diameter and area of the domain $\mathbf{B}$. Clearly, a circular domain will have a value of $F = 1$ but any value of $F > 1$ quantifies the departure from a circular shape.

3D Geometrical Parameters

Given the topographical nature of the AFM images (see Chapter 2), let $f : \mathbf{B} \to \mathbf{R}$ define the height of the gold surface for any point $(x, y) \in \mathbf{B}$, we wish to define the maximum height, H, of each gold blob, as well as the actual volume of the blob, V. However, detailed care is needed to computationally evaluate H and V since their values depend on the topography of the region of the plane neighboring the domain $\mathbf{B}$. Therefore, in practice H is obtained by considering the highest pixel value inside the domain $\mathbf{B}$ and subtracting from it the average pixel value on the segmented boundary, γ. Let Γ denote the average value of f around the boundary γ, i.e.

$$\Gamma = \frac{\int_{\gamma} \mathbf{r}(t) dt}{P}. \tag{B.11}$$

→ The (relative) *maximum height*, H, is given by

$$H = \sup_{(x,y) \in \mathbf{B}} f(x, y) - \Gamma. \tag{B.12}$$

→ Similarly, V is obtained by summing the (relative) values of f inside $\mathbf{B}$. The *volume*, V, of the gold blob is given by

$$V = \int \int_{\mathbf{B}} \Big(f(x, y) - \Gamma\Big) dx dy. \tag{B.13}$$

ALGORITHMIC IMPLEMENTATION

All the Fourier and WTMM algorithms are regrouped into one standalone customized software called Xsmurf. Xsmurf is a Tcl/Tk-based scripting software where all of the mathematical algorithms are coded in C or C++ and called from the Tcl interface. It uses several homemade algorithms as well as some open source libraries such as FFTW and Matheval.

Abstract

Most of the microscopy techniques used to study biological samples or processes relies on the use of markers (and particularly on fluorescent probes), or on physical probes (AFM or SNOM tips...), that can interact more or less strongly with the observed samples. As a consequence, these techniques may artificially modify the phenomena that are measured.
In order to propose an alternative to these techniques, a high resolution Scanning Surface Plasmon Microscope (SSPM) has been developed in the Laboratoire de Physique and the Laboratoire Joliot-Curie at the Ecole Normale Supérieure de Lyon. This microscope relies on the excitation of surface plasmon waves that consist in collective oscillations of the free electrons at the surface of a metal layer. This resonance is extremely sensitive to the variation of the dielectric index at the interface (and so, to the adsorption of objects such as biological samples). This phenomenon is already used in the global measurement of molecular interactions between two populations (such as antigen-antibody), that are not necessarily marked (Biacore-like or wide field surface plasmon microscopy techniques). The SSPM technique relies on the use of a very high numerical aperture objective lens that focuses the incident light on a small area of the metal surface. The propagation of the plasmon waves towards the center of the illuminated area leads to their structuring and it is actually because of the scanning on the sample that the local variations of the dielectric index are detected.

In the first chapter of this thesis manuscript, we present the principles of high resolution surface plasmon microscopy, both from an experimental and a theoretical point of view. We also present a model of the optical response of the microscope which is based on a multipolar expansion of the Maxwell equations.
In chapter two, we characterize layers of gold that have been deposited onto glass substrates by thermal evaporation. We demonstrate that the SSPM method is able to detect with a very high sensitivity the surface or bulk inhomogeneities of these metal layers. It can also be used to compare samples with varying structures, obtained with different preparation recipes. We address in a third chapter the problem of imaging isolated nanomaterials (metallic and dielectric particles) of different sizes (from 10 to 200 nm of diameter). We show that this method is well suited to visualize such objects and also to discriminate their size or the material they are made of (depending on their dielectric index).
Finally, we apply in the last chapter the SSPM to the visualization of unlabelled biological samples, such as nucleosomes (nucleoproteic complexes) or human fibroblasts in which we resolve several cellular structures (nucleus, nucleolus, cytoskeleton structures).

Keywords: Surface Plasmon Resonance, SPR, Interferometric Surface Plasmon Microscopy, Sub--Wavelength Resolution Imaging, Plasmon Phase Imaging, Atomic Force Microscopy, AFM, Physical Vapor Deposition, Thin Gold Films, Surface Roughness, Wavelet-Based Surface Analysis, NanoParticle, DNA, Nucleosome, Label-Free Cellular Microscopy, Sub-Cellular Structure Detection.

Résumé

La plupart des techniques de microscopie utilisées dans l'étude d'échantillons ou de processus biologiques repose sur l'utilisation de marqueurs (en particuliers fluorescents), ou de sondes physiques (pointes AFM, SNOM...), pouvant interagir plus ou moins fortement avec les échantillons observés. Potentiellement, ce type de technique risque donc de modifier artificiellement les phénomènes mesurés.
Afin de proposer une alternative à ces techniques, un microscope haute résolution reposant sur l'utilisation des plasmons de surface (Scanning Surface Plasmon Microscope, ou SSPM) a été développé au sein du laboratoire de Physique et du laboratoire Joliot-Curie de l'Ecole Normale Supérieure de Lyon. Ce microscope repose sur l'excitation des plasmons, modes d'oscillations collectives des électrons libres d'une couche métallique, dont la condition de résonance est extrÍmement sensible à la variation d'indice diélectrique (et à donc la présence d'objets, en particulier biologiques) au niveau de cette surface. Ce phénomène est déjà utilisé pour la mesure globale d'interactions moléculaires entre deux populations (type antigène-anticorps), non nécessairement marquées (techniques de type Biacore, et de microscopie plasmon en champ large). L'atout essentiel du SSPM est l'utilisation d'un objectif à forte ouverture numérique qui focalise la lumière incidente dans une petite zone de l'interface métal/milieu d'observation. La propagation des ondes plasmoniques vers le centre de la zone illuminée conduit à leur structuration et c'est grâce au balayage de l'échantillon que les variations locales d'indice diélectrique des échantillons sont révélées par cet outil.

Dans le premier chapitre de cette thèse, nous nous attachons à présenter les principes de microscopie haute résolution à plasmon de surface d'un point de vue expérimental mais aussi théorique, en particulier par la modélisation de la réponse optique du microscope par l'intermédiaire d'un développement multipolaire des équations de Maxwell.
Dans un deuxième temps, nous effectuons la caractérisation de couches minces d'or déposées par évaporation thermique sur des substrats de verre. Lors de cette étude, nous montrons que la méthode SSPM permet de détecter avec une très grande sensibilité les inhomogénéités de volume ou de surface de ces couches métalliques, ainsi que leurs variations suivant la préparation des échantillons.
Nous abordons dans une troisième partie la visualisation par microscopie SSPM de nanomatériaux synthétiques (particules métalliques et diélectriques) isolés de différentes tailles (de 10 à 200 nm de diamètre). Nous montrons ainsi que cette méthode est tout à fait adaptée pour imager de tels objets et qu'elle permet aussi de les différencier suivant leur taille ou le type de matériau dont ils sont faits (via leur indice diélectrique).
Enfin, nous appliquons l'imagerie SSPM à la visualisation d'objets biologiques non marqués comme des nucléosomes (complexes nucléoprotéiques d'une taille d'environ 5nm d'épaisseur et 11nm de diamètre), ou encore des fibroblastes humains pour lesquels nous résolvons certaines sous structures (noyau, nucléoles, structures du cytosquelette).

Mots clés: Résonance de Plasmon de Surface, SPR, Microscopie de Plasmon de Surface Interférométrique, Imagerie Sub-Longueur d'Onde, Imagerie Plasmonique par dÈtection de la Phase, Microscopie à Force Atomique, AFM, Dépôt Physique par Phase Vapeur, Couche Mince d'Or, Rugosité de Surface, Analyse de Surface par Détection en Ondelettes, NanoParticule, ADN, Nucléosome, Microscopie Cellulaire Sans Marquage, Détection de Sous-Structure Cellulaire.